WAVE

Wing-in-ground-effect Aerial Vessel for Emergencies

Adam El Assal	5727871	Marnick Stoll	5816106
Jaime de Salas Juanas	5690633	Martin Pjetri	5772168
Leonardo Sigolo	5458749	Owen Moon	5744628
Qihao Guo	5223253	Shuard Nijdam	5466725
Thomas Antens	5778328	Vincent Schorren	5778859

Delft University of Technology

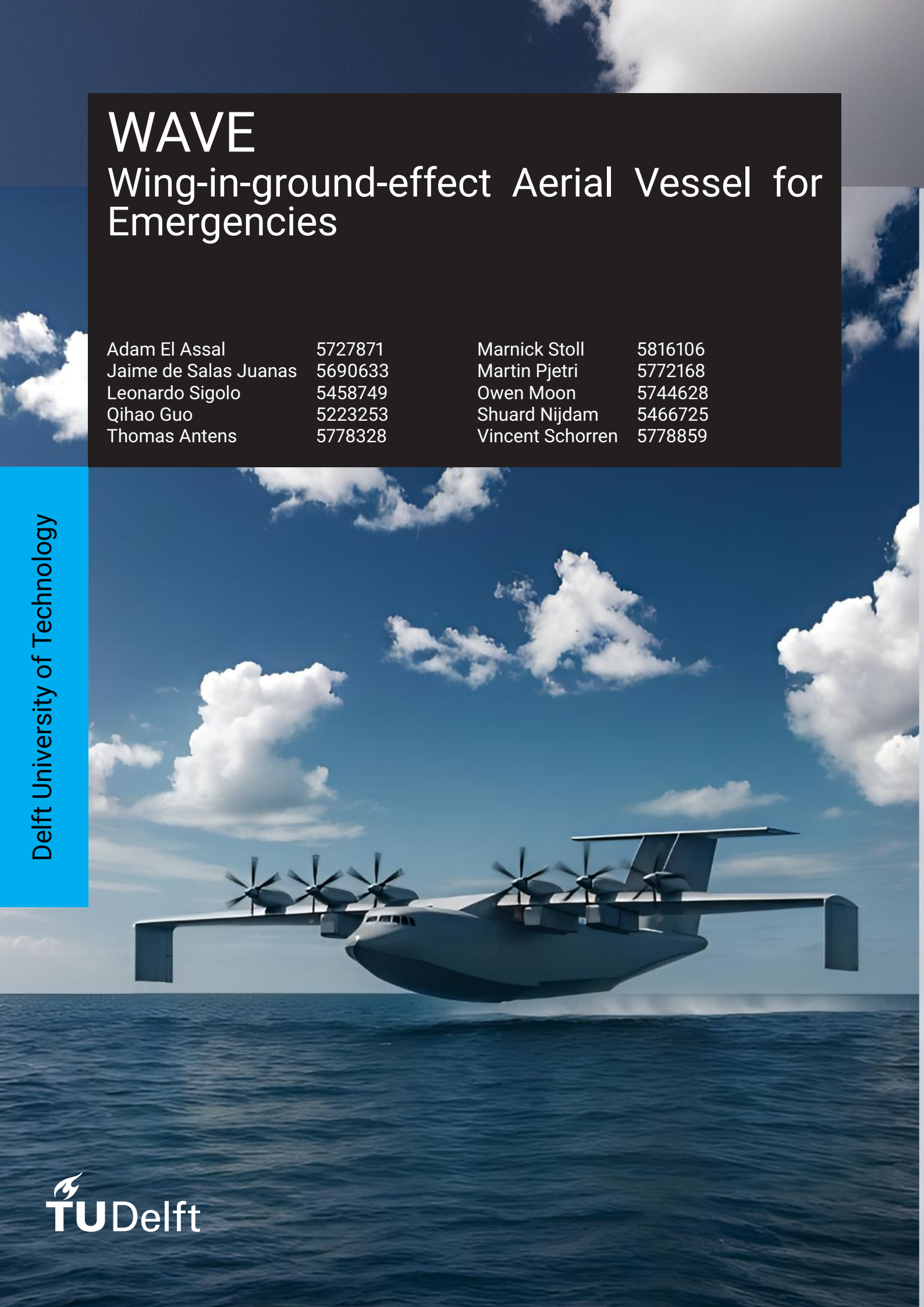

TU Delft

THIS PAGE IS INTENTIONALLY LEFT BLANK

Executive Overview

This report is part of a series created to support the design of a Wing-in-ground-effect Aerial Vessel for Emergencies vehicle (WAVE) developed during the Bachelor Design Synthesis Exercise at TU Delft Aerospace Engineering. The project objective and mission statement are presented below:

Mission Need Statement: Due to climate change and rising sea levels, a sustainable form of airborne cargo transport is needed for quick disaster response in rough sea conditions.
Project Objective Statement: Design a ground effect cargo aircraft, carrying 90 $[tonnes]$, at a minimum cruise speed of 180 $[kts]$ over a 2000 $[nmi]$ range and avoiding obstacles by flying up to 10,000 $[ft]$.

In the previous report multiple design options where set-up and the most promising design option was chosen. This ended up being design option 10, which utilizes a high wing, single fuselage and conventional tail configuration. This decision was justified by a thorough sensitivity analysis. In Figure 1, design option 10 is shown in the midterm specification. The design properties for the midterm specification is given in Table 1. In Figure 2 the configuration layout is shown.

Table 1: *Design Properties for Midterm Specification*

Parameter	Value	Unit
MTOW	$2.54 \cdot 10^6$	$[N]$
OEW	$1.26 \cdot 10^6$	$[N]$
Mission Fuel	$3.87 \cdot 10^5$	$[N]$
Max Power Required	46.2	$[MW]$
Wing Area	508	$[m^2]$
L/D in Ground Effect	27.8	$[-]$
Fuel Economy	0.070	$[L/\text{tonnes/km}]$
Wing Span	63.7	$[m]$
Wing MAC	8.5	$[m]$
Wing Root Chord	11.4	$[m]$
Wing Taper Ratio	0.4	$[-]$
Wing Sweep c/4	0.0	[deg]
Wing Dihedral	1.0	[deg]
Wing LE Position	28.6	$[m]$
Fuselage Length	75.1	$[m]$
Fuselage Diameter	8.8	$[m]$
Horizontal Tail Area	99.8	$[m^2]$
Vertical Tail Area	74.5	$[m^2]$
Horizontal Tail LE Position	67.6	$[m]$
Vertical Tail LE Position	66.0	$[m]$

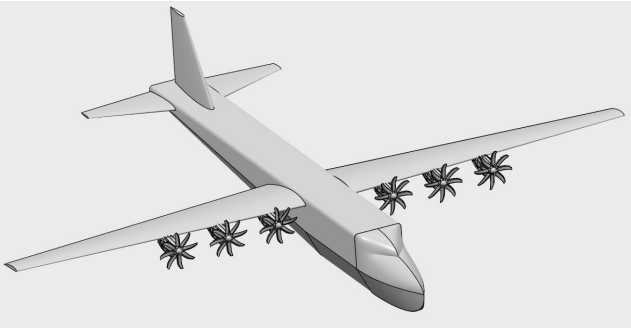

Figure 1: *Design Option 10 in Midterm Specification*

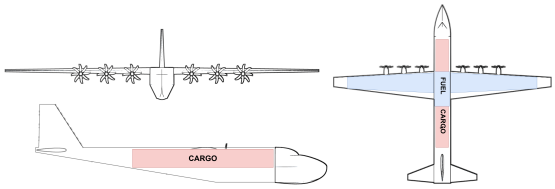

Figure 2: *Configuration Layout of Design Concept 10*

Market Analysis and Operations

To assess WAVE's purpose, it is essential to determine and analyse the target market. The first part of this analysis is the beach profile. In order to ensure the aircraft can beach on the islands, an analysis on the beach profiles has been performed. The average beach profile is shown in Figure 3.

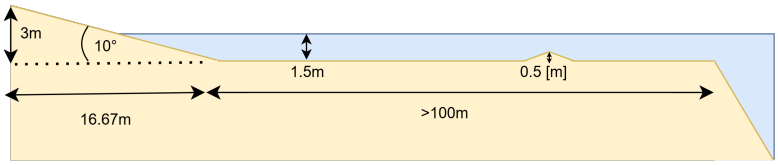

Figure 3: *Mean Beach Profile*

During beaching and offloading, several scenarios may occur. Figure 4 illustrates three potential configurations.

Aerodynamics

The aerodynamic properties of the aircraft include the airfoil, lift curve, drag polar, high lift devices, aerodynamic centre and Oswald efficiency. The airfoil selection process indicated that the Glenn Martin-2il was

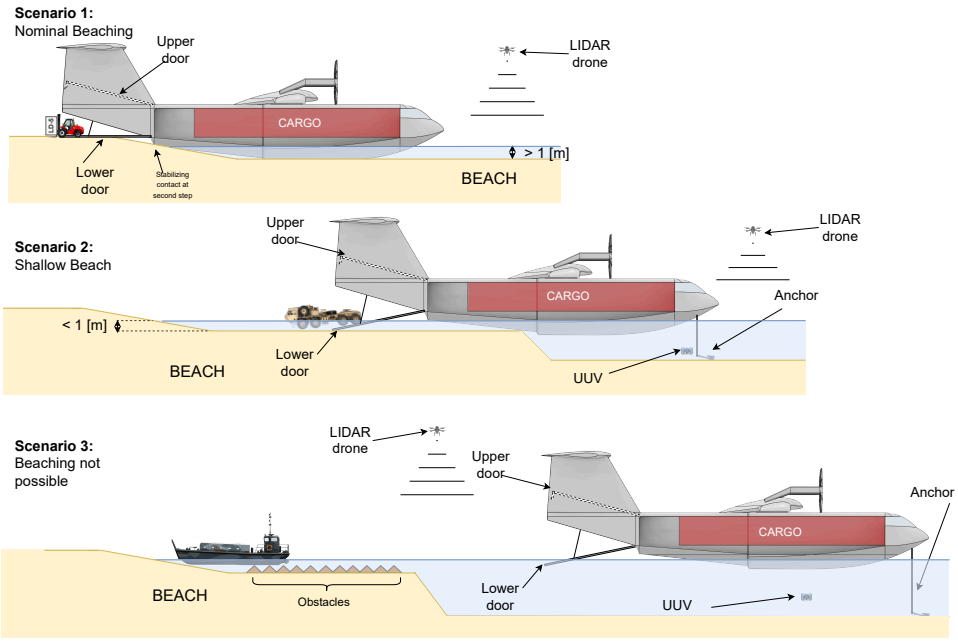

Figure 4: *Beaching Scenarios*

the most suitable choice, offering superior ground effect performance, a high thickness-to-chord ratio, and strong aerodynamic efficiency. The lift curve and drag polar, both in and out of ground effect, are shown in Figure 5a and Figure 5b. These were obtained using the method described by Phillips [1].

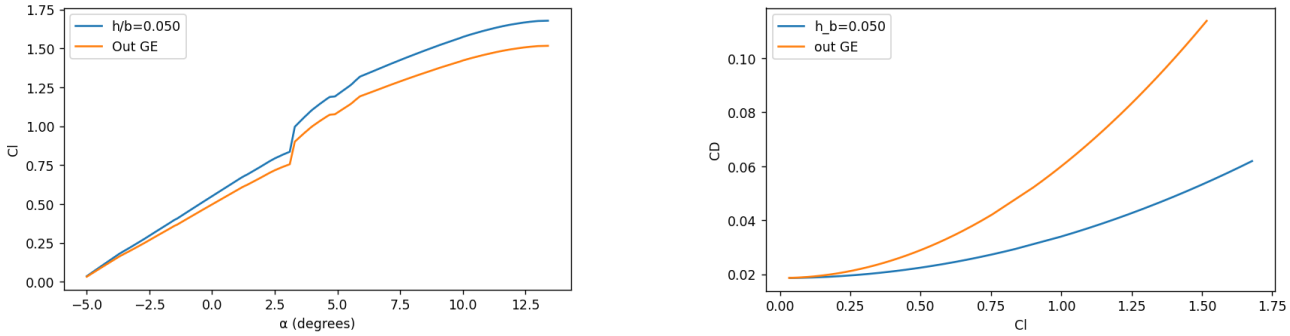

(a) *Lift Curve*

(b) *Drag Polar*

Figure 5: *Aerodynamic Characteristics: Lift Curve and Drag Polar*

There is a noticeable discontinuity at the 3.2[deg] angle of attack in Figure 5a. Further inspection found that this discontinuity represents a sudden jump in the transition point along the lower side boundary layer, possibly causing the discrepancy. Figure 5b shows that drag is lower when flying in ground effect. This reduction is primarily due to wing-tip vortices being suppressed by the proximity to the ground, which minimises downstream and consequently induced drag. The high-lift devices are designed to a maximum lift coefficient of 2.2, resulting in the flap size and wing planform shown in Figure 6.

Table 2: *Drag Breakdown*

Component	Zero Lift Drag Coefficient
Fuselage	0.0026
Wing-Tail	0.0081
Nacelles (buoys included)	0.0011
Miscellaneous	0.0032
Total	0.0150

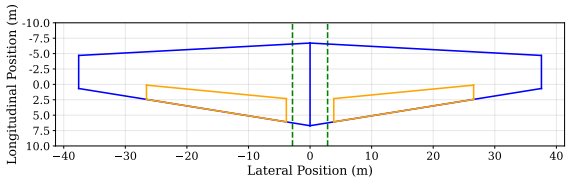

Figure 6: *High Lift Devices*

Table 3: *Aerodynamic Parameters*

Parameter	Value	Unit
b	75	$[m]$
S	706	$[m^2]$
$\bar{c}$	10	$[m]$
λ	0.4	[-]
A	8	[-]
Flap Type	Single Slotted	[-]
Relative Flap Chord	0.30	$[c]$
S_{flap}	65.9	$[m^2]$
C_{d_0}	0.015	[-]
e	0.838	[-]
x_{ac_1}	0.32	$[\bar{c}]$
$C_{m_{ac_1}}$	-0.0959	[-]
x_{ac_2}	0.40	$[\bar{c}]$
$C_{m_{ac_2}}$	-0.2609	[-]

The final sizing results of the high-lift devices, along with various aerodynamic parameters and the wing planform, are presented in Table 3. These aerodynamic parameters include the zero lift drag, the Oswald efficiency coefficient, the aerodynamic centre and the moment around the aerodynamic centre. Subscript 1 refers to the aerodynamic centre and the associated moment for angles of attack ranging from -4.5 [deg] to 3.0 [deg], while subscript 2 corresponds to the range from 6.0 [deg] to 11 [deg]. These two regions exist due to an unsteady aerodynamic centre in between these regions. Table 2 contains a drag breakdown of the major aircraft components with their contribution to the zero lift drag.

Stability and Control

To ensure stability and controllability of the aircraft, a horizontal and vertical tail must be present in the design. The horizontal tail size and position are determined based on the aircraft's centre of gravity and stability & control requirements. The most forward centre of gravity is located at 20.8 $[m]$ and the most aft is at 23.6 $[m]$. The parameters of the horizontal tail are presented in Table 4.

Table 4: *Table of Parameters Horizontal Tail*

Parameter	Value	Unit
S_h/S	0.19	[-]
S_h	134	[m^2]
b_h	24.62	[m]
c_{rh}	6.07	[m]
c_{th}	5.14	[m]
λ_h	0.847	[-]
MAC_h	5.62	[m]
$(x_{LEMAC}/l_{fus})_{wing}$	0.361	[-]

Table 5: *Table of Parameters Vertical Tail*

Parameter	Value	Unit
S_v/S	0.129	$[-]$
S_v	91.35	$[m^2]$
A_v	1.5	$[-]$
b_v	11.71	$[m]$
c_{r_v}	5.85	$[m]$
c_{t_v}	5.25	$[m]$
MAC_v	7.97	$[m]$
$\Lambda_{V_{LE}}$	42.37	$[deg]$
$\Lambda_{V_{c/4}}$	15	$[deg]$
x_{LE_V}	42.37	$[m]$

The sizing of the vertical tail is primarily driven by One Engine Inoperative (OEI) control, lateral stability and spin recovery. Unlike conventional aircraft, crosswind capability is not a factor here. This aircraft lands on water, allowing it to align with the wind and eliminate crosswind constraints.

Given the aircraft's six engine configuration, compared to the two or four engine basis of related design methods, a safety factor of 1.2 is applied. This adjustment is consistent with Torenbeek's method, particularly as illustrated in Figure 9-23 from [2, p.336]. Additionally, the design incorporates two vertical tails to allow the rear of the aircraft to fold open. The total required vertical tail area is evenly divided between these

two fins to ensure symmetric behaviour. The final parameters for the vertical tail are given in Table 5.
The elevator is primarily sized for a 2.5g pull-up manoeuvrer. While take-off rotation in water, which creates significant nose-down pitching, was also considered, the pull-up manoeuvre was determined to be the most critical case. In Table 6 the final parameters can be found along with a layout of the horizontal tail in Figure 7.

Table 6: *Outputs of Final Elevator Sizing (Half the Wing)*

Parameter	Value	Unit
Sw_e(spanned area)	64.8	[m^2]
S_e	24.3	[m^2]
τ_e(elevator effectiveness)	0.58	[-]
$C_{m_{\delta_e}}$	-1.62	[rad^{-1}]
$C_{z_{\delta_e}}$	-0.059	[rad^{-1}]
$\delta_{e_{TakeOff}}$	-3.0	[deg]
Max Elevator Lift	$3.27 \cdot 10^5$	[N]
$\delta_{e_{trim}}$	-1.66	[deg]

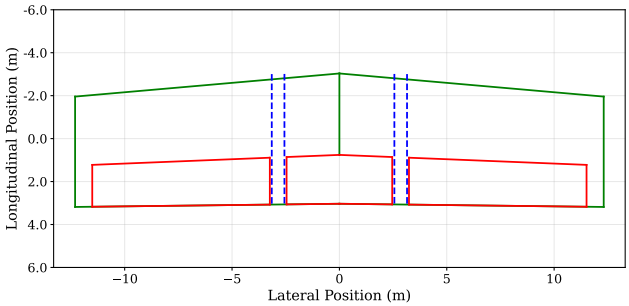

Figure 7: *Horizontal Tail Planform with Elevator Position and Size, Leading Edge is Upwards*

The rudder is crucial for the aircraft's lateral control, with its sizing primarily driven by the one-engine-inoperative condition. In this scenario, the rudder must generate sufficient control authority to counteract the yaw moment caused by asymmetric thrust. Since, the aircraft features two vertical tails, each rudder is designed to independently generate the required yaw moment in case the other fails. A safety factor of 1.5 is applied for conservative sizing and to account for the two vertical tails.

The inputs and outputs of the final rudder sizing are presented in Figure 8. Also, the configuration of the rudder on the vertical tail is shown in Figure 9.

Figure 8: *Outputs of Final Rudder Sizing*

Parameter	Value	Unit
S_r	25.3	[m^2]
τ_r(rudder effectiveness)	0.53	[-]
$C_{n_{\delta_r}}$	-0.088	[rad^{-1}]
Sw_r(spanned area)	72.3	[m^2]
$C_{l_{\delta_r}}$	0.027	[rad^{-1}]
$C_{Y_{\delta_r}}$	0.32	[rad^{-1}]
Max Rudder Lift	$1.69 \cdot 10^5$	[N]

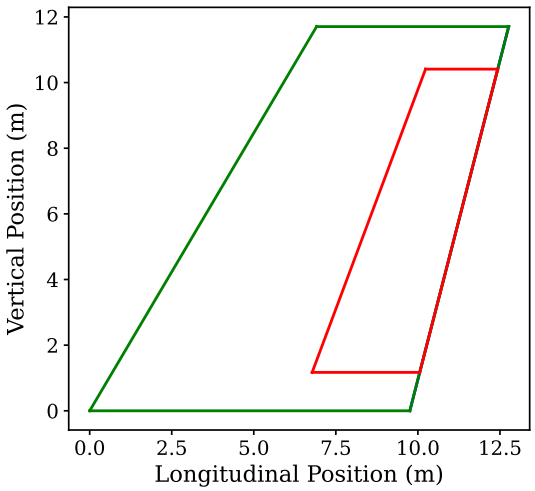

Figure 9: *Rudder Configuration*

The most critical scenario for aileron sizing is the roll rate needed for obstacle avoidance. This is defined as the rate required to achieve the maximum bank angle within the tightest possible turn radius around an obstacle. It is assumed that both ailerons will deflect equally to achieve this necessary roll rate. In Figure 7, the planform is specified along with a visualisation besides it in Figure 10.

Table 7: *Outputs of Final Aileron Sizing (Half the Wing)*

Parameter	Value	Unit
S_a	14.92	[m^2]
τ_a(aileron effectiveness)	0.47	[-]
$C_{l_{\delta_a}}$	-0.19	[rad^{-1}]
Max Aileron Lift	$1.2 \cdot 10^5$	[N]
Sw_a(spanned area aileron)	59.68	[m^2]

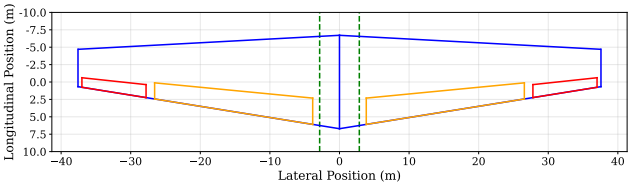

Figure 10: *Top View of Wing Planform with the Sized Ailerons, Leading Edge is Upwards*

Wing tip buoys are sized solely for stability. To minimise aerodynamic impact, preventing the aircraft from tipping over on water. To simplify complex hydrodynamics and ensure safety, the buoys are conservatively assumed to provide all roll stability, placing the rolling axis at the hull's bottom for maximum de-stabilising leverage. Both static and dynamic roll stability are considered, with a 5-degree maximum static bank angle for crew comfort. Sizing accounts for both Operating Empty Weight (OEW) (one buoy touching water) and Maximum Take Off Weight (MTOW) (both buoys providing restoring moment). WAVE's symmetric eigenmotions (phugoid and short-period) are stable. A controller with auto-throttle and elevator actuation is proposed for future implementation to provide damping to phugoid motion. While Dutch roll and aperiodic roll modes are stable, the spiral motion is unstable, which poses safety concern for ground effect cruise despite its acceptable doubling time. To counteract this, a Linear Quadratic Regulator (LQR) is implemented as part of the fly by wire system for precise holding of attitude under straight, level cruise. Further work is needed to extend this controller to a Linear Quadratic Integral (LQI) controller for achieving turning and banking.

Structural Design

This section illustrates the structural design of WAVE. First, the fuselage was designed. In Figure 11 the cross section of the fuselage is shown. In Table 8, the results of the fuselage design are tabulated.

Table 8: *Inputs and Outputs for Fuselage Lengths*

Parameter	Value	Unit
Cockpit Height	2.5	[m]
Cockpit Length	4.3	[m]
Deadrise Angle	25	[deg]
Step Height	0.5	[m]
Tail Cone Upsweep	11	[deg]
Cargo Height	4.2	[m]
Cargo Width	5.2	[m]
Nose Cone Length	6	[m]
Forebody Length	18.6	[m]
Afterbody Length	14.805	[m]
Tail Cone Length	12	[m]

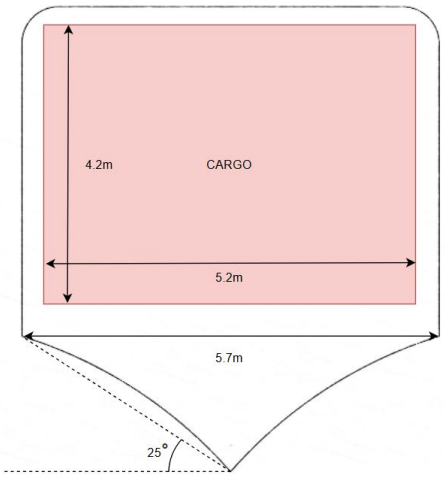

Figure 11: *Fuselage Cross-Section*

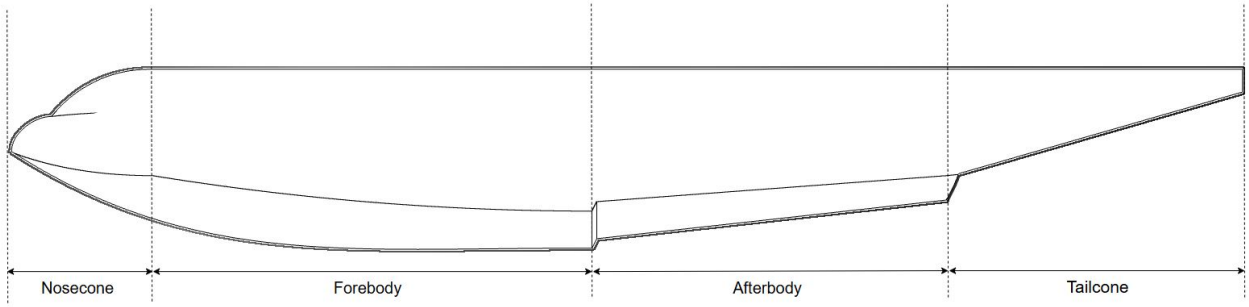

Figure 12: *Fuselage Lengths Side View*

The fuselage design illustrated in Figure 12 is capable of carrying the loads that the aircraft will encounter. This design is based on structural aspects as well as cargo housing capabilities and on-water operations. For the fuselage skin, aluminium 7075 will be used. The end of the fuselage will have a cargo opening mechanism from which the cargo will be loaded and offloaded.

The second part of the structural design is performed to ensure that the wing can sustain the aerodynamic loads. This was done by designing an appropriate wing box. The wing box of the wing has 4 spars and 3 cells. The placement of the lateral ribs is shown in Figure 13 and the appropriate thickness variation is shown in Figure 14. The wing skin sustains lower loads, which is why the lighter, less strong aluminium 5052 alloy is used for this part of the aircraft.

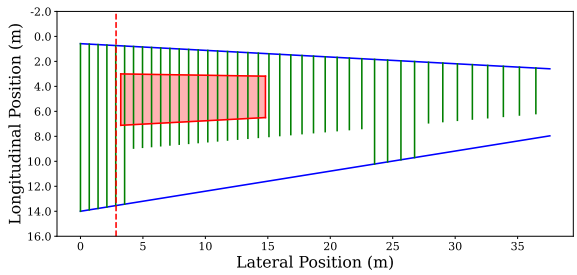

Figure 13: *Top View of the Right Wing with Ribs and Fuel Tank Shown; Leading Edge is Upwards*

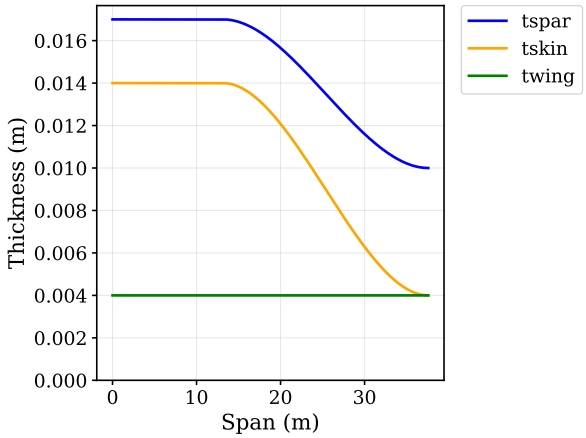

Figure 14: *Thickness Distributions Along the Wing Span*

The vertical and horizontal tails also have a wing-box, but only with one cell and two spars. For all the wing boxes aluminium 7075 will be used. To ensure WAVE can handle the sea condition, side buoys are placed on the tips as discussed earlier. This is also taken into account in the sizing of the wing box. During water operations, the aircraft must be corrosion resistant. To counter this effect, a nano material reinforced epoxy coating was applied on the exposed parts of WAVE.

Propulsion System and Powerplant

An iterative design process, utilising XROTOR, focused on optimising the propeller blade by analysing the effects of RPM, blade radius, and number of blades. Key findings indicate that, while more blades and larger radii generally increase efficiency, structural feasibility and tip speed limits led to the selection of six blades and a maximum radius of 3 meters. The final design features a thinner, unswept blade with significant twist, made from a carbon-reinforced composite to withstand high loads. Final parameters and visualisation of the propeller can be found in Figure 15 and Table 9.

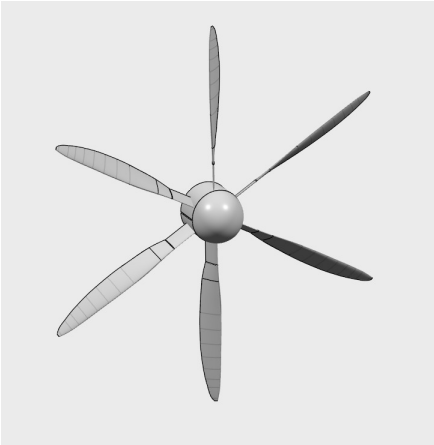

Figure 15: *Designed Propeller Blade*

Table 9: *Propeller Blade Parameters*

Parameter	Value	Unit
Disk Area	27.77	$[m^2]$
Solidity	0.233	$[-]$
Number of Blades	6	$[-]$
Blade Diameter	6.00	$[m]$
Hub Diameter	0.40	$[m]$
Base Chord	332	$[mm]$
Max Chord	442	$[mm]$
Total Twist	48.8	[deg]
Blade mass	49	$[kg]$

To meet the requirement for zero CO_2 and NO_x emissions during on-water operations (before engine start), WAVE will be primarily powered by lithium-ion batteries. Hydrogen Auxiliary Power Units (APU) and solar panels were considered but deemed too complex or unsuitable for the marine environment. Lithium-ion batteries were chosen for their longevity, energy density, and recyclability. These batteries will power essential systems, including buoy compressors (30 $[kW]$ for 22 minutes), LED lights (4.5 $[kW]$ for 4 hours), communications (15 $[kW]$ for 4 hours), air-conditioning (30 $[kW]$ for 4 hours), electric motors for the cargo door (25 $[kW]$ for 3 minutes), and the anchor winch (12 $[kW]$ for 15 minutes). A total energy capacity of ~ 1,300,000 $[kJ]$ is required, accounting for a two-way mission and typical battery efficiency.

For safety, the batteries will be placed in the 'hump' connecting the wing to the fuselage, above the waterline, and enclosed in a reinforced, coated metal casing. Additionally, a Hamilton Sundstrand APS 3240 APU will be integrated in the same location to provide bleed air for engine start and emergency power for critical flight systems.

Flight Performance

From the physical and aerodynamic properties, the performance of WAVE can be evaluated. In Figure 16, the wing and power loading diagram is given.

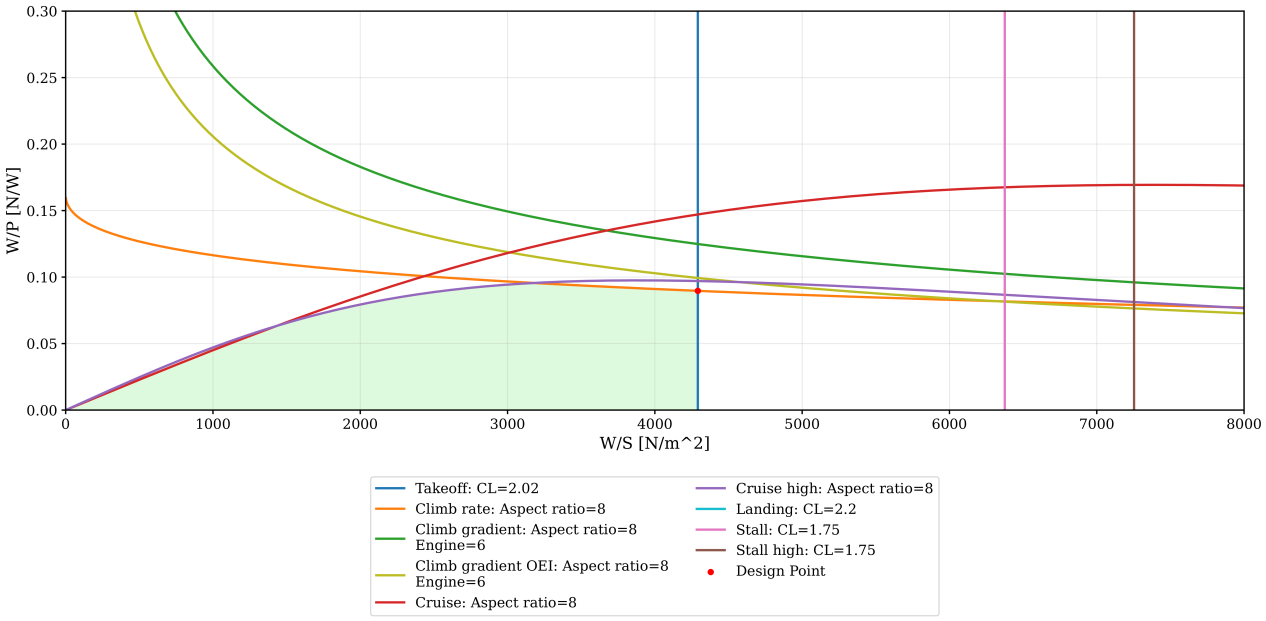

Figure 16: *Wing and Power Loading*

The second part of the performance is the payload range diagram in Figure 17a and Figure 17b for the design and altitude mission, respectively.

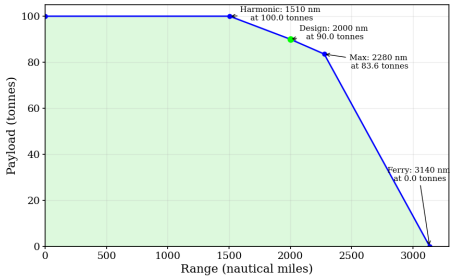

(a) *Payload Range Diagram Two Way Mission*

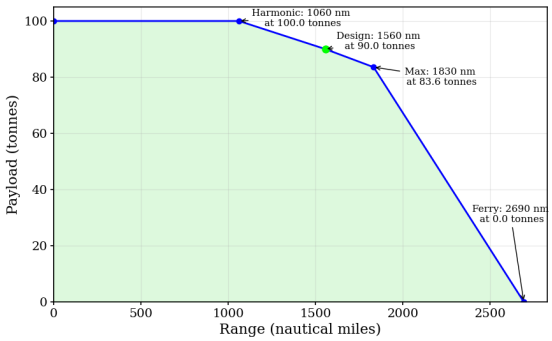

(b) *Payload Range Diagram Obstacle Avoidance Mission*

Figure 17: *Payload Range Diagram*

In Figure 17, the maximum, design, harmonic and ferry ranges are shown. The second part of the performance is shown in Figure 18, where the cruise performance is illustrated for flying at a speed that deviates from the maximum. Also, the flight envelope is shown in Figure 19.

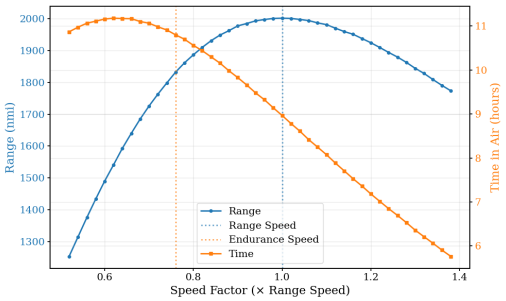

Figure 18: *Cruise Speed v.s. Achievable Range and Time in a Two Way Mission with 90 Tonnes of Payload*

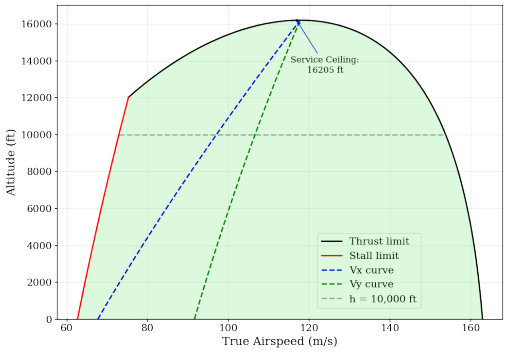

Figure 19: *Altitude-Velocity Flight Envelope*

In Figure 19, it can be seen that the maximum altitude is 16,205 $[ft]$. This is while operating the design mission, which means flying in sea state 0. Finally, in Figure 20, the effect of the sea state on the range is given.

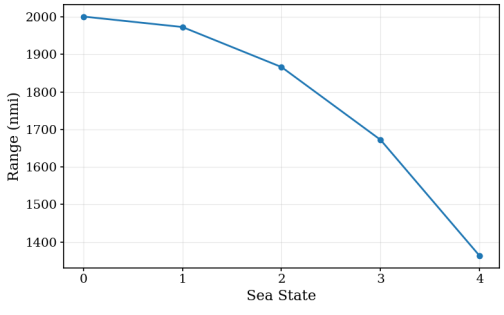

Figure 20: *Range of One Leg of Two Way with Varying Sea State*

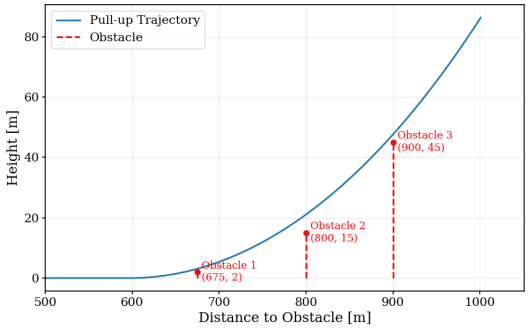

Figure 21: *Side View of Pull-Up Obstacle Avoidance Manoeuvre Trajectory*

From Figure 20, it can be seen that the sea state has a significant effect on the range, but WAVE can still operate. Additionally, in Figure 21 the side view of the obstacle avoidance mission is visualised.

Mass and Power Budgets

The mass budget is presented in Figure 22. With the whole pie chart representing the MTOM, which is 302,700 $[kg]$. These results are obtained by a class II iterative estimation. In Figure 23, the subsystem power

budget is showcased for key systems. The total subsystem power needed during cruise is 269 $[kW]$ and at altitude 463 $[kW]$. This difference is caused by the temperature change at high altitude, which means the Wing Anti Ice System (WIPS) and Environmental Control System (ECS) use significantly more power.

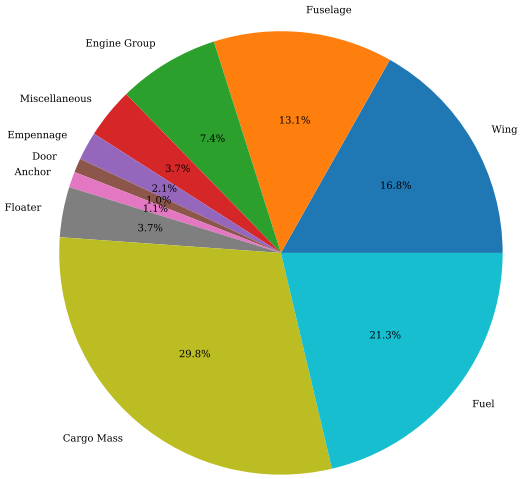

Figure 22: *Mass Budget*

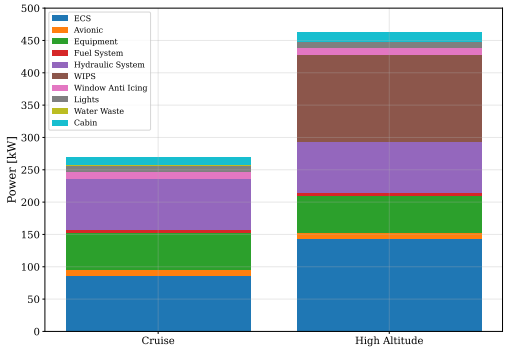

Figure 23: *Subsystem Power Budget*

A comprehensive cost analysis reveals a total program cost of $15 billion for 50 units. This translates to a single unit cost of $278 million, which is significantly more economical than the C-5 Galaxy's unit cost of $475 million. Furthermore, the operational cost is projected to be $0.35 per tonne-kilometre, notably outperforming the C-5 Galaxy's operational cost of $0.50 per tonne-kilometre.

Requirement check and Risk Assessment

The compliance matrix for WAVE shows that only one requirement needed to be reconsidered. Namely REQ-STR.5, this is related a new way of beaching, which implements inflatable buoys. After which, compliance with the requirement was achieved. Due to the work performed in the final phase, a substantial number of risks have been downgraded to non-critical without requiring mitigation. At this stage of the design, the most concerning risks remain the unstable transition from hydrodynamic to aerodynamic operation, and the risk of icing at 10,000$[ft]$ due to a rapid climb through humid conditions. Proposed mitigation strategies include conducting a more detailed stability analysis for the transition phase and applying active heating or hydrophobic coatings to address the icing risk.

Final Design

Figure 24 represents a render of the final design of the WAVE. The project timeline targets the first prototype by April 2031, with entry into service anticipated for January 2035.

Figure 24: *Final Render of WAVE*

Table of Contents

Nomenclature & Abbreviations

Parameter	Description	Unit	Parameter	Description	Unit
$\#_{ac}$	aerodynamic centre	[−]	$\#_{s1}$	section 1	[−]
$\#_{A-h}$	aircraft less tail	[−]	$\#_{s2}$	section 2	[−]
$\#_{cg}$	centre of gravity	[−]	$\#_{side}$	side	[−]
$\#_{e}$	elevator	[−]	$\#_{stall}$	stall	[−]
$\#_{f}$	flap	[−]	$\#_{stringers}$	stringers	[−]
$\#_{frame}$	frame	[−]	$\#_{top}$	top	[−]
$\#_{fuselage}/\#_{fus}$	fuselage	[−]	$\#_{trim}$	trim condition	[−]
$\#_{h}$	horizontal tail	[−]	$\#_{turn}$	turn	[−]
$\#_{hull}$	hull	[−]	$\#_{u}$	derivative with respect to velocity	$[s/m]$
$\#_{max}$	maximum	[−]	$\#_{v}$	vertical tail	[−]
$\#_{net}$	net	[−]	$\#_{w}$	wetted	[−]
$\#_{q}$	derivative to pitch rate	$[s/rad]$	$\#_{\alpha}$	derivative to alpha	$[1/rad]$
$\#_{r}$	derivative to yawing rate	$[s/rad]$	$\#_{\dot{\beta}}$	derivative to change of sideslip	$[s/rad]$
A	aspect ratio	$[m]$	n	number off / load factor	[−]
A	Derivative matrix	[−]	P	Power	$[W]$
b	span	$[m]$	p	roll rate	$[rad/s]$
B	input matrix	[−]	q	pitch rate	$[rad/s]$
b_1	start of mobile surface	$[m]$	**Q**	**LQR matrix**	[−]
b_2	end of mobile surface	$[m]$	$\bar{q}$	dynamic pressure	$[N/m^2]$
c	chord	$[m]$	r	yaw rate	$[rad/s]$
c'	chord of mobile surface	$[m]$	r	radius of the propeller	$[m]$
C_D	Drag coefficient 3D	[−]	S	wing area	$[m^2]$
C_d	Drag coefficient 2D	[−]	t	thickness	$[m]$
C_{D_0}	zero lift drag	[−]	$T_{0.5}$	half time	$[s]$
$C_{D_{misc}}$	miscellaneous drag	[−]	**u**	**input vector**	[−]
C_f	friction coefficient	[−]	$\bar{u}$	velocity deviation	[−]
C_L	Lift coefficient 3D	[−]	V	velocity	$[m/s]$
C_l	Lift coefficient 2D	[−]	W	weight	$[N]$
C_ℓ	rolling moment coefficient	[−]	w_{bouy}	width of the buoy	$[m]$
C_m	moment coefficient	[−]	x	longitudinal position	$[m]$
C_n	yawing moment coefficient	[−]	**x**	**state vector**	[−]
c_r	root chord	$[m]$	y	spanwise position	$[m]$
c_t	tip chord	$[m]$	z	lateral position	$[m]$
$\bar{c}$	MAC	$[m]$	α	angle of attack	$[rad]$
D	Drag	$[N]$	$\alpha_{L=0}$	zero lift angle of attack	$[rad]$
D	diameter	$[m]$	β	side slip angle	$[rad]$
d_{obj}	diameter to object	$[m]$	β_n	resonance coefficient	[−]
e	Oswald factor	[−]	Γ	dihedral	$[rad]$
E	young's modulus	$[N/m^2]$	δ	angle	$[rad]$
f_n	resonance frequency	$[Hz]$	Δ	change	[−]
FF	Form factor	[−]	$\frac{d\epsilon}{d\alpha}$	Downwash gradient	[−]
g	gravitational acceleration	$[m/s^2]$	ζ	damping ratio	[−]
G	shear modulus	$[N/m^2]$	θ	flight path angle	$[rad]$
i	inclination	$[rad]$	λ	taper ratio	[−]
I	Moment of inertia	$[m^4]$	Λ	sweep	$[rad]$
IF	interference factor	[−]	ν	Poisson ratio	[−]
K	gain matrix	[−]	ρ	density	$[kg/m^3]$
L	Lift	$[N]$	σ	stress	$[N/m^2]$
l	length	$[m]$	τ	shear stress	$[N/m^2]$
M	mass	$[kg]$	τ	effectiveness	[−]
M	Moment	$[Nm]$	ϕ	roll	$[rad]$

Table 10: *Abbreviations*

Abbreviation	Explanation	Abbreviation	Explanation
2D	2 Dimensional	LED	Light Emitting Diode
3D	3 Dimensional	LQR	Linear Quadratic Regulator
AE	Aerospace Engineering	MAC	Mean Aerodynamic Chord
AESA	Active Electronically Scanned Array	MAN	Maschinenfabrik Augsburg-Nürnberg
AI	Artificial Intelligence	MATLAB	MATrix LABoratory
Alxxxx	Aluminium xxxx	MDP	Master Design Package
AoA	Angle of Attack	MTOM	Maximum Take Off Mass
APG	Aberdeen Proving Ground	MTOW	Maximum Take Off Weight
APS	American Physical Society	MTR	Manufacturing Technical Risk
APU	Auxiliary Power Unit	NACA	National Advisory Committee for Aeronautics
AR	Aspect Ratio	NATO	North Atlantic Treaty Organization
ATC	Air traffic control	NGOs	Non-Governmental Organization
CAR	CARgo	NSW	New South Wales
CATIA	Computer-Aided Three-Dimensional Interactive Application	OEI	One Engine Inoperative
CG	Center of Gravity	OEM	Operating Empty Mass
CR	Cruise	OEW	Operating Empty Weight
CRTR	CRuise Technical Risk	FTC	Federal Trade Commission
CS-25	Certification Specifications	PD&D/PDD	Project Design and Development
CTS	Certified Technology Specialist	PERF	PERFormance
CUST	CUSTomer	PLTR	Post Landing Technical Risk
DAF	Doorne's Aanhangwagen Fabriek	PU	Power Unit
DAPCA	Domain Adaption Principal Component Analysis	PWR	Pressurized Water Reactor
DATCOM	DAta COMpendium	RADAR	Radio Detection and Ranging
DSE	Design Synthesis Exercise	RAT	Remote Access Trojan
ECS	Environmental Control System	REQ	REQuirement
EDP	Electronic Data Processing	RF	Radio Frequency
EOL	End Of Life	RoC	Rate of Climb
EOLTR	End Of Life Technical Risk	RPM	Rounds Per Minute
FBD	Free Body Diagram	SAF	Sustainable Aviation Fuel
FFD	Fitness For Duty	SEA	Search Engine Advertising
FMC	Fixed-Mobile Convergence	SFC	Specific Fuel Consumption
FMTV	Family of Medium Tactical Vehicles	SHC	Specific Heat Capacity
FPTR	Flight Preparation Technical Risk	STR	Short Tandem Repeat
GE	Ground Effect	SUST	SUSTainability
GEV	Ground Effect Vehicle	SWOT	Strengths, Weaknesses, Opportunities and Threats
GPU	Ground Power Unit	SYS	SYStem
GTR	General Technical Risk	TC	Traffic Control
HEMTT	Heavy Expanded Mobility Tactical Truck	TI-xxxxx	Titanium-xxxxx
HHP	Hydraulic Horse Power	TNL	Template Numerical Library
HLD	High Lift Device	TOTR	Take Off Technical Risk
IMO	International Maritime Organization	UN	United Nation
JSON	JavaScript Object Notation	UUV	Unmanned Underwater Vehicles
LATR	Landing Technical Risk	V&V	Verification and Validation
LCVP	Landing Craft, Vehicle and Personnel	VHF	Very High Frequency
LD	Liquidated Damages	WAVE	Wing-in-ground effect Aerial Vessel for Emergencies
LE	Leading Edge	WIG	Wing In Ground
LIDAR	Light Detection and Ranging	WIPS	Wing Ice Protection System
LIF	Low Insertion Force	XFLR	XFOIl for Lifting Regions

1

Introduction

Sea levels are rising, and the probability of severe weather events is increasing due to climate change. Low-lying regions and remote islands are threatened by these changes. In these regions, relying on infrastructure for disaster response is not an option. Therefore, a fast vehicle that is independent of infrastructure and is able to carry large cargo to disaster zones should is needed. Wing in ground-effect (WIG) aircraft provide the perfect solution for this problem. These aircraft utilise the ground effect to improve fuel efficiency with respect to conventional aircraft while still travelling 8 times faster than conventional marine vehicles with similar capabilities.

The goal of this project is to design a WIG aircraft for disaster response, capable of carrying a 90-tonne payload over 2,000 nautical miles to a disaster zone without infrastructure, travelling at over 180 knots, and returning empty without the need to refuel. This report describes the methods and analysis of results for the preliminary design of the aircraft. By designing this aircraft the project offers an alternative to conventional transport which is independent of infrastructure. Beyond this immediate application of the project, it contributes to the general field of large ground effect vehicles and provides some foundation for further investigation.

The report is structured in seventeen chapters, each describing one design phase. It starts with the market analysis in Chapter 2 which identifies the market gap and determines some of the requirements the aircraft should follow to be competitive with the current market. In Chapter 3 the intended operation of WAVE is described including the cargo configurations, the maintenance flow and the communications. The key system engineering organization and decisions are carried out in Chapter 4 including the results of the iteration procedure, alongside a description of the main iteration method used to converge to a final design complying with all requirements.

Chapter 5 is the first technical chapter which outlines the weight estimations and the iteration between the initial and final weight estimations. Chapter 6 goes in detail into the aerodynamic design in order to find the optimum wing for WAVE and mission. Stability and control including development of the tail and the control surfaces is in Chapter 7. The detailed structural design is in Chapter 8, where the structure of the main components is described. Chapter 9 dives deep into the optimisation of a propeller as well as including the power management systems. The architecture of the fuel, electrical, hardware, software and hydraulic systems is explained in Chapter 10. In Chapter 11 the performance of WAVE is analysed at multiple conditions such as varying speeds or sea states. Budgets are explained in Chapter 12 and the verification and validation of the models used is developed in Chapter 14.

The next steps for further design of WAVE are stated in Chapter 15. Moreover, Chapter 13 describes the strategy to ensure the final design is sustainable. Lastly, the risks that have been identified during the project with their corresponding mitigation strategies are included in Chapter 16. The report is finalised with a conclusion in Chapter 17.

2

Market Analysis

This chapter contains the market analysis for the project. This includes a stakeholder analysis in Section 2.1, an analysis of analysis on Strenghts, Weaknesses, Opportunities, and Threats (SWOT) in the current market (Section 2.2), a description of the cargo hold in Section 2.3, an analysis on the end-of-life of WAVE (Section 2.4) and an analysis of competing aircraft.

2.1. Stakeholder Analysis

This section contains the stakeholder analysis in Table 2.1 below. The figure contains the list of stakeholders, paired with their respective interest, influence, and needs. The 'Interest' column in the stakeholder matrix is analysed from the stakeholders' own perspective, not from the perspective of the design team.

Table 2.1: *Stakeholder Matrix for Disaster Relief Vehicle*

Stakeholder	Interest	Influence	Needs / Expectations
Emergency Services	High	High	Fast deployment, easy operation, reliability in extreme conditions.
Customer	High	High	Cost-effective solutions, adaptability to different disaster scenarios, long-term reliability.
Civilians	High	Low	Rapid access to safety, medical care, and essential supplies.
United Nations	High	High	Scalability, compliance with international humanitarian standards, sustainability.
European Union	High	High	Regulatory compliance, interoperability with European emergency systems, efficiency.
NATO	Medium	High	Ruggedness, tactical adaptability, interoperability with military logistics.
Traffic Control (Air & Marine)	Medium	Medium	Efficient movement and minimal disruption to existing road networks.
Ports	Medium	Medium	Fast loading/unloading, compatibility with port logistics and maritime regulations.
Crew	High	Low	Safety, ergonomic design, ease of operation and maintenance.
Manufacturers	High	Medium	Feasibility of mass production, ease of assembly, supply chain stability.
NGOs	High	High	Affordable, versatile, and durable vehicles for humanitarian missions.

2.2. Current Solutions and Issues

This section contains a SWOT analysis of the current market, an evaluation of the current disaster relief options, the introduction of a new option that does not possess the weaknesses of the current solutions and

a global overview of regions with frequent disasters.

2.2.1. SWOT Analysis

Table 2.2 below contains a SWOT analysis of the current market for disaster response. This analysis was used to explore options in composing requirements and operational options. For instance, the drones mentioned in Chapter 3 based on an opportunity and the fact that WAVE does not need an airport/sea-port to land, taken from a weakness of the current market.

Table 2.2: *SWOT Analysis of the Current Market for Fast Disaster Response*

	Helpful	**Harmful**
Internal	**Strengths** • Variety of transport: trucks, helicopters, cargo planes, ships. • Global organizations: UN, NATO, Red Cross. • Innovation: drones, mobile hospitals, modular shelters. • Public-private partnerships improving response.	**Weaknesses** • Reliance on intact infrastructure (roads, ports, airports). • Slow early-stage coordination. • High aircraft and ship operational costs. • Few purpose-built disaster vehicles.
External	**Opportunities** • Modular, multi-terrain, amphibious vehicles. • AI, automation, remote-controlled systems. • Regional disaster hubs for rapid deployment. • Tech partnerships for communications (e.g., Starlink).	**Threats** • More frequent, severe disasters from climate change. • Political instability complicating logistics. • Airspace and transport route competition. • Funding cuts to preparedness and innovation.

2.2.2. Limitations of Current Disaster Transport Options

Cargo ships are too slow for urgent relief, depend on functional ports, and cannot access inland zones without additional transport. Cargo aircraft require operational airports, are costly to operate frequently, have limited reach to isolated areas, and produce high emissions. Trains rely on intact rail infrastructure, lack flexibility, and are limited geographically. Trucks depend on usable roads, face congestion, struggle with difficult terrain, and have limited fuel availability, with similarly high emissions. Helicopters are expensive, weather-dependent, and have limited cargo capacity. Drones carry only small payloads over short ranges and face regulatory and environmental constraints.

Given these limitations, a new cargo vehicle is needed that combines aircraft speed, cargo ship capacity, and train-like sustainability, while reaching most locations. An aircraft flying in ground effect fits this profile, capable of operating without traditional infrastructure, delivering large payloads faster than ships, and allowing incorporation of advanced sustainability features (see Chapter 13).

2.2.3. Disaster Areas

To identify priority regions for project implementation, an analysis of historical earthquake and flood events has been conducted. The geographical distribution of these earthquakes and floods is depicted graphically in Figure 2.1 and Figure 2.2 [3], which shows earthquake data and flood occurrence records. This spatial analysis reveals high-risk zones where the proposed solution could provide maximum impact. One of the areas that might benefit most from quick disaster response systems is Southeast Asia (SEA). As a result of

its topography and environment, this region is particularly vulnerable to natural catastrophes including earthquakes and floods. Particularly vulnerable are nations with many islands, such as the Philippines and Indonesia. Here, it can be very difficult to promptly reach impacted residents.

Analysing the earthquake sites in Google Earth and fitting radii of design ranges shows that a design range of 2800 nautical miles will cover most of the natural-disaster prone areas in SEA with two bases (one in Manila and one in Brisbane). During analysis, initial estimates of the Maximum Take-off Mass (MTOM) and fuel economy of the design have shown that 2000 nautical miles might be a more feasible range. For this range it is found that three bases (Singapore, Brisbane and Tokyo) provide similar coverage. Consider Figure 2.3 for a visual comparison of the 2800 $[nmi]$ and the 2000 $[nmi]$ ranges.

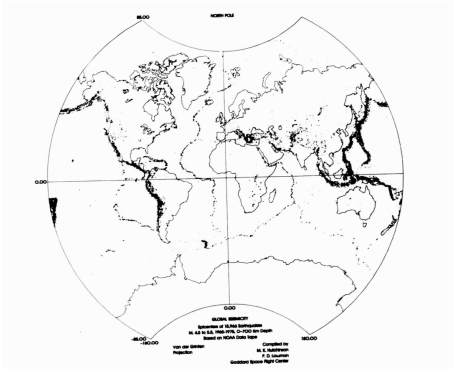

Figure 2.1: *Earthquakes of Magnitude 4.5 to 5.5 from 1965 to 1975[4]*

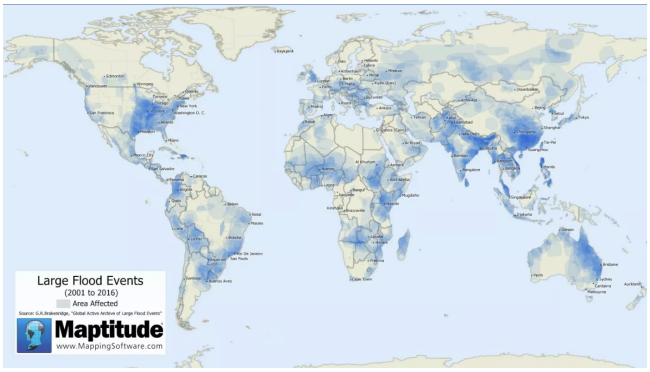

Figure 2.2: *Flood Events from 2001 to 2016 [3]*

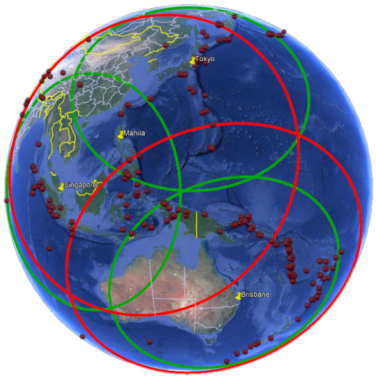

Figure 2.3: *Reach of System Range with Three Bases at 2000 $[nmi]$ (in Green) vs Two at 2800 $[nmi]$ (in Red) and Location of Earthquakes in Last 15 years*

2.2.4. Beach Profiles

In order to evaluate the beaching requirement for WAVE, an analysis needs to be done on the different types of beaches and their profiles that the aircraft can come across during operations. For fulfilling the requirement, a mean beach profile can be found and WAVE's operations can then be evaluated based on this profile. Beaches can have different material compositions, from sandy and gravel beaches to more rocky, coral or volcanic beaches. For this analysis, the focus is on sandy beaches, as, according to satellite surveys, more than 31% of global coastlines are sandy [5]. Although, this is not a majority of the coastlines, islands will mostly have a sandy beach in their coastline, which can then be targeted instead of always choosing the closest access to the island. Gravel beaches also have a similar topology to sandy beaches, but can be more damaging to the fuselage compared to the finer grains of sand.

Sandy beaches typically consist of three zones: the subaerial beach, surf zone and nearshore zone. For beaching and allowing the cargo to easily access the island, WAVE should ideally beach in the surf zone due to its low depth and short distance to land. Beaching in the subaerial beach would not be possible due to

the lack of water and the nearshore zone is too deep for effective beaching. Figure 2.4 displays the idealised cross-section of a sandy beach. It is clear to see from the diagram that the surf zone is the most optimal area for beaching. The nearshore zone would be an applicable place for anchoring with even the shortest chains exceeding the 100 [m] depth of the nearshore zone [1]. For getting the cargo out of the fuselage, the steepness of the berm also needs to be take into account. This is known as the beach-face slope.

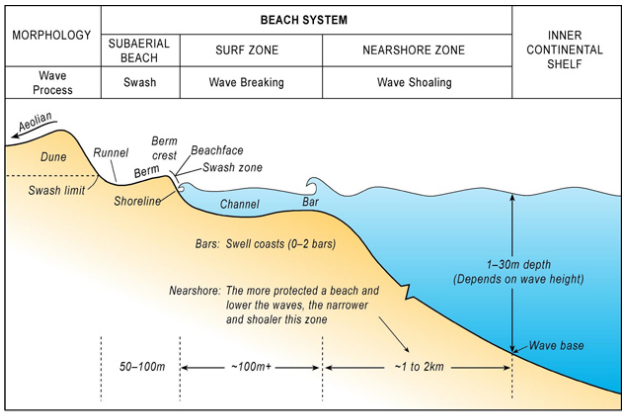

Figure 4.1

Figure 2.4: *Idealised Cross-Section of a Wave-Dominated Beach System*[3]

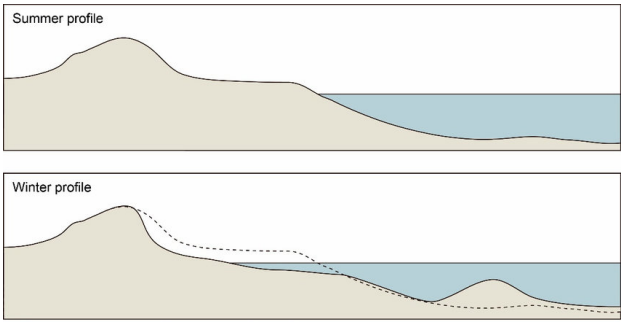

Figure 2.5: *Beach Profiles in Summer and Winter[6]*

Figure 2.4 is considered idealised due to global variability in beach topologies and seasonal changes. In summer, beaches typically have steep berms and minimal bars, whereas in winter the berm erodes and a larger bar forms, as shown in Figure 2.5. For long-term evolution, data from the New South Wales (NSW) Beach Profile Database[2] was used, which includes over 150 sites along the NSW coast since 1920. NSW was chosen due to its geographical location as being in Oceania (similar to many disaster sites in the region). Additionally, NSW has a very complete data set: along all of its beaches, the profile at every meter interval is measured and tracked over the year, quantifying seasonal effects. While using NSW as a main data source to determine beach profiles of disaster sites is an assumption, it is deemed reasonable given the climatic similarity, comprehensive measurement resolution, and temporal coverage of the dataset. Since 2006, photogrammetric measurements yield accuracies of ±0.3 [m] horizontally and ±0.2 [m] vertically. Observations show berm size and beach-face slope decrease over time, so maximum values are conservatively selected to define a mean profile for universal beaching capability.

The mean beach profile is based on the following: surf zone depth of 1.5 [m] (shallowest observed), bar height of 0.5 [m] [7], surf zone length of 500 [m] (upper bound for dissipative beaches [8]), beach-face slope of 0.18 [9], and berm height of 1.5 [m] above Mean Sea Level (MSL) [10]. These values are visualised in Figure 2.6.

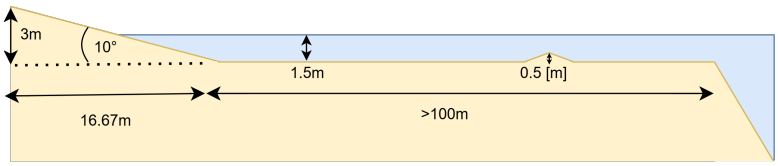

Figure 2.6: *Mean Beach Profile Diagram*

[1] https://seacat-schmeding.com/wp-content/uploads/2020/07/3Equipment_table_lloyds_register.pdf [Cited 10 June 2025]

[3] https://www.nature.com/scitable/knowledge/library/coastal-processes-and-beaches-26276621/ [Cited 10 June 2025]

[2] http://www.nswbpd.wrl.unsw.edu.au/photogrammetry/nsw/ [Cited 10 June 2025]

2.3. Cargo Hold

In the Baseline Report a small market analysis on the cargo hold has been done [11]. In this report, a more extensive market analysis is done on what the cargo hold should accommodate. The most important functions are to deliver trucks and cargo. Then, it is sometimes also necessary to deliver unconventional cargo, such as a landing craft. A more in depth analysis of the final layout of the cargo trucks is done in Section 3.2.

2.3.1. Trucks and Cars

The aircraft should be able to provide disaster relief. This means that it should also be able to accommodate trucks and cars suitable for these tasks. The best trucks for this task are military trucks: their combination of off-road capabilities, robustness, and high-load capacity are essential for disaster relief. These trucks can be grouped into three categories: large, medium, and small trucks. The first one, the large category are large military trucks such as the Scania Gryphus or the Mercedes-Benz Zetros. The medium trucks are a bit shorter, such as the Mercedes-Benz Unimog or the Oshkosh Family of Medium Tactical Vehicles (FMTV). Small trucks are pickups and off-road vehicles, such as the Toyota Hilux or Land Rover Defender. They are listed in Table 2.3. It is worth noting that of each listed truck there are multiple versions. The dimensions do not represent one single version, but rather the highest values across the versions. Special versions (extra long or heavy etc.) are excluded.

Using this data, the required space for a type of truck can be determined, which can later be used in Section 3.2 (the configuration layout) to make cargo layout easier. For the required space there is a little margin, as there should be some manoeuvring space. It is worthy to note that mirrors and other attachments should be detached or folded in.

The Land Rover Defender has the shortest range on a full tank of fuel among the trucks listed in Table 2.3. However, since the primary objective of WAVE is to serve as the first responder in island disaster scenarios, its estimated range of approximately 643 $[km]$[3] is considered sufficient. As such, all vehicles transported by WAVE are assumed to be fully fueled upon deployment, and no additional fuel is carried initially. This fuel supply is expected to last until supplementary fuel can be delivered by follow-up emergency services.

Table 2.3: *Dimensions of Various Trucks*

Group	**Producer**	**Name**	**Length** $[m]$	**Width** $[m]$	**Height** $[m]$	**Empty mass** $[tonnes]$
Large	Scania	Gryphus [4]	10.8	2.6	3.7	19
	Mercedes-Benz	Zetros [5]	10.2	2.5	3.0	13
	MAN	HX## [6]	10.3	2.5	3.3	14
	Oshkosh	HEMTT [7]	10.4	2.4	3.0	20
		Required space	11.0	3.0	4.2	20
Medium	Mercedes-Benz	Unimog [8]	6.0	2.4	2.9	7.5
	Oshkosh	FMTV [9]	6.7	2.4	2.8	10
		Required space	7.0	3.0	3.5	10
Small	Land Rover	Defender [10]	4.8	1.8	2.1	2.3
	Toyota	Hilux [11]	5.0	1.8	1.8	2.0
	Toyota	Land Cruiser [12]	5.0	2.0	2.0	2.5
		Required space	5.5	2.2	2.7	2.5

[3] https://www.landroverannapolis.com/manufacturer-information/land-rover-defender-mpg/#:~:text=The%20gas%20tank%20in%20the,of%20gas%2C%20in%20some%20circumstances. [Cited 24 June 2025]

2.3.2. Pallets and Containers

After a disaster, there is not only a need for trucks, but also a lot of disaster relief goods, such as food, medical equipment, or tools. The most efficient way to transport this is in containers, for which there are standard sizes in the aviation industry. It is already known that the cargo hold width is 5.2 [m] from Subsection 8.3.1, so this limits the choice for what containers are most efficient. The feasible containers are presented in Table 2.4 All values are taken from Roskam part 3 [12].

The use of pallets also poses another problem: the unloading of these pallets. Usage of conventional forklifts is not possible due to beach operations. Therefore, a sand capable forklift should be used to unload the cargo. More about this in Section 3.2 and Section 3.1.

Table 2.4: *Dimensions of Various Pallets*

	Length [cm]	**Width** [cm]	**Height** [cm]
LD-4	243.8	153.4	162.6
LD-7 (pallet)	317.5	223.5	162.6
Standard pallet	317.5	243.8	162.6

2.3.3. Unconventional and Other Cargo

During disaster, there may also be a need to evacuate people. These people are in various conditions: some are uninjured, some have small injuries, but others may need intensive care. The aim should be that WAVE is able to transport passengers that need zero to medium care. In practice this means that there is a normal seating area, but also some beds with some limited means to monitor patients. A fully equipped intensive care unit may not be feasible on board during flight. Some possible cargo hold configurations will be further discussed in Chapter 3, where an example of the passenger configuration is given in Figure 3.5. From the beach analysis in Subsection 2.2.4 it has become clear that some beaches are simply unreachable by the aircraft. In this case there is a need for a more flexible landing craft, that is able to reach the beach instead. As this is deemed as rather unlikely, the analysis on this is limited. In these cases, the Damen Landing Craft Vehicle Personell (LCVP) 1604 can be used to transport cargo to the beach[13]. In this case, it can be opted for the cargo hold configuration shown in Figure 3.7. Another unconventional use of the cargo hold is a small hospital. After a disaster, there is a great need of hospital capacity. However, it takes time and effort to build emergency hospitals. It may be very interesting to turn the cargo hold into a small hospital that can sustain itself for 48 hours. After this time, patients are transferred to other hospitals. 48 hours is not a very long time. However, this may be just enough time to absorb the peak load of emergency medical needs directly after a disaster. See Figure 3.5 for an example configuration.

2.4. End-of-Life

Corrosion resistant structural materials are extremely important for safety and longevity of operation of vehicles in offshore environment. Common methods used in protecting metallic structures in such conditions, is through the form of a coating or using sacrificial metals. Sacrificial anodes, such as Zinc are commonly used for corrosion protection in maritime environments [13]. Here, the sacrificial metal reacts with the salt water instead of the outer structure of WAVE. In addition, the parts that are in contact with the environment and parts that cannot be inspected can be covered with an anti corrosive coating, such

[4] https://www.defensie.nl/onderwerpen/materieel/voertuigen/scania-gryphus-vrachtwagen [Cited 9 June 2025]
[5] https://special.mercedes-benz-trucks.com/en/mercedes-benz-defence-trucks/technical-data.html [Cited 9 June 2025]
[6] https://en.wikipedia.org/wiki/RMMV_HX_range_of_tactical_trucks#cite_note-JanesTrucks-1 [Cited 9 June 2025]
[7] https://en.wikipedia.org/wiki/Heavy_Expanded_Mobility_Tactical_Truck [Cited 9 June 2025]
[8] https://special.mercedes-benz-trucks.com/en/mercedes-benz-defence-trucks/technical-data.html [Cited 9 June 2025]
[9] https://en.wikipedia.org/wiki/Family_of_Medium_Tactical_Vehicles [Cited 9 June 2025]
[10] https://en.wikipedia.org/wiki/Land_Rover_Defender [Cited 9 June 2025]
[11] https://en.wikipedia.org/wiki/Toyota_Hilux [Cited 9 June 2025]
[12] https://en.wikipedia.org/wiki/Toyota_Land_Cruiser [Cited 9 June 2025]
[13] https://www.damen.com/vessels/defence-and-security/landing-crafts/lcvp-1604 [Cited 14 June 2025]

as an epoxy coating. Opting for sacrificial anodes will not protect the entire aircraft from corrosion, only the part that is under water. This method also releases metal ions into the water, which disturbs the local environment [14]. However, metals commonly used in maritime industry that require no protective layers, such as stainless steel 316 and the titanium alloy Ti-6Al-4V, could easily be discarded from the list due to weight and cost respectively. Opting for an epoxy coating changes a lot in the sense of recyclability of the material. This is because, the coating must be burned off before the material can be recycled [15]. Not only is this energy intensive, but the combustion also releases toxic fumes. Due to the aforementioned reason, common scrapping and recycling of the airframe would not result in the lowest net emission. Therefore, new creative methods are needed for end-of-life solutions. Such methods could include using retired aircraft as emergency shelters, museums, temporary buildings, etc. Or making sure that uncoated metal parts of WAVE are recyclable.

2.5. Fuel Economy of Reference Aircraft

This section contains an analysis on the necessary fuel economy the design must achieve to stay competitive with similar military cargo aircraft. To ensure the vehicle is competitive regarding fuel economy, one considers REQ-CUST-COST.1, that requires the design to have better fuel economies than the C-5, C-17 and C-130. Estimating the fuel consumption during the respective design missions of the reference aircraft is achieved using the Breguet range equation [16]. Since the lift-to-drag ratio is a key input in this equation, its optimal value during cruise is determined using established aerodynamic relations available in the literature [16]. The inputs for the fuel economy are listed in Table 2.5, with the output being the fuel economies of the respective aircraft in litres of fuel used for 1 tonne of cargo moved for 1 kilometre.

Table 2.5: *Input and output Variables for the Breguet Range Equation to Arrive at the Fuel Economies for the Reference Aircraft*

Aircraft	Range [km]	SFC [kg/J or kg/Ns]	Cruise speed [m/s]	Prop. eff. [-]	L/D [-]	MTOM [kg]	Payload [kg]	Fuel econ. [L/tonne/km]
C-5	3,9812 [1]	$8.9 \cdot 10^{-6}$ [kg/Ns] [2]	221.2 [1]	-	11.28	381,024 [1]	122,500 [1]	0.140
C-17	4,480 [3]	$9.3 \cdot 10^{-6}$ [kg/Ns] [4]	231.5 [3]	-	10.77	265,352 [3]	77,519 [3]	0.163
C-130	5,245 [5]	$9.22 \cdot 10^{-8}$ [kg/J] [6]	-	0.85	14.13	70,305 [3]	15,876 [5]	0.384

As can be seen in Table 2.5, in order to obtain a better fuel economy than the C-5, C-17 or C-130, the design aircraft needs to be able to achieve a fuel economy no higher than 0.14 $[L/tonne/km]$(see Table 2.6). The compliance of the design with the requirement that follows from this section is given in Chapter 11.

Table 2.6: *Requirement from Fuel Economy Market Analysis[11]*

Requirement ID	Requirement Description	Category	Source
REQ-SUS.1	The fuel economy of the design aircraft over the course of the design mission shall be less than 0.14 $[L/tonne/km]$.	Operational	REQ-CUST-SUST.1

[1] https://skybrary.aero/aircraft/c5#:~:text=Without%20in%2Dflight%20refuelling%2C%20the,Cargo%20and%206300%20Nm%20empty [cited 9 may 2025]
[2] https://en.wikipedia.org/wiki/General_Electric_TF39 [cited 9 may 2025]
[3] https://www.af.mil/About-Us/Fact-Sheets/Display/Article/1529726/c-17-globemaster-iii/ [cited 9 may 2025]
[4] https://en.wikipedia.org/wiki/Thrust-specific_fuel_consumption [cited 9 may 2025]
[5] https://customer.janes.com/display/JAWA1339-JAWA [cited 9 may 2025]
[6] https://en.wikipedia.org/wiki/Allison_T56 [cited 9 may 2025]

2.6. Operational Cost Requirement

This section provides an initial estimation of the operating cost of reference aircraft. In order to evaluate competitiveness regarding operation cost, REQ-CUST-COST.1 is once again considered. A literature study is performed to find the hourly operation cost of the C-5, C-17 and C-130, while the values for range and cruise speed are taken from Table 2.5. Consider Table 2.7, which presents the inputs necessary to find the operation cost in dollars, per tonne cargo moved per kilometre. To arrive at the results, the cost estimation method proposed by Raymer is used [16].

Table 2.7: *Inputs and Outputs of the Operational Cost Estimation for Reference Aircraft. Inputs are taken from the Baseline Report [11].*

	Parameter	C-5	C-17	C-130	Unit
Inputs	Range	3,982	4,480	5,245	$[km]$
	Cruise Speed	796	833	556	$[km/h]$
	Payload	122,500	77,519	15,876	$[kg]$
	Maximum Take-off Mass (MTOM)	381,018	265,352	70,307	$[kg]$
Outputs	Fuel Cost (Design Mission)	215,751	149,362	27,219	[$]
	Crew Cost (Design Mission)	25,731	9,685	6,422	[$]
	Maintenance Cost (per Mission)	28,700	30,881	54,128	[$]
	Total Operational Cost (per Mission)	241,481	159,047	33,641	[$]
	Operational Cost per Tonne Kilometre (without maintenance)	0.50	0.46	0.40	[$/tonne/km]
	Operational Cost per Tonne Kilometre (with maintenance)	0.55	0.54	1.0	[$/tonne/km]

It can be seen from Table 2.7 that in order to meet REQ-CUST-COST.1, WAVE needs to achieve an operational cost less than 0.40 $[\$/tonne/km]$. In that section, compliance with REQ-SHC.7 (see Table 2.8) that follows from this section can be found.

Table 2.8: *Requirements Regarding the Cost of WAVE*

Requirement ID	Requirement Description	Category	Source
REQ-SHC.7	The operational cost of the designed aircraft over the course of the design mission shall be less than that of the C-5, C-17, and C-130 under non-marine operating conditions.[14]	Constraint	Client

2.7. Cargo Hold Requirements

The requirements for the cargo hold have been established in the Baseline Report [11]. It was then decided that the largest object for this would be a military truck, needed for goods distribution and transportation of first-responders. The minimum dimensions for the cargo hold were therefore based on a Dutch military truck, the DAF YA-4442 [15]. However, in Section 2.3 it has been decided that the cargo hold should also be able to accommodate larger trucks. Though, this is deemed as not an absolutely vital requirement, as medium trucks are believed to have the ability to perform most of the tasks completed by larger trucks.

The YA-4442 is 7.3 $[m]$ in length, 2.43 $[m]$ in width and 3.42 $[m]$ in height. Considering that the crew members still must be able to pass by the object and handle it, corresponding clearances are added to find the required minimum dimensions of the cargo hold. These clearances are found by adding 1.0 $[m]$ to the width and rounding to the nearest 0.50 $[m]$, while rounding the height to the nearest integer. Thus, the dimensions

[7] https://ig.space/commslink/c-130-hercules-lockheeds-do-everything-transport [cited 9 may 2025]

[14] Following a client meeting on 13-06-2025, this requirement was revised from the baseline report [11] to its current formulation in Table 2.8.

[15] https://www.defensie.nl/onderwerpen/materieel/voertuigen/daf-ya-4442 [cited 29 April 2025]

of the object that the cargo hold should be designed for are equal to: 7.32 [m] in length, 3.5 [m] in width and 4.0 [m] in height. Together, this results in REQ-CAR.2.2 and REQ-CAR.2.3(see Table 2.9). The compliance of the design with these requirements will be reported in Chapter 8.

Table 2.9: *Requirements from Cargo Hold Market Analysis[11]*

Requirement ID	Requirement Description	Category	Source
REQ-CAR.2.2	The cargo hold cross-section dimensions (width, height) shall be such that at any point along the cargo hold at least a rectangle of 3.5 [m] wide and 4.0 [m] high fits inside.	Operational	
REQ-CAR.2.3	The dimensions (width, height) of the cross-section of the door to the cargo hold shall be such that at least a cuboid of 3.5 [m] wide, 4.0 [m] in height and 7.32 [m] in length fits inside.	Operational	

2.8. End-of-Life Requirement

Considering the limitations mentioned in Section 2.4, it was decided that using sacrificial anodes will not be viable for this design. This is because, splashes of water can hit anywhere on the aircraft, meaning that not only the part that goes in the water is subjected to corrosion. Therefore, the parts of the aircraft that are in contact with the outside environment and parts that are difficult to inspect must be protected. As a result of the fact that the chemical coating must be removed first before recycling, traditional recycling processes will not be most viable. Hence, REQ-SUS.3 (see Table 2.10) was formulated.

Other, coated parts of the aircraft, can for instance be re-used as components for shelters in disaster areas as previously mentioned in Section 2.4. This can be done by flying WAVE to the area of re-use and leaving it there, or by shipping the needed parts to the area of interest.

Table 2.10: *Requirements from End-Of-Life Market Analysis[11]*

Requirement ID	Requirement Description	Category	Source
REQ-SUS.3	Metallic parts of the aircraft that are uncoated against corrosion shall be recycled.	Functional	REQ-CUST-SUST.2

The compliance matrix of the EOL requirement that followed from the market analysis can be found in Chapter 13.

2.9. Future Market Prediction

In this section, a future outlook on the market is presented. The prediction has been made considering the current developments in the aviation sector, political climate and increased occurrence of natural disasters. Given the increasing emphasis on sustainability and the rising demand for flexible, heavy-lift transport capabilities, the future market potential for this design is promising. As global logistics continue to shift toward rapid-response and decentralised operations, particularly in regions lacking robust infrastructure, the need for versatile aircraft capable of operating in harsh environments, including water, is expected to grow. Additionally, current geopolitical tensions and humanitarian challenges drive the demand for strategic and tactical airlift solutions. With the design's greater efficiency in ground effect and reduced emissions compared to conventional aircraft, this design aligns well with both military and civil sector trends. If development continues, WAVE has the potential to capture a significant share of the niche amphibious heavy transport market within the near future.

3

Operations

In this chapter, the nominal operations of WAVE are described. These include loading and unloading of the aircraft when beached, building on the beach market analysis in the previous chapter. Moreover, the sensors necessary for this nominal operation are discussed as well as the configurations of the cargo. Finally, the logistics and maintenance of the aircraft are outlined. This will be done by first showing the functional flow and functional breakdown in Section 3.1. After this the cargo configurations are given in Section 3.2. Finn ally the logistics will be shown in Section 3.3

3.1. Functional Flow and Functional Breakdown

The functional flows presented after this chapter have been heavily updated from the first version presented in the Baseline Report [11]. There are various important updates which the design has undergone which are discussed first in this chapter. Afterwards, the hardware required on-board will be explored and selected. Finally, the diagram showing all the electrical connections will be presented.

The functional flow outlines the procedures required from manufacturing to end-of-life (EOL), including recurring flight operations. Functions which may not always be required are still included, such as the obstacle avoidance climb, in order to get a full picture of the operations of the aircraft. In accordance with the systems engineering DSE lecture slides [17], functions assigned to all subsystems, except for the Complete System or the Crew, have been added to the Functional Break-down. Both the Functional Flow and Functional Break-Down can be found at the end of the Chapter.

3.1.1. Unload Cases

Not all beaches are made equally: many shorelines have steeper beach profiles, shallower channels or no (sandy) beach at all. This highlights the importance of a flexible cargo and unloading subsystem. From research, three general cargo unloading operations have been identified, shown in Figure 3.1.

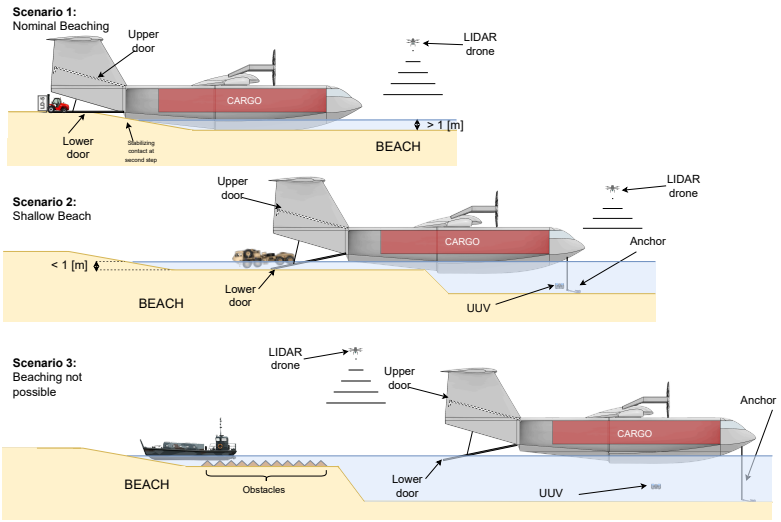

Figure 3.1: *Beaching Scenarios. Scenario 1 is a Standard Beaching Case with a Manitou M50-4 Forklift Carrying a LD-5 Container. Scenario 2 Presents Shallow Beach Unloading Featuring an OSHKOSH Truck. Scenario 3 Features a DAMEN LCVP 1604 for Difficult to Reach Shorelines. All Diagrams are to Scale, except with respect to the Unmanned Underwater Vehicle (UUV) and Light Detection and Ranging (LIDAR) drone.*

Scenario 1: Nominal Beaching

In early design phases, it was identified that the depth of the fuselage floating still in the water (based on early fuselage dimensioning) is larger than the depth of the channel. For this reason, the island accessibility requirement (REQ-CUST-PERF.11) and as a result the buoyancy depth requirement (REQ-STR.5) would not have been met. The solution to meeting this requirement has been dimensioned in Subsection 8.3.4 and involves using floaters which are inflated with compressors, temporarily improving clearance to the seabed. The aircraft will reverse towards the shoreline and once in position deflate floaters slightly, allowing the fuselage to sit in the channel sand securely. With the cargo door opened, cargo can safely be unloaded onto the beach.

Modelling of the mean beach profile and the aircraft system suggest that for optimal conditions in nominal beaching the rear-step of the hull should first make contact with the beach (with inflated floaters). Once achieved, the floaters can be deflated to allow the fuselage to sink 0.44 $[m]$ and securely sit in the sand. The hull will now make contact with the beach at both steps. Pitch stability while unloading is guaranteed due to the contact with the beach at the rearward step.

Scenario 2: Shallow Beach

In the case of a beach with a channel depth of one meter or less, nominal beaching cannot take place and the aircraft is anchored when the forward step-region of the hull touches the channel first. After anchoring, the lower door can be opened and unloading can take place. Since the depth of the channel is limited, trucks can be used to quickly transfer the payload to the beach.

Scenario 3: Beaching not Possible

Significant seabed obstacles such as rocks or corals may prevent the use of motorized vehicles to transport the cargo to the shoreline, even if the channel depth is less than one meter. In this case, the aircraft must anchor at an arbitrary distance from the shoreline and commence its unloading procedure on water. In this scenario, the cargo is expected to be a landing craft such as a LCVP 1604 with a maximum loading capacity of 8 tonnes[1]. Of importance in this scenario is the buoyant pitch stability of the aircraft when unloading on water. This will be analysed in the next design report.

Operational Risk Reduction through Sensing and Forecasting

The difference in operational structure outlined above highlights the need for accurate and fast logistics in the early stages of mission when a plan must be formulated. Incorrect determination of beach surface can lead to sub-optimal or mission critical logistical mistakes such as the decision to not take landing craft or similar water-deployable cargo onboard. Onboard sensors and scanning systems such as the drones and UUVs shown in Figure 3.1 can mitigate the operational risk. The most effective strategy is to begin mapping all disaster prone sites most likely to be serviced by the system and logging the geology of nearby beaches over time in a database. This can be done by an automated drone system which uses LIDAR to map beach profile twice a year due to seasonal effects detailed in Subsection 2.2.4 and the inherent impermanence of beach profiles.

However, the financial cost of such an operation may outweigh the benefits. The dynamic nature of floods means historical data on the beaching profile may not be trusted. A solution to this would be to integrate the emergency response system with communication from satellite-based hydrographic services that provide real-time data on water levels after a flood has taken place, such as the European Space Agency's Copernicus [18]. This will be provided to mission control as well as onboard, to both aid in the cargo decision and taxiing/unloading when reaching the disaster site.

[1] https://medialibrary.damen.com/m/7a80f3b304bf68d7/original/product-sheet.pdf [Cited 12 June 2025]

3.1.2. External Sensors Required

The system's operational environment extends beyond that of conventional aircraft in sea operation. For simplicity's sake, the majority of the sensors onboard of the Airbus A380 as defined in [19] except the landing gear related ones are required on this system due to operational overlap in the cruise at altitude condition. Special interest should be placed on operations which are atypical for standard aircraft. Based on the functional flow diagram (FFD) and functional breakdown structure (FBD), it can be seen that the ground-effect (GE) cruise and on-water operations are the main areas of interest where deviation from normal procedures occurs.

The aircraft will be equipped with two Radio Detection and Ranging (RADARs): one for weather detection and one for obstacle scanning. During all phases of flight, both will be active as per E3.6. During cruise, avoidance of larger obstacles such as large bodies of land can be planned for during the CR1.1 function before flight. Even if flight path changes during cruise due to unforeseen weather or high sea states, the new required flight path can be compared to existing topographical data on the triple redundant Flight Management Computers (FMC) onboard to arrive at a new optimal trajectory after clearance with Vehicles Tracking System (VTS). This new path can be given to the pilots via the navigation displays in the cockpit. A suitable weather radar that can be used is the Collins TWR-850 with an 18 $[in]$ flat-plate antenna, requiring only 24 $[W]$ of power [20]. This will be housed in a radome at the nose tip.

The limiting case for obstacle avoidance is much the more constraining case where smaller obstacles, such as boats or floating debris, are located close to water surface which require high resolution scanning of the horizon. This would ideally be done by using an Active Electronically Scanned Arrays (AESA) RADAR such as the APG-81. Despite its relative novelty on the market-especially for civilian applications-it is seen as the most suitable design option to be included in the aircraft for obstacle detection due to electrical steering allowing for very high RADAR steering rate, which facilitates scanning at the horizon for obstacles [21]. As seen by the Lun-Class Ekranoplans, the surface search radar is placed in the veritcal tail [2] for better ground clearance and enhanced visibility.In this aircraft system, the RADAR will be installed inside the horizontal tail, beneath the skin and positioned just ahead of the wingbox. Thanks to the relatively small dimensions of this antenna [21], it can be easily accommodated on either side of the horizontal tail's wing, outside the wingbox to facilitate easier maintenance access. The high position maximizes the range of the radar.

Other onboard sensors required mainly arise from the (post-)landing operations defined in the SYS6 and SYS7 function. As a subfunction E3.3 and E3.5 a drone multi-rotor system using the YellowScan Navigator is deployed during every landing at unknown operational disaster site, which can map seabed depths with a resolution of 3 $[cm]$ at up to two "secchi" depths [3]. Assuming, conservatively, that a Beaufort wind scale of 4 must be designed for, wind speeds will then reach up to eight $[m/s]$ [4]. This is not seen as a problem. Research suggests that the market provides many products capable of delivering this performance, among which WaveAerospace's Falcon II SE which can operate in wind speed of up to 31 $[m/s]$ well within the aforementioned envelope [22].

For even greater security and risk mitigation, an onboard UUV may be deployed from the anchor bay such as a more technologically mature version of the system presented in TURTLMap [23], equipped with stereo-cameras and sensors for a complete understanding of beach topography and seabed type (hard, sharp rocks or sandy channels). After confirmation of safe beach profiles and types for approach, the beaching procedure may be initiated.

The aircraft uses cameras to support the visual envelope and line of sight of the pilots, especially during critical phases such as beaching or pre-flight control (P/FTC) checks [24]. To aid in performing these, an array of cameras is placed on each side of the airframe which visually covers the control surfaces. One high-resolution camera is placed on each side of the cockpit pointed at the engines, while the wing ailerons and

[2] http://www.hisutton.com/images/Lun-Ekranoplan-Cutaway.jpg [Cited 15 June 2025]
[3] https://www.scandinaviandrone.com/product/yellowscan-navigator/?v=efad7abb323e [Cited 15 June 2025]
[4] https://ouco-industry.com/understanding-sea-state-a-comprehensive-guide/?utm [Cited 24th June 2025]

flaps are covered by one side view camera on each side of the fuselage afterbody pointed towards the wings. Another camera is placed on each vertical tail to aid inspection of the other tail's rudder. For inspection of the horizontal tail, a camera is positioned in the most aft-ward point of the fuselage on top of the upper door and pointing upwards. For extra visual support, the aforementioned drone can be equipped with cameras and controlled by one of the pilots for more complete visual inspection. Beaching is made possible with one camera on each wing tip pointing backwards towards the tail and behind the fuselage. All these views will be accessible from the cockpit displays during operation of CR7.3 in the FFD. This totals nine high-resolution cameras distributed across the airframe.

3.2. Cargo Configurations

Due to its dimensions, the cargo hold is very flexible in its use. It can transport trucks, cargo, passengers, landing craft, and even patient care areas. All these are outlined below. The legend is presented in Figure 3.2. The cargo hold is indicated in grey. The dimensions are: length 28.1 [m], width 5.2 [m], and height 4.2 [m]. The cargo configurations are largely based on the market analysis and those cargo dimensions are given in Table 2.3 and Table 2.4.

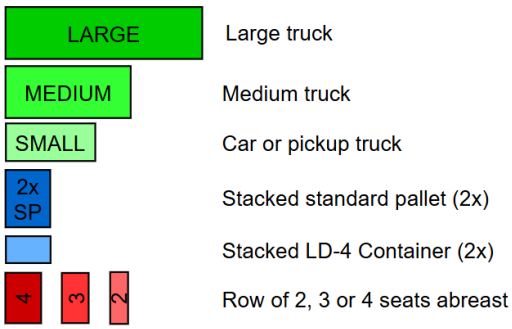

Figure 3.2: *Legend of the Configuration Layouts*

The cargo hold is divided into two sections: the main cargo hold and an extension. For stability reasons, the hold was made longer than strictly required[5]. In the configurations presented, cargo is limited to the required 28.1 [m] section. In certain cases, the load-master may choose to use the extended section, but the aircraft's centre of gravity must always remain within acceptable limits.

There is one big limitation on the cargo in case the surf zone is less deep than about 1.2 [m]. In this case, the aircraft cannot reach the shoreline. Thus, the cargo or its transporters should have a fording depth that is large enough to cross the surfzone.

As previously discussed in Subsection 2.3.1, fuel is not expected to be transported within the cargo bay; however, future studies may explore this possibility, as noted in Chapter 15.

3.2.1. Fast-Response Configurations

The most important requirement of the aircraft is being able to deliver fast and effective disaster relief capabilities. As indicated in the market analysis, this can be done by delivering trucks. The cargo hold can hold a maximum of one row of large/medium trucks and one row of small trucks, as to be seen in Figure 3.3. Without sacrificing space for these trucks, in every configuration there is some passenger space. In the first two configurations, this is about 12 passengers. In the last one this is about 24. The total weight is largely dependent on the amount of cargo loaded on the trucks.

The big advantage of these configurations is its flexibility. Loading and unloading times are very small, as the cargo does not require additional assistance when unloading. Mission flexibility is also high, as the average fording depth of the trucks discussed in the market analysis exceeds 1.0 [m]. This allows the aircraft to still operate efficiently at beaches with a surfzone shallower than 1.2 [m].

[5] The required cargo hold length is 28.1 [m]; the extension adds 5.4 [m], resulting in a total length of 33.5 [m].

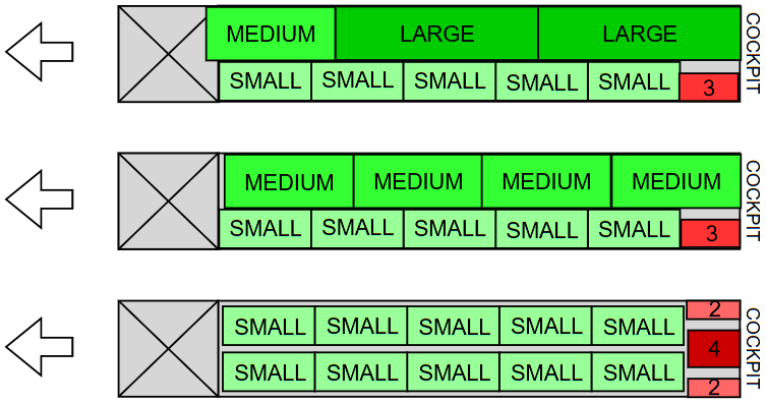

Figure 3.3: *Fast-Response Configurations*

3.2.2. Maximum Cargo Configurations

The most efficient way to deliver the most cargo using the least amount of space is by using containers. There are two possibilities for containers: the standard pallet (first configuration) and the LD-4 container (second configuration), presented in Figure 3.4. Both pallets can be stacked on top of each other, doubling the cargo capacity. There is a little space left unused to transport a forklift. The aircraft is able to transport 32 standard pallets. For a payload capacity of 90 [$tonnes$] this means that the maximum average weight of one pallet is approximately 2700 [kg]. The capacity for the LD-4 container is 72 units, making the maximum average weight about 1200 [kg]. For both configurations, about 3000 [kg] is reserved for a forklift.

In the case that perishables, such as food or medical supplies, are transported, temperature maintenance must be achieved through appropriate packaging rather than environmental control. The nominal design mission lasts only 9 hours, as outlined in Section 11.3, and even under conservative assumptions, the maximum endurance of 11 hours does not justify the need for a climate-controlled cargo hold. Instead, the use of sealed or insulated containers, such as standard pallets or LD-4 units, is deemed sufficient for short-duration cold chain integrity.

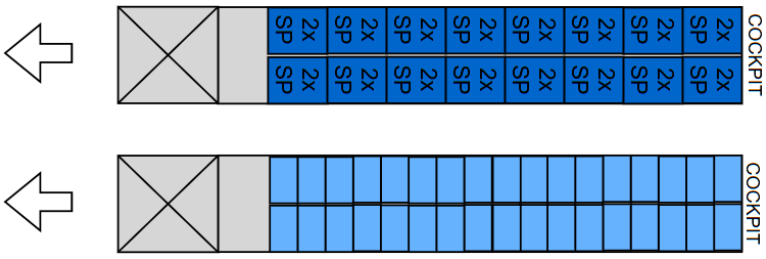

Figure 3.4: *Maximum Cargo Configurations*

3.2.3. Passenger Configurations

As mentioned in the market analysis, it may sometimes be necessary to evacuate people from an island. This can be done by placing seats in the cargo hold. This gives a maximum capacity of 288 people by placing passengers in a 2-4-2 abreast configuration. This is displayed in Figure 3.5. However, as the cargo hold is 4.2 [m] high, so there is just enough room to create two decks. This doubles the passenger capacity. In this configuration there is no room for additional cargo, but this may be added as desired. Note that the configuration needs to be organized in such a way that both passengers and cargo can be loaded and unloaded. It is also possible to turn a part of the cargo hold into a Patient Care Area. This is medium intensive care for wounded people.

There is however a big limitation to this configuration. At this point, it is not possible. Having this amount of passengers requires the aircraft to have additional (emergency) doors, which have not yet been fitted to the design. Later design stages will have to evaluate the feasibility and potential of these design changes. Additionally, it has to be noted that a Patient Care Area requires additional power. This additional required

power may never be too great such that the aircraft cannot fully perform its mission.

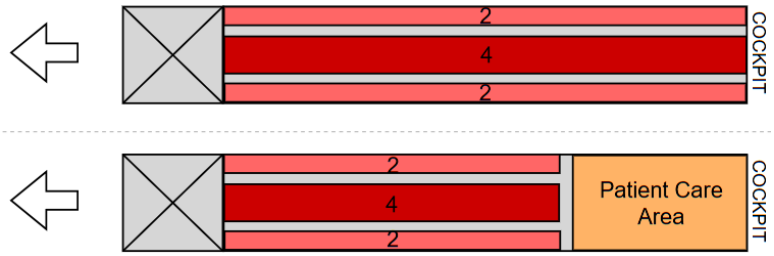

Figure 3.5: *Passenger Configurations*

3.2.4. Hybrid Configurations

Not every island is as big as the other. Therefore, not every island has a need for a huge amount of trucks or a cargo bay filled with disaster relief goods. Luckily, the cargo bay of the aircraft is highly flexible and a single deck layout gives about 150 $[m^2]$ of space to store all sorts of cargo. In Figure 3.6 two examples are given for this. However, there are many more configurations possible. Virtually any configuration can be combined, as long as operational requirements are met. As already mentioned above, it is also possible to use two decks. This expands the possibilities even further. It is possible to then use the upper deck for passengers and the lower deck for cargo or a Patient Care Area. Again, including more passengers will also require design changes.

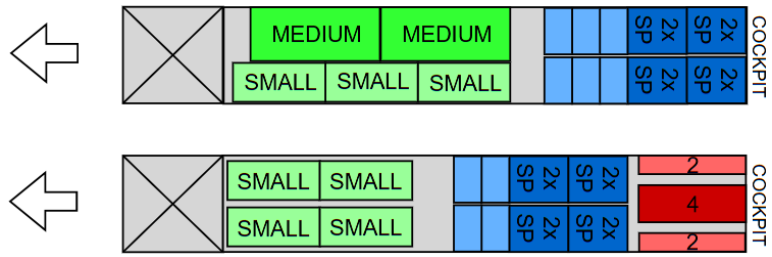

Figure 3.6: *Hybrid Configurations*

3.2.5. Unconventional Configurations

In Figure 3.7 the configuration is presented to hold a LCVP 1604 Landing Craft. This configuration can be used when beaching the aircraft is not possible. The LCVP is more flexible in its use and may be able to deliver payload when the aircraft cannot. In the configuration, the landing craft is already filled with cargo. Additional cargo can be added whenever necessary in the front.

When close to the destination, the LCVP is pushed out of the cargo hold. It then goes on to deliver the payload. After this is done, it may return to the aircraft to dock and load additional cargo. This mechanism can also be employed for multiple aircraft. The landing craft stays on-site and unloads all arriving aircraft. The aircraft is however not capable of retrieving the landing craft again, as it does not have the capability to lift high loads out of the water. Retrieval is to be done with ships from a third party.

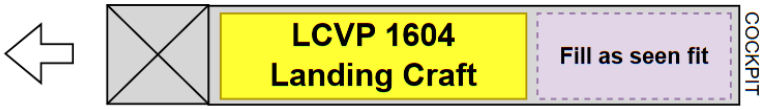

Figure 3.7: *No-Beach Configuration*

The last possible configuration is the two deck hospital configuration, presented in Figure 3.8. As described in the market analysis, considering the high power load of a fully operating hospital, it may not be possible to operate this in flight. However, on site the power load may be satisfied by using (zero-emission) generators. Addtionally, this configuration generates further requirements on the climate-control of the aircraft

during flight where additional power and subsystems are needed for refrigeration of medical supplies.

Due to the expected relative low load of the hospital configuration, it may be possible to extend the used cargo hold space all the way to the end, thus making the total available area for the hospital approximately 350 $[m^2]$ per aircraft. If it is not possible, the total area will be about 300 $[m^2]$.

Figure 3.8: *Hospital Configuration*

Arranging a fully capable hospital is time consuming, especially for more intensive care or even operating rooms. As the main goal of this configuration is to be able to deploy a fully functional hospital within hours, it is required that these aircraft are in a permanent hospital configuration, always ready to deploy within hours. It may even be the case that these aircraft need significant design changes, making a whole different version. In later design stages the benefits and feasibility of this version will be evaluated.

For larger islands one aircraft may not be sufficient to provide enough emergency capabilities. In that case, multiple aircraft may be operated in tandem. An example is presented in Figure 3.9. All aircraft are rotated by approximately 20 $[deg]$ to save space. At the beach, there is a small entrance at which patients are checked in and distributed between the aircraft. The red lines are the corridors between the aircraft. Different aircraft may have different roles. It should be noted that this hospital configuration is only possible if the aircraft can reach the shoreline.

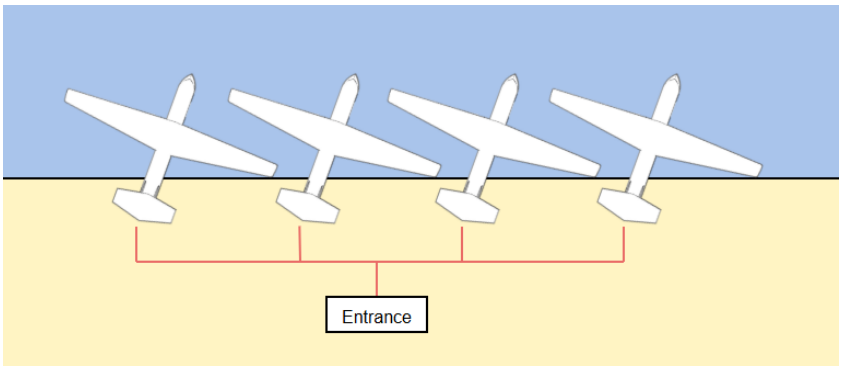

Figure 3.9: *Hospital Aircraft Operating in Tandem*

Lastly, in case that the deployment of the LCVP is not possible, the cargo may also be put on rafts to reach the beach. Depending on the raft size, the available cargo volume is greatly reduced. Therefore, this option is the least preferred configuration.

3.3. Logistics Diagrams

In this section, Section 3.3 presents a high-level overview of the entire logistics process, highlighting how the chain of command and actions. Each phase is mapped with its respective diagram and key decision points—from mission kickoff and preflight checks, through dynamic cruise adjustments and water landing, to payload deployment and the return to base.

3.3.1. Logistics Diagrams

The logistics diagrams display how the logistical chain around the aircraft is organised. These are split up in five phases: preflight and taxi, take-off, cruise, landing, and on-site operations. This flight is from the home-base to the disaster location, with cargo loading done at home-base. There are many more flights possible but this flight is the most logistically demanding. To fly back to base, the aircraft will go through the same procedure, only the ground crew is swapped with the on-site ground crew and vice-versa. The

on-site ground crew is likely less well-equipped, making failure handling less effective.

There are five different parties involved with the logistical operations. The first is the flight crew, in the figures indicated in blue. This includes the pilot, co-pilot, load-master(s), and other staff that is on the aircraft. The second is the home-base ground crew, indicated in green. This is among others the crew chief and maintenance crew. The on-site crew is indicated in orange. The red boxes are Traffic Control (TC). The fifth box is a miscellaneous party. This includes high-ranking decision making officials or other staff that is not directly affiliated to the aircraft.

Traffic Control (TC) in this context refers to the coordination and management of both air and surface traffic. Unlike traditional Air Traffic Control (ATC), which primarily focuses on preventing collisions between aircraft, TC here encompasses a broader responsibility. Because the aircraft in question operates often close to the sea surface, there is also a significant risk of conflicts with maritime or ground traffic. As a result, TC may include coordination with or integration of vessel or surface traffic control services. This combined oversight could be managed by a unified entity responsible for the aircraft's operation. The specific structure and organization of such integrated traffic control systems are beyond the scope of this report.

The identification system is as follows: L-[Phase abbreviation]#(A/B/C)(.#.#), in which L stands for logistics. The blue boxes share a lot of similarity with the functional diagram. However, to improve readability of this diagram, it is chosen not to use the identifiers of that diagram.

Preflight and Taxi Phase

In Figure 3.10 the preflight and taxi phase is displayed. The flight starts with a decision for a disaster relief mission. After initial mission planning, the cargo type is decided based on whether beaching can occur and the landing sight. This is then loaded into the aircraft and the preflight inspection is done. While normal preflight inspections include visual inspection of the various aircraft systems by use of a walk-around, this aircraft will deploy a drone when beached on water, before taking off at the disaster sight. This will be operated by the load masters. The aircraft is designed to start up without the usage of a Ground Power Unit (GPU). However, when this malfunctions an external GPU is needed, this is done in L-P4.1. After getting engine start clearance from TC, this is attempted. When then all other systems are properly started and taxi clearance is given, the aircraft will taxi to the designated take-off location.

There are two instances in which the ground crew may fix an issue: L-P3.1 and L-P4.1. It should be noted that this fix must hold the entire mission. For example, a quick reboot of a system or the replacement of a fuse will likely not cause problems for on-site operations. However, when in case of battery malfunction a GPU is needed for engine startup, this is a problem. Due to the nature of operations a GPU will likely not be available on-site. Thus, in this case, the aircraft is not able to fly.

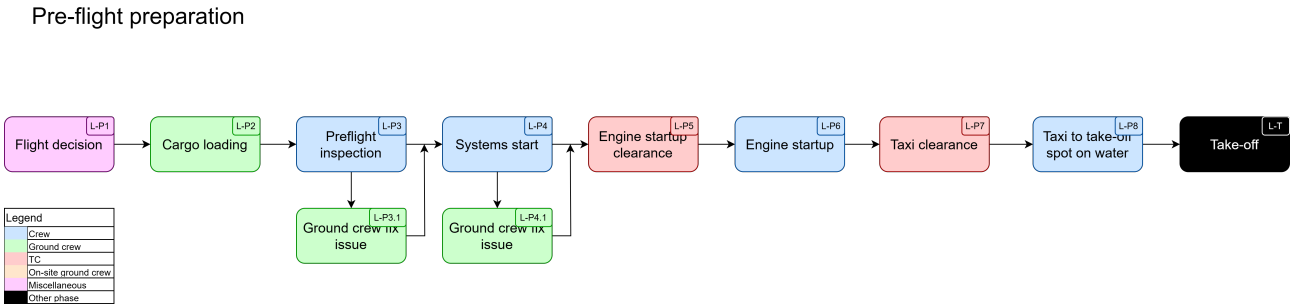

Figure 3.10: *Preflight and Taxi Logistical Operations*

Take-off Phase

Next, the aircraft will take-off, which is displayed in Figure 3.11. After completing checklists, the crew will receive take-off permission. After climbing to the desired altitude, the aircraft will await further instructions from TC.

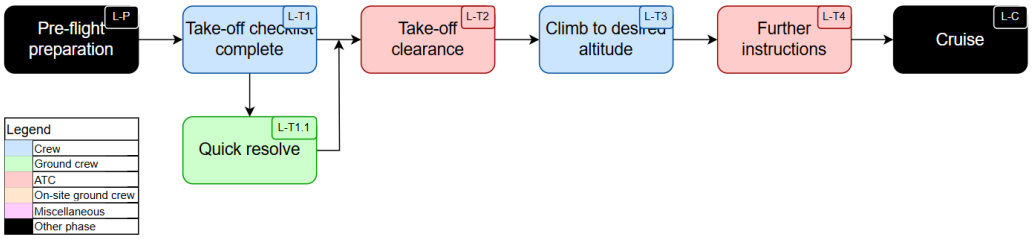

Figure 3.11: *Take-Off Logistical Operations*

Cruise Phase

The biggest part of the flight is the cruise phase, displayed in Figure 3.12. If a critical operating system fails, the crew will declare an emergency to TC and follow emergency procedures. If these procedures are unsuccessful, the crew may resort to an emergency landing on water. Though, in the case of an emergency landing the aircraft will likely have malfunctioned and needs to be retrieved by a team of specialists.
Another possibility in flight is obstacle avoidance, such as land or a storm. In this case, the crew is required to deviate from their flight plan to avoid the obstacle. This should always be done in discussion with TC to avoid collisions with other aircraft or sea vessels.

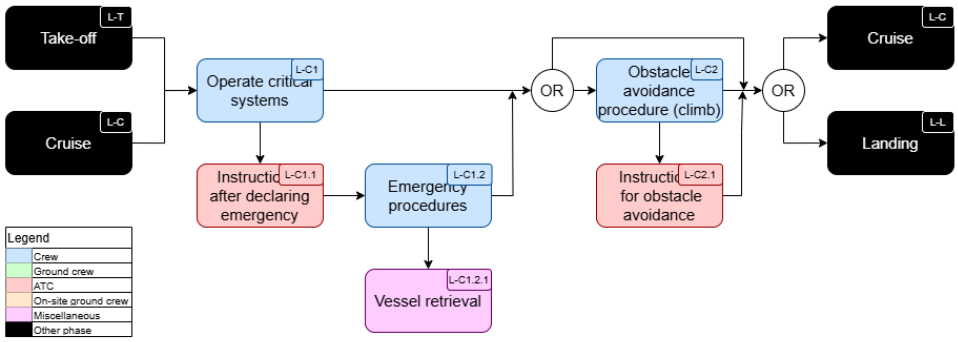

Figure 3.12: *Cruise Flight Logistical operations*

Landing Phase

The landing phase is displayed in Figure 3.13. First of all the aircraft is configured, issues are resolved and after given landing clearance, the aircraft executes landing on water. Following this, stationing of aircraft is performed after stationing clearance is given. As described under Section 3.1, there are three possibilities for cargo delivery: beach landing, surfzone landing, and on-water deployment. In terms of logistics, not much changes. Some sort of on-site crew will always be required to accept the cargo, even if its capabilities are severely limited.

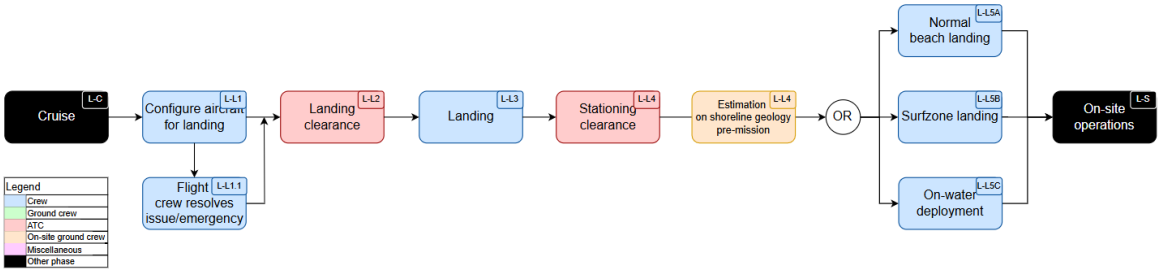

Figure 3.13: *Landing Logistical Operations*

Payload Delivery and Return Flight

With the aircraft stationed and cargo delivery method chosen, steps can be taken to finally deliver the cargo to the disaster area. The phase starts by putting the engines on standby, before that the on-site ground crew cannot safely approach the aircraft. Then the cargo can start to be unloaded by the on-site ground crew. Note that for raft cargo offloading, on-site crew is advised to have some sort of towing boat available.

This reduces raft cost and increased payload capacity. If possible and before returning to the base, the aircraft will need to be refuelled. After which, reverse thrust and possibly the inflatable buoys are used to propel the aircraft out of its stationing position. This is through engaging the engine into reverse-pitched blade position. For anchored delivery of payloads, the anchor is raised before this process. The aircraft is then aligned with a designated take off path using thrust differential. After which, the aircraft takes off and performs a return to base-camp flight. The full logistics is shown in Figure 3.14. Detailed analysis of fuselage loads, anchor mass, and required power are done in Chapter 9 and Chapter 8.

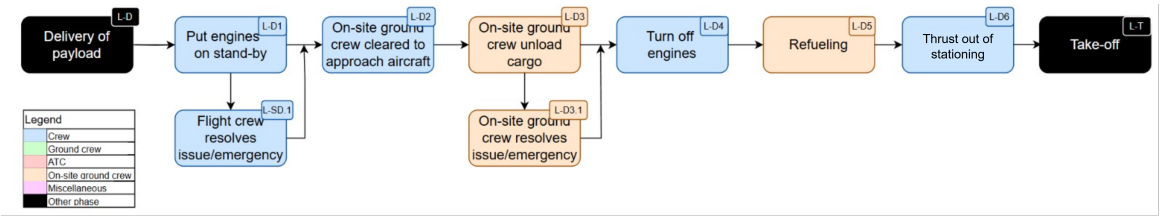

Figure 3.14: *Payload Delivery and Return*

3.4. Communications Diagram

The communication flow diagram shown in Figure 3.15 focuses on the aircraft's interactions within a disaster response system. It shows data and voice exchanges between the aircraft, base ground station, other ships, air and maritime traffic control, and satellites. Communication occurs via Very High Frequency (VHF) radio and data links. The legend categorizes elements as system components (green), external entities (orange), and supporting tools (blue).

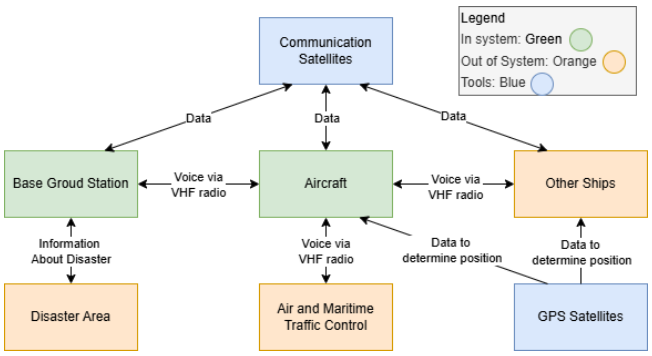

Figure 3.15: *Communications Flow Diagram*

3.5. Reliability, Availability, Maintainability, and Safety Characteristics Analysis

Analysis on reliability, availability, maintainability, and safety characteristics, abbreviated by RAMS, is essential for safe flight of an aircraft. The requirements regarding this analysis are presented in Table 3.1. The RAMS analysis consists of three parts: the general redundancy philosophy (Subsection 3.5.1, the operational reliability (Subsection 3.5.2), and the maintenance (Subsection 3.5.3).

Table 3.1: *Requirements for RAMS[11]*

Requirement ID	Requirement Description	Category	Source
REQ-LIF.1	The seaplane shall have a minimum service life of 20 years in a marine (saltwater) environment.	Functional.	

3.5.1. General Redundancy Philosophy

The general redundancy philosophy dictates how many systems should be designed. Structurally, in general, it is chosen that all critical systems should be able to sustain 1.5 times the maximum load suspended on the system. However, this safety factor may sometimes be higher if deemed necessary. The philosophy also has a major influence on system architecture. For every system, there should be at least one backup

system, except for non-critical equipment such as power outlets or galley equipment. For highly critical systems[6] a third backup system should be present. This includes for example the flight controls and cockpit power.

3.5.2. Operational Reliability

In this section, the operational reliability is discussed. Some of the scenarios are connected with risks from Chapter 16. Here, only scenarios are evaluated that can pose a direct threat for the passengers and crew on board or scenarios that may cause failure of cargo delivery. Scenarios that are caused by improper maintenance or flight planning[7] are not analysed. This is because these have a direct cause rather than a random occurrence. The operational failures are tabulated in Table 3.2. The probabilities are given per flight hour.

Table 3.2: *Operational Failures of the WAVE*

Failure	Risk	Probability	Redundancy strategy
Communication failure	CRTR-2	1E-05	It is important to climb out of ground effect with communication loss due to the absence of sea traffic control. Then, follow local communication loss procedures.
Hydraulic pressure loss (single system)	CRTR-3	1E-04	Total hydraulic pressure loss means no flight controls. However, there are three independent hydraulic systems that can all power the primary flight controls
Power loss (single system)	CRTR-3	1E-05	There are multiple sources of power. If generators in both engines fail, electrical power can be generated by batteries and/or the Ram Air Turbine (RAT).
Engine failure	CRTR-4	1E-05	For the WAVE, an engine failure is not very much of a problem, as there are 6 available. If an engine fails that provides power or hydraulic pressure, another engine takes over this task
Multiple engine failure	CRTR-4	1E-10	The failure of multiple engines can be more critical. Hydraulics and electronics will if necessary be powered by batteries and/or the RAT
Obstacle avoidance radar loss	FPTR-2	1E-05	Immediately climb out of ground effect and follow procedures for loss of radar.
Propeller hits water	TOTR-3	1E-04	Propeller may break. Shut off engines of damaged propellers and evacuate space in plane of rotation of the blades.

3.5.3. Scheduled and Unscheduled Maintenance

Maintenance consists of two elements: scheduled and unscheduled. In Table 3.3 the scheduled maintenance is presented. These intervals are defined as the number of missions instead of the usual flight hours. A mission is the equivalent of one disaster. During one mission, the aircraft may fly a different number of flights or flight hours. However, it is highly impractical to perform scheduled maintenance during missions, as the aircraft are likely to be used almost uninterruptedly. It should be noted that periodic inspection is mainly to ensure operation readiness. In case of a disaster, WAVE should be able to deploy as quickly as possible. Therefore, its readiness should be periodically examined. In addition, A, B, C, and D checks are performed at regular intervals to ensure the aircraft has an operational life of at least 20 years. In Table 3.4 the most relevant system failures are displayed, along with their Mean Time Between Failure (MTBF) and relative uptime.

[6] These systems are defined as being so critical, that loss of these systems result in a high probability on fatalities

[7] For example improper securement of cargo, exceeding center-of-gravity (CG) limits, lacking maintenance etc.

Table 3.3: *Scheduled Maintenance Intervals*

Inspection Type	Frequency	Duration	Notes
Preflight inspection	Before flight	30 minutes	Integrity of aircraft, floatation, visual checks
Periodic inspection	Weekly-quarterly[8]	2 hours	Visual checks, hull, floatation of the aircraft and operation readiness
A-check	1 mission	1 day	Fluids and filters, airframe
B-check	5 missions	2 days	Nanocracks, corrosion and floatation
C-check	15 missions	10 days	All systems and coating
D-check	30 missions	30 days	Full teardown and recoating

Table 3.4: *Unscheduled Maintenance Intervals*

System	Failure Mode	Estimated MTBF $[h]$	Downtime $[h]$	Relative uptime
Engines	General failure	1,000	8	99.20%
Nano-coating	Erosion	1,000	6	99.40%
Avionics	General failure	3,000	4	99.87%
Electrical System	Short circuit, power loss	4,000	8	99.80%
Propellers	Damaged blade	5,000	6	99.88%
Hydraulic Systems	Leak, actuator failure	6,000	15	99.75%
Structure	Cracks, element failure	7,000	30	99.57%
Fuel System	Blockage, leak	8,000	12	99.85%
Control Surfaces	Cable failure, actuator failure	8,000	10	99.88%

3.5.4. Compliance Matrix

In Table 3.5 the compliance matrix for the RAMS analysis is presented. It is visible that all requirements have been met

Table 3.5: *Compliance Matrix for RAMS*

Requirement ID	Description	Compliance Justification	
REQ-LIF.1	The seaplane shall have a minimum service life of 20 years in a marine (saltwater) environment.	With the maintenance described in Table 3.3, it is believed the aircraft has a service life of at least 20 years.	

[8] Frequency depends on usage and storage of aircraft.

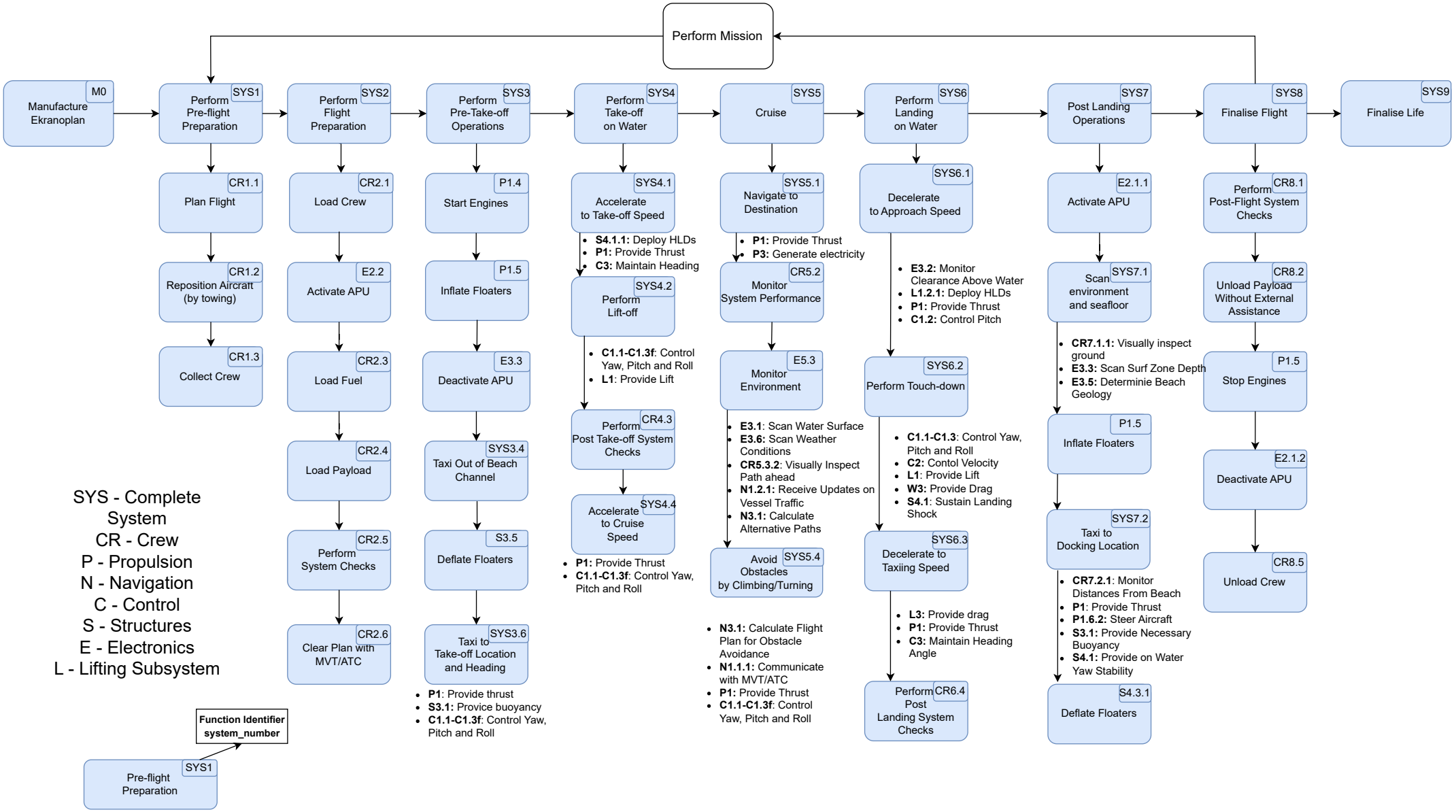
Perform Mission
M0 Manufacture Ekranoplan
SYS1 Perform Pre-flight Preparation
CR1.1 Plan Flight
CR1.2 Reposition Aircraft (by towing)
CR1.3 Collect Crew
SYS2 Perform Flight Preparation
CR2.1 Load Crew
E2.2 Activate APU
CR2.3 Load Fuel
CR2.4 Load Payload
CR2.5 Perform System Checks
CR2.6 Clear Plan with MVT/ATC
SYS3 Perform Pre-Take-off Operations
P1.4 Start Engines
P1.5 Inflate Floaters
E3.3 Deactivate APU
SYS3.4 Taxi Out of Beach Channel
S3.5 Deflate Floaters
SYS3.6 Taxi to Take-off Location and Heading
P1: Provide thrust
S3.1: Provice buoyancy
C1.1-C1.3f: Control Yaw, Pitch and Roll
SYS4 Perform Take-off on Water
SYS4.1 Accelerate to Take-off Speed
S4.1.1: Deploy HLDs
P1: Provide Thrust
C3: Maintain Heading
SYS4.2 Perform Lift-off
C1.1-C1.3f: Control Yaw, Pitch and Roll
L1: Provide Lift
CR4.3 Perform Post Take-off System Checks
SYS4.4 Accelerate to Cruise Speed
P1: Provide Thrust
C1.1-C1.3f: Control Yaw, Pitch and Roll
SYS5 Cruise
SYS5.1 Navigate to Destination
P1: Provide Thrust
P3: Generate electricity
CR5.2 Monitor System Performance
E5.3 Monitor Environment
E3.1: Scan Water Surface
E3.6: Scan Weather Conditions
CR5.3.2: Visually Inspect Path ahead
N1.2.1: Receive Updates on Vessel Traffic
N3.1: Calculate Alternative Paths
SYS5.4 Avoid Obstacles by Climbing/Turning
N3.1: Calculate Flight Plan for Obstacle Avoidance
N1.1.1: Communicate with MVT/ATC
P1: Provide Thrust
C1.1-C1.3f: Control Yaw, Pitch and Roll
SYS6 Perform Landing on Water
SYS6.1 Decelerate to Approach Speed
E3.2: Monitor Clearance Above Water
L1.2.1: Deploy HLDs
P1: Provide Thrust
C1.2: Control Pitch
SYS6.2 Perform Touch-down
C1.1-C1.3: Control Yaw, Pitch and Roll
C2: Contol Velocity
L1: Provide Lift
W3: Provide Drag
S4.1: Sustain Landing Shock
SYS6.3 Decelerate to Taxiing Speed
L3: Provide drag
P1: Provide Thrust
C3: Maintain Heading Angle
CR6.4 Perform Post Landing System Checks
SYS7 Post Landing Operations
E2.1.1 Activate APU
SYS7.1 Scan environment and seafloor
CR7.1.1: Visually inspect ground
E3.3: Scan Surf Zone Depth
E3.5: Determinie Beach Geology
P1.5 Inflate Floaters
SYS7.2 Taxi to Docking Location
CR7.2.1: Monitor Distances From Beach
P1: Provide Thrust
P1.6.2: Steer Aircraft
S3.1: Provide Necessary Buoyancy
S4.1: Provide on Water Yaw Stability
S4.3.1 Deflate Floaters
SYS8 Finalise Flight
CR8.1 Perform Post-Flight System Checks
CR8.2 Unload Payload Without External Assistance
P1.5 Stop Engines
E2.1.2 Deactivate APU
CR8.5 Unload Crew
SYS9 Finalise Life
SYS - Complete System
CR - Crew
P - Propulsion
N - Navigation
C - Control
S - Structures
E - Electronics
L - Lifting Subsystem
Function Identifier system_number
SYS1 Pre-flight Preparation

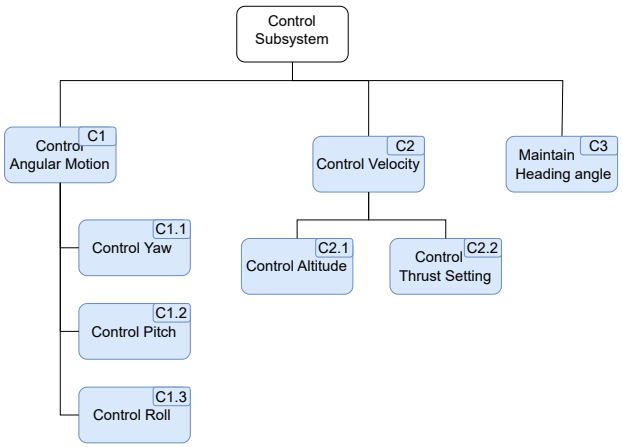
Control Subsystem
C1 Control Angular Motion
C1.1 Control Yaw
C1.2 Control Pitch
C1.3 Control Roll
C2 Control Velocity
C2.1 Control Altitude
C2.2 Control Thrust Setting
C3 Maintain Heading angle

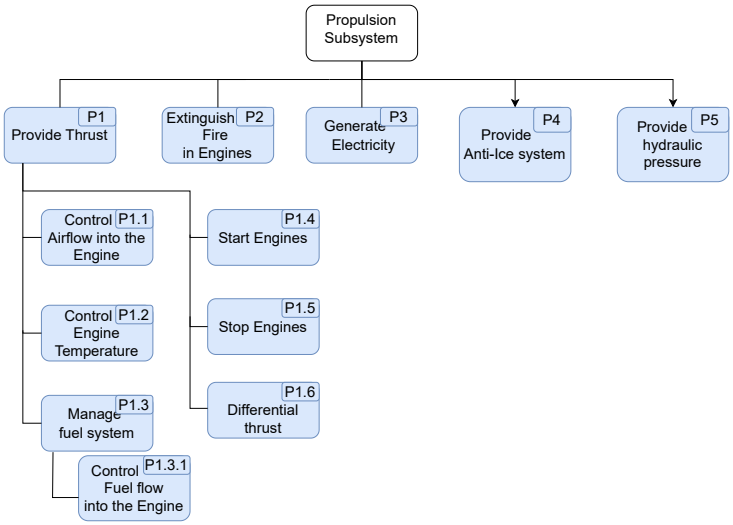
Propulsion Subsystem
P1 Provide Thrust
P2 Extinguish Fire in Engines
P3 Generate Electricity
P4 Provide Anti-Ice system
P5 Provide hydraulic pressure
P1.1 Control Airflow into the Engine
P1.2 Control Engine Temperature
P1.3 Manage fuel system
P1.3.1 Control Fuel flow into the Engine
P1.4 Start Engines
P1.5 Stop Engines
P1.6 Differential thrust

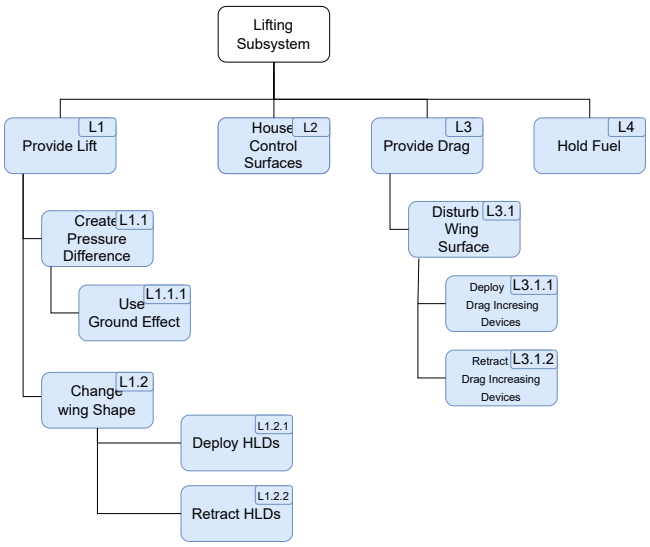
Lifting Subsystem
L1 Provide Lift
L2 House Control Surfaces
L3 Provide Drag
L4 Hold Fuel
L1.1 Create Pressure Difference
L1.1.1 Use Ground Effect
L1.2 Change wing Shape
L1.2.1 Deploy HLDs
L1.2.2 Retract HLDs
L3.1 Disturb Wing Surface
L3.1.1 Deploy Drag Incresing Devices
L3.1.2 Retract Drag Increasing Devices

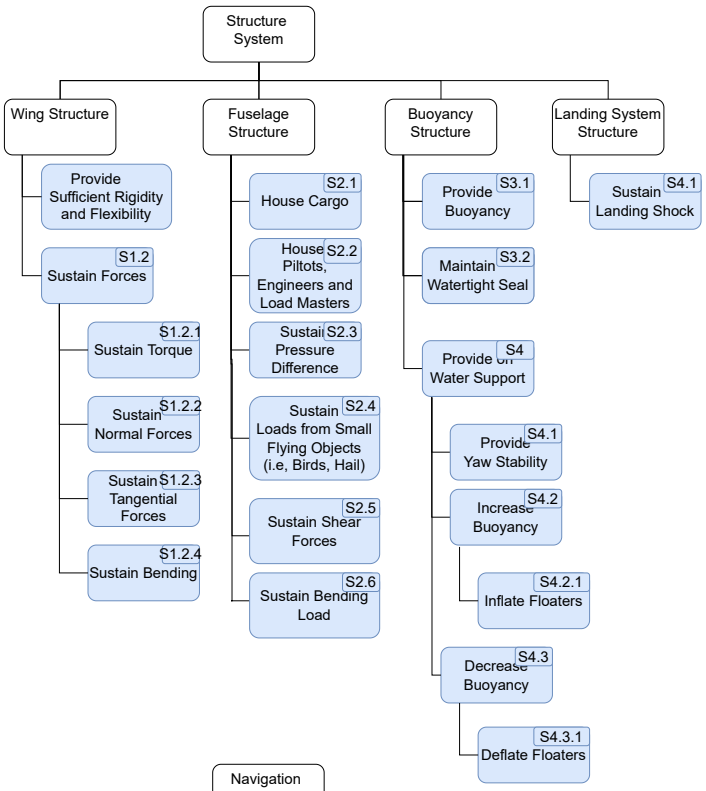
Structure System
Wing Structure
Fuselage Structure
Buoyancy Structure
Landing System Structure
Provide Sufficient Rigidity and Flexibility
S1.2 Sustain Forces
S1.2.1 Sustain Torque
S1.2.2 Sustain Normal Forces
S1.2.3 Sustain Tangential Forces
S1.2.4 Sustain Bending
S2.1 House Cargo
S2.2 House Piltots, Engineers and Load Masters
S2.3 Sustain Pressure Difference
S2.4 Sustain Loads from Small Flying Objects (i.e, Birds, Hail)
S2.5 Sustain Shear Forces
S2.6 Sustain Bending Load
S3.1 Provide Buoyancy
S3.2 Maintain Watertight Seal
S4 Provide Water Support
S4.1 Provide Yaw Stability
S4.2 Increase Buoyancy
S4.2.1 Inflate Floaters
S4.3 Decrease Buoyancy
S4.3.1 Deflate Floaters
S4.1 Sustain Landing Shock

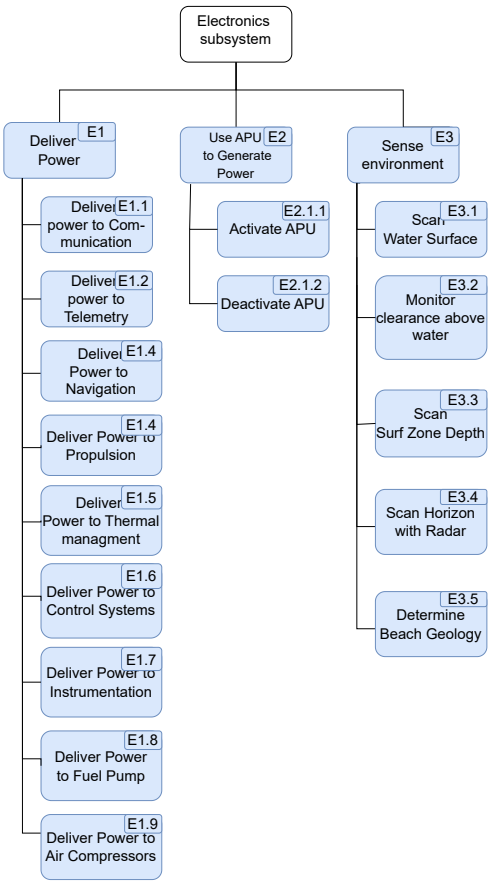
Electronics subsystem
E1 Deliver Power
E1.1 Deliver power to Com-munication
E1.2 Deliver power to Telemetry
E1.4 Deliver Power to Navigation
E1.4 Deliver Power to Propulsion
E1.5 Deliver Power to Thermal managment
E1.6 Deliver Power to Control Systems
E1.7 Deliver Power to Instrumentation
E1.8 Deliver Power to Fuel Pump
E1.9 Deliver Power to Air Compressors
E2 Use APU to Generate Power
E2.1.1 Activate APU
E2.1.2 Deactivate APU
E3 Sense environment
E3.1 Scan Water Surface
E3.2 Monitor clearance above water
E3.3 Scan Surf Zone Depth
E3.4 Scan Horizon with Radar
E3.5 Determine Beach Geology

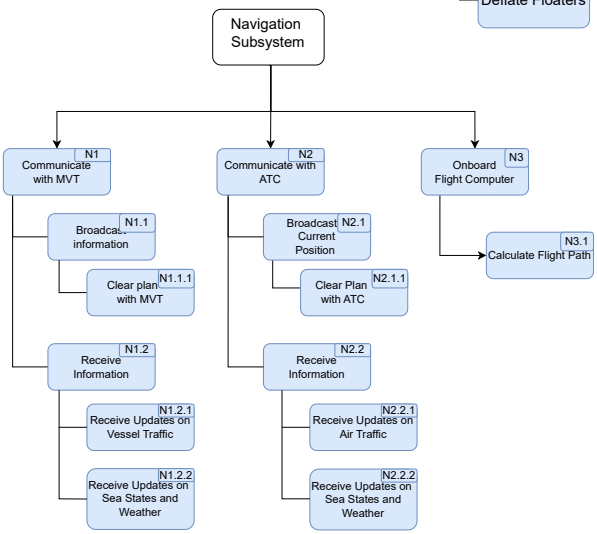
Navigation Subsystem
N1 Communicate with MVT
N2 Communicate with ATC
N3 Onboard Flight Computer
N1.1 Broadcast information
N1.1.1 Clear plan with MVT
N1.2 Receive Information
N1.2.1 Receive Updates on Vessel Traffic
N1.2.2 Receive Updates on Sea States and Weather
N2.1 Broadcast Current Position
N2.1.1 Clear Plan with ATC
N2.2 Receive Information
N2.2.1 Receive Updates on Air Traffic
N2.2.2 Receive Updates on Sea States and Weather
N3.1 Calculate Flight Path

4

Systems Engineering

The previous chapters have outlined the functions and operations of the complete design. Naturally, the complete design is the result of the integration of multiple interdependent systems, each developed and optimized by different team members within their specific domain. To achieve a coherent and consistent overall design, careful integration of these systems is essential. This integration is primarily realised through iterative coordination, where outputs from one discipline influence the inputs of another, necessitating multiple design loops. The following chapter explains how this iterative integration process was implemented to ensure consistency and convergence across all subsystems.

4.1. System Interdependencies

To properly integrate the various systems, it is essential to first identify their interdependencies within the conceptual design process. For this purpose, an N2 chart has been created, which is shown in Figure 4.1. This version of the N2 chart differs slightly from the one presented in the Midterm Report [25]. Specifically, it has been made more concise by merging some of the diagonal elements into a single block, thereby simplifying the chart's structure without omitting critical information.

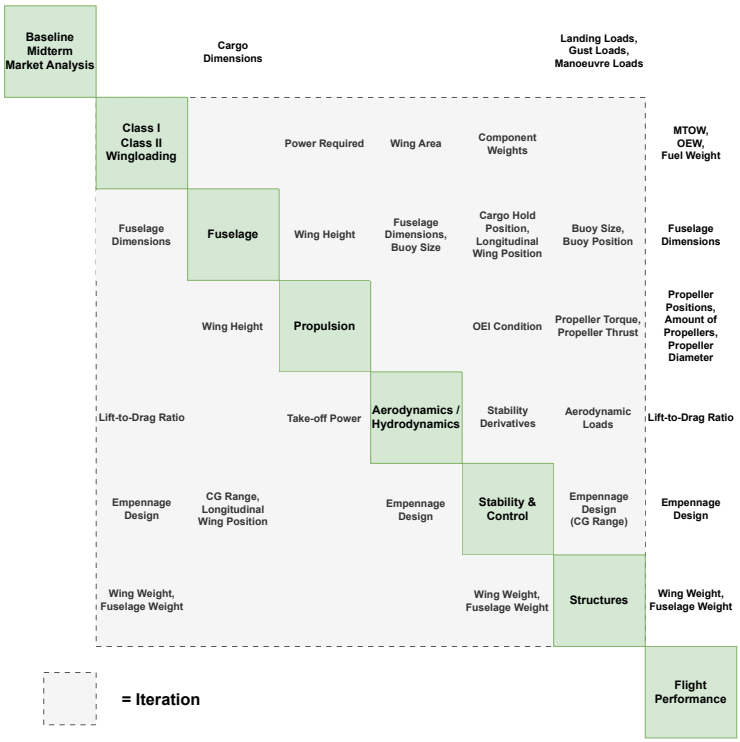

Figure 4.1: *N2 Chart of Design Iteration*

In Figure 4.1, the green diagonal boxes represent the core disciplines involved in the aircraft conceptual design process. These disciplines form the primary sequence of the design workflow. The grey squares highlight the subset of these disciplines that are tightly interconnected through iterative relationships. Within this region, outputs from one discipline, such as geometry, weight, or aerodynamic data, serve as critical inputs to others, and vice versa. This interdependency requires iterative refinement to ensure consistency

and convergence of the overall design.

The process begins with Class I and Class II estimations, which involve early weight breakdowns and wing loading assessments based on empirical relationships. While useful for initial sizing, these estimates rely on assumptions regarding parameters, such as control surface areas, load factors, and airfoil geometries, which themselves depend on the weight and configuration of the aircraft. As the design progresses, more accurate analyses, particularly in the structural domain, yield refined estimates of wing, fuselage, and empennage weights. These updated values often diverge from the initial estimates, prompting the need to iterate upstream disciplines, such as aerodynamics, stability, and weight estimation to maintain consistency across the entire design loop. Meanwhile, the boxes and parameters outside the grey iterative region represent important design inputs or boundary conditions that influence the process but are not themselves recalculated within the iteration loop. Examples include cargo dimensions, mission requirements, MTOW, and fuel weight. These remain relatively fixed and serve as constraints or initial conditions throughout the design process. Ultimately, the N2 diagram offers a clear and structured visualization of the complex interdependencies between disciplines in aircraft design. It highlights where iteration is required and where assumptions can remain fixed, supporting a more systematic and coordinated approach to multidisciplinary conceptual design.

4.2. Data Handling

To ensure consistency and efficiency in the multidisciplinary design process, a centralised and automated design environment was developed. This enables seamless interaction between different disciplines by structuring all relevant data and storing it at a single location. The aim of this section is to explain the implementation of this system and how it facilitates data exchange, iteration control, and ultimately convergence across the full aircraft design loop. To manage the large number of parameters across various disciplines in the design process, a centralized data structure based on a comprehensive JavaScript Object Notation (JSON) file was developed. This design state file consolidates all input parameters, intermediate calculations, and final outputs for each discipline, including aerodynamics, structures, propulsion, weights, and control surfaces. Each discipline is implemented as a modular code file that reads from and writes to this shared JSON file, ensuring all data remains synchronized throughout the design loop. This structure not only allowed the team to keep track of discipline-specific data with clarity, but also greatly simplified the implementation of the iterative design process. By calling the discipline modules sequentially, the JSON is automatically updated at each stage, enabling seamless convergence through repeated iterations. The final integrated system thus becomes a streamlined execution of sequential function calls, each of which updates and responds to the shared state. The full implementation is available on the team's GitHub repository [1], which is used to arrive at the technical results.

4.3. Final Iteration Results

In the final iteration, all main functions of the disciplines are sequentially called according to Figure 4.1. Due to the streamlined set-up with the JSON structure, it allowed the iteration to compare every single output parameter to the previous values for those parameters. Thus, when the iteration has converged, it can safely be said that every output of every discipline has converged. Since, in total there are about 600 outputs, it is redundant to show the convergence of every single parameter, however, in Figure 4.2 the change in key parameters for the customer are presented.

[1] https://github.com/PaSieg0/Ekranoplan-DSE [Cited 17 June 2025]

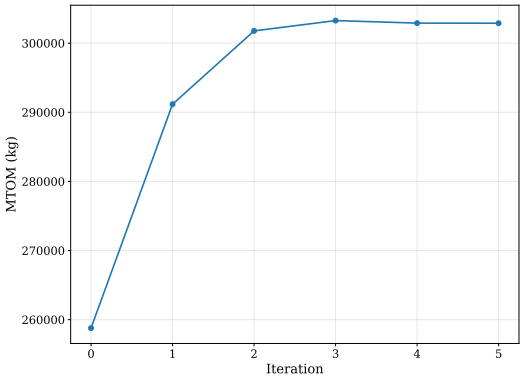

(a) *Convergence of Maximum Take-Off Mass*

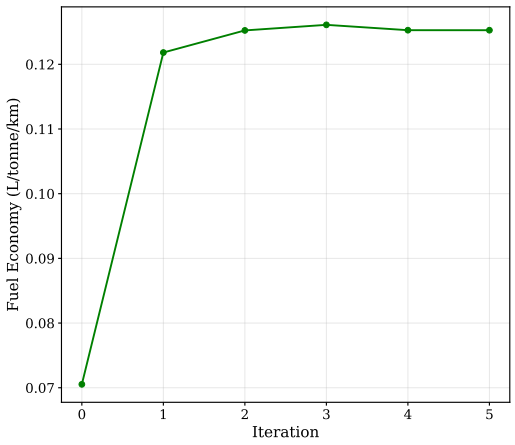

(b) *Convergence of Fuel Economy*

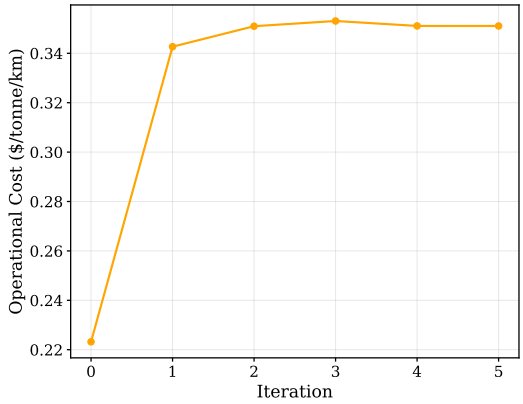

(c) *Convergence of Operational Cost*

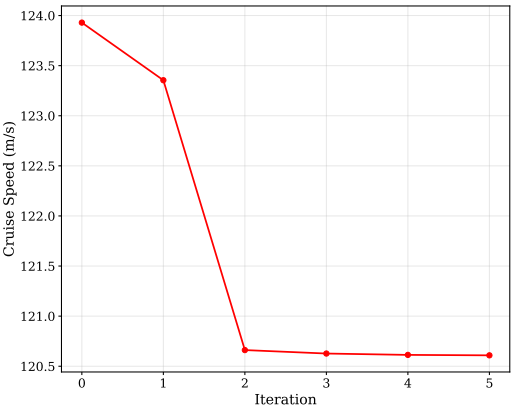

(d) *Convergence of Cruise Speed*

Figure 4.2: *Key Performance Indicators v.s. Iterations in the Final Design Loop*

As seen in the results for MTOM, fuel economy, and operational cost, there is a significant upward trend: approximately a 15% increase in MTOM, now 303 $[tonnes]$, an 80% rise in fuel consumption, now 0.125 $[L/tonne/km]$, and a 60% increase in operational cost, now 0.35 $[\$/tonne/km]$. Regarding the cruise speed iteration, the optimal cruise speed for maximum range has decreased from approximately 124 $[m/s]$ to about 120 $[m/s]$. These changes are generally undesirable: the aircraft becomes heavier, less efficient, more expensive to operate and slower. Nevertheless, such outcomes were anticipated beforehand and are thus not a problem.

The final outputs following the iteration are discussed for each discipline in the following chapters. Thus, any input or output seen from this point onwards, are the final converged values.

5

Class I & Class II Weight Estimations

This chapter presents the iterative process of the Class I weight estimation, initially outlined in the baseline report[11], and the subsequent Class II component-level weight estimation. The methodology used for estimating individual component weights is described in Section 5.1. Following that, Section 5.2 details the iterative procedure employed to refine the Maximum Take-Off Mass (MTOM). In Section 5.3, the determination of the centre of gravity (CG) range is discussed, accounting for both the Operating Empty Weight (OEW) and variations due to loading scenarios. Finally, Section 5.4 evaluates whether all applicable requirements have been satisfied. The relevant requirements addressed in this chapter are summarised in Table 5.1.

Table 5.1: *Relevant Requirements - Class I, Class II & Wing Loading Estimations [11]*

Requirement ID	Requirement Description	Category	Source
REQ-SHC.3	The Maximum Take-Off Mass (MTOM) shall be below 500[$tonnes$].	Constraint	REQ-CUST-BUDG.1

5.1. Determining Component Weights

To improve the estimate of OEW and Center-of-Gravity (CG) range, a Class II weight estimation is performed using Raymer's method for cargo and transport aircraft [16, pp. 395–409]. This section contains the results of the component weight estimation. The weight of additional components that are not included in this method, are also estimated and included in this section.

For the amphibious design, a fuselage weight 'fudge factor' of 1.25 accounts for the hull's added mass. Additional components not covered by Raymer, including the battery, engines, cargo door, anchor, buoys, and endplate floaters, are estimated separately.

The battery mass is derived from the required energy of 1.30×10^6 [kJ] (see Section 9.3) and a lithium-ion specific energy of 972 [kJ/kg] [1], resulting in approximately 1336 [kg] of uninstalled mass and a volume of 765 [L] based on an energy density of 471.5 [Wh/L] [1].

Engine weight is estimated using a general aviation relation, as Raymer's cargo section lacks one. The cargo door weight is assumed similar to the Airbus Beluga XL's 3100 [kg] [2]. The anchor and chain weights are taken from Lloyd's Register [3] standards as 1100 [kg] and 2370 [kg], respectively (see Subsection 8.3.6). Float weight follows Canamar and Smrcek's relation $W_f = 0.0365 \cdot MTOW + 43.5$ [26], with buoys accounting for 75% and endplate buoys 25%. Inputs and assumptions are listed in Table A.1 and Table A.3 (Appendix A), with component weights summarised in Table 5.2.

[1] https://en.wikipedia.org/wiki/Lithium-ion_battery [Cited 15 June 2025]
[2] https://aviator.aero/press/stelia-aerospace-delivers-the-first-belugaxl-cargo-door/ [Cited 16 June 2025]
[3] https://seacat-schmeding.com/wp-content/uploads/2020/07/3Equipment_table_lloyds_register.pdf [Cited 15 June 2025]

Table 5.2: *Estimated Component Weights and OEM Fractions*

Component	Mass [kg]	OEM %
$M_{air\ conditioning}$	300	0.27%
$M_{anti-ice}$	595	0.53%
M_{apu}[4]	450	0.40%
$M_{battery}$[5]	2004	1.7%
$M_{avionics}$	971	0.86%
$M_{electrical}$	790	0.70%
$M_{furnishings}$	3903	3.4%
$M_{fuselage}$[6]	23416	20%
$M_{handling\ gear}$	89	0.079%
$M_{horizontal\ tail}$	4408	3.9%
$M_{instruments}$	414	0.37%
$M_{nacelle}$	3736	3.3%

Component	Mass [kg]	OEM %
$M_{starter}$	128	0.11%
$M_{vertical\ tail}$	1764	1.6%
M_{wing}	34337	30%
$M_{engines}$	15316	14%
$M_{engines\ controls}$	116	0.10%
$M_{fuel\ system}$	347	0.31%
$M_{flight\ control}$	207	0.18%
$M_{cargo\ handling\ system}$	2307	2.0%
M_{door}[2]	3100	2.7%
M_{anchor}	3470	3.1%
M_{buoys}	8158	7.2%
$M_{endplate\ floater}$	2719	2.4%
OEM	**112,745**	**100%**

The final operating empty mass (OEM) has decreased from 127,000 $[kg]$ to 113,000 $[kg]$ since the end of the midterm phase, representing an 11% reduction. This is without the inclusion of the structural mass of the fuselage and wing.

5.2. Iteration

To determine the final MTOM, the OEW is used as an input in the Class I weight estimation, replacing the initial linear relationship between MTOW and OEW derived from similar aircraft, as described in the baseline report [11]. The results from this estimation are then used to update all relevant design parameters, as detailed in the midterm report [25]. These updated parameters are subsequently used as inputs for the component weight estimation process described in Section 5.1. This iterative process is repeated until the change in MTOM between iterations is less than 1%. The final values after convergence are summarised in Table 5.3. The **mission fuel mass** refers to the fuel required for the 2000 $[nmi]$ two-way mission. The **reserve fuel mass** corresponds to the fuel needed for the 100 $[nmi]$ reserve requirement. The **total fuel mass** is the sum of the mission and reserve fuel masses. Finally, the **maximum fuel mass**, used for the ferry mission, is defined as 1.1 times the total fuel mass.

Table 5.3: *Final Weights*

	Parameter	Value	Unit
Outputs	MTOW	$2.97 \cdot 10^6$	$[N]$
	MTOM	$3.03 \cdot 10^5$	$[kg]$
	OEW	$1.45 \cdot 10^6$	$[N]$
	OEM	$1.48 \cdot 10^5$	$[kg]$
	Mission Fuel Mass	$6.34 \cdot 10^4$	$[kg]$
	Reserve Fuel Mass	$8.70 \cdot 10^2$	$[kg]$
	Total Fuel Mass	$6.43 \cdot 10^4$	$[kg]$
	Max Fuel Mass	$7.07 \cdot 10^4$	$[kg]$
	Max Fuel Volume	$9.10 \cdot 10^4$	$[L]$

5.3. Center-of-Gravity Range Estimation

To determine the CG range, the CG corresponding to the OEW configuration must first be established. This is done using the component weights from Section 5.1 and their respective positions, shown in Table 5.4. These positions are based on the known layout of the components. For any components with undetermined

[4] This is an installed mass estimate, the dry mass of the chosen APU (see Section 9.3) is 136$[kg]$[27]. For the calculations, a mass of 300$[kg]$ is used for the APU, to ensure a conservative estimate is made regarding the wet mass.
[5] Initial value for the installed battery mass. The 1336$[kg]$ is the uninstalled battery mass.
[6] Including 1.25 fudge factor [16, p. 405].

placement, their CG is assumed to lie at the midpoint of the fuselage. The coordinate system used is defined in Figure 5.1.

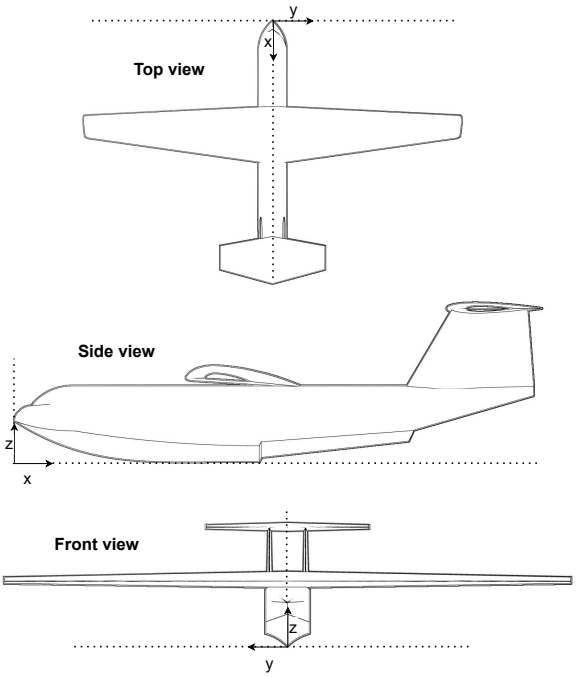

Figure 5.1: *Defined Coordinate System*

Table 5.4: *Component Positions*

Component	x	y	z
Air Conditioning	26.05	0.00	3.80
Anti-Ice	26.05	0.00	3.80
Battery	3.00	0.00	4.30
Avionics	26.05	0.00	3.80
Electrical	26.05	0.00	3.80
Furnishings	26.05	0.00	3.80
Fuselage	23.45	0.00	3.80
Handling Gear	26.05	0.00	3.80
Horizontal Tail	52.04	0.00	19.31
Instruments	26.05	0.00	3.80
Nacelle	16.40	0.00	9.64
Pneumatic Starter	26.05	0.00	3.80
Vertical Tail	46.35	0.00	13.45
Wing	23.49	0.00	8.40
Engine	16.40	0.00	9.64
Engine Controls	26.05	0.00	3.80
Fuel System	26.05	0.00	3.80
Flight Control	6.00	0.00	3.80
Cargo System	20.06	0.00	5.30
Door	45.86	0.00	3.80
Anchor	3.00	0.00	1.90
Buoys	23.49	0	8.40
Endplate Floats	18.50	0	2.60

During loading or unloading of cargo and fuel, the CG can shift depending on the sequence and distribution of mass. To quantify this shift, the cargo hold is assumed to be filled from front to back, in accordance with REQ-CAR.2 [11], using a cargo density of 160 $[kg/m^3]$. Only front-to-back loading is considered, as the aircraft's cargo door is located at the rear. Additionally, to evaluate the extreme CG condition, the cargo density is increased based on REQ-CAR.1, which states that the cargo hold must accommodate 100 $[tonnes]$. This leads to an effective cargo density given by:

$$\rho_{\text{cargo}} = \frac{100,000}{V_{\text{cargo}}}$$

Here, V_{cargo} is the volume of the cargo hold. The input parameters and results from the CG analysis are summarised in Table 5.5 andTable 5.6. The CG ranges in the three spatial dimensions are visualised in Figure 5.2, Figure 5.3, and Figure 5.4, with the combined XZ-plane shown in Figure 5.5.

Table 5.5: *Input for CG Range*

	Parameter	Value	Unit
Inputs	Cargo Density	160	$[kg/m^3]$
	Cargo Floor Height	3.20	$[m]$
	Cargo Hold Width	5.20	$[m]$
	Cargo Hold Height	4.20	$[m]$
	Cargo Hold Length	28.1	$[m]$
	x_{cargo}	6.00	$[m]$

Table 5.6: *Outputs for CG Range*

Outputs	Most Aft CG	23.6	$[m]$
	Most Aft CG (LEMAC Reference Frame)	0.506	$[\%mac]$
	Most Forward CG	20.8	$[m]$
	Most Forward CG (LEMAC Reference Frame)	0.227	$[\%mac]$
	Highest CG	7.04	$[m]$
	Lowest CG	2.96	$[m]$
	MTOW CG	$\begin{pmatrix} x \\ y \\ z \end{pmatrix} = \begin{pmatrix} 22.6 \\ 0.00 \\ 7.26 \end{pmatrix}$	$[m]$
	OEW CG	$\begin{pmatrix} x \\ y \\ z \end{pmatrix} = \begin{pmatrix} 22.6 \\ 0.00 \\ 6.77 \end{pmatrix}$	$[m]$

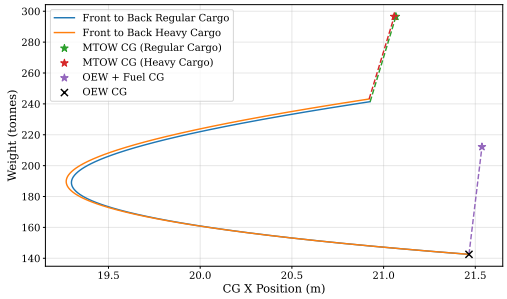

Figure 5.2: *CG Range X-Dimension*

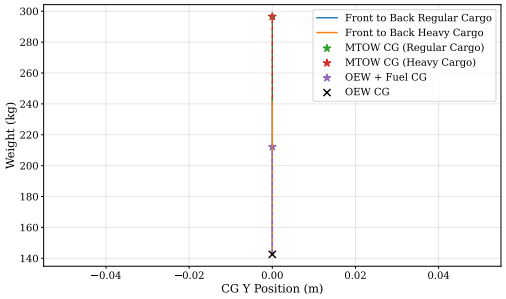

Figure 5.3: *CG Range Y-Dimension*

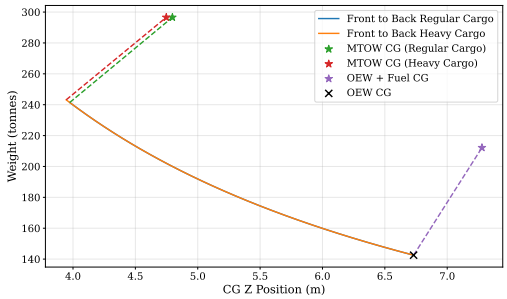

Figure 5.4: *CG Range Z-Dimension*

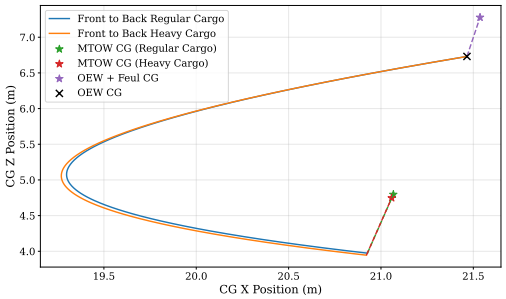

Figure 5.5: *CG Range XZ Projection*

The distance to the step from the nose is 24.8 $[m]$. The x position of the CG is always in front of this. This means the stability during floating will not be an issue in any loading case.

5.4. Compliance

This section demonstrates compliance with the requirements relevant to the CG analysis and weight estimation presented in this chapter. As shown in Table 5.7, all applicable requirements are currently being met.

Table 5.7: *Compliance Matrix – CG and Mass Requirements*

Requirement ID	Requirement Description	Compliance Justification	
REQ-SHC.3	The Maximum Take-Off Mass shall be below 500 $[tonnes]$.	The requirement is satisfied: the current MTOM is **303** [tonnes].	

6

Aerodynamics

In this chapter, the aerodynamic performance of the aircraft is discussed. This is done by first selecting the airfoil as explained in Section 6.1. The selected airfoil is used to construct the lifting properties of the wing in Section 6.4. For the take-off and landing conditions, the lifting performance of the wing is not sufficient and thus high lift devices (HLD's) must be designed. These HLD's are designed in Section 6.5. The performance of the aircraft is highly dependent on the drag, which is discussed in Section 6.6. The determination of the aerodynamic centre is done in Section 6.7. For structural design it is necessary to know the distribution of the lift, drag and moment. These aerodynamic distributions are given in Section 6.8. The Oswald efficiency, which is an important design parameter is discussed in Section 6.9. Finally, the stability derivatives will be discussed in Section 6.10. At the end of the chapter, in Section 6.11, the compliance with the relevant requirements is shown. Table 6.1 presents the relevant requirements for this chapter from the baseline report[11].

Table 6.1: *Relevant Requirements Aerodynamics [11]*

Requirement ID	Requirement Description	Category	Source
REQ-STB.1.1	The change in pitching moment coefficient of the aircraft with respect to the angle of attack shall be less than 0 ($C_{M_\alpha} < 0$).	Functional	REQ-CUST-SAFE.3
REQ-STB.1.3	The change in yawing moment coefficient of the aircraft with respect to the sideslip angle shall be greater than 0 ($C_{n_\beta} > 0$).	Functional	REQ-CUST-SAFE.3
REQ-CRU.1	The aircraft shall operate in ground effect at an altitude lower than 100 [ft].	Operational	REQ-CUST-PERF.4

6.1. Airfoil Selection

Selecting an appropriate airfoil is essential, especially for an aircraft operating in ground effect, where lift is enhanced and induced drag is reduced due to altered pressure distributions [28]. This section presents the evaluation of various airfoils, using a Reynolds number of $6.30 \cdot 10^6$ and a Mach number of 0.30, assessed at the mean aerodynamic chord (MAC).

Due to the characteristics of the project, the airfoil selection must be carefully considered. When close to a rigid surface, the operation of an airfoil is significantly different. The incoming airflow is restricted below the lifting surface. This results in additional lift when compared to free stream [28]. Furthermore, a substantial decrease in induced drag occurs due to the reduction of downwash angle as a result of the proximity to the surface [28].

The selection of airfoils is a combination of common airfoils, such as the NACA 0012 and uncommon ones, for example the S1223. Furthermore, airfoils, which have been mentioned in WIG literature, were also included in the selection [28]. All analysed airfoils are displayed in Figure 6.1. The performance of the airfoil is then illustrated in a series of plots, provided in Figure 6.2.

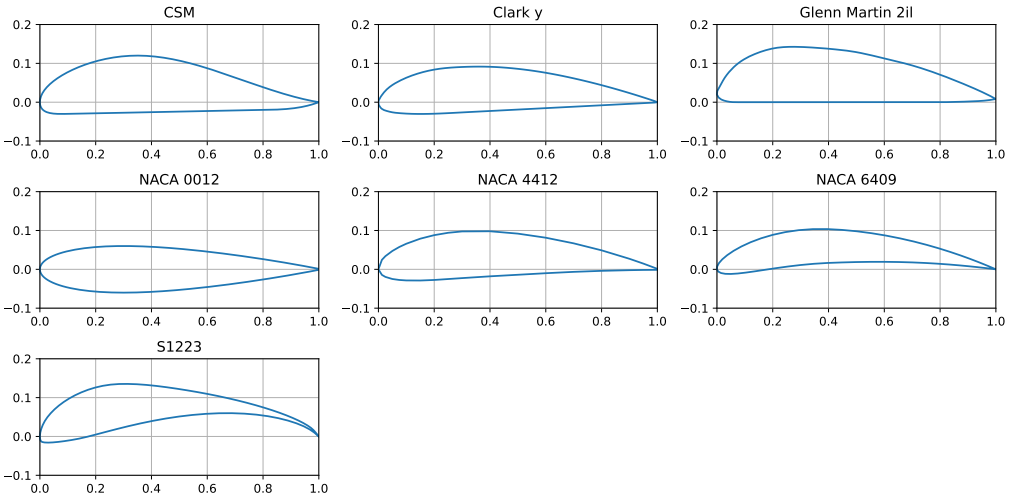

Figure 6.1: *Airfoil Shapes*

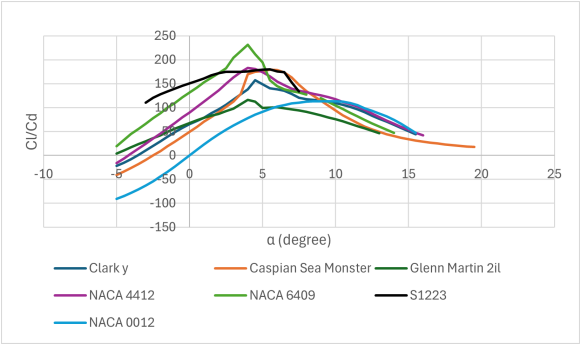

(a) *Aerodynamic Efficiency for Multiple Angles of Attack (XFLR5)*

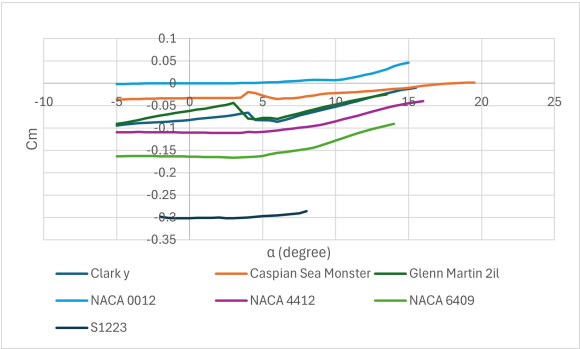

(b) *Moment Coefficient for Multiple Angles of Attack (XFLR5)*

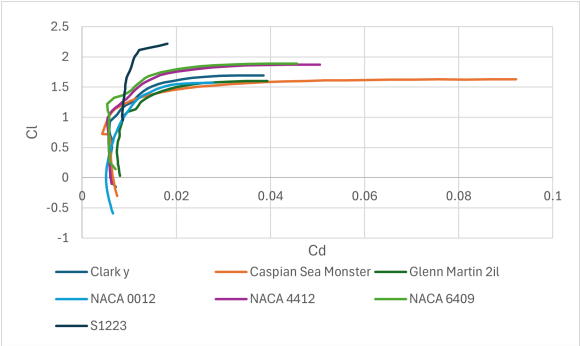

(c) *Drag Polar (XFLR5)*

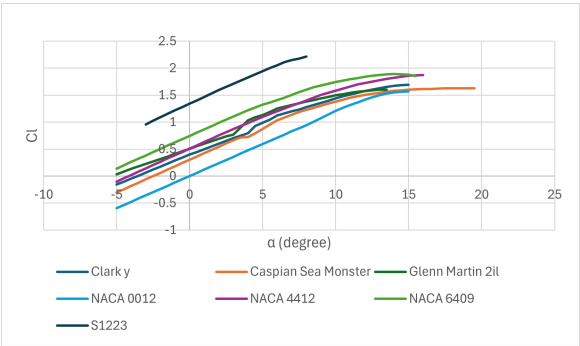

(d) *Lift Curve (XFLR5)*

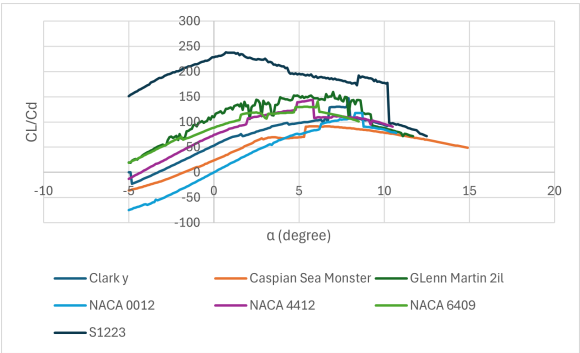

(e) *Aerodynamic Efficiency (Java Foil)*

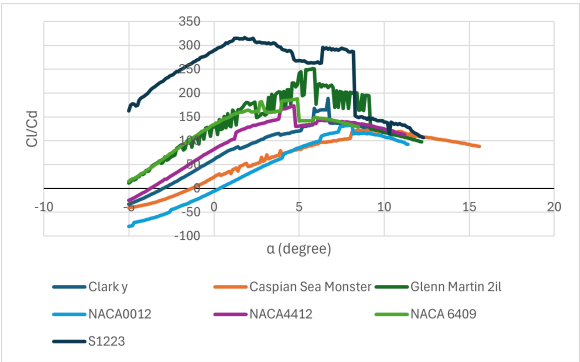

(f) *Aerodynamic Efficiency in Ground Effect (Java Foil)*

Figure 6.2: *Airfoil Performance*

Note that the four upper plots in Figure 6.2 are generated using XFLR5, whereas Figure 6.2e and Figure 6.2f are based on JavaFoil. This distinction arises, because XFLR5 does not support ground effect analysis, a key consideration in this project. It is also important to note that for all software tools used in this chapter, the behaviour beyond stall is highly unreliable and has, therefore, been excluded from the analysis.

Turning the attention to Figure 6.2a, which displays the lift-to-drag ratio (L/D) of various airfoils, it can be observed that the NACA 6409 and S1223 perform the best. However, both of these airfoils feature unconventional geometries, which introduce structural complexities. According to Liang et al. [28], airfoils with flat bottoms are preferred for maximizing wing-in-ground (WIG) effect. This flat-bottom design is only feasible if the airfoil's shape is compatible with such modification. Unfortunately, due to their curvature, the NACA 6409 and S1223 are not suitable for flattening and were thus excluded from further consideration.

The next best performers in L/D from Figure 6.2 are the NACA 4412, Clark Y, and CSM airfoils. However, as seen in Figure 6.2b, the CSM exhibits a positive moment coefficient, which makes the controllability and stability more difficult. In addition, it was specifically designed to operate only within ground effect, making it a poor candidate for scenarios requiring obstacle avoidance. This narrows down the viable options to the NACA 4412, Clark Y, and Glenn Martin 2il airfoils. Both the NACA 4412 and Clark Y have similar profiles and can accommodate a flattened bottom, aligning well with ground-effect optimization.

To further evaluate performance, especially in ground effect, the selected airfoils were analysed using JavaFoil, which supports ground proximity modelling. The results are shown in Figure 6.2e. Interestingly, JavaFoil outputs differ significantly from XFOIL, even without ground effect. While both tools generally agree on the performance ranking of the airfoils, JavaFoil indicates a notably improved performance for the Glenn Martin 2il, particularly in ground effect conditions.

It can be observed from Figure 6.2b that the Glenn Martin airfoil exhibits signs of pitch break behaviour near the point of maximum lift-to-drag ratio (L/D), as predicted by XFLR5 (Figure 6.2a). Notably, XFLR5 and JavaFoil disagree significantly on the location of this optimal L/D point. According to Bergmann et al. [29], XFLR5 generally provides more accurate aerodynamic predictions than JavaFoil, although the difference is not substantial. Given this, the final airfoil selection prioritizes strong performance in ground effect as indicated by JavaFoil, while aerodynamic data and behaviour predictions will primarily be based on the more reliable outputs from XFLR5. This approach takes a conservative stance by prioritizing the worst-case aerodynamic behaviour predicted by XFLR5, while still considering the potentially better ground-effect performance suggested by JavaFoil. It should also be noted that both JavaFoil and XFLR5 are simplified predictive tools, and more accurate analysis using Computational Fluid Dynamics (CFD) simulations is recommended for future work.

Given that the aircraft will operate primarily within ground effect, the Glenn Martin 2il was ultimately selected. Besides its superior aerodynamic performance in non GE, it also offers advantages in terms of structural simplicity and internal volume. This extra volume is needed for housing the structure of inflatable buoys required for the design, as will be explained in Subsection 8.3.4. The Glenn Martin 2il possesses the highest thickness-to-chord ratio of 14.2% of all airfoils, resulting in the lightest wing. The final selected airfoil shape is shown in Figure 6.3.

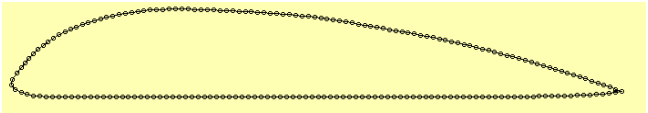

Figure 6.3: *Glenn Martin 2il Airfoil*

6.2. Wing Planform

This section presents the design of the wing planform, following a methodology proposed by Torenbeek [2]. The inputs and outputs associated with the wing planform design are summarised in Figure 6.2. Next to the

table, a visualization of the planform is presented.

Table 6.2: *Wing Planform Parameters*

	Parameter	Value	Unit
Inputs	A	8	$[m]$
	S	706	$[m^2]$
	λ	0.4	$[-]$
	$\Lambda_{c/4}$	0	[deg]
	Γ	0	[deg]
Outputs	b	75	$[m]$
	$\bar{c}$	10	$[m]$
	c_r	13.4	$[m]$
	c_t	5.4	$[m]$

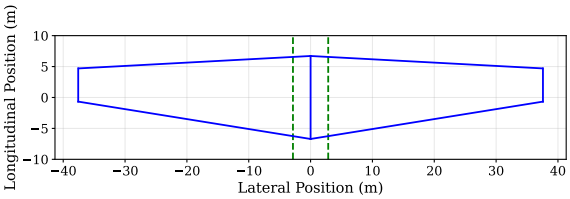

Figure 6.4: *Visualization of Wing Planform*

6.3. Endplates

As described in Subsection 7.2.4, side buoys have been added to the design to improve stability. These buoys inherently function as endplates, which are 5.8$[m]$ in height. According to Lange and Moore [30], the presence of endplates increases the effective aspect ratio (AR) of the wing, raising it from 8.0 to 9.175. In addition to improving AR, the endplates are expected to enhance aerodynamic performance by increasing lift—through an intensified ground effect cushion—and reducing induced drag by limiting wingtip vortex leakage [31]. However, due to time constraints, these secondary aerodynamic benefits could not be fully incorporated into the design calculations. Only the increase in aspect ratio was considered, which results in a conservative estimate of the aircraft's performance.

6.4. Lift Estimation

In this section, the lift estimation will be discussed. This is done using a method suggested by Phillips [1]. This method uses a 3D lift coefficient in non GE operation and transfers it to GE operation.

To obtain the out of GE 3D lift distribution, a 2D lift distribution must be transferred to 3D. For this, the downwash must be taken into account [1]. The 2D data is obtained using XFLR5 (uses the exact same method as XFOIL), which was chosen since it outputs more accurate results than JavaFoil [29]. Also, the general wing properties, such as taper, sweep and aspect ratio are utilised in this method. The 3D lift curve for GE operation is shown until the maximum lift coefficient, because stall is not implemented correctly in XFLR5, as was already discussed in Section 6.1. In Figure 6.5, the 3D lift curve in operation is shown for out of ground effect (blue) and in ground effect (orange).

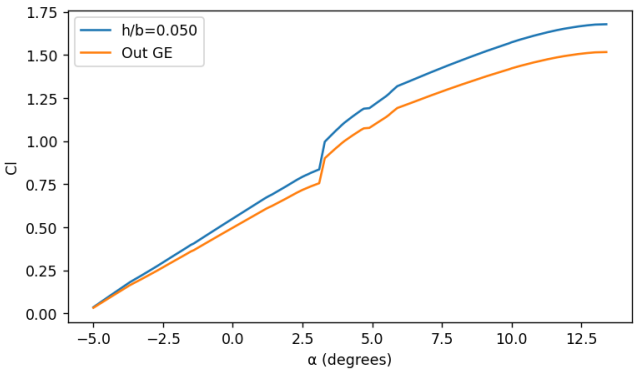

Figure 6.5: *Lift Curves of the Aircraft*

In Figure 6.5 it can be seen that the lift increases in ground effect. The shape of the ground effect curve has

[1] https://www.grc.nasa.gov/www/k-12/VirtualAero/BottleRocket/airplane/downwash.html [Cited 11 June 2025]

a similar shape to the non ground effect curve. In the region of angle of attack of 3.2 [deg] it is observed that the lift changes suddenly. When looking closer at this region it was observed that the transition of the boundary layer on the bottom side of the airfoil is delayed from 0.384 to 0.994, which could attribute to this effect. Next up, it can be seen that stall occurs after an angle of attack of 12.5 degrees. In Table 6.3 some selected parameters of the lift curve are shown.

Table 6.3: *Lift Curve Parameters*

Parameter	No GE	GE	Unit
C_{l_α}	0.105	0.118	$[\frac{1}{deg}]$
$C_{l_{max}}$	1.506	1.690	[-]
$\alpha_{L=0}$	-5.307	-5.307	[deg]

From Table 6.3 it can be seen that the lift curve slope and the maximum lift coefficient increase with GE. The zero lift angle of attack is constant over GE and non GE operation.

6.5. Sizing of High Lift Devices

A landing maximum lift coefficient ($C_{L_{max}}$) of 2.2 is assumed for the initial weight, wing loading, and take-off power estimations, as was determined in the midterm report [25]. However, as shown in Section 6.4, the clean configuration only provides a $C_{L_{max}}$ of 1.69, which is insufficient. This discrepancy necessitates the use of high-lift devices (HLD) to increase the maximum lift coefficient by 0.51. This section describes the sizing of the HLD's and documents the results.

To achieve this, the method proposed by Torenbeek is applied [2, pp. 252–256] and [32]. In this method, the increase in $C_{L_{max}}$ achieved through flaps depends on three key factors: the flapped surface area (i.e., the span-wise portion of the wing equipped with flaps), the flap type (influences the increment in sectional lift coefficient), and the total wing area.

Given the required lift augmentation and the flexibility to select a suitable flap type, the method can be used to determine the necessary flapped area and, consequently, the span-wise placement of the flaps. The flap chord is defined as a ratio of the local wing chord and is chosen to avoid interference with the main wing spars, which are typically located at 15% and 65% of the chord. Trailing-edge flaps are the primary means of increasing $C_{L_{max}}$, due to their effectiveness. Leading-edge devices, by contrast, are only considered when absolutely necessary. Specifically, when the available span for trailing-edge flaps alone is insufficient to achieve the required lift augmentation (for example, due to control surface interference). This is caused by the additional complexity and mass penalties associated with leading-edge systems. To ensure adequate lift and compatibility with structural constraints, conservative values are used for the relative flap chords: 30% of the local chord for trailing-edge devices and 10% for leading-edge devices. In Subsection 6.5.1 and Subsection 6.5.2 below, the flap type is selected and the final flap sizing results are presented.

6.5.1. Selection of Flap Type

As mentioned above, a distinction is made between leading edge high-lift devices and trailing edge devices. Within these types of devices, another distinction is made between wing-surface altering devices and devices that do not alter the wing-surface. The increment in the maximum section lift coefficient of the former is dependent on the fraction: c'/c, which is the flap-extended chord length divided by the original chord length. A selection of various flap types and their corresponding $C_{l_{max}}$ is presented in Table 6.4.

Table 6.4: $\Delta C_{L_{max}}$ *of Various High-Lift Devices when Fully Deployed [2, 32]*

	High-Lift Device	$\Delta C_{L_{max}}$ (Fully Deployed)
TE Devices	Plain and Split Flap	0.9
	Slotted Flap	1.3
	Fowler Flap	$1.3 \cdot c'/c$
	Double Slotted Flap	$1.6 \cdot c'/c$
	Triple Slotted Flap	$1.9 \cdot c'/c$
LE devices	Fixed Slot	0.2
	Leading Edge Flap	0.3
	Kruger Flap	0.3
	Slat	$0.4 \cdot c'/c$

As shown in Table 6.4, trailing-edge (TE) devices that increase wing surface area, such as Fowler, double-slotted, or triple-slotted flaps, offer the greatest lift augmentation. However, their complexity and associated mass penalties present significant integration challenges. In contrast, TE devices that do not increase wing area are simpler and lighter, though typically less effective in enhancing lift. Among these, the single-slotted flap provides the highest increase in maximum sectional lift coefficient, offering an optimal balance between aerodynamic performance and integration complexity. Therefore, it is selected for this application.

6.5.2. Flap Sizing Results

With the flap type selected, the sizing can be performed. In Figure 6.6, the results are presented along with the relevant inputs to arrive at the results.

	Parameter	**Value**	**Unit**
Inputs	$\Delta C_{L_{\max}}$	0.51·1.5[1]	[−]
	$\Delta c_{l_{\max}}$[2]	1.3	[−]
	b_1 (1 m from fuselage)	3.85	[m]
	δ_f	40	[deg]
	Flap type	Single slotted	[−]
	Relative flap chord	0.3	[−]
	S	705.9	[m^2]
Outputs	b_2	26.6	[m]
	S_{wf}	231	[m^2]
	S_{flap}	65.9	[m^2]
	$C_{L_{\max,\text{LND}}}$	2.20	[−]
	$C_{L_{\max,\text{TO}}}$	2.02[3]	[−]

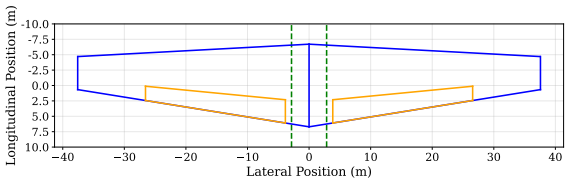

Figure 6.6: *Inputs and outputs for HLD design (left) and the final flap sizing visualized on the wing planform (right).*

Note that the outputs shown in Figure 6.6 are for a single wing, so in order to get the HLD of the other wing, the values are simply mirrored. This is the final design of the HLDs, as will become clear in Section 7.2.

6.6. Drag Estimation

In this section the drag estimation is discussed. This will be done by first estimating the zero lift drag coefficient and than combining it with the induced drag coefficient using the same method as in Section 6.4 [1]. The zero lift drag (C_{D_0}) has been estimated using the component drag build up method using the following formula:

$$C_{D_0} = \frac{1}{S_{\text{ref}}} \sum_c C_{f_c} \cdot FF_c \cdot IF_c \cdot S_{\text{wet}_c} + C_{D_{\text{misc}}} \tag{6.1}$$

The drag from three main components has been added to give the total C_{D_0}. The fuselage, the wing-tail combination and the engine nacelles. For each of this the wetted area, S_{wet} has been estimated from the

[1] Safety factor of 1.5 to ensure conservative sizing
[2] This value is different for each flap type
[3] Achieved by extending the flaps by 60% (24 [deg])

method suggested by Torenbeek [2]. The skin friction coefficients, form factors and interference factors have been estimated from the methods from DATCOM [33].

Additionally, to account for the endplates, the wetted area of the wing has been increased accordingly. For the inflatable buoys, it is assumed that their wetted area when deflated is equivalent to that of a single engine nacelle. This area is accounted for under the nacelle component, as the buoys are mounted beneath the engines. Moreover, as a result of the uncertainty of the engine wetted area, a safety factor of 1.5 has been applied. Finally, the fuselage up-sweep has been included in miscellaneous drag. With all the assumptions stated, the result of the zero lift drag of each component can be found in Table 6.5.

Table 6.5: *Zero Lift Drag by Component*

Component	Zero Lift Drag Coefficient
Fuselage	0.0026
Wing-Tail	0.0081
Nacelles (buoys included)	0.0011
Miscellaneous	0.0032
Total	0.0150

The second part for the drag estimation is obtained by the induced drag, which is created by the lift. The induced drag will be estimated using a method provided by Phillips [1]. The inputs for these methods are the shape of the wing, the flying height and the Oswald efficiency factor, which is discussed in Section 6.9. In Figure 6.7a the drag curve is presented and in Figure 6.7b the drag polar is shown.

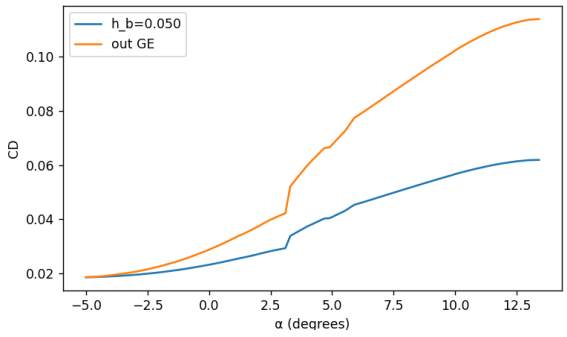

(a) *Drag Curve*

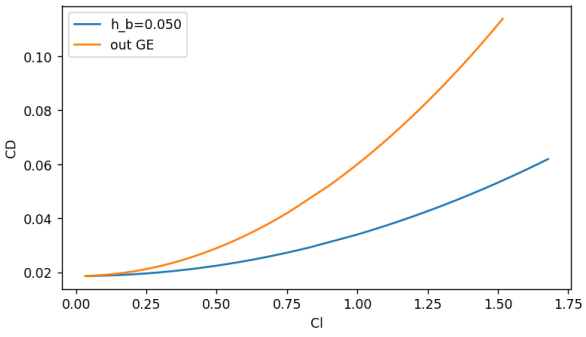

(b) *Drag Polar*

In Figure 6.7a and Figure 6.7b it can be seen that the drag reduces significantly when flying in ground effect. Combining this with the lift in Section 6.4 the aerodynamic efficiency is obtained and shown in Figure 6.8.

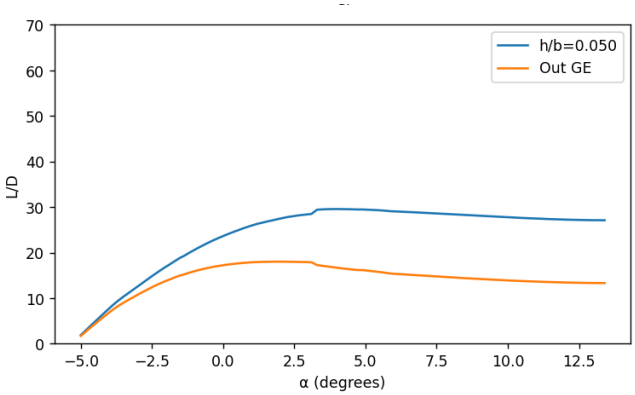

Figure 6.8: *Aerodynamic Efficiency*

In Figure 6.8, it can be seen that the aerodynamic efficiency increases when flying in ground effect. The maximum efficiency of 29.6 is achieved at an angle of attack of 4.0 [deg], which represents the optimal

condition. However, this does not imply that the aircraft is flying at exactly this angle. What matters is that the angle of attack is sufficient for the lift coefficient (C_l) to be large enough, at the given speed, to counteract the aircraft's weight.

6.7. Aerodynamic Centre

In this section the determination of the position and moment of the aerodynamic centre will be determined. For this, the data of the moment coefficient around the quarter chord position is extracted from XFLR5 as shown in Figure 6.9.

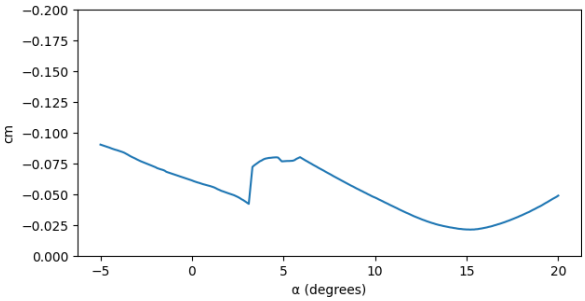

Figure 6.9: *Moment Coefficient at Quarter Chord Position*

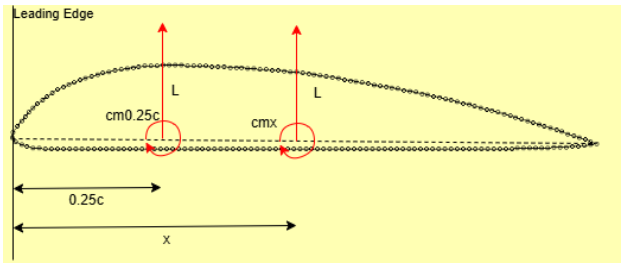

Figure 6.10: *FBD Airfoil*

In Figure 6.9 it can be seen that the moment at the quarter chord point changes abruptly at an angle of attack of 3.2 [deg]. This behaviour was not expected, but it was noticed that the transition point at the bottom of the airfoil moves backwards significantly. Namely from 0.384 to 0.994, which can contribute to some significant changes in the behaviour of the flow field. This behaviour is not desirable for a stable aircraft and should be treated carefully. Further research is needed to confirm why this phenomenon occurs. Using the data from XFLR5, the aerodynamic moment is placed at an arbitrary point. In Figure 6.10 a free body diagram (FBD) of the airfoil is given. Using the FBD in Figure 6.10, a formula is derived for the placement of the moment at an arbitrary point on the airfoil, which is presented in Equation 6.2.

$$C_{m_x} = C_{m_{0.25c}} + C_l \cdot (\frac{x}{c} - \frac{1}{4}) \tag{6.2}$$

After this the position at which the moment coefficient is constant with respect to its immediate neighbour is found ($C_{m_{ac_{i+1}}} - C_{m_{ac_i}} = 0$). Here, i represents the selected value of C_m and $i+1$ its immediate neighbour to the right, which thus corresponds to a slightly higher angle of attack. Using this in combination with Equation 6.2, Equation 6.3 is obtained.

$$\frac{x_{ac}}{c} = \frac{C_{m_{0.25c_{i+1}}} - C_{m_{0.25c_i}}}{C_{l_i} - C_{l_{i+1}}} + \frac{1}{4} \tag{6.3}$$

The position that is found using Equation 6.3, is the position of the aerodynamic centre at this angle of attack. In Figure 6.11, the aerodynamic centre for multiple angles of attack is shown.

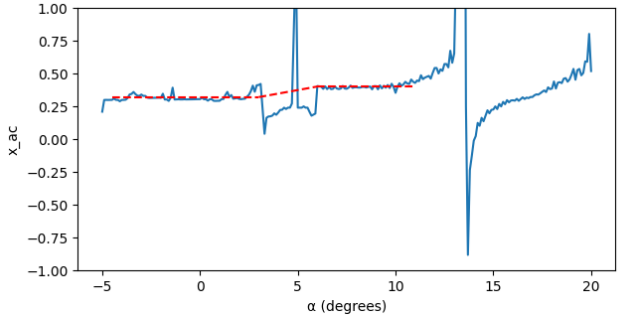

Figure 6.11: *Position of the Aerodynamic Centre with Varying Angles of Attack*

In Figure 6.11, it can be seen that the aerodynamic centre has a constant position for two segments. The first segment is between an angle of attack of -4.5 to 3.0 [deg] and 6.0 to 11 [deg] for the second segment. The average aerodynamic centre is located at 0.32c and 0.40c, respectively. The moment around the aerodynamic centre for the first segment is -0.096 and -0.261 for the second segment. This is determined by evaluating the moment about the aerodynamic centre for each section using Equation 6.2, and then averaging the results across the segment. In between these two segments, a region exists where the aerodynamic centre changes drastically. This can be observed by the jump in Figure 6.9 as discussed earlier. The steep increase of the graph after 11 [deg] can be attributed to starting flow separation.

6.8. Lift, Drag and Moment Span-Wise Distribution

In this section, the span-wise lift, drag and moment distribution will be discussed. These span-wise distributions will be considered when flying in the most critical condition. These are the conditions when the lift coefficient is at its maximum, in ground effect. In ground effect, the central portion of the wing experiences higher loading compared to the tips [34]. This load distribution reduces the bending moment, which is typically a critical factor for structural design, compared to a configuration with greater tip loading. For this analysis, the non ground effect lift distribution will be found using XFLR5. After this, the distribution is scaled to the lift coefficient in ground effect. This is a conservative approach, since in this method the lift/drag will be more pronounced on the tips than in reality. The same method is used to obtain a moment distribution. The drag distribution in XFLR5 is scaled with the lift coefficient squared. In Figure 6.12, the lift, drag and moment distributions are illustrated. Note that in the lift distribution, the effect of the full aileron deflection is included, of which the sizing is discussed in Subsection 7.2.3.

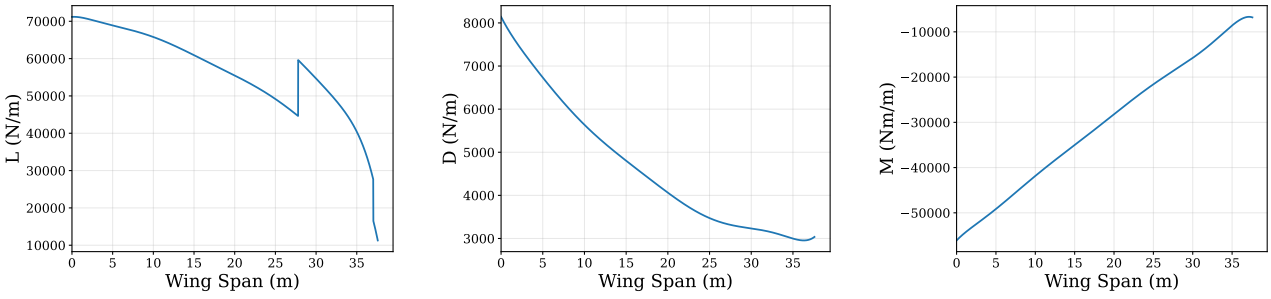

(a) *Span-Wise Lift Distribution* **(b)** *Span-Wise Drag Distribution* **(c)** *Span-Wise Moment Distribution*

Figure 6.12: *Span-Wise Distributions of Lift, Drag, and Moment*

The lift distribution also needs to be evaluated for the horizontal and side force for the vertical tail. This is done by using XFLR5. In Figure 6.13a and Figure 6.13b the horizontal lift and vertical side force distribution are given respectively. This includes an additional component due to the elevator and rudder, the effects and sizing of which are discussed in Section 7.2. Note that in Figure 6.13a, the discrepancy at around 3 [m] is attributed to the presence of the vertical tail, splitting the elevator into different segments.

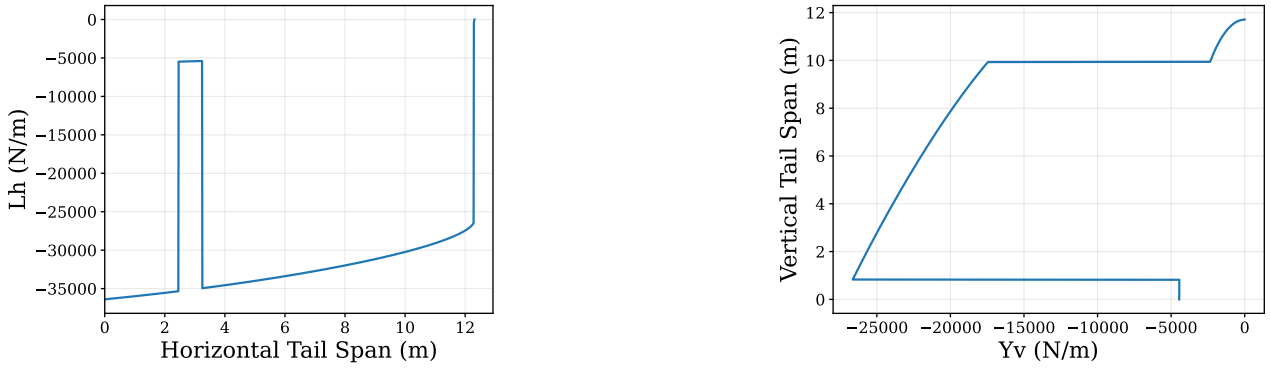

(a) *Lift Distribution of the Horizontal Tail* **(b)** *Side Force of the Vertical Tail*

Figure 6.13: *Span-wise Distributions for the Horizontal and Vertical Tails*

6.9. Miscellaneous Parameters

In this section, some important aerodynamic parameters are discussed, which were deemed critical to know at this stage of the design. First, the Oswald efficiency factor is discussed, after which the downwash gradient is considered.

Oswald Efficiency

For the calculation of the Oswald efficiency factor, the methodology from Torenbeek was used. This is applicable for a symmetrical untwisted wing [35]. The dimensionless lateral centre is a required input for this method, which can be obtained in a similar way to the centre of pressure [1]. For this, numerical integration is used and the data from XFLR5 as in Section 6.8. This yielded an Oswald efficiency factor of $e = 0.838$.

Downwash Gradient

For the estimation of the downwash gradient, it is considered that the design has an H-tail configuration. The downwash gradient for an H-tail can be estimated by a method proposed by Scholz [36]. This method uses inputs for the height of the horizontal stabilizer, as well as geometrical and aerodynamic properties of the wing. The final value for the downwash is calculated to be $\frac{d\epsilon}{d\alpha} = 0.46\ [rad^{-1}]$.

6.10. Stability Derivatives

In this section, the stability derivatives are discussed. In order to calculate these coefficients, DATCOM has been used as the main source and supplemented with methods from AE3202 Flight Dynamics lecture notes[37] and an academic source[38]. These sources can be found in the last column of Table 6.6. An overview of all symmetric and asymmetric aerodynamic coefficients are given in Table 6.6 and Table 6.7, respectively. Note that, due to the time constraints of the project only the stability coefficients during low altitude cruise are presented. If one is interested in elevator, aileron and rudder deflection coefficients, please refer to Section 7.2.

Table 6.6: *Symmetric Stability Coefficients*

Parameter	Value	Source
C_{m_q} [−]	-28.8	DATCOM
C_{z_α} $[rad^{-1}]$	-5.6	Flight Dynamics Course
C_{x_α} $[rad^{-1}]$	0.13	Flight Dynamics Course
C_{m_α} $[rad^{-1}]$	-0.55	Flight Dynamics Course
C_{Z_u} [−]	-1.0	Flight Dynamics Course
C_{X_u} [−]	-0.045	DATCOM
C_{m_u} [−]	0.0	Flight Dynamics Principles[38]
$C_{m_{\dot\alpha}}$ $[s/rad]$	-3.5	DATCOM

Table 6.7: *Asymmetric Stability Coefficients*

Parameter	Value	Source
C_{Y_β} $[rad^{-1}]$	-1.1	DATCOM
C_{l_β} $[rad^{-1}]$	-0.064	DATCOM
C_{n_β} $[rad^{-1}]$	0.34	DATCOM
C_{Y_p} [−]	-0.028	DATCOM
C_{l_p} [−]	-0.46	DATCOM
C_{n_p} [−]	-0.054	DATCOM
C_{Y_r} [−]	-	-
C_{l_r} [−]	0.16	DATCOM
C_{n_r} [−]	-0.18	DATCOM
$C_{Y_{\dot\beta}}$ $[s/rad]$	0.079	DATCOM
$C_{l_{\dot\beta}}$ $[s/rad]$	-0.013	DATCOM
$C_{n_{\dot\beta}}$ $[s/rad]$	-0.022	DATCOM

The term C_{Y_r} has been neglected in the state-space formulation, as its contribution is insignificant compared to the dominant μ factor [37]. In subsonic flight, the pitching moment coefficient C_m is largely independent of changes in velocity or Mach number. Consequently, the derivative C_{m_u}, is often assumed to be negligibly small and is commonly omitted from stability analyses under these conditions[38]. Some noticeable values among the symmetric stability derivatives are C_{m_q}, C_{z_α}, and $C_{m_{\dot\alpha}}$, as they are significantly larger compared to the other coefficients. These values have been validated using aerodynamic data from similarly sized aircraft found in [37], specifically from the Boeing 747-100, which has a wingspan of 60 m and a length of 70 m in a flaps-up configuration. For this configuration, the Boeing 747-100 exhibits $C_{m_q} = -19.45$, $C_{z_\alpha} = -4.487$, and $C_{m_{\dot\alpha}} = -3.39$.

[1] https://www.grc.nasa.gov/www/k-12/VirtualAero/BottleRocket/airplane/cp.html [Cited 13 June]

While the final coefficients obtained for our aircraft show some discrepancies with those presented in [37], these can be reasonably explained by the fact that the two aircraft differ significantly in wing planform and operate in different flight regimes (ground effect vs. non-ground effect). Notably, when considering the Boeing 747-100 with flaps deployed, $C_{m_q} = -21.98$, $C_{z_\alpha} = -5.293$, and $C_{m_{\dot{\alpha}}} = -3.45$, the coefficients become more comparable to those of our aircraft. This configuration, which produces more lift, is potentially more representative of our vehicle operating in ground effect. Therefore, the similarity in aerodynamic derivatives supports the overall validity and stability of our aircraft model.

By examining the calculated stability values, one can make an initial prediction regarding spiral stability using Equation 6.4[37].

$$C_{l_\beta} C_{n_r} - C_{n_\beta} C_{l_r} > 0, \text{ for spiral stability} \tag{6.4}$$

This formula yields -0.044, which makes the spiral of this aircraft unstable. Spiral instability is generally considered a minor issue in aircraft design, as the instability develops slowly over time. A properly trained pilot will be able to accommodate for this. Nonetheless, this issue will be further addressed in Subsection 7.2.5.

6.11. Compliance

In this section, the compliance of the relevant requirements to this chapter are presented. In Table 7.8, the compliance with relevant requirements is shown, along with the justification.

Table 6.8: *Compliance Matrix - Aerodynamics*

Requirement ID	**Description**	**Compliance Justification**	
REQ-STB.1.1	The change in pitching moment coefficient of the aircraft with respect to the angle of attack shall be less than 0 ($C_{m_\alpha} < 0$)	$C_{m_\alpha} = -0.55 < 0$ (see Table Table 6.6)	
REQ-STB.1.3	The change in yawing moment coefficient of the aircraft with respect to the sideslip angle shall be greater than 0 ($C_{n_\beta} > 0$)	$C_{n_\beta} = 0.34 > 0$ (see Table Table 6.6)	
REQ-CRU.1	The aircraft shall operate in ground effect at an altitude lower than 100[ft]	Aerodynamic design ensures sustained ground effect operation, as demonstrated in Section 6.8	

7

Stability & Control

In the previous chapter, the aerodynamic characteristics of the aircraft were analysed. Building on that, this chapter focuses on the design of the empennage and control surfaces, which are driven by aerodynamics. Furthermore, the water stability of the aircraft is examined to appropriately size the wingtip buoys and an eigenmotion analysis is conducted based on the stability derivatives found in the aerodynamics chapter. For Stability & Control the relevant requirements are displayed in Table 7.1 below.

Table 7.1: *Relevant Requirements Stability and Control [11]*

STB	Stability	Category	Source
REQ-STB.1	The aircraft shall be statically stable during all stages of flight.	Functional	REQ-CUST-SAFE.3
REQ-STB.2	The aircraft shall be dynamically stable during all stages of flight.	Functional	REQ-CUST-SAFE.3
REQ-STB.3	The aircraft shall be controllable on all axes during all stages of flight.	Functional	
REQ-STB.3.1	The aircraft shall be pitch controllable during all stages of flight.	Functional	
REQ-STB.3.2	The aircraft shall be roll controllable during all stages of flight.	Functional	
REQ-STB.3.3	The aircraft shall be yaw controllable during all stages of flight.	Functional	

7.1. Empennage Design

The empennage plays a critical role in ensuring the stability and controllability of an aircraft throughout its flight envelope. It typically consists of the horizontal and vertical stabilisers, which provide pitch and yaw stability, respectively. Proper sizing of the empennage is essential for achieving desired handling characteristics, trim capabilities, and overall aerodynamic performance. In this section, the sizing of both the horizontal and vertical tail surfaces is carried out using the method described by Torenbeek [2]. The horizontal tail sizing process is detailed in Subsection 7.1.1, followed by the vertical tail sizing in Subsection 7.1.2.

7.1.1. Horizontal Tail

For the sizing of the horizontal tail, two key aspects must be considered during the design process:

- **Controllability:** The horizontal tail must provide sufficient control authority to effectively pitch the aircraft. This ensures that the aircraft can perform required manoeuvrers, such as pitching up or down, within the desired performance envelope.
- **Stability:** The horizontal tail should contribute to the aircraft's dynamic stability. This means that, in the event of a change in angle of attack (AoA) (α), the aircraft should return to a trimmed flight condition, thereby preventing uncontrollable pitching motions.

The sizing of the horizontal tail depends on the position of the center of gravity (CG), which was determined in Chapter 5. Combined with the required control and stability criteria, this information defines both the optimal longitudinal placement of the wing and the necessary surface area of the horizontal tail. The results of these analyses are shown in Figure 7.1 and Figure 7.2. The planform of the horizontal tail is derived by

setting the chord at the attachment point with the vertical tail equal to the tip chord of the vertical tail. With a chosen aspect ratio, leading-edge sweep, and quarter-chord sweep, the full planform geometry is then defined. The resulting key parameters of the horizontal tail design are summarised in Table 7.2.

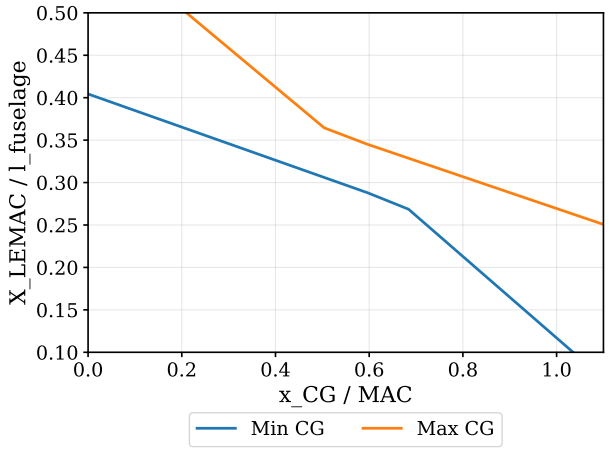

Figure 7.1: *CG Range for Various Wing Positions*

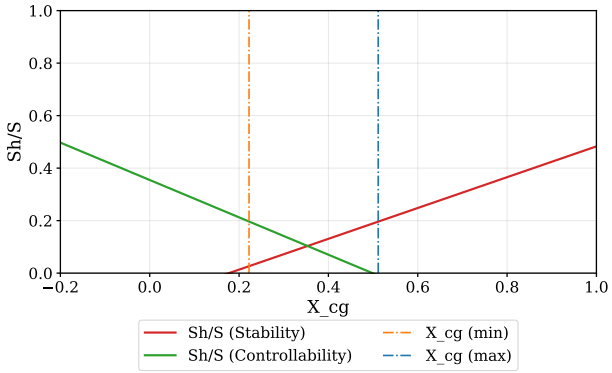

Figure 7.2: *Scissor Plot with CG Range*

7.1.2. Vertical Tail

Several key factors must be considered in the sizing of the vertical tail.

- **Control During One Engine Inoperative (OEI) Condition:** In the event of an engine failure, especially on a multi-engine aircraft, asymmetric thrust causes a yawing moment. The vertical tail must provide sufficient control authority to counteract this and maintain coordinated flight.
- **Lateral Stability:** The vertical tail contributes to the aircraft's weathercock stability. A larger or more effective vertical tail improves the ability to resist sideslip and enhances yaw stability.
- **Crosswind Landing:** In conventional aircraft design, crosswind capability can be a limiting factor during landing. However, in this case, crosswind landings are not considered in the vertical tail sizing. Since the aircraft is designed to land on water rather than on a runway, it has the flexibility to align into the wind during landing, effectively eliminating crosswind constraints.
- **Spin Recovery:** In case of a spin, effective yaw control is crucial for recovery. A sufficiently sized vertical tail and rudder help generate the aerodynamic forces needed to exit the spin safely.

Since Torenbeek's design relation in figure 9-23 is intended for two or four-engine aircraft, a safety factor of 1.2 is applied in these relations to account for this design's six-engine configuration [2, p.336]. Furthermore, unlike Torenbeek's original method, this design incorporates two vertical tails to allow for the rear of the aircraft to fold open, as will be illustrated in Section 8.3. As a result, the vertical tail area (S_v) obtained from the method is divided equally between the two fins to determine the planform of each vertical tail. The inputs and outputs for the vertical tail sizing are shown in Table 7.3.

7.1.3. Empennage Sizing Results

Table 7.2: *Inputs and Outputs for Horizontal Tail*

	Parameter	Value	Unit
Inputs	Most Aft CG	0.506	$[mac]$
	l_{fus}	52.1	$[m]$
	Fuel Mass	$6.43 \cdot 10^4$	$[kg]$
	S	705	$[m^2]$
	C_{L_h}	0.590	$[-]$
	$C_{L_{A-h}}$	1.13	$[-]$
	$C_{L_{\alpha_h}}$	0.119	$[-]$
	$C_{L_{\alpha_{A-h}}}$	0.101	$[-]$
	x_{ac}	0.277	$[mac]$
	Stability Margin	0.100	$[-]$
	$\frac{V_h}{V}$	1.00	$[-]$
	mac	9.97	$[m]$
	$C_{m_{ac}}$	-0.250	$[m]$
	$\frac{d\epsilon}{d\alpha}$	0.460	$[-]$
	A_h	4.50	$[-]$
	$\Lambda_{h_{LE}}$	5.0	[deg]
	$\Lambda_{h_{c/4}}$	0.0	[deg]
Outputs	S_h/S	0.190	$[-]$
	S_h	134	$[m^2]$
	b_h	24.6	$[m]$
	c_{r_h}	6.07	$[m]$
	c_{t_h}	5.14	$[m]$
	λ_h	0.847	$[-]$
	MAC_h	5.62	$[m]$
	x_{LEMAC}/l_{fus}	0.361	$[-]$

Table 7.3: *Inputs and Outputs for Vertical Tail*

	Parameter	Value	Unit
Inputs	C_{n_β}	0.341	$[-]$
	$C_{y_{\beta_v}}$	-0.0274	$[-]$
	l_v	20.8	$[m]$
	S	706	$[m^2]$
	A_v	1.50	$[-]$
	b	75.2	$[m]$
	MAC	75.2	$[m]$
	$\frac{V_v}{V}$	0.900	$[-]$
	y_{engine}	17.9	$[m]$
	P_{engine}	$7.40 \cdot 10^6$	$[W]$
	V_{stall}	61.7	$[m/s]$
	S_{rudder}	17.7	$[m^2]$
	c_{rudder}	0.250	$[-]$
	b_v	11.7	$[m]$
	$\Lambda_{c/4_v}$	15.0	[deg]
	Max Structural Payload	$100 \cdot 10^3$	$[kg]$
	MTOM	$303 \cdot 10^3$	$[kg]$
Outputs	S_v/S	0.129	$[-]$
	S_v	91.4	$[m^2]$
	b_v	11.7	$[m]$
	c_{r_v}	9.75	$[m]$
	c_{t_v}	5.85	$[m]$
	MAC_v	7.97	$[m]$
	$\Lambda_{v_{LE}}$	30.6	[deg]
	x_{LE}	42.4	$[m]$

7.2. Control Surfaces

With the empennage now sized, the attention turns to enabling controlled flight along all three axes. Beyond providing stability, the empennage and the aircraft's control surfaces are needed to actively manage pitch, roll, and yaw. Accordingly, the following subsections detail the sizing of the elevator, rudder and ailerons.

7.2.1. Elevator Sizing

Elevator sizing begins by identifying the most critical loading condition. Two scenarios are evaluated: a 2.5g pull-up manoeuvre, as defined in Section 8.1, and the take-off rotation during waterborne operations. The latter involves significant water drag and reduced pitch-up moment due to the over-wing engine placement. Despite this, sizing is based on the 2.5g pull-up case, followed by a verification that waterborne rotation remains achievable. The elevator sizing process follows an analytical approach based on the required steady pitch rate and the elevator effectiveness coefficient ($C_{m_{\delta e}}$). The critical flight condition considered is at a lift-off speed of 65 $[m/s]$ with the center of gravity at its most aft position, where elevator authority is minimal. Despite this, the elevator must still be capable of performing a 2.5g pull-up.

Steady State Pitch Rate

For a 2.5g pull-up, the aircraft is assumed to follow a circular path with a load factor of $n = 2.5$. The required steady-state pitch rate is defined by Equation 7.1:

$$q = \frac{(n-1)g}{V}, \tag{7.1}$$

where q $[rad/s]$ is the pitch rate, g $[m/s^2]$ is gravitational acceleration, and V $[m/s]$ is the flight speed.

To link this to elevator sizing, the pitching moment coefficient around the centre of gravity is evaluated as shown in Equation 7.2:

$$M = \bar{q}Sc\left(C_{m_{\delta_e}}\delta_e + C_{m_q}\frac{q\bar{c}}{V}\right) = 0, \tag{7.2}$$

$$C_{m_{\delta_e}} = -\frac{q\bar{c}}{V\delta_e}C_{m_q} \tag{7.3}$$

where $\bar{q}$ is dynamic pressure, S is wing area, $\bar{c}$ is mean aerodynamic chord, C_{m_q} is the pitch damping derivative, and δ_e is elevator deflection. Rearranging for $C_{m_{\delta_e}}$, yields Equation 7.3. The sign convention assumes positive elevator deflection is clockwise; thus, a nose-up moment requires a negative elevator deflection.

Derivation of Elevator Effectiveness

The elevator effectiveness is derived from the pitching moment due to elevator deflection, given by the equations below.

$$dM = -2\bar{q}c_{l_{\alpha_h}}\delta_e\tau_e l_h S_e \tag{7.4}$$

$$C_{m_{\delta_e}} = -\left(\frac{V_h}{V}\right)^2 \frac{2c_{l_{\alpha_h}}\tau_e l_h}{S\bar{c}}\int_{b1}^{b2} c_h(y)dy \tag{7.5}$$

Here, $c_{l_{\alpha_h}}$ is the 2D lift curve slope of the horizontal tail, τ_e is the elevator effectiveness factor (based on chord ratio, see Figure 7.3), l_h is the tail arm, and S_e is the elevator area. Expressing S_e as $c_h(y)dy$ and integrating over span, we obtain the effectiveness in Equation 7.5. In this expression, $\left(\frac{V_h}{V}\right)^2$ represents the dynamic pressure ratio at the tail. For a T-tail, this is typically small but conservatively accounted for in the safety factor of Equation 7.1. The remaining terms are defined as before, with $c_h(y)$ the chord distribution of the horizontal tail. The procedure is as follows: a maximum elevator deflection is chosen, and Equation 7.3 is used to compute the required $C_{m_{\delta_e}}$. Based on literature recommendations [2, p. 329], an initial inboard location b_1 and relative elevator chord are selected. The outer limit b_2 is then determined using Equation 7.5, ensuring the elevator span does not interfere with the vertical tail structures.

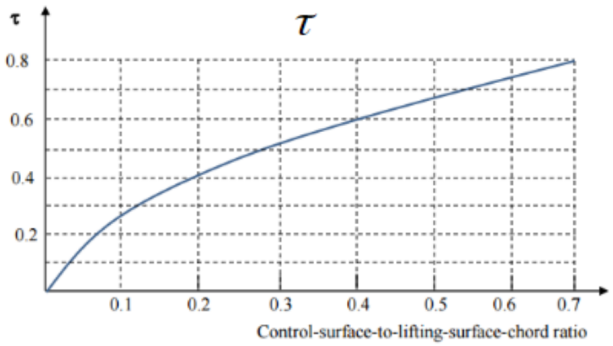

Figure 7.3: *Control Surface Effectiveness as a Function of Relative Chord to local Lifting Surface Chord [39]*

Elevator Sizing Results

In Table 7.4, the results are presented along with the relevant inputs to arrive at the results.

Table 7.4: *Inputs and Outputs of Final Elevator Sizing (Half the Wing)*

	Parameter	Value	Unit
Inputs	q	0.23	[rad/s]
	S	706	[m^2]
	$c_{l_{\alpha_h}}$	0.120	[rad^{-1}]
	l_h	27.2	[m]
	δ_e	-35.0	[deg]
	$\bar{c}$	9.97	[m]
	V	65	[m/s]
	C_{m_q}	-28.8	[-]
	b_1	0.0	[m]
	$c_{elevator}$	0.375	[-]
Outputs	$b_{2,s1}$	2.46	[m]
	$b_{1,s2}$	3.24	[m]
	$b_{2,s2}$	12.3	[m]
	Sw_e	64.8	[m^2]
	S_e	24.3	[m^2]
	τ_e	0.58	[-]
	$C_{m_{\delta_e}}$	-1.62[1]	[rad^{-1}]
	$C_{z_{\delta_e}}$	-0.059[1]	[rad^{-1}]
	$\delta_{e_{TO}}$	-3.0	[deg]
	Max Elevator Lift	$3.27 \cdot 10^5$	[N]
	$\delta_{e_{trim}}$	-1.66	[deg]

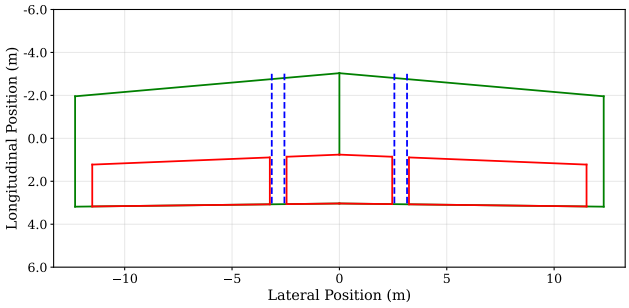

Figure 7.4: *Horizontal Tail Planform with Elevator Position and Size, Leading Edge is Upwards*

The take-off rotation case, introduced earlier, is reassessed via a simplified moment balance considering water drag, thrust, lift, and wing pitching moment. The required elevator deflection is found to be -3.0 [deg], well within the allowable ± 25 [deg] range. The corresponding elevator lift from Table 7.4 is superimposed on the nominal horizontal tail lift to determine the critical case for structural design, as detailed in Subsection 8.4.4. Note that, the elevator lift appears lower here, because the safety factor is excluded to avoid duplication in Subsection 8.4.4. The calculated $C_{m_{\delta_e}}$ is used in the eigenmotion analysis in Subsection 7.2.5.

7.2.2. Rudder Sizing

Lateral control is provided by the rudder, which is sized for the one-engine-inoperative (OEI) condition, consistent with the vertical tail sizing in Subsection 7.1.2. While the vertical tail nullifies the resulting yaw rate, the rudder must counteract the yaw acceleration caused by asymmetric thrust. Since, climb is the most critical phase with all six engines operating, sizing is based on take-off thrust and lift-off velocity, as then the OEI has the most influence and the rudder the least. Given the alternating propeller rotation (clockwise and counter-clockwise from left to right), failure of engine 1 produces the largest yawing moment. The yawing moment coefficient due to asymmetric thrust is given in Equation 7.6:

$$C_{n_e} = \frac{1.5 T_p}{\bar{q} S b} \left(\sum_{i=2}^{3} \left(y_{i_{\text{left}}} + (-1)^i \frac{1}{4} D_p \right) - \sum_{i=1}^{3} \left(y_{i_{\text{right}}} + (-1)^{i+1} \frac{1}{4} D_p \right) \right) \tag{7.6}$$

In this expression, T_p is the thrust per engine, D_p is the propeller diameter, $\bar{q}$ is the dynamic pressure, S is the wing reference area, b is the wingspan, and $y_{i_{\text{left/right}}}$ are the span-wise engine positions. The alternating signs account for the direction of propeller rotation, and a 1.5 safety factor is applied for conservatism. As the aircraft features two vertical tails, each rudder must be capable of fully countering the yawing moment independently in case of a single-rudder failure.

[1] Note that this is with the contribution of both sides of the horizontal tail

Derivation of Rudder Effectiveness

Analogous to elevator sizing, rudder effectiveness is derived from the yawing moment balance. The steady-state yaw moment during OEI must satisfy Equation 7.7:

$$N = \bar{q}Sb\left(C_{n_{\delta_r}}\delta_r + C_{n_e}\right) = 0. \tag{7.7}$$

Solving for the rudder effectiveness yields $C_{n_{\delta_r}} = -\frac{C_{ne}}{\delta_r}$. The change in yaw moment due to rudder deflection is expressed in Equation 7.8:

$$dN = -\bar{q}c_{l_{\alpha_v}}\delta_r\tau_r l_r S_r \tag{7.8}$$

$$C_{n_{\delta_r}} = -\left(\frac{V_v}{V}\right)^2 \frac{c_{l_{\alpha_v}}\tau_r l_r}{Sb}\int_{b_1}^{b_2} c_v(y)\,dy \tag{7.9}$$

Following the same derivation steps as for elevator effectiveness and integrating over the vertical tail span, the rudder effectiveness becomes as shown in Equation 7.9. Here, $\left(\frac{V_v}{V}\right)^2$ represents the ratio of dynamic pressures between the vertical tail and freestream; while typically low for T-tail configurations, its influence is conservatively covered by the applied safety factor. $c_{l_{\alpha_v}}$ is the lift curve slope of the rudder airfoil, τ_r is the rudder control effectiveness factor, l_r is the moment arm to the vertical tail's aerodynamic center, and $c_v(y)$ is the chord distribution across the vertical tail. The rudder span extends from b_1 to b_2, chosen to ensure the rudder does not interfere with other empennage components. The sizing procedure mirrors that of the elevator: the required effectiveness is first computed, and then the rudder geometry is determined via integration of Equation 7.9.

Rudder Sizing Results

In Figure 7.5, the rudder sizing results are presented along with the relevant inputs to arrive at the results. Moreover, a left side view of the rudder planform on the vertical tail is provided.

	Parameter	Value	Unit
Inputs	S	706	$[m^2]$
	b	75.2	$[m]$
	$c_{l_{\alpha_v}}$	0.120	$[rad^{-1}]$
	l_v	20.8	$[m]$
	δ_r	-25.0	[deg]
	c_{rudder}	0.35	[-]
	b_1	1.17	$[m]$
	C_{Ne}	-0.039	$[-]$
	V	65	$[m/s]$
Outputs	b_2	10.41	$[m]$
	S_r	25.3	$[m^2]$
	τ_r	0.53	[-]
	$C_{n_{\delta_r}}$	-0.088	$[rad^{-1}]$
	Sw_r	72.3	$[m^2]$
	$C_{l_{\delta_r}}$	-0.027	$[rad^{-1}]$
	$C_{Y_{\delta_r}}$	0.32	$[rad^{-1}]$
	Max Rudder Lift	$1.69 \cdot 10^5$	$[N]$

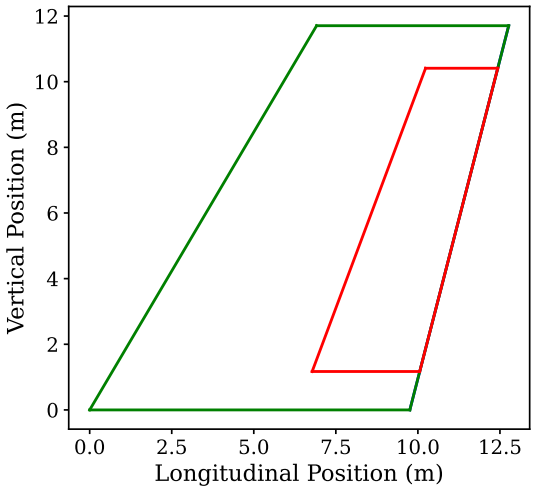

Figure 7.5: *Inputs and Outputs of Final Rudder Sizing (Single Vertical Tail) and Side View of Vertical Tail and Rudder Configuration, Leading Edge is Left.*

The maximum rudder lift shown in Figure 7.5 is superimposed on the nominal rudder lift distribution to get the critical load case for the vertical tail structural design, as will be outlined in Subsection 8.4.4. Again, the safety factor on the rudder lift is omitted to avoid redundant application in Subsection 8.4.4. The rudder control derivatives are used in Subsection 7.2.5.

7.2.3. Ailerons Sizing

Finally, the ailerons are sized for control about the longitudinal axis. Again, first the required roll rate of the aircraft should be determined. It has been identified that the most critical case for the roll rate would be

the roll rate required for obstacle avoidance, if climbing over the obstacle is not an option. This roll rate is defined as the rate needed to obtain the maximum bank angle within the time it takes for the aircraft to be within a distance of the tightest turn radius [1] of the obstacle, at the velocity for the maximum bank angle. Note that this roll rate is more critical than the roll rate defined in CS-25, under AMC 25.147 (d) and (f) [40]. To reach the defined roll rate, it is assumed that both ailerons deflect equally. The method is, again quite similar to the other control surfaces. The required aileron effectiveness follows from lateral moment equilibrium, and is given by Equation 7.10:

$$Cl_{\delta_\alpha} = -\frac{pb}{2V\delta_\alpha} Cl_p \tag{7.10}$$

$$Cl_{\delta_\alpha} = -\frac{2c_{l_\alpha}\tau_a}{Sb}\int_{b1}^{b2} c(y)dy \tag{7.11}$$

Equation 7.10 estimates the required aileron control effectiveness $C_{l_{\delta_\alpha}}$ $[rad^{-1}]$ based on the desired roll rate. Here, p [rad/s] is the target roll rate, b $[m]$ is the wingspan, V $[m/s]$ is the flight velocity and δ_α $[rad]$ is the aileron deflection. The term C_{l_p} $[-]$ is the roll damping derivative, defined in Section 6.10. The analytical expression for the aileron effectiveness is derived similarly to the other control derivatives, and is represented by Equation 7.11. In this expression, c_{l_α} $[rad^{-1}]$ is the lift curve slope of the wing airfoil, and τ_a $[-]$ is the aileron control effectiveness factor. S $[m^2]$ is the wing reference area, and b $[m]$ is the wingspan. The function $c(y)$ $[m]$ represents the local chord length of the wing as a function along the span, bounded between b_1 and b_2, the aileron start and end point. The method is performed using the same approach as defined for the other control surfaces.

Aileron Sizing Results

In Figure 7.5, the results of the aileron sizing are presented along with the relevant inputs to arrive at these results.

Table 7.5: *Inputs and Outputs of Final Aileron Sizing (Half the Wing)*

	Parameter	Value	Unit
Inputs	d_{obj}	829	$[m]$
	r_{min}	460	$[m]$
	ϕ_{max}	54.2	[deg]
	p	0.610	$[rad/s]$
	S	706	$[m]$
	c_{l_α}	0.10	$[rad^{-1}]$
	b	75.2	$[m]$
	δ_α	-20.0	[deg]
	V	79.1	$[m/s]$
	C_{l_p}	-0.46	$[-]$
	b_2	37.0	$[m]$
	$c_{aileron}$	0.25	$[-]$
Outputs	b_1	27.8	$[m]$
	S_a	14.9	$[m^2]$
	τ_a	0.47	$[-]$
	$C_{l_{\delta_\alpha}}$	-0.19	$[rad^{-1}]$
	Max Aileron Lift	$1.20 \cdot 10^6$	$[N]$
	Sw_a	59.7	$[m^2]$

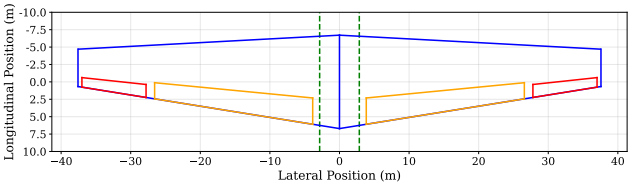

Figure 7.6: *Top View of Wing Planform with the Sized Ailerons, Leading Edge is Upwards*

As can be seen in Figure 7.5, the minimum distance of an object that could be avoided by turning away from it is $d_{obj} = 829[m]$. Moreover, the maximum aileron lift shown is superimposed on the maximum lift distribution as one of the critical loading cases for wing structural design, as will be outlined in Subsection 8.4.3. For the aileron lift, the safety factor is omitted as well, to avoid redundant application of the safety factor in Subsection 8.4.3. The calculated $C_{l_{\delta_\alpha}}$ is used in Subsection 7.2.5.

[1] Both the maximum bank angle and tightest turn radius are defined in Chapter 11

7.2.4. Wingtip Buoys

Side buoy sizes must be minimised to reduce their compromise on aerodynamic efficiency. Therefore, the side buoys are sized only for stability and not for float. Due to the large wingspan of the aircraft, only a small roll-angle is permitted for on-water operations before the aircraft 'tips over', where one wing-tip gets submerged in the water. This is not only an uncomfortable ride, but also renders the aircraft impossible to take-off, which is mission critical. The hull-shaped fuselage can provide some roll stability, however, the addition of side buoys aims at fully guaranteeing elimination of the risk of tipping-over events.

An accurate estimation on restoring moment of the hull-shaped fuselage is rather difficult, especially when the hull profile is a preliminary profile. A conservative assumption is made to simplify the system mechanics, such that roll axis stability for both the static and dynamic case are entirely provided by the buoys. On the other hand, due to the combination of hydro forces and gravity terms, the dynamic rolling axis will not be through the centre of mass. This location is inherently difficult to estimate with precision. Therefore, the rolling axis of the aircraft has been conservatively assumed to lie at the bottom of the hull. This assumption gives the longest possible lever arm and the most adverse destabilising moment, leading to the design of oversized buoys and an overestimation of wing loading due to buoyancy and aerodynamic drag. However, this approach is considered justified due to its conservative bias toward safety. Moreover, it does not compromise other performance aspects as the design becomes more refined. The reduction in preliminary design complexity is, as a result, a worthwhile trade-off.

Both static and dynamic roll stability on water must be considered. Static equilibrium is achieved at the largest allowable static bank angle. The aircraft's steady state bank will not exceed this bank angle during on-water operations. The dynamic stability ensures a stable dynamic response on the roll axis, and that any disturbance causing the aircraft to deviate from equilibrium bank angle will result in a restoring moment stiff enough to return the aircraft to the equilibrium condition. The limiting case will result in the final buoy size.

It is also taken into account that the aircraft must remain stable at both OEW and MTOW. To accommodate this, the buoys are sized such that at OEW, they just touch the water surface in sea state 0. As a result, during a banked condition, only one buoy contributes to the restoring moment. At MTOW, however, both buoys are partially submerged under equilibrium conditions, and the restoring moment is determined by the difference in their submerged volumes.

Sizing for Static Roll Stability on Water

For the static roll stability on water, a simple statics problem can be formed, such that at some maximum acceptable bank angle, the end buoy(s) provide exactly enough Archimedes force to create static equilibrium with the moment due to leaning weight of the aircraft.
The equation for OEW is therefore given below as Equation 7.12.

$$\rho_{water} \cdot g \cdot V_{bs} \cdot \frac{b}{2} = OEW \cdot \sin(\phi) l_{arm} \tag{7.12}$$

Where b is the wing span, ϕ is the allowed bank angle. And for MTOW, Equation 7.13, is given.

$$\rho_{water} \cdot g \cdot V_{diff,bs} \cdot \frac{b}{2} = MTOW \cdot \sin(\phi) l_{arm} \tag{7.13}$$

The maximum allowable bank angle has been determined manually, based on several potential limiting criteria. The first consideration involves critical subsystems that must not be exposed to water. However, as all subsystem air inlets are positioned high on the aircraft, this is not the limiting factor. The second criterion relates to maintaining aerodynamic functionality, the wings must remain clear of the water surface during operation. This is governed by the wing height and half-span. The final criterion concerns crew comfort. Even at the maximum static bank angle, simple objects, such as a coffee cup should remain stable in the cockpit. For reference, commercial ships typically consider a bank (or heel) angle of around 5 degrees to be acceptable for comfort [41]. Since, this is the most restrictive of the three considerations, a maximum static bank angle of 5 degrees is selected as the design limit for waterborne stability.

Dynamic Roll Stability on Water

As aforementioned, the restoring moment due to the hull is difficult to estimate. Again, a simplified system is needed. In this case, the buoyancy force provided by the buoys increases linearly with the submerged height. With the small angle approximation, the height scales linearly with bank angle, meaning that the system could be idealised as a first order mass spring system. The simplified system forms a linearly inverted rigid body supported through a massless beam, with the centre of pivot having some spring constant that is provided by the buoys. The system equation is given by Equation 7.14.

$$I\ddot{\phi} = mgl\phi - n \cdot k\phi, \tag{7.14}$$

where k is the buoys' restoring moment per radian of bank. For a single buoy, this is given by Equation 7.15.

$$k = l_{buoy} \cdot w_{buoy} \cdot 0.5 \cdot b^2 \cdot \phi \tag{7.15}$$

Where l_{buoy} is the length of the buoy, w_{buoy} is the width of the buoy. ϕ is the bank angle.

For cases where both buoys are submerged underwater, the effective k value will be the difference in between the k value of both buoys. Also, k reduces to zero when the buoy is lifted out of the water. Damping within the system due to the hull and hydro forces is not considered, therefore, once the system could obtain oscillatory behaviour, the system is deemed stable due to the intrinsic damping. An assumption made in this case, is that the wingtip buoys are infinitely tall. As the linear system in Equation 7.14 imposes no limit on how deep the buoys could be submerged under water. The buoy height is selected, such that it touches the sea surface at OEW in sea state zero, and extends all the way to the wingtip, which is as high as the buoy could possibly go. This value is 5.8 meters. For the system proposed in Equation 7.14, oscillatory behaviour happens when $k > mgl$. The k value can then be used to obtain the dimension of buoys using simple Archimedes principle. Both OEW and MTOW is evaluated, and the most critial case is considered. The end result, considering both static and dynamic roll stability, yields the cuboid wingtip buoy sizes: buoy length 4.5$[m]$, buoy width 1.0$[m]$ and buoy height 5.8$[m]$. The cuboid buoys are then mapped to an airfoil shape with the same volume per submerged depth. Since the buoys are quite thin, they are merged together with the end plate, under one uniform airfoil shape to provide better aerodynamics.

7.2.5. Eigenmotions and Dynamic Response

The eigenmotion characteristics of this particular aircraft are extremely important. Since, during the majority of its operation, the operational altitude is close to the ground. Meaning that there is practically no room for recovery, if significant motion in any of the 6 degrees of freedom is excited. In which case, the aircraft could easily crash into the ocean with virtually no time for pilot intervention. On the other hand, only the MTOW condition under cruise configuration is studied for the current eigenmotion analysis.

Longitudinal Dynamic Stability

The symmetric dynamic model is constructed based on state space representation of the symmetric dynamic model of conventional aircraft. Since, the trim tab characteristics are not designed at this current stage. The state-space model then a four state, single input system, with only the elevator deflection. The state vector, input vector and output vector are then given in Equation 7.16.

$$\mathbf{x} = \begin{bmatrix} \hat{u} \\ \alpha \\ \theta \\ \frac{q\bar{c}}{V} \end{bmatrix}, \quad \mathbf{u} = [\delta_e], \quad \mathbf{y} = \begin{bmatrix} \hat{u} \\ \alpha \\ \theta \\ q \end{bmatrix}. \tag{7.16}$$

The numerical values of the eigenvalues, damping ratio, period, and time to half amplitude of the eigenmodes are tabulated in Table 7.6.

Table 7.6: *Eigenvalues for Symmetric Eigenmotions*

Eigenmode	Eigenvalue	Damping ratio ζ	Period [s]	$T_{\frac{1}{2}}$ [s]
Phugoid	$-0.0016 \pm 0.0951i$	0.0168	66.07	433.2
Short-period (Fast)	$-38.5094 + 0i$	1.0	N/A	0.018
Short-period (Slow)	$-0.9563 + 0i$	1.0	N/A	0.725

It can be noticed that the phugoid is highly oscillatory. The short period, on the other hand, is critically damped, for both poles. The eigenmotions are excited using an elevator deflection δ_e of 0.10$[rad]$ for a duration of 2.0$[s]$. With the symmetric eigenmotions being shown in Figure 7.7.

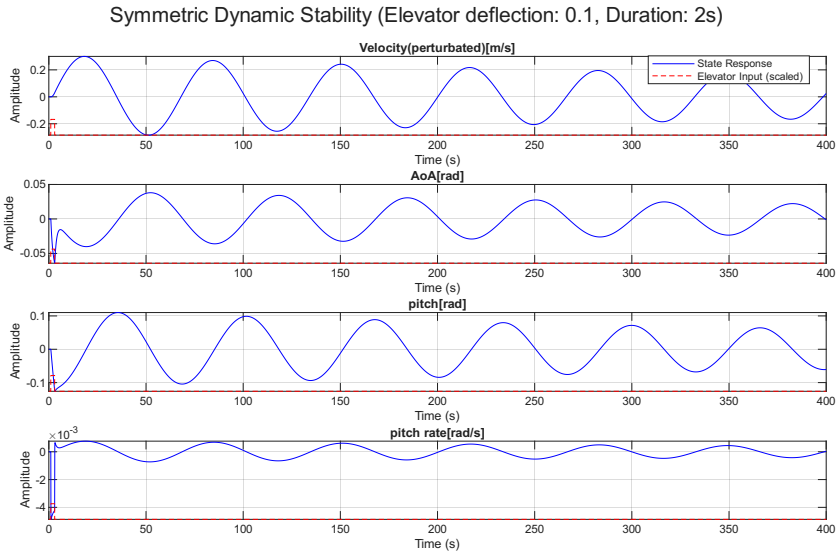

Figure 7.7: *Symmetric Eigenmotion Under Elevator Deflection*

Both eigenmotions are found to be decaying, therefore, the longitudinal dynamic stability of the aircraft model satisfy the requirement REQ-STB.2.

Lateral Dynamic Stability

For the lateral eigenmotion, the states are: sideslip angle, roll angle, roll rate, and yaw rate. The inputs are aileron deflection and rudder deflection. The state vector, input vector and output vector are shown in Equation 7.17, below.

$$\mathbf{x} = \begin{bmatrix} \beta \\ \phi \\ \frac{pb}{2V} \\ \frac{rb}{2V} \end{bmatrix}, \quad \mathbf{u} = \begin{bmatrix} \delta_a \\ \delta_r \end{bmatrix}, \quad \mathbf{y} = \begin{bmatrix} \beta \\ \phi \\ p \\ r \end{bmatrix}. \tag{7.17}$$

Three different eigenmodes are investigated, being the Dutch roll, the aperiodic roll, and the spiral motion. The asymmetric state-space model produced the eigenvalues for cruise configuration at MTOW that are tabulated in Table 7.7.

Table 7.7: *Eigenvalues for Lateral-Directional Eigenmotions, MTOW, Cruise*

Eigenmode	Eigenvalue	Damping ratio ζ	Period [s]	$T_{\frac{1}{2}}$ [s]	Doubling time[s]
Dutch roll	$-0.0573 \pm 0.6938i$	0.0823	9.056	12.097	N/A
Aperiodic roll	$-0.6295 + 0.0000i$	1.0	N/A	1.101	N/A
Spiral	$0.0289 + 0.0000i$	N/A	N/A	N/A	23.984

It can be seen that the eigenvalues corresponding to the Dutch roll are under damped, which is expected. The eigenvalue responsible for the aperiodic roll is critically damped and to the left half plane. Finally, for the spiral motion, the doubling time is around 24 seconds, which is acceptable for conventional aircraft according to [42].

Aileron and rudder inputs are fed into the system to excite the eigenmotions. Both the rudder and ailerons are deflected to 0.05 $[rad]$ for a duration of 1.0 $[s]$ and then released. Figure 7.8 shows the eigenmotion plot of the Dutch roll.

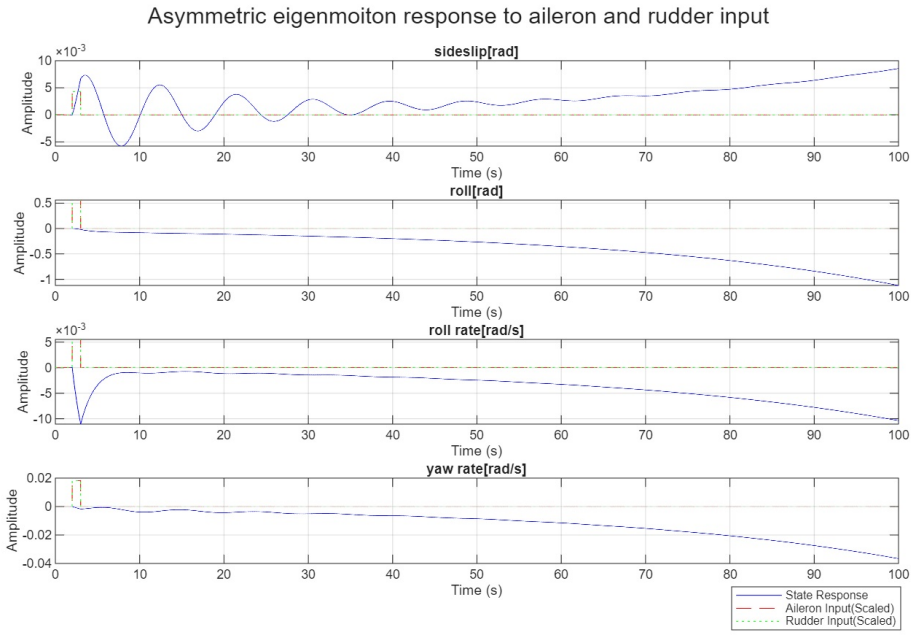

Figure 7.8: *Asymmetrical Eigenmotion Under Aileron and Rudder Input*

It could be observed that the Dutch roll motion dominates the overall response during the initial transient. After which, the spiral becomes the primary eigenmotion. Note that Dutch roll oscillations on the roll axis are difficult to observe. This is due to the difference in scale caused by the relatively much larger spiral motion.

For cruise under ground effect, precise attitude holding with respect to sea surface must be guaranteed at all cost. This is because any considerable bank or pitch will have parts of the aircraft coming in contact with the water, possibly causing serious structural damage and resulting in loss of aircraft and crew. Therefore the aforementioned spiral becomes unacceptable when it is evaluated for a WIG vehicle. On the other hand, it is impractical for the pilot to keep constant monitoring on the aircraft bank through long-haul flights. Hence why REQ-STB.2 requires all eigenmodes to be stable. For this, the pole responsible for the unstable spiral must be placed to the left half plane using a controller. An autopilot system is therefore implemented for holding and tracking cruise states. In the process, the spiral is rejected altogether due to the controller. This will be explored in Subsection 7.2.6.

Sensitivity Analysis on Aircraft Inertial Parameters

The inertial properties used in both eigenmotion studies are highly approximated. The inertia matrix values were first obtained by considering the fuselage as a cylinder with a distributed mass. The wing is assumed to be a rectangular plate with a distributed mass. While the subsystems are considered as point masses, all values are finally lumped together into one rigid body. Using the parallel axis theorem, an observation was made that aside from the I_{yy} value, the rest of the inertial values seem significantly underestimated when compared to two reference aircraft, Boeing 747 and the C-5[2]. While I_{yy} is larger than the I_{yy} value for 747 and C-5 by a reasonable amount, the rest of the inertias were significantly smaller than 747 and C-5, despite the fact that weight of this aircraft is larger than either reference aircraft. Having a larger wingspan and bigger empennage. These estimated inertial values simply do not pass a sanity check.

An explanation is that subsystem design is the most complete along the x-z plane of the aircraft, while rather lagging behind for the other planes. On the other hand, for I_{xx} specifically, in reality, the fuselage weight is distributed nearly entirely along the fuselage skin. Therefore, considering it as a solid cylinder would likely yield an underestimated result, since the centre of mass of the empennage is not really far from aircraft CG, as viewed from x-y plane. This then means that the dominant factor in the empennage's contribution to I_{xx}

[2] https://jsbsim.sourceforge.net/MassProps.html [Cited 16 June 2025]

is likely the distributed inertia term instead of the parallel axis term.

This is unlike I_{yy} estimation, where due to the long tail lever and arm length, the parallel axis term likely dominates. A final decision is made to compute the I_{xx}, I_{zz} and I_{xz} based on the ratio of these inertial values to I_{yy}. For the reference aircraft, Boeing 747 and C-5, then multiply these ratios with current I_{yy} to obtain the rest of the inertial parameters. Although the two reference aircraft share similar overall size as the aircraft developed in this report, the body plant is not exactly the same. The C-5, being a high wing T-tail aircraft yields higher similarity, while the Boeing 747 yields less. Granted, neither could fully represent the relation between I_{yy} and the rest of the inertial values for the to be developed aircraft.

A sensitivity analysis is formed to visualise how a change in inertial values affects the accuracy of the previously demonstrated stability characteristics. Instead of numerical representation, plots are produced to see how varying the inertial values from 0.5 to 3.0 times the current values drags the poles of the system within the pole-zero plot. This resembles visualising how control gain changes pole location for a root locus plot. These plots can be found below in Figure 7.9.

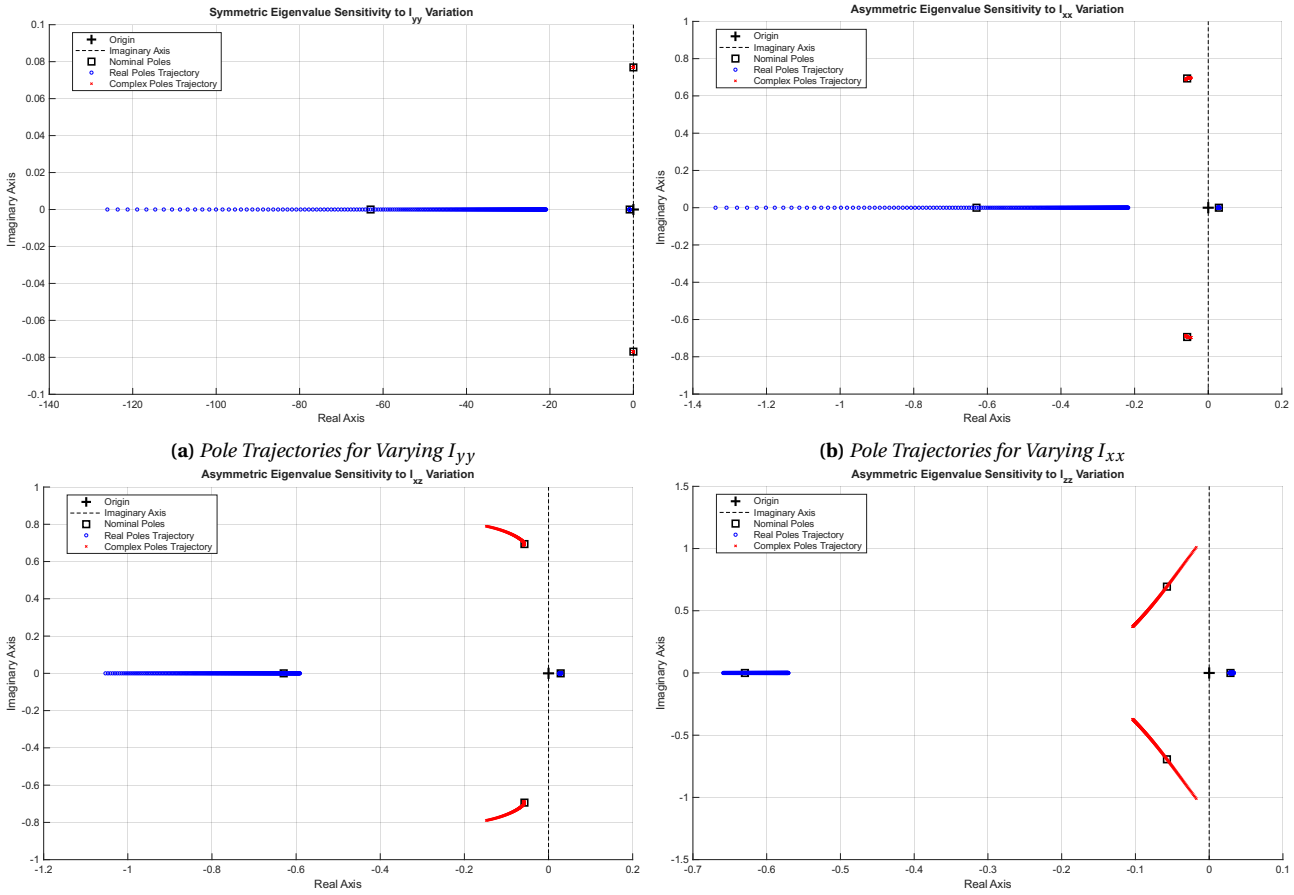

(a) *Pole Trajectories for Varying I_{yy}*

(b) *Pole Trajectories for Varying I_{xx}*

(c) *Pole Trajectories for Varying I_{xz}*

(d) *Pole Trajectories for Varying I_{zz}*

Figure 7.9: *Pole Trajectories for Varying Inertial Values from 50% to 300% of Original Value*

The observation indicated that for the symmetric case, the pole responsible for the fastest short period gets dragged aggressively to the left half plane with an increase in I_{yy}. The imaginary poles for symmetric eigenmotion do not have meaningful shifts during I_{xx} variations, therefore, the phugoid mode is rather insensitive from I_{yy} accuracy. So is the case for the slower short period, with no obvious shift in pole location.

For the asymmetric case, a shift in I_{xx} value seems to only affect the aperiodic roll mode significantly. With increasing I_{xx}, the poles for Dutch roll and spiral are nearly unchanged. For I_{xz}, increasing it causes the Dutch roll poles to oscillate more, while shifted more to the left half plane. Asymmetric roll observes similar behaviour, as increasing I_{xx}, while the pole responsible for spiral stays the same. For increasing I_{zz}, the poles responsible for Dutch roll get closer to the real axis, meaning they become less oscillatory. The pole

responsible for asymmetric roll shifts to the right, becoming less stable. Granted plentiful space before it could start to become unstable. The spiral pole is nearly unchanged as all other cases. Overall, it can be concluded that under almost all cases, the change in inertial values only affects the fast modes. Most not in a destabilising manner. The longer modes are nearly not affected by changing the inertias. On the other hand, even though the inertia values are estimates, they would likely not exceed the 50% to 300% margin range. Therefore, conclusions drawn for longitudinal and lateral stability are likely to be accurate.

7.2.6. Controllers In the Loop

This subsection focuses mainly on the lateral axis linear controller implemented within the fly-by-wire system. On the other hand, augmentation to phugoid characteristics will also be discussed.

Spiral Rejection and Dutch Roll Damping

As explained earlier, a controller is needed to reject the spiral, therefore alleviating pressure off of pilots during long haul missions. A yaw damper is a common implementation in the lateral motions for dampen out the Dutch roll and provide some spiral stability. However, an optimal control scheme, being the Linear quadratic regulator (LQR), is selected due to its ability to guarantee optimal closed loop response across all states. This is beneficial especially for multi-input-multi-output systems such as the asymmetric dynamic model. This controller makes use of the rudder and elevator as input actuators and keeps the aircraft tracking a straight, steady flightpath under cruise condition.

For a continuous-time linear time invariant system with state $\mathbf{x}$ input $\mathbf{u}$, the LQR controller finds the control inputs $\mathbf{u}(\mathbf{t})$ that minimises the infinite horizon cost function J, see Equation 7.18.

$$J = \int_0^\infty \left(\mathbf{x}^T(t)\mathbf{Q}\mathbf{x}(t) + \mathbf{u}^T(t)\mathbf{R}\mathbf{u}(t)\right) dt \tag{7.18}$$

Within Equation 7.18, $\mathbf{Q}$ matrix defines the state weighting function, and R defines the control input weighting function. The Algebraic Riccati equation [43] is solved based on the cost function in Equation 7.18 and linear system dynamics, obtaining feedback gain matrix $\mathbf{K}$. The exact mathematical derivation of the Algebraic Riccati equation is outside the scope of this report, its implementation is performed using the LQR function [3] in MATLAB 2025a.

The K matrix is then fed back into the system to close the control loop, see Equation 7.19.

$$\dot{\mathbf{x}}(t) = \mathbf{A}\mathbf{x}(t) + \mathbf{B}(-\mathbf{K}\mathbf{x}(t)) \tag{7.19}$$

The feedback loop is implemented in to the asymmetric dynamic model. Its response to a de-stabilising initial condition is simulated. The system is first put into a sideslip angle of $0.05[rad]$, a roll angle of $0.05[rad]$, a roll rate of $0.01[rad/s]$ and a yaw rate of $0.01[rad/s]$. The controller is shown to be able to reject the spiral motion in Figure 7.10.

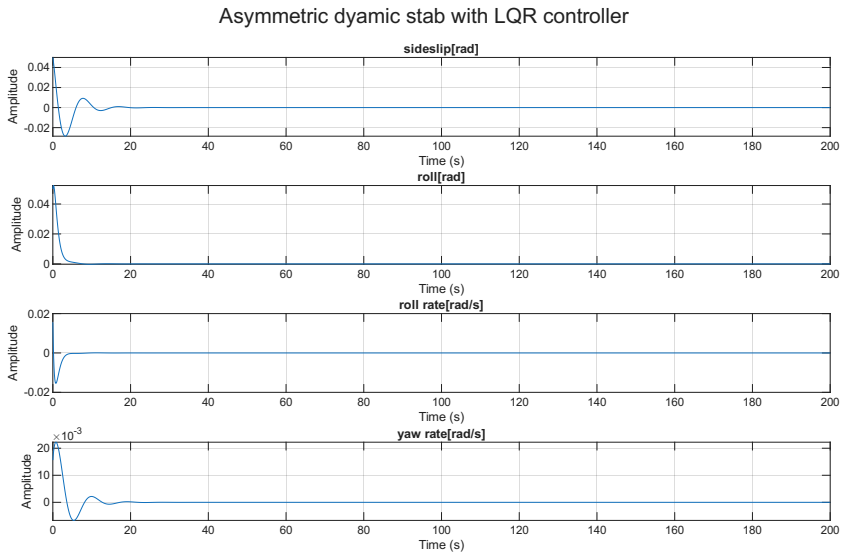

Figure 7.10: *Asymmetric Dynamic Response with LQR Controller*

[3] https://nl.mathworks.com/help/control/ref/lti.lqr.html [Cited 16 June 2025]

The above behaviour is achieved at a tuning with Q and R matrix with values, see the matrices in Equation 7.20.

$$Q = \begin{bmatrix} 100 & 0 & 0 & 0 \\ 0 & 1000 & 0 & 0 \\ 0 & 0 & 1 & 0 \\ 0 & 0 & 0 & 1 \end{bmatrix} \quad R = \begin{bmatrix} 100 & 0 \\ 0 & 100 \end{bmatrix} \tag{7.20}$$

Note that this particular R matrix significantly punishes the control surface input. This is to avoid excessive aileron and rudder deflection. A critically damped response to disturbance could be achieved with an R matrix with lower values on the diagonal. The tuning of such a controller is outside the scope of this report, however, it does demonstrate that such controllers can be implemented to correct the unstable spiral. Therefore, this allows the aircraft to fully satisfy REQ-STB.2.

A problem occurs when turning and banking motion is initiated on the aircraft. With a yaw damper, a washout filter could be implemented to bypass steady-state signals while allowing higher frequency disturbances to pass through and be damped out, thereby offering controllability by pilot while rejecting oscillations. This however, cannot be implemented on an optimal controller. Therefore, problematically, the pilot inputs will be rejected by the controller, as the the latter drives all states back to zero anyway. It is decided that a fully fly-by-wire scheme will be used such that the pilot inputs result in a certain state request with side stick yielding a roll rate request. This is similar to the Airbus fly-by-wire system[4]. This pilot request then gets fed as the new reference state, and the controller will regulate the error down to zero for this new reference state. This is of course based on the assumption that the plant dynamics is linear enough. For better steady state response, the controller should be extended to a Linear Quadratic Integral (LQI) controller to track time varying non-zero reference states. For high altitude flights, gain scheduling must be used as the plant dynamics likely varies greatly under these conditions. On the other hand, the current implementation is performed in the continuous time domain. For real world digital system implementation, a discretised linearisation and control scheme must be used.

Phugoid Damping Control

The lightly damped phugoid could be further damped out to reduce unwanted oscillations. This is particularly important for ground effect operations since small changes in height above water could result in massive changes in aerodynamic properties. One common method to dampen a phugoid motion is implementation of a proportional controller using auto-throttle. However, since the engines are positioned above the wing and CG, an increase in thrust leads to a rise in airspeed but also induces a nose-down pitching moment. This restores speed at the peak of the phugoid oscillation but worsens the pitch angle, and at the trough, it restores pitch but worsens airspeed. As a result, effective damping of the phugoid requires coordinated control of both throttle and elevator deflection. Due to time constraints, such a controller has not been developed at this stage.

At a higher level, the LQR controller and the phugoid damping controller function as linear inner-loop controllers within a larger, cascaded control architecture, similar to the control system proposed for the Flying-V aircraft by Atmaca et al [44]. This system regulates the aircraft states in all 6 degrees of freedom based on reference state requests from either the autopilot or the pilot. For most of the flight envelope, the autopilot is active and generates reference trajectories for the control system to follow. For cruising under ground effect, autopilot should be on at all time for maximum safety in rejecting the spiral and damping out other oscillations. Sensors onboard including the Inertial Measurement Unit (IMU), lidar, and computer vision could be used to generate accurate height estimate above water surface, allowing the controller to do accurate attitude holding, and controlled turns. For higher altitude flight, the unstable spiral mode becomes less safety critical, and manual flying could be performed. Phugoid damper and yaw damper could be used to assist pilots in dynamic behaviour of the aircraft. For skilled pilots, no augmentation is needed due to the inherently stable longitudinal modes and a rather long time to doubling amplitude for the spiral.

[4] http://www.airbusdriver.net/airbus_fltlaws.htm [Cited 24 June 2025]

7.3. Compliance

In Table 7.8 the compliance matrix for the stability and control is presented. It is visible that all requirements are met.

Table 7.8: *Compliance Matrix - Stability & Control*

Requirement ID	Description	Compliance Justification	
REQ-STB.1	The aircraft shall be statically stable during all stages of flight.	C_{m_α} is negative.	
REQ-STB.2	The aircraft shall be dynamically stable during all stages of flight.	All poles have a negative real part.	
REQ-STB.3	The aircraft shall be controllable on all axes during all stages of flight.	All relevant control derivatives are the right sign.	
REQ-STB.3.1	The aircraft shall be pitch controllable during all stages of flight.	$C_{m_{\delta_e}}$ should be negative. The actual value is -1.3	
REQ-STB.3.2	The aircraft shall be roll controllable during all stages of flight.	$C_{l_{\delta_a}}$ should be negative. The actual value is -0.19	
REQ-STB.3.2	The aircraft shall be yaw controllable during all stages of flight.	$C_{n_{\delta_r}}$ should be negative. The actual value is -0.16	

8

Structural Design

With initial weight estimates and aerodynamic and control surface sizing established in previous chapters, this chapter focuses on the structural analysis of the design. It covers general material properties used throughout the structure, considering the marine environment in Subsection 8.2.2, the main fuselage design in Section 8.3, and the load and structural design of the fuselage, wing, and empennage. Additionally, a flutter analysis is presented in Equation 8.4.5. The relevant requirements addressed in this chapter are summarized in Table 8.1.

Table 8.1: *Relevant Requirements - Fuselage and Structural Systems*

Requirement ID	Requirement Description	Category	Source
REQ-TNL.2	The aircraft shall be able to land in sea states up to and including sea state four.	Operational	REQ-CUST-SAFE.1 & REQ-CUST-SAFE.2
REQ-TNL.3	The aircraft shall be able to access islands.	Functional	REQ-CUST-PERF.11
REQ-TNL.3.1	The aircraft shall be able to dock on beaches without external assistance.	Functional	
REQ-TNL.3.2	The aircraft shall be able to leave beaches without external assistance.	Functional	
REQ-TNL.4	The aircraft shall be equipped with an anchor.	Constraint	IMO
REQ-CAR.1	The structures shall be able to hold a maximum structural payload of 100 [$tonnes$].	Functional	REQ-CUST-PERF.8
REQ-CAR.2.1	The dimensions (length, width, height) of the cargo hold shall be such that it can hold payload which has a volume of at least 562.5 [m^3].	Functional	
REQ-CAR.2.2	The cargo hold cross-section dimensions (width, height) shall be such that at any point along the cargo hold at least a rectangle of 3.5 [m] wide and 4.0 [m] high fits inside.	Operational	
REQ-CAR.2.3	The dimensions (width, height) of the cross-section of the door to the cargo hold shall be such that at least a cuboid of 3.5 [m] wide, 4.0 [m] in height and 7.32 [m] in length fits inside.	Operational	
REQ-CRU.5.1	The minimum cruise clearance of the wing to the water wave-peaks in ground effect shall be at least 1.5 [m] for sea states up to and including three.	Operational	
REQ-STR.1	The lifting structure shall have a maximum tip deflection of 15% of the length of the lifting structure at the most critical loading condition [45].	Operational	CS-25
REQ-STR.2	The aircraft structure shall sustain the critical loading condition without any structural damage.	Functional	CS-25

Requirement ID	Requirement Description	Category	Source
REQ-STR.3	The aircraft structure shall be able to house sufficient fuel to perform all design missions.	Functional	REQ-CUST-SAFE.4 & CS-25
REQ-STR.4	Flutter of the aerodynamic surfaces shall not occur within the flight envelope.	Functional	CS-25
REQ-STR.5	The aircraft shall maintain buoyancy for all on-water operations and for beaching on the mean beach profile.	Functional	IMO
REQ-STR.6	Outer structure shall be watertight.	Constraint	IMO
REQ-STR.6.1	All aircraft outer panels shall be watertight.	Functional	
REQ-STR.6.2	All aircraft sealings shall be watertight.	Functional	IMO
REQ-STR.7	The aircraft shall be towable [46].	Constraint	IMO
REQ-STR.8	The aircraft shall be able to fly in the required flight envelope [40].	Constraint	CS-25
REQ-STR.8.1	The aircraft shall be able to withstand all manoeuvre loads as specified in CS-25 [40].	Constraint	CS-25
REQ-STR.8.2	The aircraft shall be able to withstand all gust loads as specified in CS-25 [40].	Constraint	CS-25

8.1. Manoeuvre and Gust Loading Diagram

The limit load factors from manoeuvre loads and gust loads are a key input to perform the structural design of the aircraft. Both manoeuvre and gust load diagrams have been constructed following the method suggested in CS-25 [40]. The combined plot for a single load factor-velocity envelope is shown in Figure 8.1.

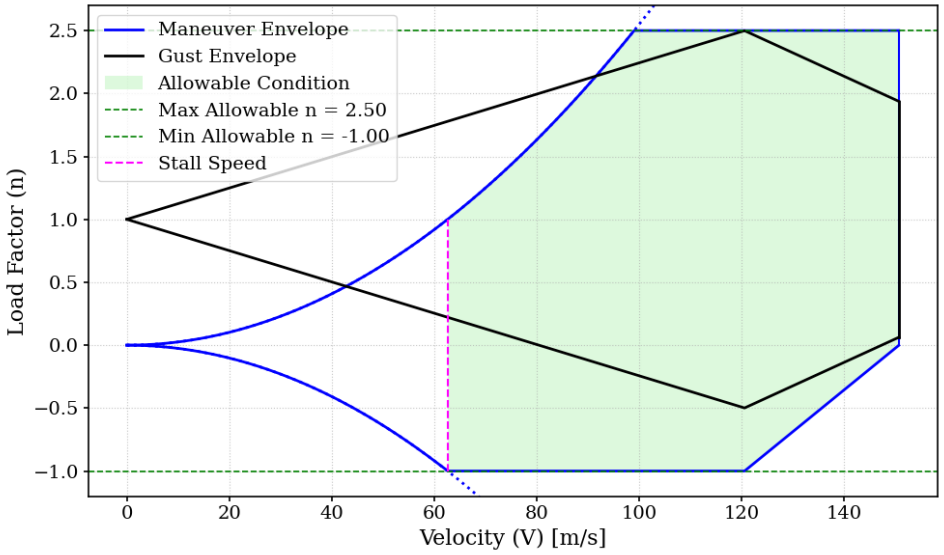

Figure 8.1: *Combined Loading Diagrams*

Figure 8.1 shows the manoeuvre loads in blue and the gust loads in black. The green-shaded region represents the possible flight conditions (operating points). This region is fully enclosed by the manoeuvre envelope, bounded by the stall and dive speeds. The maximum and minimum load factors due to gusts and manoeuvres are n=2.5 and n=-1, respectively. These loads, together with those from other critical mission phases, will be used to inform the structural design.

8.2. Material Characteristics

This section contains an overview of all the materials that have been considered in the design and their properties. Also, specifying for which subsystems these materials have been selected.

Aluminium Alloys

Aluminium alloys provide high strength and good manufacturability, while being lightweight and cost effective. Therefore, aluminium is the metal that is used the most in aircraft. For corrosive purposes, aluminium is mostly a suitable option for general aviation, because it forms an outside layer of aluminium-oxide after coming in contact with oxygen [47]. This layer protects the rest of the material from corrosion in atmospheric conditions. Here, the aircraft is mostly operated in marine conditions, where this 'natural' protection against corrosion is not present[47]. So, a protective coating will be needed to apply aluminium alloys in this design, which will further be discussed in Subsection 8.2.1 below. Table 8.2 shows the material properties of five selected aluminium alloys.

Table 8.2: *Material Properties of Different Aluminium Alloys*

Alloy	ρ **[kg/m^3]**	E **[GPa]**	**Poisson's Ratio**	G **[GPa]**	σ_y **[MPa]**
Al7075[1]	2810	71.7	0.33	26.9	503
Al6061[2]	2700	68.9	0.33	26.0	276
Al2024[3]	2780	73.1	0.33	28.0	324
Al5052[4]	2680	70.03	0.33	25.9	193

Titanium Alloys

Titanium alloys have good strength-to-weight ratios, corrosion resistance, and high-temperature performance [48, 49]. Unlike aluminium, titanium maintains its mechanical integrity at temperatures exceeding 400[$^\circ C$], and does not require coatings to resist marine or chemical corrosion [48]. This makes it particularly suitable for aircraft operating in saltwater or thermally intense environments.

However, the high cost of raw titanium, along with its difficult machinability due to low thermal conductivity and high chemical reactivity, limits its use [50, 51]. Welding titanium also requires controlled environments and inert gas shielding to avoid contamination and embrittlement [52]. Table 8.3 shows the material properties of selected titanium alloys.

Table 8.3: *Material Properties of Different Titanium Alloys*

Alloy	ρ **[kg/m^3]**	E **[GPa]**	**Poisson's Ratio**	G **[GPa]**	σ_y **[MPa]**
Ti10v2Fe3Al[5]	4650	107	0.32	42.1	1170
Ti6Al4v [6]	4430	113.8	0.342	44.0	880

Nickel Based Alloys

Nickel-based alloys are primarily used in applications that demand high-temperature performance, such as turbine blades, combustion chambers, and exhaust systems [53]. These alloys retain their mechanical strength, oxidation resistance, and creep resistance at temperatures exceeding 1000 [$^\circ C$], where aluminium and even titanium would fail [54]. Additionally, they offer excellent resistance to thermal fatigue and chemical degradation [55].

However, nickel-based alloys are among the heaviest and most expensive structural metals used in aerospace [53]. Their high density and poor machinability limit the use to only regions where thermal resistance is critical. Table 8.4 presents the material properties of selected nickel-based alloys.

[1] https://asm.matweb.com/search/specificmaterial.asp?bassnum=ma7075t6 [Cited 11 June 2025]
[2] https://asm.matweb.com/search/specificmaterial.asp?bassnum=ma6061t6 [Cited 11 June 2025]
[3] https://asm.matweb.com/search/specificmaterial.asp?bassnum=ma2024t4 [Cited 11 June 2025]
[4] https://asm.matweb.com/search/specificmaterial.asp?bassnum=ma5052h32 [Cited 11 June 2025]
[5] https://asm.matweb.com/search/SpecificMaterial.asp?bassnum=NTIME1023 [Cited 11 June 2025]
[6] https://asm.matweb.com/search/specificmaterial.asp?bassnum=mtp641 [Cited 11 June 2025]

Table 8.4: *Material Properties of Different Nickel-Based Alloys*

Alloy	ρ [kg/m^3]	E [GPa]	Poisson's Ratio	G [GPa]	σ_y [MPa]
INCONEL718 [7]	8190	113.8	0.30	43.7	760
WASPALOY[8]	8200	213	0.31	81.2	910
Rene 41[9]	8240	218	0.31	83.2	793
HASTELLOY X[10]	8220	205	0.32	77.6	245

8.2.1. Corrosion Protective Coating

As mentioned above, aluminium must be coated to be adequately protected against corrosion. This can be done using different kinds of coatings. The first option is to use a metal coating, for instance plating the skin with a layer of a high purity aluminium alloy. The thickness of this layer is typically about 10% (5% on both sides of the plate) of the thickness [11]. This layer will function as a sacrificial anode for corrosive reactions, making sure that the actual aircraft skin remains unaffected [56]. Also, this method is beneficial for the recyclability of the coated parts. This is because, the plating will not have to be removed before melting the material. Therefore, plated parts will not have any additional issues with conventional recycling. However, the molten alloy will incorporate additional aluminium from the plating, resulting in a composition that differs from the original alloy. While it may no longer possess the exact properties of the base material, it can still be repurposed for applications with different performance requirements. Despite the better recyclability, this kind of metal coating releases metal ions into the environment, which has negative effects on the environment. According to Rosseland, aluminium acts as a toxic agent in marine and terrestrial ecosystems, especially affecting gill breathing organisms [57].

Another option is a polymer coating, such as an epoxy coating. This coating will shield the metal from coming in contact with the environment, which will prevent corrosion. A large advantage being that the density of an epoxy is almost half of that of aluminium alloys (approximately 1.2 - 1.3 [g/cm^3])[58]. In these polymer coatings, a major problem is microcrack formation after curing, which results into ions breaking through the epoxy layer [59]. This cracking will also result into microplastics being released into the environment due to the chipping of the coating. Nano material reinforced polymer coatings prevent the microcracks from forming [59]. This will not only reduce the required maintenance for the coating, but due to the prevention of the coating chipping, the amount of microplastics that are released into the environment are also reduced. With appropriate maintenance of the coating, the release of microplastics can further be minimised.

However, as mentioned in Chapter 2, the recyclability becomes drastically more difficult with an epoxy coating. On the other hand, multiple other purposes for the aircraft at end-of-life (EOL) were found and named in Section 2.4.

Additionally, one could opt for self healing polymer coatings[12]. The usage of these coatings will reduce maintenance and increase its reliability. At this moment not much information has been made available about such polymers, so the implementation is difficult as of now. However, the application of self healing coatings is promising and is advised to be reconsidered in future design stages.

After evaluating these coating options, a nanoparticle reinforced epoxy coating was selected due to its strong adhesion to metal surfaces and its proven effectiveness in corrosion protection. While recyclability remains a challenge, since the removal of the coating is energy intensive, several EOL applications have been identified (see Section 2.4) that do not require remelting of the coated components. Moreover, with appropriate

[7] https://asm.matweb.com/search/specificmaterial.asp?bassnum=ninc34 [Cited 11 June 2025]
[8] https://asm.matweb.com/search/specificMaterial.asp?bassnum=NHWASA [Cited 11 June 2025]
[9] https://virgamet.com/offer/rene-alloy-41-n07041-2-4973-nicr19como [Cited 11 June 2025]
[10] https://asm.matweb.com/search/SpecificMaterial.asp?bassnum=NHAXAB [Cited 11 June 2025]
[11] These values are based on an conversation with the expert Jos Sinke on 11/06/2025
[12] https://www.european-coatings.com/news/coatings-technologies/self-healing-and-fluorescent-anti-\corrosion-coatings-for-aluminum-alloys/ [Cited 11 June 2025]

maintenance, the release of microplastics can be minimized, thereby reducing the environmental impact of the coating over the aircraft's lifecycle.

For the entire outer skin of the aircraft, it has been chosen to coat the skin with a layer of coating that is 5.0% of the thickest part of the skin. On the inside of the aircraft is where there will be differences in the coating's thickness. It has been deemed excessive to have the same amount of coating on the inside of both the vertical and horizontal tail(s), as it will not be in direct contact with sea water. Therefore, it has been chosen to coat the inside of the vertical and horizontal tail(s) with a layer of approximately 2.5% of the part's maximum skin thickness.

8.2.2. Material Choice

Now that the material characteristics of a shortlist of considered materials have been determined, the materials for the structural elements can be selected. Due to the highly corrosive marine environment, initial instinct would push one towards the choice for a titanium or nickel based alloy. However, these alloys are respectively almost twice or triple the weight of aluminium alloys. Even with the addition of the external nano material reinforced epoxy coating, aluminium parts are significantly lighter. The additional weight from the use of titanium or nickel alloys would negatively impact the capabilities of the aircraft design that it is unfeasible to use large quantities of these materials in this design. Also, the difficult machinability and the high cost of titanium and nickel alloys make them unsuitable for application in these aircraft structures. So, the majority of aircraft parts will be manufactured using an aluminium alloy.

The other alloys will still be considered for smaller, difficult to inspect/maintain parts of the aircraft. For these parts, maintaining the epoxy coating is difficult and thus, a corrosive resistant material is needed. As these parts will probably not carry high loads, titanium alloys are expected to be preferred for this application. This is because nickel based alloys are significantly heavier than titanium. However, due to time restrictions of this project, these actual parts will not be identified at this design stage.

Wing Structure

Due to the significant stresses experienced by the wing structure, an aluminium alloy with a high elastic modulus and yield strength is required. Since the majority of structural loads are carried by the wingbox, the high-strength aluminium alloy Al7075, commonly used in aerospace applications, is selected for all its components, including the spars, ribs, and wingbox skin. In contrast, the outer wing skin is subjected to much lower loads, allowing for the use of a lighter and less strong material. As a result, Al5052 is chosen for the wing's outer skin to reduce weight without compromising structural integrity.

Fuselage & Empennage Structure

Once again, the fuselage structure must withstand substantial aerodynamic and inertial loads. Therefore, a high-strength aluminium alloy is required, and Al7075 was selected for this purpose due to its superior mechanical properties. This material will be used both for the fuselage skin and the longerons.

Similarly, the empennage experiences considerable structural loading, particularly during manoeuvring and stabilisation. Using Al7075 for the empennage ensures sufficient strength and stiffness while maintaining a relatively low weight, which is essential for ensuring stability and control effectiveness without compromising overall aircraft performance.

8.3. Fuselage Main Design

This section defines the primary fuselage cross-sectional shape, overall fuselage length and segmentation, as well as the cargo door design and beaching solutions incorporated into the fuselage. From choosing the final concept, it was clear that the aircraft would have a single large buoyant fuselage to transport the necessary cargo.

8.3.1. Fuselage Cross-Section Shape

Chapter 2 established the dimensions of the cargo hold. With these dimensions, the cross-sectional shape of the fuselage can be established. The cross-section needs to accommodate the cargo, the required structure for the aircraft, and extra space for other required subsystems. Since pressurization of the fuselage is not required, it is not required for the fuselage to have a circular cross-section. The shape needs to assist the fuselage in floating and beaching. This requires using seaplane design to find the optimum dimensions for both flying and on-water conditions. Using Thurston [60], the ideal deadrise angle for large flying boats is 25 [deg], which is labelled in Figure 8.2.

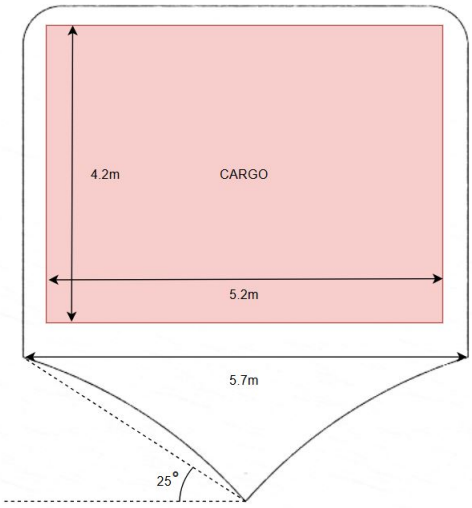

Figure 8.2: *Fuselage Cross-Section*

The top corners of the cross-section have been rounded to reduce the creation of vortices and thus reducing overall drag. The lower corners are kept sharp to promote the generation of vortices since these vortices add energy to the boundary layer on the bottom surface of the fuselage, which delays separation. The height has not been labelled because it is not constant throughout the length of the fuselage. The width of 5.7 [m] was chosen to hold the cargo and account for the thickness of the fuselage structure.

8.3.2. Fuselage Lengths

Since the design process is following Thurston [60], the lengths for standard seaplanes and flying boats needs to be established. In Figure 8.3, the nose cone, forebody, afterbody, and tail cone are defined. Unlike a regular cargo or transport aircraft, this fuselage does not have a constant cross-sectional area between the nose and the tail. It also has a step separating the forebody and afterbody for reducing drag during take-off and landing. Note that in this case, the tail cone is separate from the afterbody which is normally not the case for seaplanes due to their small size.

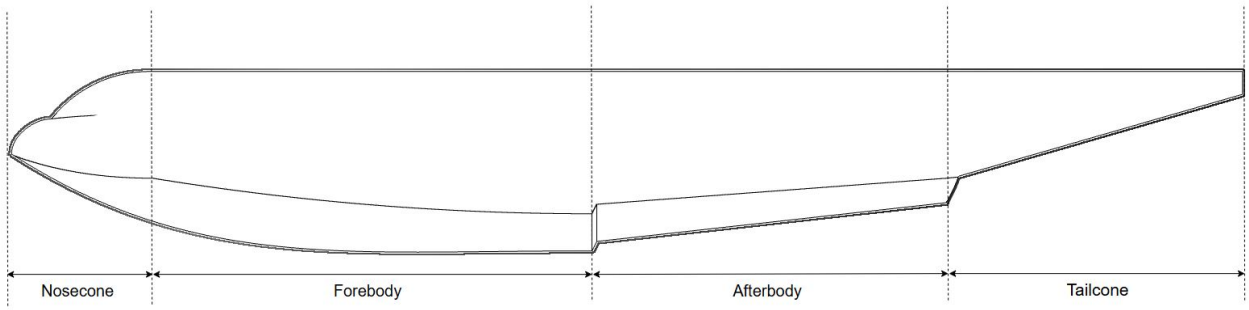

Figure 8.3: *Fuselage Lengths Labelled*

For the nose cone length, the limiting factor is the drag divergence mach number. Since the aircraft is not flying above Mach 0.5, the fineness ratio of the nose cone geometry is not heavily limiting. The nose cone also needs to house the cockpit, which was sized using Roskam [12].

The other lengths are determined using Thurston [60], where different empirical graphs are used to find new

values. In order to start the process, initial values for the deadrise angle, step height and tail cone upsweep angle are chosen. This is done in collaboration with other aspects in the iteration, including the centre of gravity calculations since the centre of gravity needs to be in front of the step for stable on water take-off and landing. The inputs and outputs can be found in Table 8.5 using the methods of Thurston and with assistance of modelling the fuselage on CATIA to ensure the cargo volume fits.

Table 8.5: *Inputs and Outputs for Fuselage Lengths*

	Parameter	**Value**	**Unit**
Inputs	Cockpit Height	2.5	[m]
	Cockpit Length	4.3	[m]
	Deadrise Angle	25	[deg]
	Step Height	0.5	[m]
	Tail Cone Upsweep	11	[deg]
	Cargo Height	4.2	[m]
	Cargo Width	5.2	[m]
Outputs	Nose Cone Length	6	[m]
	Forebody Length	18.6	[m]
	Afterbody Length	14.8	[m]
	Tail Cone Length	12	[m]

8.3.3. Cargo Door Sizing

REQ-CAR.2.3 is the main requirement for the cargo door size and position. From the midterm report [25], the cargo door was chosen to be at the front of the fuselage opening upwards. During the design phase, however, it became clear that with the chosen requirements, opening the cargo door at the front would mean over designing the cargo hold volume. All the volume behind the cockpit could be usable but would result in a large wetted area since the front of the fuselage would need the area for both the cargo and the cockpit. It would not be possible to put the cockpit upwards, so it was decided to put the cargo door at the back.

When sizing the rear cargo door, it was also discovered that unless the cargo comes out parallel to the fuselage, the cargo would not be able to get out with the current selected fuselage height. For very steep beaches, the cargo would not be able to get out of the fuselage since the cargo door would be going upwards meaning the cargo would come into contact with the tail when exiting the aircraft. This means not satisfying REQ-CAR.2.3, so either the fuselage height needs to increase or the cargo door needs to change.

Figure 8.4 shows a different way of having the rear of the fuselage open. With this method, the cargo can come out irrespective of the beach profile. After modelling the tail cone and cargo door requirement, it was found that the bottom cargo door has to be at least the length of the tail cone when using the mean beach profile established in the Chapter 2. A steep beach with this system can be seen in Figure 8.5 to demonstrate further the need for the upper rear cargo door.

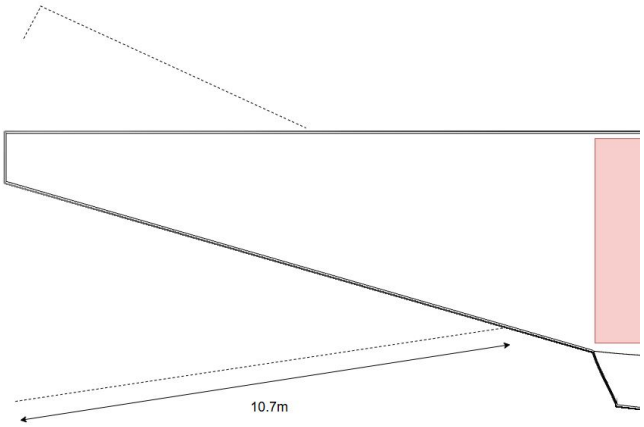

Figure 8.4: *Cargo Door Opening (Sideview)*

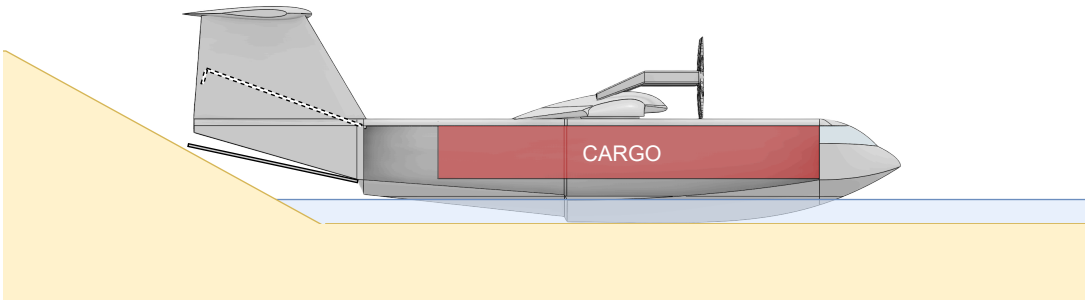

Figure 8.5: *Steep Beach Demonstrating the Rear Cargo Door*

Note that with the cargo door opening upwards, a single vertical tail positioned in the middle of the tail-cone is not possible. Therefore, the suggestion of two vertical tails was provided to the stability & control team, which was accepted, as mentioned in Chapter 7.

8.3.4. Effective Beaching

As mentioned in the operations of the aircraft and made clear by the beach profiling, the aircraft is currently too deep to properly beach since surf zones depths vary from 1.5m to 2.5m. Since the aircraft is going 3m deep into the water with class I weights, a solution needs to be found to satisfy REQ-TNL.3.1. This becomes more difficult to satisfy with the cargo door opening at the rear of the fuselage instead of the front. There are two possible solutions.

The first solution relates to a method of displacing the sand. This requires shaping the hull, or bottom of the fuselage, not only for on water operations but also to plough through the sand. This would also mean reinforcing the hull to withstand the loads that would be associated with this. Since the surf zone is more then 100m long, this would mean that at minimum, 143$[m^3]$ of sand or other beach composition would need to be displaced. This is unrealistic to achieve and an aircraft that could achieve this would require a large amount of maintenance. Also when it comes to debeaching (REQ-TNL.3.2.), it would be very difficult since the aircraft would be embedded in the sand. This is why this solution was not brought any further.

The next solution would be using buoys in order to reduce how deep the fuselage is in the water. This requires large buoys since a large volume needs to be underwater to raise the fuselage. Larger buoys would need to be well placed or a method needs to be found for storing them to minimise overall aerodynamic drag. A preference is given for storing them since this can be more beneficial to minimizing the aerodynamic drag during in air operations.

Since the buoys are only dependent on volume underwater, inflatable buoys can be an option. These can be inflated during on water operations and deflated for flying in air. When deflated, they can be folded up similar to temporary life raft. The placement of these buoys is crucial for the structures of the aircraft and the stability during on water operations. Inflation can be completed using either bleed air from the engines or batteries onboard. After preliminary calculations using Archimedes' principle, it was found that this was the best option to allow for beaching.

8.3.5. Floater Sizing

The shape of the floaters was decided to be a cylinder with spherical ends. This is easily inflatable since cylinders and spheres are best for pressurisation. Initial calculations assumed the floater itself to be of negligible thickness. For initial maximum take-off mass, a volume of 250$[m^3]$ is needed to keep the whole aircraft afloat. Even though the design will have endplate buoys, these will be pure for stability and should not be relied upon to keep the aircraft afloat.

Table 8.6: *Inputs and Outputs for Floater Sizing*

	Parameter	Value	Unit
Inputs	Maximum Take-off Mass	302700	$[kg]$
	Number of Floaters	4	[-]
	Desired Fuselage Depth	1	[m]
Outputs	Floater Radius	2	[m]
	Floater Length	6	[m]

In Table 8.6, the ideal floater size dimensions are shown as the output. When it comes to placement, having them on the wing is best since that is where the most available space is. Since there is a chance that bleed air from the engine can be used to fill the floaters, it is then most ideal to place each of the floaters beneath an engine. Although originally six floaters were chosen with one for each engine, it was found that having four lowered the drag largely and had little impact on floater size. If needed, additional floaters could be added for redundancy.

8.3.6. Anchoring and Towing

REQ-TNL.4 requires the aircraft to have an anchor. This is as an alternative to beaching and is also highly recommended for all wing in ground effect vehicles by the International Maritime Organization. For this specific aircraft, keeping weight low is of upmost importance to maintain high efficiency, so a High Holding Power (HHP) anchor was chosen. Using Lloyd's register [13], the suitable size and chain length was found. With the equipment number found to be 86, the anchor is 236 $[kg]$ and requires a chain length of 82.5 $[m]$ and chain diameter of 22 $[mm]$. Since the aircraft will operate only near beaches where a 82.5$[m]$ anchor is not necessary, the length of the chain has been reduced to 50 $[m]$ to save weight. This leads to a chain mass of 1850 $[kg]$. The most optimal position for the anchor was found to be the nose. There is suitable space underneath the cockpit and it moves the center of gravity slightly forwards which is beneficial for the take-off and landing procedures on water.

REQ-STR.7 requires the aircraft to be towable. To comply with this requirement without compromising, the ring for towing is placed at the rear of the aircraft where the change from afterbody to tail occurs. This can be structurally reinforced to ensure that towing does not have

8.4. Fuselage, Wing and Empennage Structural Design

This section presents the structural design of the primary load-bearing components of the aircraft: the fuselage, wing, and empennage. The structural requirements are first outlined in Table 8.1, forming the basis for the subsequent analyses. The internal loads for each of the components are derived in Subsection 8.4.1,

[13] https://seacat-schmeding.com/wp-content/uploads/2020/07/3Equipment_table_lloyds_register.pdf

considering both aerodynamic and operational conditions. These loads are used to size the fuselage structure through idealised cross-section analysis in Subsection 8.4.2, and to determine the thicknesses, stringer configurations, and rib layouts of the wing in Subsection 8.4.3. A similar approach is applied to the empennage in Subsection 8.4.4, with results shown separately for the horizontal and vertical tails. Finally, Equation 8.4.5 presents a flutter analysis of all lifting surfaces, ensuring aeroelastic stability across the full flight envelope.Note that, in the stress analysis, all applied stresses are multiplied by a safety factor of 1.5, as will be demonstrated throughout the section.

8.4.1. Internal Loads

The fuselage structure and aerodynamic surfaces are subjected to a multitude of loads under nominal operations. However, designing for aircraft structures requires consideration of the worst-case-scenario loads, as the structure must nonetheless be capable of sustaining these critical loads (as specified in Table 8.1). The following subsections present the calculation and results of the internal loads for fuselage and the aerodynamic surfaces.

Fuselage Internal Loads

The main difference from conventional aircraft design in the fuselage structural design is the fact that it is unpressurised. Thus, excluding that, two critical cases were identified when considering fuselage loads: maximum load factor during cruise as specified in Chapter 5 and maximum landing loads. For both cases, the same relative load distribution as that presented in Figure 8.6 was utilised, that is, the upwards loads on the fuselage are applied at the same longitudinal location. This is deemed justifiable for the following reasons. It is specified in [61] that the structure of seaplane hulls must be able to withstand step first landing. Furthermore, [62] states that the upswept forebody and nose can be assumed to be free from any significant landing loads. Additionally, the downward acting distributed load of the weights is assumed not to vary, since both scenarios assume MTOM (which has constant distribution) along the fuselage length.

Some further approximations are made to make calculation more feasible. All loads are considered to be distributed and act uniformly along their length. The tail is assumed to not only produce lift, but also a distributed moment along its root to close the internal moment. All other point or distributed bending moments are omitted from analysis. With these assumptions, the FBD can be constructed, as shown below in Figure 8.6.

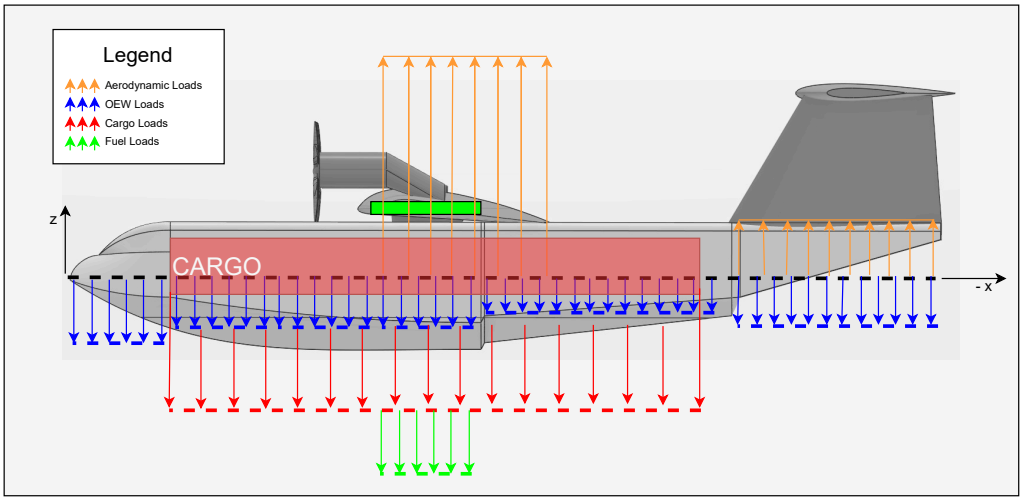

Figure 8.6: *FBD of Fuselage Under Loads Loads not Drawn to Scale*

The landing load factor is found by applying the equation stated by [62, p. 5] and dividing by MTOM. This requires calculation of the aircraft's radius of gyration, centre of pressure (assumed to be located at the quarter-chord point of the wing), hull dead-rise angle and stall speed. The radius of gyration was determined by assuming point masses of all components about the centre of gravity apart from the fuselage and cargo, which were assumed to be infinitely thin rods. Applying the These values yield a landing load factor equal to $n_{land} = 4.04$. While the relation is intended to be used in sea state 0, the extra safety factor

implemented later on in the stress calculation in Subsection 8.4.2 is assumed to cover the increased loads due to wave interference at landing. On the other hand, the maximum in-cruise load factor is presented as being equal to $n_{cruise} = 2.5$ in Section 8.1. The former landing load factor n_{land} will therefore be considered for the load diagrams below in Figure 8.7. These were generated by following the instruction described on [60, p. 180]. The safety factor is then added to the stresses, which is presented below in Subsection 8.4.2.

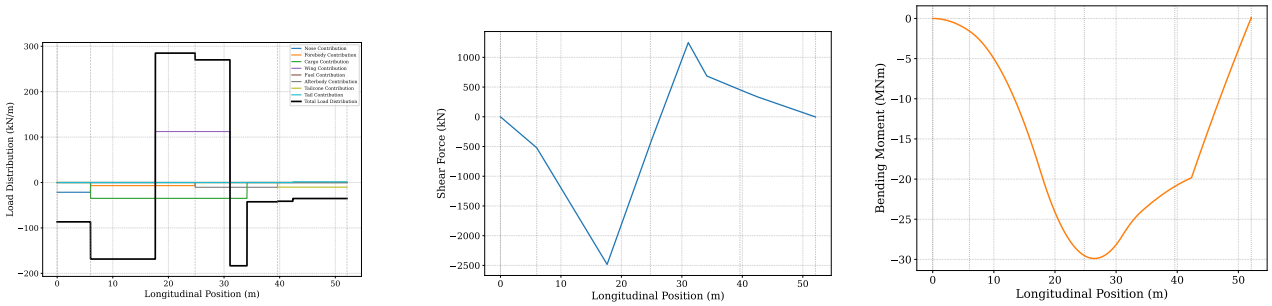

(a) *Resultant Load Distribution* **(b)** *Shear Force Distribution* **(c)** *Bending Moment Distribution*

Figure 8.7: *Load, shear, and moment distributions along the fuselage*

It can be seen that the majority of the bending moment loads concentrate around the wing area, reaching a maximum of $-20.55\,[MNm]$ at the mid-point of the wing root. The maximum absolute internal shear force occurs at the LE of the wing root, where a maximum of $2.00\,[MN]$ is reached. The results align with the example provided in [60, p. 180].

Wing Internal Loads

In this section, the internal wing design logic and corresponding results are presented. All calculations use a consistent, right-handed body-fixed coordinate system, as defined in the Flight Dynamics course [63]. To ensure structural integrity across the flight envelope, two critical loading scenarios are considered. The first case is a $2.5g$ pull-up with full flap and aileron deflection, as described in Section 8.1 and Subsection 7.2.3. The second involves water impact from the buoys (designed in Subsection 7.2.4) contacting the surface during a maximum roll-rate turn, introducing a slamming point load at the wing tip along with drag and torque due to the buoy's offset. Figure 8.8c shows the vertical wing load distribution for the $n_{max} = 2.5$ manoeuvre, one of the two dominant loading cases. The base lift distribution (from Section 6.8) is superimposed with additional loads: the wing's own weight scaled by n_{max} and distributed span-wise by local chord, which updates during iterations; the fuel weight (max fuel mass 70729 $[kg]$) distributed over the tank length (Table 8.8); engine weights distributed over nacelle width and scaled by n_{max}; and the flap lift load, modelled using $C_{L_{max}} = 2.2$ over the flap span (Subsection 6.5.2).

The second case, water slam during a $n_{turn} = 1.7$ banked turn (Chapter 11), is treated similarly. Wing, fuel, and engine loads are scaled by n_{turn}, but a key addition is the slamming force at the wing tip. This is computed using an empirical coefficient [14] with $C_S = 2$ and the vertical impact velocity derived from the roll-induced tip motion, yielding a tip load of 883 $[kN]$.

As shown in Figure 8.8c, the manoeuvre case leads to higher shear near the root due to broader distributed loading, while the slam case causes higher shear near the tip due to the concentrated point load. However, the slam case produces a higher overall bending moment, exceeding the manoeuvre root moment by 4.542 $[MNm]$, consistent with the larger moment arm of the tip force. The envelope of maximum internal shear at each span-wise location defines the governing shear case, while the slam case dictates the bending moment design inputs in Subsection 8.4.3. Although horizontal shear and torsional loads are included in the analysis, their impact is secondary compared to the dominant vertical loads shown in Figure 8.8. Note that in the resultant distributions, three 'candles' are visible, representing the engine weight contributions.

[14] https://www.orcina.com/webhelp/OrcaFlex/Content/html/Slammingtheory.htm5ykjik, ,

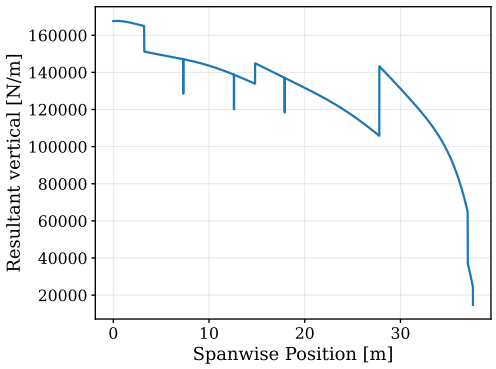

(a) *Resultant Vertical Distribution (2.5g Pull-Up)*

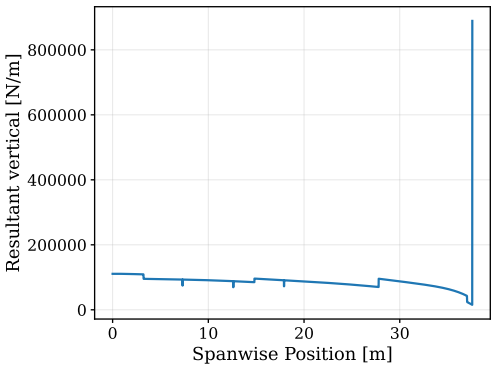

(b) *Resultant Vertical Distribution (Buoy Slam)*

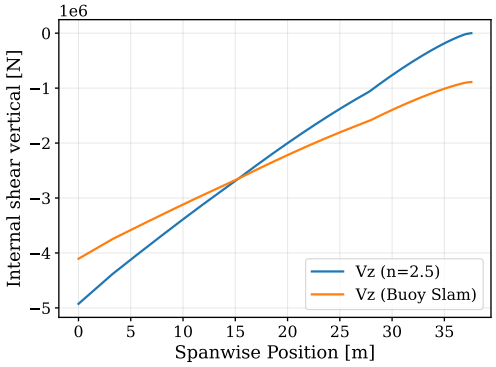

(c) *Internal Vertical Shear Force (Both Cases)*

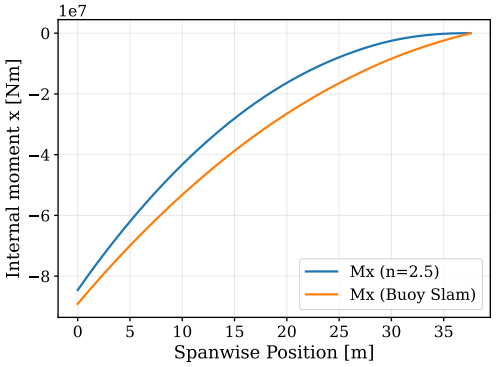

(d) *Internal Moment Around x-axis (Both Cases)*

Figure 8.8: *Comparison of 2.5g Pull-Up and Buoy Slam Load Distributions and Internal Forces*

Horizontal Tail Internal Loads

The horizontal tail is structurally analysed in a similar manner to the wing. The critical loading case for the horizontal tail is assumed to be landing: when the pitching moment due to the wing and its HLDs generate the largest longitudinal moments required to be counteracted. With the elevator geometry defined in Figure 7.2.1 the landing speed equal to 65 $[m/s]$, the total lift required for trim is calculated and the maximum elevator lift from Figure 7.2.1 is distributed evenly across the elevator span. The internal shear and moment diagrams are plotted alongside in Figure 8.9.

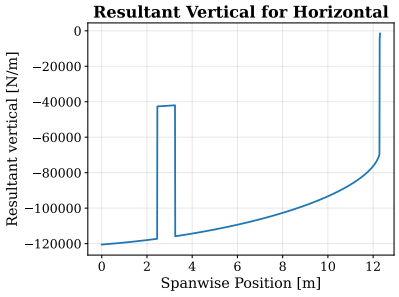

(a) *Resultant Vertical Load Distribution on the Horizontal Tail.*

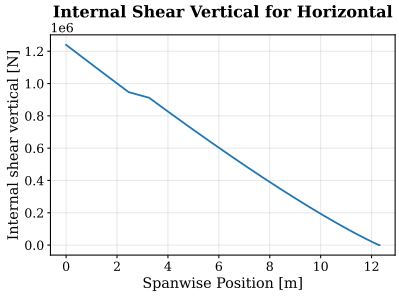

(b) *Internal Shear Force Distribution on the Horizontal Tail.*

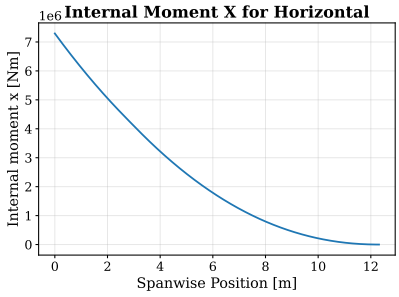

(c) *Internal Moment Distribution on the x-axis of the Horizontal Tail.*

Figure 8.9: *Load, Shear, and Moment Distributions on the Horizontal Tail.*

Since the empennage is a H-tail, the elevator cannot extend fully across the interface with the vertical fins, hence explaining the drop in load to the elliptical at ~3 $[m]$. As can be seen in Figure 8.10b, the internal shear force more or less varies linearly throughout the span with a small flattening due to the aforementioned break in the elevator, ranging from a root moment of ~1.25 $[MN]$ to zero at the tips. The horizontal tail moment can be seen to max out at 6.81 $[MN/m]$ at the root.

Vertical Tail Internal Loads

The vertical tail is composed of two fins and the plots presented below relate to one of the fins which, due to symmetry, is assumed to be identical for both. To obtain the maximum critical load, the OEI condition is applied to the outermost engine as explained in Subsection 7.2.2 and yielding the max rudder lift shown in Figure 7.5. Applying this lift proportionally to the rudder chord at every lengthwise position yields the load distribution shown below in Figure 8.10a. The internal shear and moment distribution are plotted alongside in Figure 8.10.

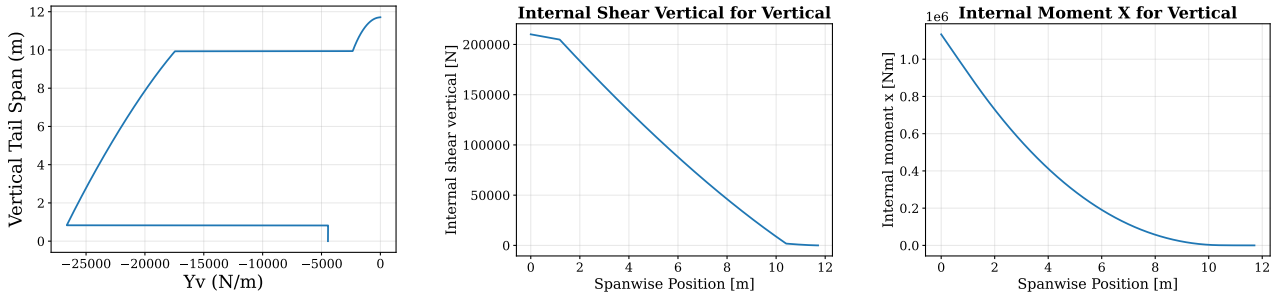

(a) *Resultant Lateral Load Distribution on the Vertical Tail.*

(b) *Internal Shear Force Distribution on the Vertical Tail.*

(c) *Internal Moment Distribution on the x-axis of the Vertical Tail.*

Figure 8.10: *Load, Shear, and Moment Distributions on the Vertical Tail.*

Similarly to the wing and horizontal tail, the vertical tail load distribution is integrated to arrive at the internal shear and bending moment loads. This yields a root bending moment of 322 $[kN]$, about half of that of the horizontal tail and an order of magnitude less than the wing. These values make sense considering the H-tail design and relatively lenient OEI condition.

8.4.2. Fuselage Structural Design

This section contains an analysis of the structural design of the fuselage. The objective is to ensure that the different loads identified in Subsection 8.4.1 can be confidently sustained. For this, the idealization approach suggested by Megson is used [64, pp. 599–604]. The fuselage cross-section is approximated as an idealised section with five booms positioned relative to the fuselage width, and the stringers are modelled as point areas along the cross-section. This idealisation, as shown in Section 8.3, renders the cross-section straight/rectangular and divides it into five discrete segments. Based on the boom and stringer point areas, the moments of inertia are easily computed via Steiner's theorem. Since the cross-section varies along the fuselage length (Figure 8.3), three stations are defined: Station 1 marks the end of the nose, Station 2 the end of the forebody, and Station 3 the end of the afterbody, with Station 3 parameters extended through the tail. The idealised cross-section at Station 2 is shown alongside in Figure 8.11.

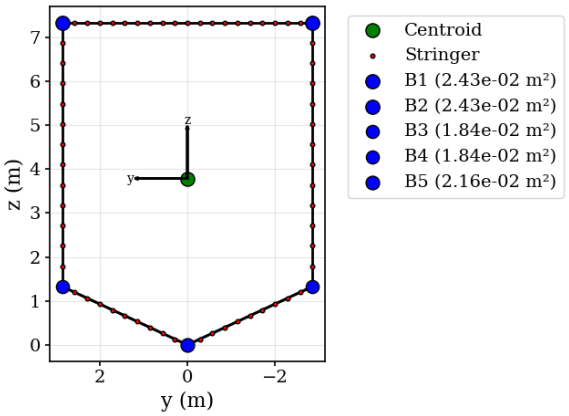

Figure 8.11: *Idealised fuselage cross-section at Station 2 (Forebody).*

The bending stress at each boom is computed using the standard asymmetric bending stress equation, applied to the symmetric fuselage cross-section [64, p. 464]. Shear flow is evaluated following the method by Megson for idealised sections [64, p. 600]. This involves calculating the base shear flow from differences in boom area contributions (neglecting stringers due to their relatively small size), and solving for the standard

shear flow via moment equilibrium, by conceptually 'cutting' the top section of the fuselage.

To assess various buckling modes, boom areas are converted into equivalent skin thicknesses by inverting Megson's idealisation method [64, p. 560]. For skin and shear buckling, the approach in [64, pp. 297–298] is used, which applies different buckling constants depending on the support conditions. A skin buckling constant of $C = 6.98$ and a shear buckling constant $k_s = 11$ are used, assuming simply supported edges and a low spar height-to-length ratio [64, p. 298]. These equations depend on plate thickness, effective width (adjusted for stringer interference), and material properties. Column buckling is evaluated following Megson's method as well [64, pp. 256–258].

The structural fuselage sizing is implemented through an iterative process. Initial values are set for boom areas, number of stringers, and stringer area. Stress analysis is then performed and safety margins evaluated. If any margin falls below one at a given station, the corresponding boom area(s), number of stringers, and stringer area are proportionally increased. The updated geometry is used in the next iteration, and the process continues until convergence.

Fuselage Frame Design and Spacing

For the fuselage frame design, both thickness and width are considered. Frame spacing is based on lateral skin buckling and derived using Megson's conventional buckling equation, rearranged to solve for the spacing s_{frame}, as shown in Equation 8.1 [64]:

$$s_{frame} = t_{skin}\sqrt{\frac{C_{fus}\pi^2 E_{fus}}{12(1-\nu_{fus}^2)\sigma_x}}, \tag{8.1}$$

Here, t_{skin} is the fuselage skin thickness, C_{fus} is the buckling coefficient (typically 4 for simply supported plates), E_{fus} and ν_{fus} are the Young's modulus and Poisson's ratio, and σ_x is the axial compressive stress from local bending. The final spacing at each location is taken as the minimum of the calculated value and the standard limit of 24 $[in]$ [16]. Once spacing is set, frame positions are fixed, enabling calculation of the required frame thickness. It is conservatively assumed that the frame carries the full local shear flow, from which thickness is computed based on allowable shear stress. Frame width is then determined by shear buckling, using an equation analogous to Equation 8.1, replacing C_{fus} with the shear buckling constant and σ_y with the local shear stress. The final width is the minimum of the calculated value and 150 $[mm]$ [16]. Figure 8.12 shows the resulting frame layout along the fuselage.

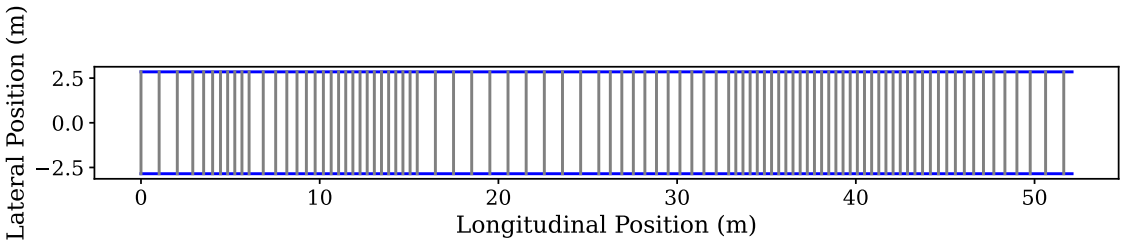

Figure 8.12: *Fuselage Frame Positions Along the Fuselage Length*

Fuselage Structural Analysis Results

In Table 8.7, the results of the fuselage structural analysis are presented along with the relevant inputs to arrive at those results.

Table 8.7: *Inputs and Outputs Table of Fuselage Structural Design*

Inputs			Outputs		
Parameter	Value	Unit	Parameter	Value	Unit
B_{initial}	2000	[mm^2]	**Station 1**		
$n_{\text{stringers}}$[1]	10	[−]	t_{frame}	2.6	[mm]
A_{stringer}	200	[mm^2]	t_{side}	2.6	[mm]
C_{fus}	6.98	[−]	t_{hull}	2.2	[mm]
k_s	11	[−]	t_{top}	2.2	[mm]
$t_{\text{ep}_{\text{in}}}$	5	[%t][2]	$n_{\text{stringers}}$	31	[−]
$t_{\text{ep}_{\text{out}}}$	5	[%t]	Bending vs. Buckling	1.20	[−]
Station 2			t_{frame}	14.9	[mm]
			t_{side}	14.9	[mm]
			t_{hull}	13.5	[mm]
			t_{top}	14.7	[mm]
			$n_{\text{stringers}}$	64	[−]
			Bending vs. Buckling	1.13	[−]
			Shear vs. Buckling	1.20	[−]
Station 3			t_{frame}	8.0	[mm]
			t_{side}	8.0	[mm]
			t_{hull}	5.4	[mm]
			t_{top}	7.3	[mm]
			$n_{\text{stringers}}$	37	[−]
			Bending vs. Buckling	1.80	[−]
General			n_{frames}	93	[−]
			m_{frames}	6589	[kg]
			m_{fuselage}	39,367	[kg]

As can be seen in Table 8.7, not all stress margins for all combinations of sections, stations and stresses are included. Only the margins closer to 1 are presented, as those are more critical. Note that a margin of 1 means that the actual stress is 1.5 times lower than the critical stress at that position along the fuselage. The fuselage structural mass, being equal to 39367 $[kg]$, mismatches the fuselage weight computed in Chapter 5. Therefore, an iteration is necessary to ensure consistent design, as outlined in Chapter 4.

8.4.3. Wing Structural Design

In Figure 8.4.1, internal loads are translated into bending and shear stresses, which are compared against critical values such as material (shear) yield stress and buckling stresses of the skin, web, and stringer-supported panels. This comparison guides the wing box structural design, informing skin and web thicknesses, cell count, stringer sizing and quantity, rib spacing, and material selection, including fuel housing integration. The design employs an iterative approach: starting with an initial wing box geometry, stresses are analysed and checked against limits. If criteria are unmet, the geometry is adjusted and reassessed until all criteria are satisfied. Though the wing box is primarily a cross-sectional problem, analysis is performed span-wise along half the wing to ensure compliance across varying bending moments, shear forces, and torsion. Bending stress and buckling evaluations follow methods in Subsection 8.4.2, with a simplified shear stress distribution and more detailed torsional analysis due to multiple cells. Stringers are modelled as I-beams to estimate crippling stress and effective sheet widths for skin buckling. Skin and shear buckling use the same methods as in Subsection 8.4.2 but with adjusted buckling coefficients. The following sections detail the shear flow, torsional analysis, and sizing methodology for the wing box.

Shear Stress on the Wing Box

In order to obtain the shear stress in the wing box efficiently, it is assumed that the spar webs carry the shear stress resulting from the vertical shear force, while the skin panels carry the stress due to the horizontal shear force. Instead of performing a detailed shear flow analysis, the stress is approximated by assuming a constant average shear flow distribution scaled to yield the maximum shear stress. The expressions used

[1] The amount of stringers per fuselage station.

[2] The thickness of the epoxy is the mentioned percentage of the thickness of the structure to which it is applied, as mentioned in Subsection 8.2.1.

are:

$$\tau_{\text{spar}} = \frac{k_{\text{spar}} V_z}{\sum_{i=1}^{n_{\text{cells}}+1} h_{\text{spar},i}\, t_{\text{spar},i}} \tag{8.2}$$

$$\tau_{\text{skin}} = \frac{k_{\text{skin}} V_x}{\sum_{i=1}^{n_{\text{cells}}} b_{\text{skin},i}\, t_{\text{skin},i}} \tag{8.3}$$

Here, k_{spar} and k_{skin} are correction factors to relate the average shear flow to the maximum. Since shear flow in a spar web typically follows a parabolic profile, $k_{\text{spar}} = 1.5$. In contrast, for a linear distribution in the skin panels starting from zero at the edge, $k_{\text{skin}} = 2$. V_z and V_x are the internal vertical and horizontal shear forces respectively, as defined in Figure 8.4.1. h_{skin} is the spar height, t_{spar} the spar thickness, b_{spar} the panel width, and t_{skin} the skin thickness. The calculated stress is then multiplied by a safety factor of 1.5 to ensure conservative sizing.

Torsion on the Wing Box

As was explained in Figure 8.4.1, the wing box also has to deal with internal torque. For a wing box with 3 cells, Figure 8.13 shows the shear flow distribution along these cells when a clockwise torque is applied:

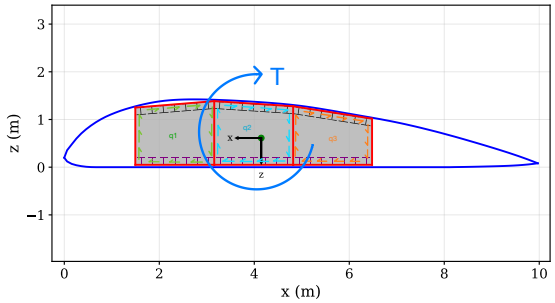

Figure 8.13: *Wing Cross-Section at the Root Chord, with Applied Torque and Associated Shear Flow Directions q1, q2 and q3.*

Naturally, as the cells of the wing box differ in geometry, the shear flow in each cell varies, as shown in Figure 8.13. The shear flow in each cell is determined by equating torque equivalence across the entire wing cross section and ensuring that the rate of twist is compatible and continuous throughout all cells, which is the suggested approach by Megson [64, pp.609-610]. This results in a system of equations that can be solved to find the shear flow distribution within each cell. This analytical approach provides flexibility in wing box design, allowing different cell configurations, geometries, and material layouts to be evaluated while satisfying both torque balance and twist compatibility. Consequently, it enables optimization of the wing box structure by controlling the shear flow distribution due to the internal torque.

The maximum torsional shear stress is found by locating the peak shear flow in the wing box and dividing it by the minimum wall thickness, then applying a safety factor of 1.5. To find the total shear stress at each span-wise station, torsional and shear flows are summed around the wing box cells. The critical location is where these shear components align with the highest magnitude, lowest thickness, or combination, producing the highest combined stress. This total shear stress is checked against the material's shear yield and web buckling limits.

Wing Rib Design and Spacing

At this design stage, wing ribs are preliminarily sized considering cutouts, spacing, and thickness. The total rib area without cutouts equals the wing cross-sectional area at the rib location. Lightening hole cutouts reduce stress concentrations and target roughly 25% mass reduction[1]. Rib spacing along the span is primarily governed by the critical skin buckling stress. Using Megson's skin buckling equation rearranged to solve for rib spacing s_{rib} (cf. Equation 8.1) and applying a safety factor of 1.5 to the local skin bending stress, spacing is established as in Subsection 8.4.2. Once spacing is set, rib positions and count follow, allowing thickness determination by considering: interference of vertical shear flow with cutouts, horizontal shear flow interference, and shear buckling resistance. The first two are evaluated by Equation 8.4 and Equation 8.5:

$$\tau_{\text{net}_v} = \frac{S_v}{A_{\text{net}_v}} = \frac{q_v h_{spar}}{t_{rib}(h_{spar} - D))} \tag{8.4}$$

$$\tau_{\text{net}_h} = \frac{S_h}{A_{\text{net}_h}} = \frac{q_h b_{skin}}{t_{rib}(b_{skin} - D)} \tag{8.5}$$

[1] Greater reductions require detailed analysis beyond this scope.

Here, q_v, q_h are shear flows; $h_{\text{spar}}, b_{\text{skin}}$ the spar height and skin width; t_{rib} the rib thickness; and D the cutout diameter. Net shear stress divides shear force by reduced cross-sectional area due to cutouts. Equating τ_{net} to allowable shear stress (factoring yield or critical web stress with safety factor 1.5) yields required thickness. Shear buckling thickness is similarly computed from the buckling equation (cf. Equation 8.1). The maximum thickness from these criteria defines each rib's thickness. Figure 8.14 shows the rib and cutout geometry at the wing root.

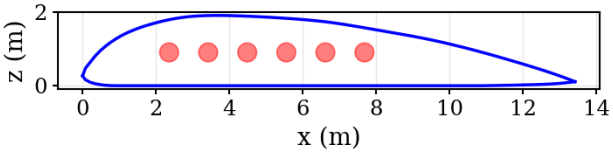

Figure 8.14: *Wing Rib with Cutouts at the Root of the Wing*

Wing Box Sizing Results

In Table 8.8, the results for the structural analysis of the wing are presented along with the relevant inputs to arrive at those results. The wing twist is found by integration of the span-wise variation of $\frac{d\theta}{dy}$, while the wing tip deflection is found by integrating the applied span-wise moment divided by the stiffness of the wing twice (Euler-Bernouilli deflection).

Table 8.8: *Input and Output Parameters for Wing Box Structural Analysis (one side)*

Inputs			**Outputs**		
Parameter	Value	Unit	Parameter	Value	Unit
$\frac{x_{\text{front spar}}}{c}$	0.15	[−]	**2.5g pull-up**		
$\frac{x_{\text{rear spar}}}{c}$	0.65	[−]	Bending vs Yield	1.10	[−]
t_{skin}	14	[mm]	Bending vs Column Buckling	3.96	[−]
t_{spar}	17	[mm]	Bending vs Panel Buckling	4.58	[−]
t_{wing}	4	[mm]	Shear vs Yield	4.28	[−]
$t_{\text{ep}_{\text{out}}}$	5	[%t]	Shear vs Web Buckling	1.29	[−]
$t_{\text{ep}_{\text{in}}}$	5	[%t]	Wing Bending vs Yield	1.07	[−]
A_{stringer}	1800	[mm^2]	Wing Tip Deflection	1.09	[m]
$n_{\text{stringers}}$	40	[−]	Wing Twist	1.46	[deg]
n_{cells}	3	[−]	**Buoy Slam**		
C	4	[−]	Bending vs Yield	1.04	[−]
L_{stringer}[1]	200	[mm]	Bending vs Column Buckling	1.47	[−]
$t_{\text{skin,min}}$	4	[mm]	Bending vs Panel Buckling	1.37	[−]
$t_{\text{spar,min}}$	10	[mm]	Shear vs Yield	3.58	[−]
Thickness Threshold[2]	0.35	[−]	Shear vs Web Buckling	1.08	[−]
s_{cutout}	0.3	[m]	Wing Bending vs Yield	1.01	[−]
Fuel Tank Size[3]	0.6	[−]	Wing Tip Deflection	1.68	[m]
t_{tank}	2	[mm]	Wing Twist	0.19	[deg]
$A_{cutouts}$[4]	0.25	[−]	**General Outputs**		
k_s	11	[−]	Rib Amount	41	[−]
$\frac{x_{\text{mid spar1}}}{c}$	0.32	[−]	Total Rib Mass	2457.24	[kg]
$\frac{x_{\text{mid spar2}}}{c}$	0.48	[−]	Wing Structural Mass	28383	[kg]
			Fuel Tank b_1	3.23	[m]
			Fuel Tank b_2	14.81	[m]
			V_{tank}	51.2	[m^3]

[1] This is the base length of the stringer, the other sections of the I-beam are ratios from this base length.
[2] This is the relative position on the wing at which the thickness starts gradually decreasing.
[3] This is the relative area of the fuel tank to the equivalent rectangular area of the wing box at the local chord.
[4] This is expressed as a ratio of the total cutout area and the local wing section area.

As can be seen in Table 8.8, the buoy slam contains the most critical stress margin (close to 1, where a safety margin of 1 means that the actual stress is a factor of 1.5 lower than the critical stress). The 2.5g pull-up case also shows various margins close to 1, showing an overall optimized design for both considered load cases. Note that in the buoy slam case the wing twist is lower due to the buoy drag. Moreover, structural mass of half of the wing is considerably higher than the estimated weight in Section 5.1, this is solved by iteration, as outlined in Chapter 4. Note that the maximum wing tip deflection is due to the buoy slam, reaching 1.68 [m], well within REQ-STR.1, which allows a deflection of up to 5.62 [m]. Figure 8.15 and Figure 8.16 represent a top view of the wing planform with rib position and length, as well as the fuel tank. The volume of the fuel tank is taken as 10% larger than half of the maximum fuel volume, defined in Chapter 5 (accounting for expansion, for example). Note that no further structural analysis is performed on the fuel tank, only that the ribs intersecting with the fuel tank do not have the mentioned cutouts, but a large enough opening for the fuel tank to pass through. For a visualization of the final wing box, consider Figure 8.13 once more.

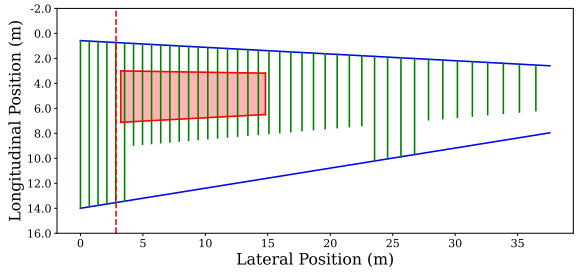

Figure 8.15: *Top View of the Right Wing with Ribs and Fuel Tank Shown; Leading Edge is Upwards.*

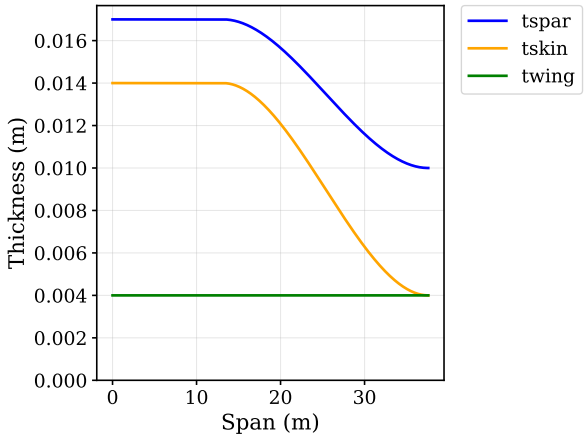

Figure 8.16: *Thickness Distributions Along the Wing Span.*

As shown in Figure 8.15, the wing ribs are spaced more closely near the root, which aligns with structural expectations due to higher loads in this region. In Figure 8.16, it is observed that the spar and skin panel thicknesses gradually decrease along the span, whereas the wing thickness remains constant. Chapter 15 outlines how this variable thickness will be implemented from a manufacturing perspective. It should be noted that the displayed number of stringers cannot be accommodated uniformly along the entire span. As the wing box tapers towards the tip, the available space for stringers reduces. Although the stringers are distributed evenly along the designated skin panels, they are discontinued where the spacing becomes too small or insufficient space is available. Consequently, stringer lengths vary along the span, with sections closer to the root featuring more stringers in the cross-section than those near the tip.

8.4.4. Empennage Structural Design

For the structural design of the empennage, the same procedures are followed as as in the structural design of the wing outlined in Subsection 8.4.3. However, instead of two possible critical cases, for the horizontal tail as well as the vertical tails only one critical case is identified: a 2.5g manouevre on top of a maximum control surface deflection. The applied loads due to these critical cases are outlined in Subsection 8.4.1 and 8.4.1. In the sections below, the results of the horizontal tail and vertical tails wing box design are provided.

Horizontal Tail Structural Design Results

In Table 8.9, the results of the structural analysis on the horizontal tail are presented along with the corresponding inputs.

Table 8.9: *Input and Output Parameters for Horizontal Tail Wing Box (one side)*

Inputs			**Outputs**		
Parameter	Value	Unit	Parameter	Value	Unit
$\frac{x_{\text{front spar}}}{c}$	0.15	[−]	**2.5g load factor**		
$\frac{x_{\text{rear spar}}}{c}$	0.6	[−]	Bending vs Yield	1.20	[−]
t_{skin}	8	[mm]	Bending vs Column Buckling	4.22	[−]
t_{spar}	10	[mm]	Bending vs Panel Buckling	5.45	[−]
t_{wing}	1.5	[mm]	Bending vs Yield (bottom)	1.30	[−]
$t_{\text{ep}_{\text{out}}}$	5	[%t]	Shear vs Yield	1.32	[−]
$t_{\text{ep}_{\text{in}}}$	2.5	[%t]	Shear vs Web Buckling	1.33	[−]
A_{stringer}	375	[mm^2]	Wing Bending vs Yield	1.02	[−]
$n_{\text{stringers}}$	25	[−]			
n_{cells}	1	[−]			
C	4	[−]	**General Outputs**		
L_{stringer}	150	[mm]	Rib Amount	27	[-]
$t_{\text{skin,min}}$	2	[mm]	Total Rib Mass	528.22	[kg]
$t_{\text{spar,min}}$	4	[mm]	Structural Mass	2002	[kg]
Thickness Threshold	0.3	[−]			
s_{cutout}	0.2	[m]			
$A_{cutouts}$	0.25	[−]			
k_s	11	[-]			

Again, as can be seen in the table, the structural mass of the horizontal tail (twice the value in the table) differs from the one estimated in Chapter 5, which is solved again by the iteration discussed in Chapter 4. Like the main wing, the horizontal tail also has slight thickness variation along the span. Figure 8.17 and Figure 8.18 represent the final horizontal tail wing box cross-section at the mean aerodynamic chord and the position and length of the ribs, respectively.

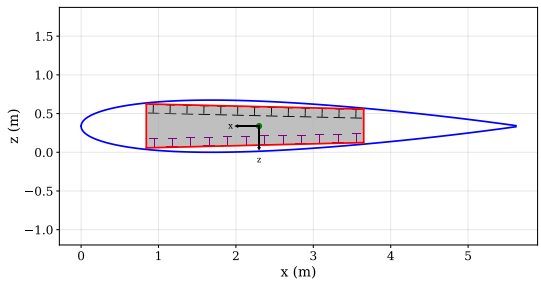

Figure 8.17: *Final Wing-box Design of the Horizontal Tail*

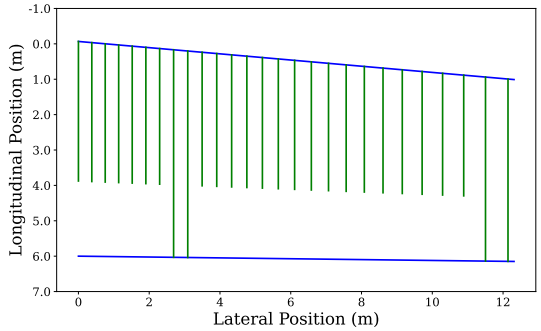

Figure 8.18: *Top View of the Horizontal Tail with Span-wise Positions of the Ribs of the Horizontal Tail (right side)*

Vertical Tail(s) Structural Design Results

In Table 8.10, the results of the vertical wing box structural design are presented, along with the relevant inputs to arrive at those results.

Table 8.10: *Input and Output Parameters for Vertical Tail Wing Box (one vertical tail)*

Inputs			Outputs		
Parameter	Value	Unit	Parameter	Value	Unit
$\frac{x_{\text{front spar}}}{c}$	0.15	[−]	**2.5g load factor**		
$\frac{x_{\text{rear spar}}}{c}$	0.65	[−]	Bending vs Yield	5.16	[−]
t_{skin}	7	[mm]	Bending vs Panel Buckling	1.74	[−]
t_{spar}	10	[mm]	Bending vs Yield (bottom)	5.14	[−]
t_{wing}	1	[mm]	Shear vs Yield	5.72	[−]
$t_{\text{ep}_{\text{out}}}$	5	[%t]	Shear vs Web Buckling	1.96	[−]
$t_{\text{ep}_{\text{in}}}$	2.5	[%t]	Wing Bending vs Yield	4.40	[−]
A_{stringer}	400	[mm^2]			
$n_{\text{stringers}}$	25	[−]			
n_{cells}	1	[−]			
C	4	[−]	**General Outputs**		
L_{stringer}	100	[mm]	Rib Amount	17	[-]
$t_{\text{skin,min}}$	1	[mm]	Total Rib Mass	553.36	[kg]
$t_{\text{spar,min}}$	10	[mm]	Structural Mass	2159.89	[kg]
Thickness Threshold	0.65	[−]			
s_{cutout}	0.2	[m]			
$A_{cutouts}$	0.25	[−]			
k_s	11	[-]			

As expected, for the vertical tail the structural mass (twice the mass shown in the table) also differs from the estimated mass in Chapter 5, which the final iteration solves. Figure 8.19 and Figure 8.20 represent the final vertical tail wing box cross-section at the mean aerodynamic chord and the position and length of the ribs, respectively.

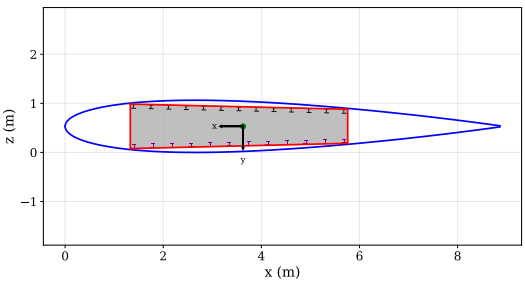

Figure 8.19: *Final Wing-box Design of the Vertical Tail (one vertical tail)*

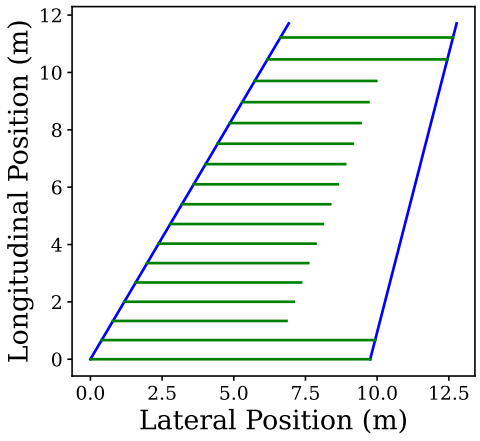

Figure 8.20: *Side View of the Vertical Tail with Span-wise Positions of the Ribs (one vertical tail)*

8.4.5. Flutter Analysis

To satisfy REQ-STR.4 from Table 8.1, a flutter analysis is performed on the wing and empennage. This analysis follows the two-dimensional pitch–plunge–control model presented by Dimitriadis [65, pp. 557–564] [1]. The model considers a section at the mean aerodynamic chord of the wing and evaluates its behaviour under pitch (rotation), plunge (vertical translation), and control surface flutter. The latter, being more complex, is beyond the current scope and is deferred to a later stage in the design process. Since the vibration frequencies and damping ratios vary with airspeed, the method is evaluated across the entire flight enve-

[1] Following a consultation with Dr. J. Sodja (TU Delft, 10 june 2025), a specialist in aeroelasticity, his Python implementation of the method was provided to the team and used for this model.

lope (defined in Section 8.1) to ensure that the damping coefficient remains positive. A damping coefficient of zero or less would indicate the onset of flutter.

The method requires the initialisation of the structure's natural frequencies in bending and torsion. These are calculated using classical closed-form expressions for Euler–Bernoulli beams, given in Equation 8.6 and Equation 8.7:

$$f_{n,\text{bending}} = \frac{\beta_n^2}{2\pi L^2}\sqrt{\frac{EI}{\rho A}} \tag{8.6}$$

$$f_{n,\text{torsion}} = \frac{n}{2L}\sqrt{\frac{GJ}{I_p}} \tag{8.7}$$

In these equations, $f_{n,\text{bending}}$ and $f_{n,\text{torsion}}$ represent the natural frequencies of bending and torsion, respectively. Here, L is the (half) span length, E is Young's modulus, I is the second moment of area, ρ is the material density, and A is the cross-sectional area. G is the shear modulus, J is the torsional constant, and I_p is the polar moment of inertia. The bending mode shape factor β_n takes values 1.875 and 4.694 for the first and second modes, while the torsional mode number n is evaluated for 1 and 2.

From these frequencies, equivalent stiffness and initial damping coefficients are calculated. The damping is modelled as a fraction of the critical damping, typically ranging from 2% to 5%, based on expert input from Dr. Sodja. Once initialised, the flutter analysis is performed across all flight envelope velocities to detect any occurrence of negative damping, which would indicate instability due to flutter.

Flutter Analysis Results

In Table 8.11, the velocities at which the minimum damping coefficient occurs are presented along with the relevant inputs to arrive there. All inputs in the table are defined in the book by Dimitriadis [65, p.557].

Table 8.11: *Inputs and Outputs for Flutter Analysis of Wing, Horizontal and Vertical Tail*

	Parameter	Wing	Horizontal Tail	Vertical Tail	Unit
Inputs	m	6.68	1.15	1.46	$[kg]$
	S_m	5.60	0.59	0.52	$[kgm^2]$
	I_α	60.04	3.33	7.93	$[kgm^2]$
	$\bar{c}$	9.97	5.62	7.97	$[m]$
	$\bar{c}/2$	4.98	2.81	3.98	$[m]$
	x_f	4.15	2.30	3.63	$[m]$
	a[1]	-0.89	-0.81	-0.38	$[-]$
	ρ_{air}	1.225			$[kg/m^3]$
	$f_{n,\text{bend},1}$	8.94	4.67	7.76	$[rad/s]$
	$f_{n,\text{tors},1}$	28.26	24.50	22.71	$[rad/s]$
	$f_{n,\text{bend},2}$	56.06	29.25	48.65	$[rad/s]$
	$f_{n,\text{tors},2}$	56.51	49.01	45.42	$[rad/s]$
Outputs	$V_{\zeta_{min}}$	69.69	162.89	162.89	$[m/s]$
	ζ_{min}	0.02	0.22	0.02	$[-]$

As seen in Table 8.11, the damping coefficients of the wing and vertical tail are the lowest. For the wing, this occurs near take-off and landing speeds, while for the vertical tail it corresponds to the maximum flight speed. At that same speed, the horizontal tail shows a noticeable increase in damping. In Figure 8.21 and Figure 8.22, the variation of natural frequencies and damping coefficients with flight speed is shown for the wing, horizontal tail, and vertical tail.

[1] This value is obtained by equating $\frac{x_f}{b/2} - 1$, and represents the distance between the leading edge and flexural axis of the section.

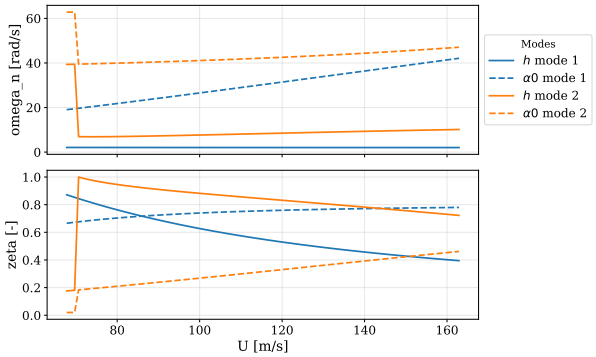

(a) *Wing: Natural Frequencies and Damping Coefficients of Pitch and Plunge States for Different Velocities and Modes.*

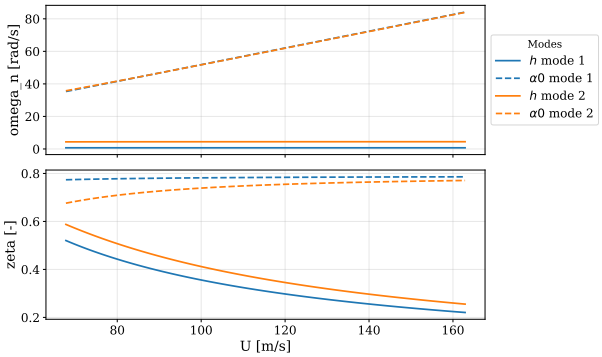

(b) *Horizontal Tail: Natural Frequencies and Damping Coefficients of Pitch and Plunge States for Different Velocities and Modes.*

Figure 8.21: *Flutter Analysis Results for Wing and Horizontal Tail*

As shown in Figure 8.21a, the angle of attack vibrations in mode 2 are nearly undamped near take-off speed. At higher speeds, the damping coefficient increases for the angle of attack, while the damping of the plunge state decreases but remains clearly above zero. Therefore, no flutter risk is present for the wing within the flight envelope. In Figure 8.21b, a decreasing trend in plunge damping is observed with increasing speed, but the damping remains positive across all states and modes. Thus, the horizontal tail also shows no flutter risk within the flight envelope.

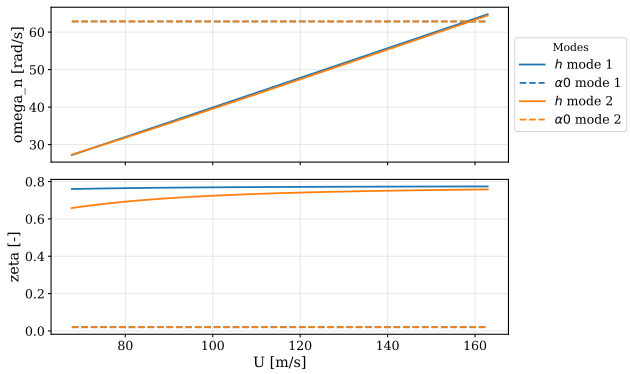

Figure 8.22: *Natural Frequencies and Damping Coefficients of Pitch and Plunge state of the Vertical Tail for Different Velocities and Modes*

From Figure 8.22, it is evident that the damping coefficient of the angle of attack (sideslip angle for the vertical tail) remains close to zero and even slightly decreases at higher speeds. However, damping remains positive throughout, indicating no flutter risk. The sideslip oscillations are long-lasting and show flutter-like behavior, but they remain bounded. Therefore, while no flutter is predicted for the vertical tail, this conclusion is made with caution.

8.4.6. Structural Design Compliance

Here, the relevant structural requirements from Table 8.1 are revisited and checked for compliance, shown in Table 8.12.

Table 8.12: *Compliance Matrix - Fuselage and Structural Systems*

Requirement ID	Requirement Description	Compliance Justification	
REQ-TNL.2	The aircraft shall be able to land in sea states up to and including sea state four.	The stress analysis consist of analyzing the landing loads, the structure does not fail.	

Requirement ID	Requirement Description	Compliance Justification	
REQ-TNL.3	The aircraft shall be able to access islands.	Of the three beaching options (Chapter 2) there is always at least one possibility to access the island. The cargo door is designed for the most critical beach profile.	
REQ-TNL.3.1	The aircraft shall be able to dock on beaches without external assistance.	The buoys and floaters provide sufficient buoyancy to lift the aircraft sufficiently out of the water in order to dock on the most critical beach profile.	
REQ-TNL.3.2	The aircraft shall be able to leave beaches without external assistance.	The buoys and floaters provide sufficient buoyancy to overcome getting stuck on the beach.	
REQ-TNL.4	The aircraft shall be equipped with an anchor.	The aircraft is equiped with an anchor (Subsection 8.3.6.	
REQ-CAR.1	The structures shall be able to hold a maximum structural payload of 100 $[tonnes]$.	The structure was designed as if the actual payload was 100$[tonnes]$ with an additional safety factor of 1.5.	
REQ-CAR.2	TThe aircraft shall be able to carry a payload of 90 $[tonnes]$ at payload density of 160 $[kg/m^3]$.	Show the cargo hold is large enough and perform stress analysis.	
REQ-CAR.2.1	The dimensions (length, width, height) of the cargo hold shall be such that it can hold payload which has a volume of at least 562.5 $[m^3]$.	The volume of the cargo hold is 614.25 $[m^3]$, which is enough.	
REQ-CAR.2.2	The cargo hold cross-section dimensions (width, height) shall be such that at any point along the cargo hold at least a rectangle of 3.5 $[m]$ wide and 4.0 $[m]$ high fits inside.	The width of the cargo hold is 5.2 $[m]$ and the height is 4.2 $[m]$.	
REQ-CAR.2.3	The dimensions (width, height) of the cross-section of the door to the cargo hold shall be such that at least a cuboid of 3.5 $[m]$ wide, 4.0 $[m]$ in height and 7.32 $[m]$ in length fits inside.	The cuboid can fit through the cargo door while on the most critical beach profile (Subsection 8.3.3	
REQ-CRU.5.1	The minimum cruise clearance of the wing to the water wave-peaks in ground effect shall be at least 1.5 $[m]$ for sea states up to and including three.	The wing tip clearance is 2.5 $[m]$.	
REQ-STR.1	The lifting structure shall have a maximum tip deflection of 15% of the length of the lifting structure at the most critical loading condition [45].	The deflection at the wingtip is 1$[m]$, which is about 3% of the wingspan.	
REQ-STR.2	The aircraft structure shall sustain the critical loading condition without any structural damage.	The structures were designed to sustain the critical loading conditions with an additional safety factor of 1.5.	

Requirement ID	Requirement Description	Compliance Justification	
REQ-STR.3	The aircraft structure shall be able to house sufficient fuel to perform all design missions.	The total fuel volume for the most limiting mission is 93 $[m^3]$. The volume of one tank 46.5$[m^3]$. Therefore, the total fuel tank volume is sufficient for the mission.	
REQ-STR.4	Flutter of the aerodynamic surfaces shall not occur within the flight envelope.	Flutter does not occur before or at the aircraft's maximum speed of 162$[m/s]$.	
REQ-STR.5	The aircraft shall maintain buoyancy for all on-water operations and for beaching on the mean beach profile.	Floating depth without floater is 3.1 $[m]$. The buoys provide sufficient clearance for beaching. The aircraft remains buoyant during operations.	
REQ-STR.6	Outer structure shall be watertight.	The aircraft outside structure will be fully coated with a nano material reinforced epoxy coating, which is hydrophobic.	
REQ-STR.6.1	All aircraft outer panels shall be watertight.	The aircraft outer panels will be fully coated with a nano material reinforced epoxy coating, which is hydrophobic.	
REQ-STR.6.2	All aircraft sealings shall be watertight.	The sealings will be fully coated with a nano material reinforced epoxy coating, which is hydrophobic.	
REQ-STR.7	The aircraft shall be towable [46].	These is a hook on the transition of the transition from afterbody to tail.	
REQ-STR.8	The aircraft shall be able to fly in the required flight envelope [40].	The stress analysis is performed for the critical load case in the flight envelope. The structure does not fail.	
REQ-STR.8.1	The aircraft shall be able to withstand all manoeuvre loads as specified in CS-25 [40].	The stress analysis is performed for the critical manoeuvre load case. The structure does not fail.	
REQ-STR.8.2	The aircraft shall be able to withstand all gust loads as specified in CS-25 [40].	The stress analysis is performed for the critical gust load case. The structure does not fail.	

9

Powerplant

In the Midterm Report a lot of work has been done on the powerplant. The biggest achievements were the determination of the system (propeller, jet or mixed propulsion) and the engine. For this aircraft, the Europrop TP400-D6, used on the Airbus A400M, has been selected[25]. Three things are still to be determined for the aircraft: the propeller geometry, done in Section 9.1, the engine placement, in Section 9.2, and lastly the battery/APU design, done in Section 9.3. The requirements regarding the powerplant are presented in Table 9.1. All these are verified on compliance in Section 9.4.

Table 9.1: *Relevant Requirements - Powerplant*

Requirement ID	Requirement Description	Category	Source
REQ-PWR.1	The powerplant shall provide enough thrust to complete all phases of the flight.	Functional	REQ-CUST-PERF.1 - REQ-CUST-PERF.9
REQ-PWR.2	The lowest part of the engine shall be more than 2.5 $[m]$ above the water line in sea state 0 at MTOW.	Functional	
REQ-PWR.3	The aircraft shall have two or more engines [40].	Constraint	CS-25
REQ-SUS.2	The on-water operations of the aircraft shall be without any CO_2 or NO_x emissions.	Operational	REQ-CUST-SUST.3

9.1. Propeller Design

The design of the propeller is of vital importance to the aircraft. A well-designed propeller improves fuel efficiency and available power. The propellers that are currently used on the engine are the same as for the Airbus A400M. These propellers can do the mission, but are not optimized for the flight profile of this aircraft. The main difference is the cruise mach number, which is $M0.33$ instead of around $M0.7$ of the A400M. In this section, first, the general relations between various propeller parameters and efficiency are discussed. Then, according to these relations, the propeller blade is optimized. After this, the iteration process and limitations are discussed.

To simplify the analysis, some assumptions and simplifications are made. First of all, structural aspects of the design are only qualitatively considered. No detailed structural analysis is done on the propeller blades during the trade-off although the structural feasibility is still examined in Subsection 9.1.4. Next, it is assumed the ground effect does not have an influence on propeller performance. This assumption can be made because the slipstream generally is assumed not to interfere with the ground. Lastly, the propeller perfomance is based on a propeller that is in an infinitely large medium of air without foreign objects. Implementation of wing and aircraft geometry is beyond the scope of this project and largely beyond the capabilities of the used software.

Due to the complexity of the propeller design the design process is approached iteratively. As said, first, a propeller in cruise is analysed. Various parameters are adjusted to seek an optimized propeller. This is where the iteration loop starts. Using this knowledge, initial values are chosen for the propeller. Then, an optimized propeller is made for each phase of flight is made and analysed for all phases of flight. Then, structural considerations may decide if this process is repeated for other values, for example when a blade is too thin to be structurally feasible. This process may be repeated a few times.

It is also worth noting that all analysis on the propeller has been done using XROTOR. Therefore, all unsourced values or claims have been analysed using XROTOR. [1] This program is able to generate a minimum induced loss propeller from certain inputs.

9.1.1. Setup

As the design process is iterative, the process needs some initial estimates. These estimates have been done using cruise conditions. Mainly the effect of RPM, number of blades, and the radius have been analysed accross the following ranges. Also the step size is indicated.

- Rotational speed: 700 - 900 [RPM] (step: 100 [RPM])
- Blade radius: 2.7 - 3.5 [m] (step: 0.2 [m])
- Number of blades: 4 - 8 (step: 1)

Although these estimations do not cover a very big interval, especially the RPM, it proved to be enough to establish their general effects and the limitations of XROTOR.

Airfoil

As stated by Ohad Gur, the influence of the airfoil on the overall propeller performance is minor. [66] However, structurally, it has a major influence. The higher the design lift coefficient, the thinner the blade. As will become clear from the structural analysis in Subsection 9.1.4, a fully optimized blade geometry with the optimal[2] $C_L = 0.65$ everywhere is not feasible. Therefore, the blade has to be reinforced at the base. This is done by locally increasing the thickness and chord of the airfoil, as seen in Table 9.2. Also, at the tip, the thickness and lift coefficient is reduced. This is to reduce the effects of tip drag divergence.

Table 9.2: *Design Lift Coefficient and Airfoil of the Propeller Blade*

r/R	C_L	**Airfoil**
0.13	0.3	NACA 64-020
0.5	0.65	NACA 64-012
0.85	0..65	NACA 64-012
1	0.4	NACA 64-008

Number of Blades

The amount of blades for these types of aircraft can vary considerably: generally this amount is four, six, or eight. From analysis it has been determined that an increased amount of blades equals a higher efficiency. Across the mentioned ranges, six blades are approximately 0.5% to 1.7% more efficient than four blades, and eight blades 0.6% to as much as 2.5%. Thus: the more blades the higher the efficiency of the propeller. However, if a propeller is optimized for RPM and radius, the gain in efficiency for an additional blade is small.

However, there is a big connotation to this statement. With an increasing number of blades, the base chord[3] overall chord of the blade becomes smaller. For example, for an 8 blade propeller, the base chord easily gets below 10 [cm], which means that its thickness is only around 1 [cm]. Considering the high loads on the propeller, this may structurally become unfeasible. Therefore, using engineering judgement. the best compromise between propulsive and structural efficiency at this point is six blades.

Blade Radius

The effect of blade radius is simple: the greater the blade radius, the higher the efficiency. However, there is a limit on how big the propeller blade can be. As explained under Section 9.2, the engine is place above the wing. In sea state 4, this gives a distance of 4.7 [m] from sea level to the centre of rotation of the engine. Even with a conservative safety factor of 1 [m] this still gives an maximum radius of 3.7 [m], which is structurally unrealistic. This is because similar to the blade number, the greater the radius, the smaller the chord. A detailed trade-off to get the optimal ratio between structural and propulsive efficiency is not possible, considering the available time for this project and the limitations of XROTOR. It is assumed that the maximum

[1] https://web.mit.edu/drela/Public/web/xrotor/
[2] Calculated using JavaFoil https://www.mh-aerotools.de/airfoils/jf_applet.htm [cited 17 June 2025]
[3] The base chord is defined as the length of the chord where the propeller is attached to the hub

structurally feasible radius is 3 [m] and applies for all configurations. This a bit bigger than the 2.67 [m] of the A400M. [67] Thus, in sea state 0 there is 4.2 [m] clearance between the tip of the propeller and sea line, meeting REQ-PWR.2.

Rotational Speed

The rotational speed of the propeller also influences the efficiency. The TP400 has a rotational speed also in the range of 700 - 900 [RPM]. The observed trend in this range is that the higher the RPM, the higher the efficiency although the rotational speed cannot be increased indefinitely. Eventually, tip speed will exceed the critical Mach number, causing a significant increase in drag. In the flight performance analysis, it is revealed that the aircraft flies at a cruise speed of 140 [m/s] at 10,000 [ft], see Chapter 11. In these conditions, the operation of the propeller should be without tip drag divergence as well. With some margin, the minimum speed that the propeller should be able to achieve is 150 [m/s] at 10,000 [ft]. Using a maximum tip speed of $M0.88$, this results in a maximum rotational speed of about 830 [RPM].

Other Inputs

Finally, the hub radius and hub wake displacement radius need to be determined. The hub radius is easy to determine. This is simply 40 [cm] for the TP400. There is only little documentation on how to quantify this radius. Therefore, this radius is assumed to be equal to the hub radius, which is considered acceptable for this design stage. The propeller efficiency and geometry is not very sensitive to this radius.

Lastly, in the Midterm Report it has been stated that only 4 out of 6 engines are operated in cruise. [25] However, this is changed. Now, all engines are used at all times. The reduced power loading resulting from this change increases the total efficiency by about 2.0%.

9.1.2. Optimization of Propeller Blade Geometry

There four power intensive phases of flight: take-off, climb, cruise, and cruise at high altitude. The take-off phase is simplified as the moment just before take-off at 65 [m/s], as this is usually the part of the take-off with the highest resistance. The climb phase is split in two: the start of the climb and the end of the climb. For each of these phases, XROTOR is used to design an optimized propeller for that phase. Next, each of these propellers is analysed in each flight phase. The result is presented in Table 9.3. In the upper part the flight conditions are displayed, in the lower part the resulting efficiencies in all flight conditions. Although the differences are not very big, it is evident that the highest average efficiency is obtained using a climb-optimized propeller, specifically end of climb. The blade reinforcements as described in Subsection 9.1.1 are not used here. However, this does not influence the trade-off.

Table 9.3: *Propeller Analysis for Different Phases of Flight*

	Take-off	**Cruise**	**Start of climb**	**End of climb**	**Altitude cruise**
Velocity [m/s]	65	120	92	107	140
Required power [MW]	max	3.786	6.066	4.909	4.403
Rotational speed [RPM]	830	820	830	800	750
Take-off efficiency	75%	68%	75%	75%	75%
Cruise efficiency	90.5%	92.5%	91.4%	91.6%	91.9%
Start of climb efficiency	84.7%	84.4%	84.9%	84.7%	84.2%
End of climb efficiency	86.5%	86.2%	86.9%	86.8%	86.4%
Altitude cruise[4] efficiency	88.8%	90.7%	90.1%	90.7%	91.1%
Total efficiency	85.1%	84.4%	85.7%	85.8%	85.7%

There are two things that stand out in the table: the 'max' for take-off and that not all rotational speeds are equal to 830 [RPM], as calculated in Table 9.1.1. The latter is simple to explain: this is the maximum rotational speed that XROTOR could process in calculations under these conditions. The 'max' for take-off is due to another limitation of XROTOR. It is only possible to enter the power the propeller *actually*

[4] Altitude cruise is cruise at 10,000 [ft]

generates, not the available power. However, the efficiency of the propeller also depends on the power it should generate. Therefore, the required power input should be manually and iteratively adjusted until the generated power matches the available power using $P_a = P_r/\eta$. Available power is taken as 8.00 $[MW]$ instead of uprated take-off power of 8.25 $[MW]$ of the TP400. This is so that there is enough power available for all other systems in the aircraft during take-off, as quantified in the Baseline Report [11]. Due to the iterative nature of the take-off efficiency determination, this cannot be determined as accurate as the other phases of flight. This is also the reason that these efficiencies have less significant digits. This is displayed in a wingloading diagram in Figure 11.1.

9.1.3. Optimization of Blade Performance

Even though the propeller blade is optimized, there is still room for optimization in the rotational speed of the propeller. First, it was found that the maximum possible rotational speed at the design point is 808 $[RPM]$. We know that in general, the peak efficiency RPM lies beyond the maximum possible RPM. However, this may not be the case for every phase of flight. It has been found that for take-off, a higher rotational speed is more efficient, around 910 $[RPM]$. The optimal rotational speed for cruise at low and high altitude is lies close to each other, namely 760 $[RPM]$ and 770 $[RPM]$ respectively. Therefore, it has been decided to cruise at 765 $[RPM]$. The loss of both phases not being at the exact optimal rotational speed is negligible. By doing this optimization, the take-off and low altitude cruise efficiency gain almost an extra percent of efficiency. High cruise efficiency does not gain very much: only around 0.1%.

9.1.4. Structural Design

While structural design considerations are not incorporated into the trade-off, it is very important to evaluate the structural feasibility. Namely, as already said in Subsection 9.1.1, the blades in Table 9.3 are structurally unfeasible. Maximum stresses are as high as 5,000 $[MPa]$. Completely unrealistic for any aerospace material to withstand. Thus, the reinforcements described in Subsection 9.1.1 are used. For analysis, the model has been simplified. The conservative estimate has been made that the base has an incidence angle of 90 [deg]. Structurally, the airfoil is analysed as a rectangle 70% of the original thickness. The bending moments are taken from XROTOR for the take-off scenario. Additionally, a safety factor of 1.5 is taken into account.

After this analysis, the best material for this blade has proved to be a carbon reinforced composite. This material is lighter than metal and more resistant against corrosion in marine environments[5]. The average density of these materials is 1420 $[kg/m^3]$[6]. These materials can withstand the required 200 $[MPa]$ for normal operations. The specific material composite and fibre layup directions are beyond the scope of this analysis however. In Figure 9.1 and Table 9.4 the resulting propeller blade is presented. The propeller is very different than the one on the A400M. The blade is thinner and unswept. Also, the blade has a larger twist. While there is some twist on the A400M blade, this is far from the 48.8 [deg] of the designed blade. Note that the blade mass is discussed in Subsection 9.1.4.

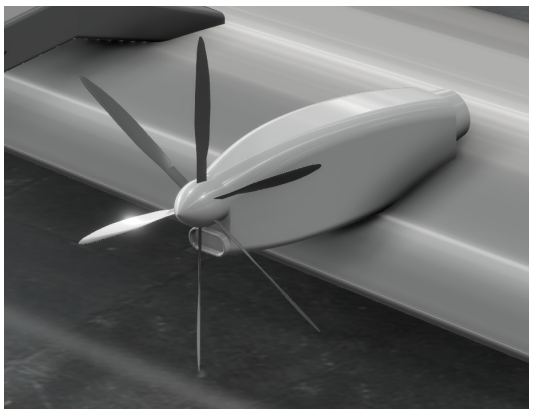

Figure 9.1: *Designed Propeller Blade*

Table 9.4: *Propeller Blade Parameters*

Parameter	Value	Unit
Disk area	27.77	$[m^2]$
Solidity	0.233	$[-]$
Number of blades	6	$[-]$
Propeller diameter	6.00	$[m]$
Hub diameter	0.40	$[m]$
Base chord	332	$[mm]$
Max chord	442	$[mm]$
Total twist	48.8	[deg]
Blade mass	49	$[kg]$

[5] https://www.tandfonline.com/doi/full/10.1080/17445302.2023.2229160? [cited 24 June 2025]

[6] https://www.matweb.com/search/datasheet_print.aspx?matguid=39e40851fc164b6c9bda29d798bf3726 [cited 17 June 2025]

In Table 9.5 the results are displayed, along with other important parameters. It is also visible that in all cases the required shaft power does not exceed the engine's available power. This means that also REQ-PWR.1 is met.

Table 9.5: *Final Parameters for the Propeller*

Parameter	**Take-off**	**Cruise**	**Start of climb**	**End of climb**	**High cruise**
Efficiency [%]	75.8%	91.4%	84.7%	86.8%	90.5%
Rotational speed [RPM]	910	765	808	808	765
Velocity [m/s]	65	120	92	107	140
Engine power [MW]	6.000	3.786	6.066	4.909	4.403
Base incidence angle [deg]	65.9	77.5	73.9	76.4	82.4
Disk loading [kN/m]	2.52	1.04	2.01	1.43	1.03
Advance ratio [−]	0.71	1.57	1.14	1.32	1.83

9.1.5. Limitations of the Process and Considerations

Sadly, there are some limitations to this process. The biggest limitation is the used software XROTOR. The main limitation is that larger data inputs are not possible. As a result, the workload of creating Table 9.3 is very high. For every cell, inputs have to be set manually one by one. Usually, these calculations are automated so that iterations due to changing aircraft parameters can be done quickly. Due to the reasons stated, this is not possible for the propeller. Still one iteration has been done for the propeller with the final values for velocity and power required. As this resulted in a only slightly higher efficiencies for cruise and take-off, the most critical phases of flight, it has been decided not to change the efficiencies used in the calculations. The reasoning for this is explained below.

To further optimize the propeller, different software should be used. As mentioned in the introduction, the propeller XROTOR designs is a minimum induced loss propeller. However, this does not mean that the propeller is the most optimal for the mission. To further improve the estimation, the model should incorporate aircraft geometry as well. Also the take-off performance is hard to quantify. Firstly because of the fact that there is no option to enter shaft power and secondly because the efficiency can only be examined at one speed at a time, while the efficiencies differ significantly over the take-off run.

In Table 9.5 the final parameters are presented, under which the base incidence angle. This ranges from 68.7 [deg] to 83.3 [deg]. However, this is not the total range of the incidence angle. The maximum incidence angle needs to be higher, to allow for higher speeds than the cruise speed. To determine this, further analysis is needed. The minimum incidence angle is determined by the reverse thrust case, as this is required in operations. However, XROTOR cannot work with inputs for power and velocity close to or below zero. Thus, a zero thrust incidence angle at zero velocity could also not be determined.

9.2. Engine Placement

The engine placement consists of three parts: longitudinal, lateral and vertical placement. The most important placement is vertical: this is because REQ-PWR.2 limits the design space. Then, the longitudinal and lateral placement can be chosen.

As described, the vertical placement will be determined first. From REQ-PWR.2 we know that the clearance from the water in sea state 0 should be at least 2.5 [m]. The lowest point on the wing is about 5 [m]. Assumed that the hub needs at least 1 [m] vertical clearance from the wing, the maximum radius of the propeller is 1.5 [m] if the engine is placed below the wing. This is unfeasible. Therefore, the engine should be placed on top of the wing. From the general dimensions of the TP400 it is known that the center of the hub is about 0.9 [m] from the bottom of the engine [7]. Thus, the center of the propeller is placed 90 [cm] above the top of the wing.

[7] https://www.rolls-royce.com/products-and-services/defence/aerospace/transport-tanker-patrol-and-tactical/tp400-d6.aspx [cited 2 June 2025]

The lateral placement is done using a method proposed by E. Torenbeek. It is proposed to have a propeller tip clearance of at least 10 $[cm]$ plus 1.65 $[cm]$ per 100 $[hp]$ of engine power [2]. As, the TP400 produces 11,000 $[hp]$[8], the tip clearance should be at least 191.5 $[cm]$. Therefore, the lateral placement of the first engine is 5.00 $[m]$ from the fuselage. The clearance between the engines is advised to be at least 23 $[cm]$. However, due to the large diameter of the propeller 75 $[cm]$ is taken as inter-tip clearance. Thus, the distance between two engines is 6.75 $[m]$.

The longitudinal placement is an arbitrary estimation that is based on sufficient clearance in front of the wing for the inner propeller. It is argued that it is desirable for the thrust to have the same longitudinal action point, so that the outer propeller is further in front of the wing than the inner, due to the wing sweep. The final longitudinal propeller positions, in terms of distance from the wing, are 2.8 $[m]$ for the inner, 3.1 $[m]$ for the middle and 3.5 $[m]$ for the outer propeller.

9.3. Battery & APU

This section discusses how the aircraft will be powered without running engines. Both, in normal operations, and in emergency situations. To ensure sustainable operations, REQ-SUS.2 was formulated. This requirement stated that the aircraft shall have zero CO_2 and NO_x emissions on water in normal operations. Here, on water operations are identified as the powering of all systems until starting the engines. So, starting the engines is not included in the on-water operations.

Table 9.1 contains the requirement REQ-SUS.2 regarding the APU/Battery that was established in the baseline report [11]. Ensuring this requirement is met, different solutions have been considered. A hydrogen powered APU and solar powered batteries emerged as top choices to provide power for on-water operations. However, hydrogen fuel cell APU's, such as Airbus' HyPower, were concluded to be too complex to integrate considering the crash safety of the aircraft. In addition, solar panels were deemed unfeasible for use in the salty marine environment. For the solar panels to function accordingly, many supporting systems, such as 'wipers' to clear the salt and the water from the panels, adding a lot of complexity and weight.

Therefore, it was decided to opt for lithium-ion batteries that power all necessary aircraft systems when the engines are not running during normal operations. Lithium-ion batteries have been selected due to their long life-span, high energy density and the fact that these batteries can be recycled[9]. These batteries must be fully charged before starting the mission. For maximised sustainability, it is advised to use electricity generated by renewable sources.

Table 9.6 provides an overview of the systems that must be powered by the battery, the minimum amount of time that power must be delivered and a conservative estimation of the actual power that the systems require.

The aircraft contains four inflatable buoys, each with a volume of about $226 \cdot 10^3 [L]$. Using forty compressors, with a capacity of $1050 [L/min]$ that require $750 [W]$ each, about $20 [min]$ are needed to fully inflate the buoys. Meaning that $30 [kW]$ must be provided by the batteries for this system. For the lights, a LED light was selected that consumed $30 [W/m]$. Assuming the aircraft would need $150 [m]$ of lighting, this system requires $4.5 [kW]$.

The estimated power and times of the remaining systems were based on the Hamilton Sundstrand APS 3240 APU. This is the APU that is used in the Airbus A400M, which uses the same turboprop engines as this design. With its similar cockpit and cargo door, it was assumed that the total power ($90 [kW]$[10]) of the APU is

[8] https://www.rolls-royce.com/products-and-services/defence/aerospace/transport-tanker-patrol-and-tactical/tp400-d6.aspx [cited 2 June 2025]

[9] https://www.epa.gov/hw/lithium-ion-battery-recycling#:~:text=Recycling%20Overview,more%20sustainable%20approach%20than%20disposal. [Cited 15 June 2025]

[10] https://www.prattwhitney.com/en/products/auxiliary-power-units [Cited 15 June 2025]

necessary to start one engine. Using this information and engineering judgement, a power estimation was completed on the systems, for which the results are documented in Table 9.6.

For the anchor, a winch motor is required to release and lift up the anchor. The power needed for the winch can be found by finding the force needed to lift up both the anchor and chain as well as the speed needed to achieve this. As seen in Section 8.3, it was concluded that the anchor and chain are 3470 [kg] combined. If assumed that the anchor should be lifted up within five minutes (if fully extended) and that the buoyancy force aiding the anchor in lifting up is the same as the weight of water right above the anchor. Then the power is simply the force multiplied by velocity, which means a power of 8.9$[kW]$. With a safety factor for both the time and power since many assumptions were made, the system can now use 12$[kW]$ total for 15 minutes. This has been added to Table 9.6.

For the cargo doors, two winch motors per door will be used for each door. The explanation of the system can be found in Section 10.2. The required power for all the motors is approximately 25 [kW] and it takes 45 seconds maximum to open the cargo doors. If this is done twice per mission, then a minimum of 3 minutes is needed.

The communications system includes all sensors described previously in Subsection 3.1.2.
Also, a 'Miscellaneous' category was added in Table 9.6. This functions as additional power that the battery can provide as a back-up. So, the battery will have the capacity to provide another 53$[kW]$ during a 1.5$[h]$ period. This could, for instance, be used to operate the cargo doors multiple more times, use more power to unstuck the anchor or re-inflate the floaters.

Table 9.6: *Systems Powered by Batteries During On-Water Operations*

System	**Time**	**Estimated Power**$[kW]$
Compressors	22 $[min]$	30
LED Lights	4.0 $[h]$	4.5
Communications (Radio, Sensors, etc.)	4.0 $[h]$	15
Air-Conditioning	4.0 $[h]$	30
Electric Motors (Cargo Door)	3.0 $[min]$	25
Starting APU	5.0 $[min]$	1.0
Anchor	15 $[min]$	12
Miscellaneous	1.5 $[h]$	53

For systems that must be active the entire time that the engine is off, a time period of 4 hours was chosen. This is because, REQ-CAR.3 specifies that all the cargo must be unloaded within 180 $[min]$[11], thus sizing the battery for 4 hours gives a 'safety net' of 1 hour.

Using the values in Table 9.6, the total energy that must be provided by the batteries can be calculated. After multiplying the time in seconds with the power in Watt, an initial energy estimation of 768,000$[kJ]$ was found. However, this number assumes 100% efficiency and a one-way mission. Hence, this number was then divided by 0.85[11] (typical efficiency of a Lithium-ion battery) and the operations that must be performed twice are multiplied by two (Compressors, Starting APU and Anchor), to account for a two-way mission. Giving a total energy of 963,177 $[kJ]$ needed. An additional 336,823 $[kJ]$ of battery energy has been accounted for in the 'Miscellaneous' category. After multiplying with the efficiency, 286,299$[kJ]$ is available for power. Meaning that 1,300,000 $[kJ]$ must be provided by the batteries.

Moreover, following the mass and volume estimation of the battery system (see Section 5.1), its placement within the aircraft had to be carefully considered. Several potential locations were evaluated, with the preferred option being above the waterline, at a higher position within the fuselage. This configuration offers enhanced protection in the event of a crash or hull breach, as it reduces the likelihood of water reaching the

[11] https://en.wikipedia.org/wiki/Lithium-ion_battery [Cited 15 June 2025]

battery system, thus mitigating the risk of fire or electrocution due to compromised battery integrity.

Therefore, it has been decided to place the batteries in the 'hump' that connects the wing to the fuselage. This placement maximises the distance to the waterline, thus minimising the risk of battery caused fire or electrocution. The shift in CG position due to the placement of the batteries at this location is marginal, which is another advantage. To ensure safety during emergency scenarios, the battery system will be enclosed in a reinforced metal casing, which is fully coated with the nanoparticle-reinforced epoxy coating for additional structural and environmental protection.

Furthermore, the Hamilton Sundstrand APS 3240 APU will also be integrated in the design for bleed air to start the engines and to provide emergency power to the power flight controls and flight critical systems when the engines fail. As this specific APU is also used in the A400M, it is also suitable for the application in this aircraft.

Since, the design incorporates a clam shell cargo door, it is not possible to place the APU at the back. Therefore, it has been decided to also place the APU within the 'hump', where the wing bridges into the fuselage, similar to the placement of the APU in the A400M.

9.4. Compliance Matrix Powerplant

In Table 9.7 the compliance matrix of the requirements given in Table 9.1. It is visible that all requirements have been met.

Table 9.7: *Compliance Matrix - Powerplant*

Requirement ID	Requirement Description	Compliance Justification	
REQ-PWR.1	The powerplant shall provide enough thrust to complete all phases of the flight.	The most limiting power is in take-off which is 20.9 $[MW]$. This is reached with the 6 propellers in the design.	
REQ-PWR.2	The lowest part of the engine shall be more than 2.5 $[m]$ above the water line in sea state 0 at MTOW.	The distance between the propeller tip and water level at sea state 0 is 4.7 $[m]$.	
REQ-PWR.3	The aircraft shall have two or more engines	The aircraft has 6 engines.	
REQ-SUS.2	The on-water operations of the aircraft shall be without any CO_2 or NO_x emissions.	The batteries used for on-water operations do not have emissions.	

10

System Architecture

10.1. Fuel System Layout

The fuel system is a critical subsystem of any aircraft. This section provides a schematic overview of the aircraft's fuel system layout, illustrated in Figure 10.1.

The figure shows the two primary fuel tanks, both located within the aircraft's wings. As stated in Table 5.3, the maximum fuel volume amounts to 46.5 $[m^3]$, which is equally distributed between the two tanks. However, the actual total volume of the fuel tank is higher, with each tank holding up to $51.2 \cdot 10^3$ litres, as detailed in Table 8.8.

The layout in Figure 10.1 demonstrates the system's redundancy. Each fuel line is equipped with its own dedicated pump and control valve to maintain pressurised flow independently. This redundancy ensures continued fuel distribution even under emergency conditions. Each engine is supplied by a separate fuel line directly connected to the tanks. Given that only four engines are required for cruise, the system can tolerate the failure of up to one-third of the pumps or lines without compromising cruise capability. This level of redundancy also allows safe take-off with a single fuel line or pump out of operation.

A cross-feed line is incorporated into the system to optimise aircraft stability during engine-inoperative scenarios. Additionally, two fuel dumping nozzles are included to enable rapid fuel discharge in the event of an aborted flight. This allows the aircraft to quickly reach its maximum landing weight in emergency situations, ensuring a safe and compliant landing. For safety, each engine is also fitted with a dedicated shut-off valve, allowing fuel flow to be terminated in the event of engine failure or fire.

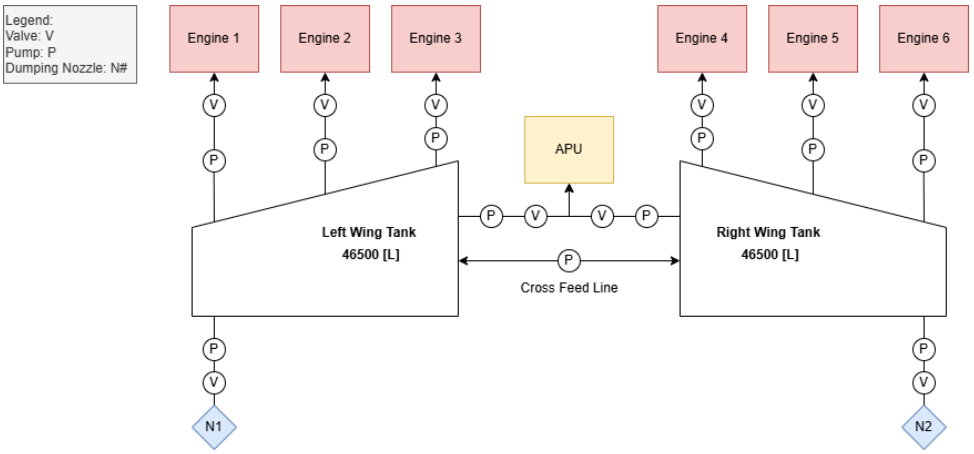

Figure 10.1: *Fuel System Layout*

10.2. Electrical System Layout

The electrical system is powered by the batteries mentioned Section 9.3. In Table 9.6, the different electrical systems were mentioned along with their estimated power. A diagram can be created to clearly show these different systems, which is Figure 10.2. The batteries, auxiliary power unit and engines are hooked onto the same electrical power system, Upon which, they can provide electrical power to each other, and other subsystems that draws power, as shown by the orange boxes.

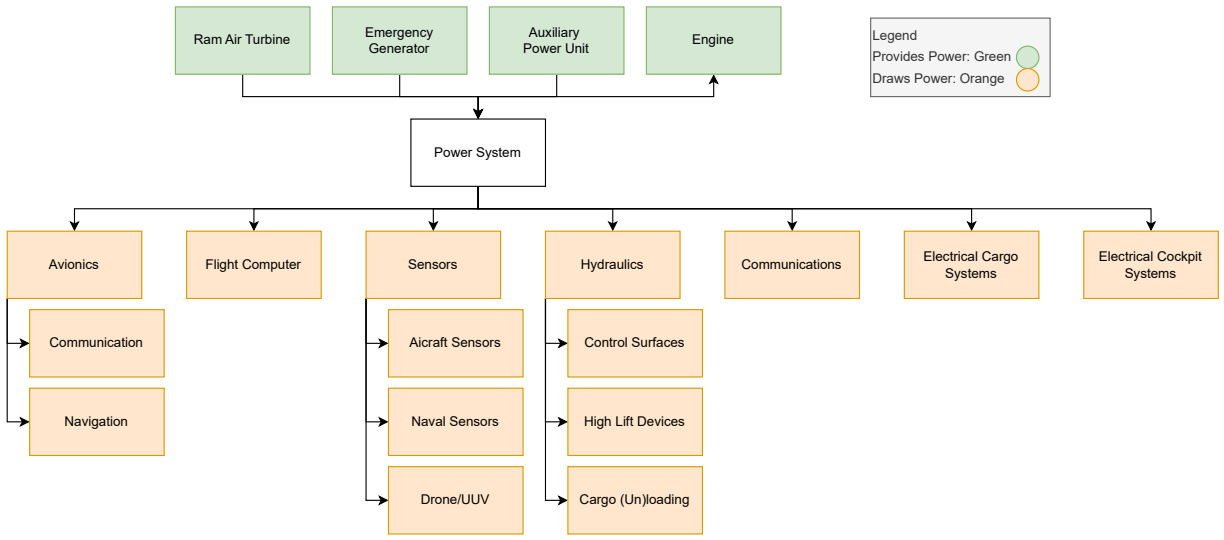

Figure 10.2: *Preliminary Electrical System Diagram*

A crucial part of the electrical system are the motors. These are used for both the cargo doors at the back as well as the anchor. The motors for the clam shell cargo doors were selected based on the predefined size and mass of the doors, which had already been established during the fuselage design phase. Rather than sizing the doors around available actuation systems, the motor selection process was driven by the selecting that the doors open at a controlled rate of 0.5 degrees per second during beaching operations. This specific speed was chosen to balance mechanical reliability, crew safety, and overall system control during cargo deployment. For the door opening mechanism, electric motor driven cable system have been selected. Cable drive mechanisms enables large speed reduction. It can also be routed through compact spaces to maximise leverage. Therefore, a small motor is able to lift very large cargo doors. From power and weight calculations calculations, it was determined that each door would weigh approximately 3100 [kg] and would require two motors each capable of delivering 4.405 [kW] of mechanical power. This rating ensures the system can perform consistently under normal and marginal conditions, providing the necessary force and control authority without overloading the drive components or compromising door alignment.

For the anchor motor, a larger power is required since it is raised much faster than the cargo door. It was established in Chapter 5 that the weight of the anchor and chain combined is 3470 [kg]. Calculating work done with a 50 [m] long chain and assuming constant buoyancy force, the power required is found to be 10 [kW]. This also assumes that the anchor can be put down or lifted up within 5 minutes. These values were considered during the battery estimations in Section 9.3 and thus no more extra batteries are required.

10.3. Hardware-Software Diagram

The hardware and software diagram in shows how the different aircraft systems interact with each other. In the diagram shown in Figure 10.3, the flight computer is the central node which collects all the information. It processes all the feedback data from the navigation sensors, power system and pilot inputs to arrive at the outputs for the control surfaces and the power setting, which are presented it in the output screen. The navigation sensors onboard the aircraft include, but are not limited to, those shown in Figure 10.3. Some other conventional aircraft sensors will be used in combination.

10.4. Hydraulic System Layout

The hydraulic system powers a lot of essential systems in the aircraft. It is displayed in Figure 10.4. As the aircraft does not have a landing gear and the cargo door is operated using an electrical motor, the systems powered by the hydraulic system are the flight controls (aileron, rudder, elevator) and the air-brakes and flaps. There are three hydraulic systems: the primary (green), secondary (yellow), and backup or standby

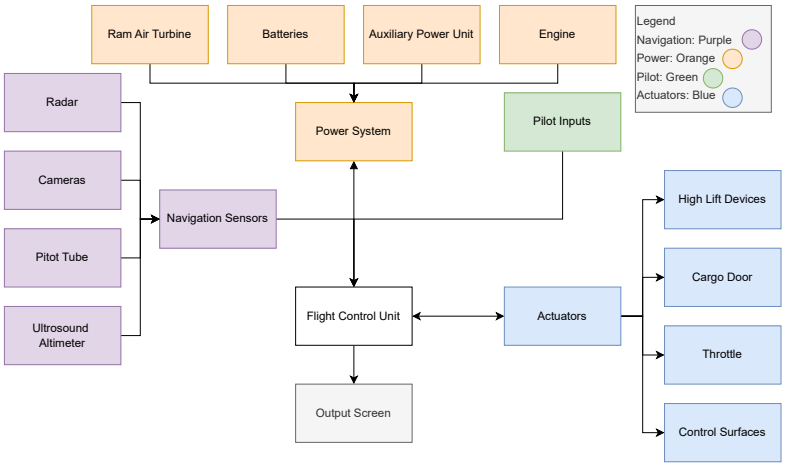

Figure 10.3: *Hardware-Software Diagram*

(blue). The latter will take over the hydraulic system in case of a double engine failure. The flight controls are primarily controlled by the green system and the air-brakes and flaps by the second system. The flight controls are the most critical system, so they have the most redundant system. The hydraulic system is based on a two engine aircraft, even though there are 6 engines to power the hydraulics. Though, it is highly unlikely that there are two individual engine failures on engine 3 and 4. If both engines are inoperative, chances are very high that the other engines are also inoperative, due to for example contaminated fuel.

All systems have roughly the same layout. It starts with the reservoir of hydraulic fluid. Then, the fluid is pumped by either an Engine Driven Pump (EDP), a Main Demain Pump[1] (MDP), or a Ram Air Turbine (RAT). After this, there is the ground supply. This is for the ground crew to pressurize a certain system without making use of the aircraft's systems. The accumulator smooths out spikes in the hydraulic pressure and can sustain pressure for a short while in case of a pump failure. The green and yellow system make use of a Power Transfer Unit. This system can exchange pressure without fluid intermixing. This makes it possible to keep both systems pressurized in case of an engine failure.

The system is pressurized to 3,000 $[psi]$, the same as the hydraulic system of the A400M[2]. Using the methods by Ian Moir and Allan Seabridge, flow rate has been estimated to be 100 $[L/min]$ for all systems [68]. This should allow all systems to operate the flight controls individually. Resulting from this, the reservoir for each system should be around 330 $[L]$.[3] Then, the power required to operate the hydraulic system is around 40 $[kW]$ per system, given an efficiency of around 85%[4]. Thus, in normal operation the maximum required power is around 80 $[kW]$.

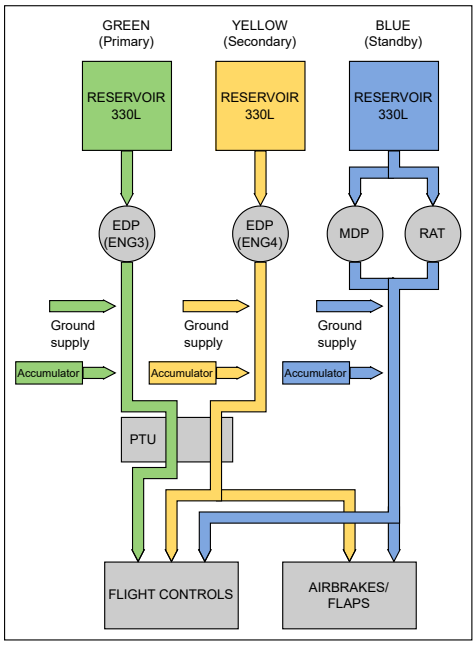

Figure 10.4: *Preliminary Hydraulics Layout*

[1] In this case this is an electrical pump.
[2] https://en.wikipedia.org/wiki/Airbus_A400M_Atlas [cited 16 June 2025]
[3] https://www.sealingandcontaminationtips.com/size-hydraulic-reservoirs-aircraft-hydraulic-systems [cited 16 June 2025]
[4] https://www.zeushydratech.com/knowledge-base/hydraulic-power-packs/hydraulic-power-unit-sizing/ [cited 16 June 2025]

11

Flight Performance

This chapter presents the analysis and optimization of the performance of the aircraft. It starts with the payload-range diagrams for multiple missions including the design mission, an obstacle avoidance mission and a maximum ferry range mission. The cruise strategy is then analysed to show the trade-off between cruise speed, range and endurance. This is followed by an analysis of the flight envelope, which defines the operational boundaries in speed and altitude, and then by a take-off performance analysis, including high sea state considerations. The climb and descent strategy is then presented, followed by the obstacle avoidance analysis, ensuring safety during fast low-altitude cruise. Additionally, the impact of high sea states on range performance is evaluated. Finally, the section concludes with a compliance matrix that maps all performance aspects against the defined requirements to ensure their fulfilment. Table 11.1 presents the relevant requirements covered in this chapter.

Table 11.1: *Relevant Requirements - Flight Performance [11]*

Requirement ID	Requirement Description	Category	Source
REQ-SUS.1	The fuel economy of the design aircraft over the course of the design mission shall be less than 0.14 $[L/tonnes/km]$.	Operational	REQ-CUST-SUST.1
REQ-CRU.2	The design range shall be at least 2000 $[nmi]$ carrying 90 $[tonnes]$ cargo in ground effect.	Operational	REQ-CUST-PERF.1 & REQ-CUST-PERF.7
REQ-CRU.2.1	The aircraft shall be capable of returning to at least the starting location with no payload of cargo without refuelling in the design mission.	Operational	
REQ-CRU.3	The ferry range shall be at least 6500 $[nmi]$ in ground effect without additional temporary fuel tanks.	Functional	REQ-CUST-PERF.9
REQ-CRU.4	The design cruise speed shall be at least 180 $[kts]$ in ground effect.	Operational	REQ-CUST-PERF.3
REQ-CRU.5	The aircraft shall be able to cruise in all sea states up to and including sea state 3.	Operational	REQ-CUST-SAFE.3
REQ-CRU.6	The aircraft shall be able to cruise at up to 10,000 $[ft]$ of altitude for 250 $[nmi]$.	Functional	REQ-CUST-PERF.2 & REQ-CUST-PERF.5
REQ-CRU.7	The aircraft shall be able to achieve a climb rate of at least 1,000 $[ft/min]$ with a payload of 90 $[tonnes]$.	Functional	REQ-USR-PERF.9
REQ-CRU.7.1	The aircraft shall be able to achieve a climb gradient of at least 3.2% with a payload of 90 $[tonnes]$.	Functional	CS-25
REQ-CRU.7.2	In the case of OEI, the aircraft shall be able to achieve a climb gradient of at least 2.4% + 0.3% times the number of engines beyond 2, with a payload of 90 $[tonnes]$ during second segment climb (S2).	Functional	CS-25

Requirement ID	Requirement Description	Category	Source
REQ-CRU.8	The aircraft shall have a stall speed in ground effect of at most 150 [kts].	Functional	
REQ-CRU.9	The aircraft shall have a stall speed of at most 160 [kts] at 10,000 [ft].	Functional	
REQ-CRU.10	The aircraft shall have a design range of 800 [nmi] while performing an obstacle avoidance manoeuvre of 250 [nmi] at 10,000 [ft] in each of the two mission legs.	Operational	REQ-CUST-PERF.6
REQ-TNL.1	The aircraft shall be able to take off in sea states up to and including sea state four.	Functional	REQ-CUST-SAFE.1 & REQ-CUST-SAFE.2
REQ-TNL.1.1	The aircraft take-off distance on water shall be no larger than 4 [km].	Functional	

11.1. Wing and Power Loading Diagram

In order to determine the required wing loading and power loading for the aircraft, we use Figure 11.1, which illustrates the key performance constraints. Each curve represents a different flight condition, such as take-off, climb, cruise, and landing, and their intersection defines the feasible design space. By analysing these constraints collectively, we can identify suitable values for both wing loading and power loading that ensure the aircraft meets its mission requirements. In this diagram, the selected design point is constrained by the take-off and climb rate requirements. This leads to final design values of $\frac{W}{S} = 4205$ and $\frac{W}{P} = 0.088$.

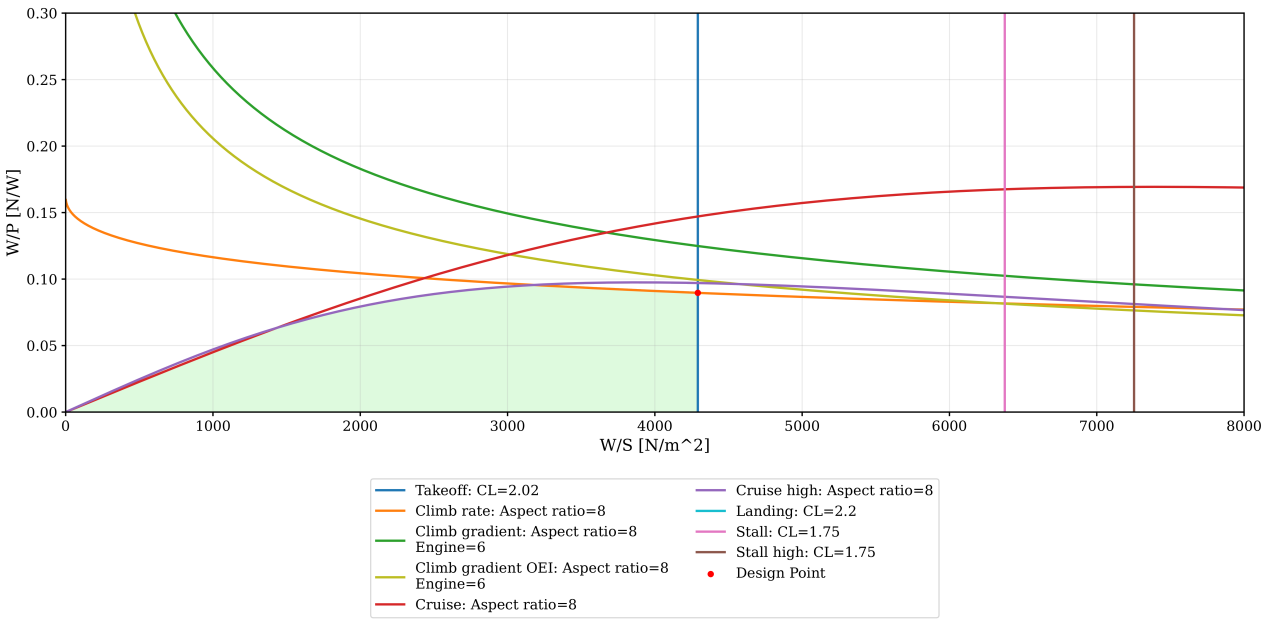

Figure 11.1: *Wing Loading and Power Loading Diagram with Design Point*

11.2. Payload Range

The payload-range diagram for a cargo Ground Effect Vehicle (GEV) is an essential tool to visualize the trade-off between the payload capacity and the achievable range. Unlike conventional aircraft, GEVs benefit from a reduced induced drag which results in an increased range. This allows for incredible cargo transporting capabilities.

The aircraft's requirements specify three target missions. REQ-CRU.2, the design mission (two-way); REQ-CRU.10, the obstacle avoidance mission (two-way) and REQ-CRU.3, the ferry mission (one way). All of these mission profiles are depicted below in Figure 11.2.

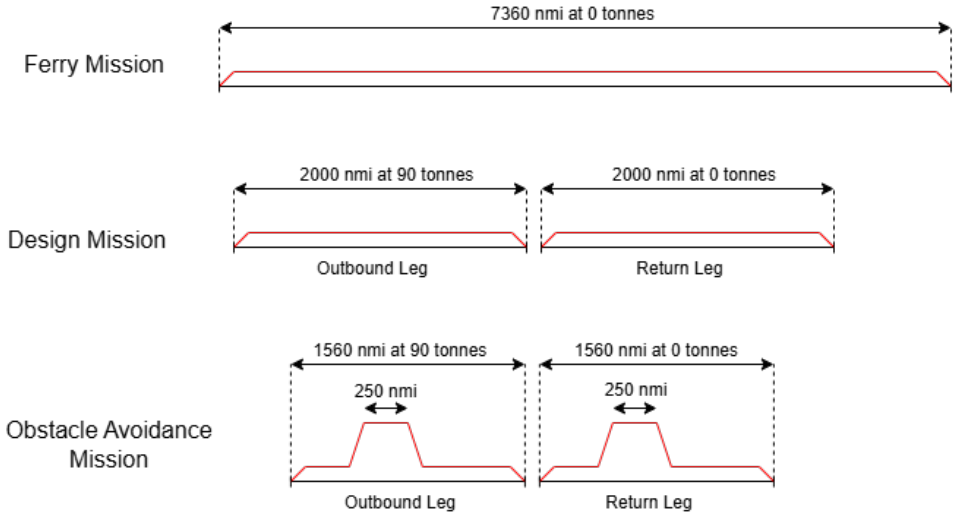

Figure 11.2: *Mission Profiles*

To construct the payload-range diagrams, the following assumptions were adopted: All missions have been flown at speed of maximum range (max L/D). Although this speed is not constant as the weight of the aircraft decreases, the corresponding maximum lift to drag does not vary as fuel is burnt. Moreover, all of the missions carry reserve fuel to have an extra range of 100 $[nmi]$ as required by REQ-CUST-SAFE.4. Finally, the maximum fuel tank size has been assumed to be 10% larger than the total fuel used in the design mission including reserve fuel. For each of the missions, a different payload range-diagram has been constructed, in order to ensure all of the requirements are met and analyse the flexibility of the cargo carrying capabilities of the aircraft.

11.2.1. Two Way Mission

Figure 11.3 shows the payload-range diagram for the two way mission with its corresponding profile shown in Figure 11.2 named "Design Mission". The range in the horizontal axis of the diagram shows the range of one of the two mission legs and the payload in the vertical axis shows only the payload for the first leg of the mission. After this, the payload is dropped at the chosen location and leg two of the mission is flown without payload. Notably, the design point with 2000 $[nmi]$ of range at 90 $[tonnes]$ of payload aligns perfectly with REQ-CRU.2 as the aircraft has been optimized exactly for this mission achieving an impressive fuel economy of 0.125 L/ton/km, beating the competition. The rest of the points with their corresponding fuel economies are summarised in Figure 11.2.

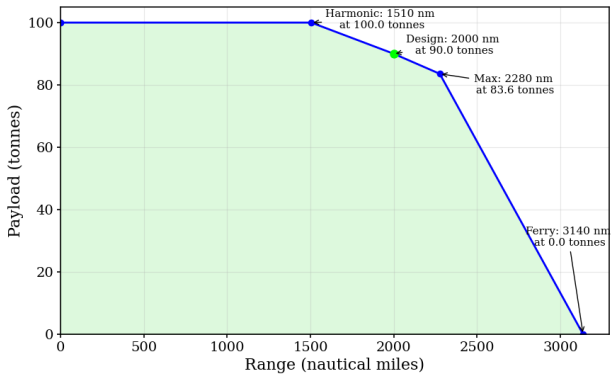

Figure 11.3: *Payload Range Diagram Two Way Mission*

Table 11.2: *Summary of Points in Two Way Payload-Range Diagram*

Point	**Payload** $[tonnes]$	**Range** $[nmi]$	**Fuel Economy** $[L/tonnes/km]$
Harmonic	100.0	1510	0.126
Design	90.0	2000	0.125
Max Range	83.6	2280	0.129
Ferry	0.0	3240	N/A

11.2.2. Two Way Mission with Obstacle Avoidance

Figure 11.4 shows the payload-range diagram for the obstacle avoidance mission with its corresponding profile in Figure 11.2 named "Obstacle Avoidance Mission". The axis of this plot are set exactly the same as in the design mission Figure 11.3. The obstacle avoidance mission includes a climb to 10,000 $[ft]$ a cruise at that altitude of 250 $[nmi]$ and a descent back to the original cruise height of 10 $[m]$. The important point to highlight here is the design point which achieves an impressive range of 1550 $[nmi]$ almost doubling what REQ-CRU.10 stated. The table summarizing the other performance points is shown in Figure 11.3.

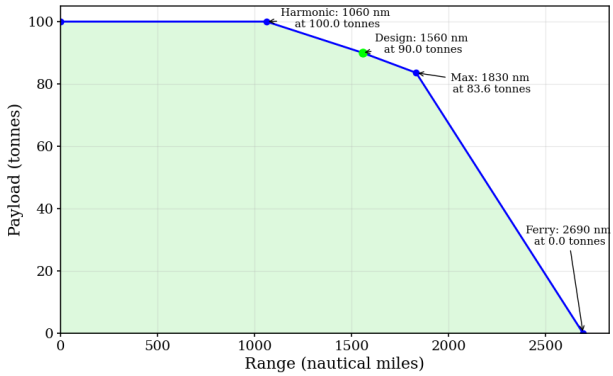

Figure 11.4: *Payload Range Diagram Obstacle Avoidance Mission*

Table 11.3: *Summary of Points in Obstacle Avoidance Payload-Range Diagram*

Point	**Payload** $[tonnes]$	**Range** $[nmi]$	**Fuel Economy** $[L/tonnes/km]$
Harmonic	100.0	1060	0.179
Design	90.0	1560	0.161
Max Range	83.6	1830	0.160
Ferry	0.0	2690	N/A

11.2.3. One Way Mission

Figure 11.5 shows the payload-range diagram for the one way mission with its corresponding mission profile in Figure 11.2 named "Ferry Mission". The horizontal axis shows now the range for the only leg in the mission and the vertical axis the payload for that leg. The key point is this diagram is the ferry point, the range is 7360 $[nmi]$ at 0 payload. This exceeds the required 6500 $[nmi]$ range specified in REQ-CRU.3. Figure 11.4 summarizes the rest of the results of the diagram.

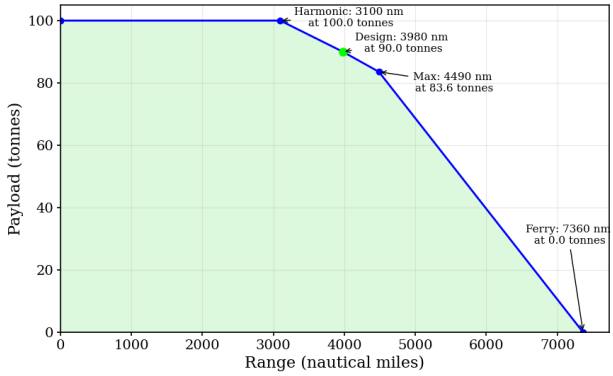

Figure 11.5: *Payload Range Diagram One Way Mission*

Table 11.4: *Summary of Points in One Way Payload-Range Diagram*

Point	**Payload** $[tonnes]$	**Range** $[nmi]$	**Fuel Economy** $[L/ton/km]$
Harmonic	100.0	3100	0.123
Design	90.0	3980	0.125
Max Range	83.6	4490	0.131
Ferry	0.0	7360	N/A

As can be seen in Figure 11.4, the fuel economy of each mission remains better than the economies obtained in the market analysis shown in Table 2.5. This shows that REQ-SUST.1 is met. For the one way ferry mission, the possibility of carrying fuel tanks in the cargo compartment is analysed. Assuming the weight of the fuel tanks to carry any amount of fuel is about 12% of the fuel weight, with 90 $[tonnes]$ in total, the aircraft is able to carry 80 $[tonnes]$ of fuel leaving 10 $[tonnes]$ for the fuel tank mass. With these parameters set, the aircraft can have a range of 12800 $[nmi]$ which is more than half the circumference of the Earth.

11.3. Cruise Strategy

Flying the entire mission at the speed corresponding to the maximum lift-to-drag ratio clearly results in the maximum possible range for the aircraft. However, it is also important to consider the time the aircraft is

airborne. Some scenarios might require fast delivery without significantly compromising range, such as in disaster response, and some other scenarios might require maximum endurance, such as in a surveillance mission. This section analyses the trade-off between cruise speed, range and time in the air.

It is important to present some of the cruise speed strategies available before performing the comparison: the optimum range speed (maximum L/D), the maximum endurance speed (minimum power required), the maximum speed (thrust-limited), and the stall speed. To calculate these speeds, both a two term drag polar and, as suggested by Anderson [69], an invariant power required with airspeed have been assumed. Each of these speeds as a function of aircraft mass can be seen in Figure 11.6 below. It can be observed that range, endurance and stall speed follow the same trend downwards, as to maintain a constant C_L, whilst max speed increases with weight. This is due to the fact that a lower weight results in less lift coefficient for the same speed, resulting in less induced drag which allows for higher speeds. Additionally, the maximum stall speed in ground effect can be extracted from the plot as 63 $[m/s]$ (123 $[kts]$) meeting REQ-CRU.8. At 10,000 $[ft]$ this speed is 73 $[m/s]$ (142 $[kts]$) complying with REQ-CRU.9.

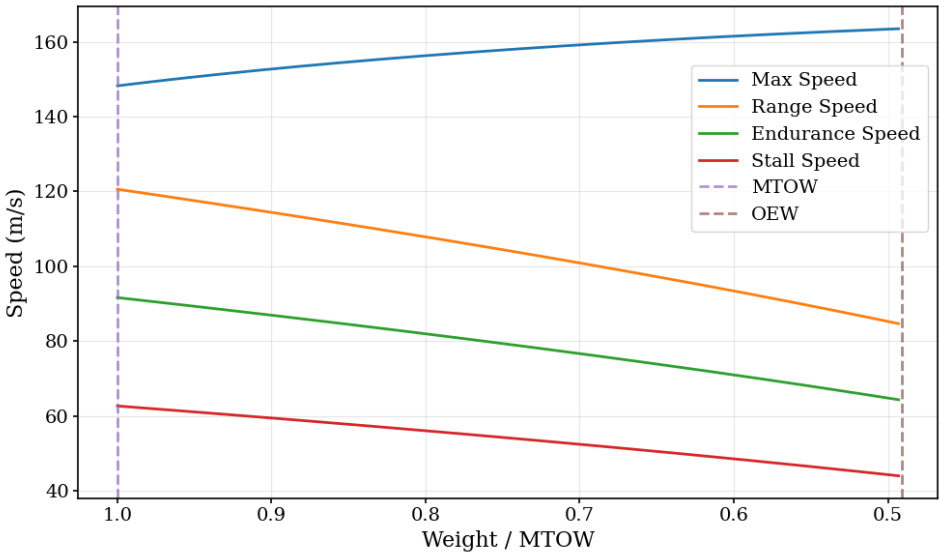

Figure 11.6: *Different Speeds as a Function of Aircraft Weight*

Reaching the disaster location as quickly as possible is one of the key operational goals. Therefore, the desired cruise speed for the outbound leg of each mission should be chosen as the speed which allows for shortest travel time whilst leaving fuel to be able to return to the origin at optimum range speed. To determine this, speeds which are multiples of the maximum range speeds are analysed and their corresponding range and time to destination are plotted in Figure 11.7. From the figure, the trade-off between cruise speed and range can be visualized. At 1.0 in the x-axis is the speed for maximum range, to the right of this point the range is always reduced but so does the time, depending on the mission to be undertaken a different cruise speed can be selected to arrive at the required location as quickly as possible. For example, if the destination is 1800 $[nmi]$ away, the cruise speed can be increased by about 35 [%] to arrive faster at the destination. All points in the range line, consume the same total mission fuel. Any combination of speed of the outbound leg and range which results in a point below this line can be flown.

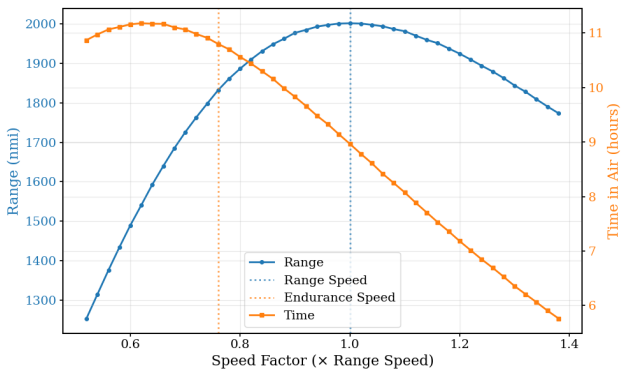

Figure 11.7: *Cruise Speed vs. Achievable Range and Time of the Outbound Leg in a Two Way Mission with 90 Tonnes of Payload*

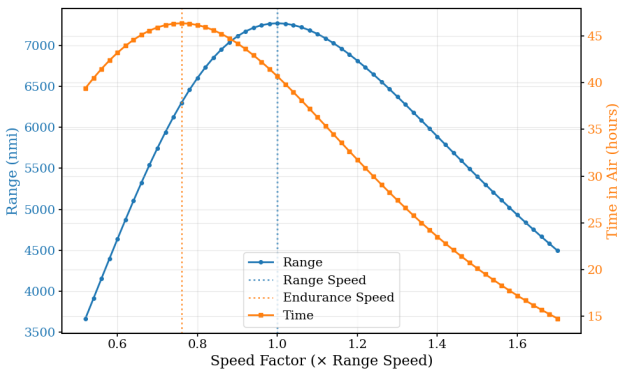

Figure 11.8: *Cruise Speed vs. Achievable Range and Time in a One Way Mission with no Payload*

Moreover, the speed corresponding to the longest time in air in Figure 11.7 does not coincide with the instantaneous speed for maximum endurance. This is because, in the plot above, the return leg is flown at maximum range speed not at maximum endurance speed. Below, in Figure 11.8, both legs use the same cruise strategy and the payload is reduced to 0, simulating a surveillance mission where maximum endurance is key. Now both maximum range speed and maximum endurance speed coincide with their respective peak values in the curves. The maximum endurance of the aircraft is impressive achieving more than 45 hours in the air. Naturally, this long time in the air will come with its corresponding difficulties that will be analysed in the future phase of the project. A summary of the final performance values and key cruise speed trade-offs discussed in this chapter is presented in Table 11.5, providing a concise overview of the most relevant figures for range and endurance under various operational scenarios. For the sake of consistency the entries about two way missions only specify the range and endurance of the first leg.

Table 11.5: *Summary of Range and Endurance*

Point	**Payload** [tonnes]	**Range** $[nmi]$	**Endurance** $[h]$
Max Range Two Way	90	2000	9.0
Max Endurance Two Way	90	1540	11.2
Max Range One Way	0	7360	40.6
Max Endurance One Way	0	6300	46.3

Cruise at High Altitude

The cruise strategy at high altitude follows the same approach as that used for low-altitude missions, with the equivalent airspeed maintained constant between the two. However, overall efficiency is reduced at higher altitudes due to the absence of ground effect. This results in higher cruise speeds and reduced engine efficiency which leads to overall higher fuel consumption. The performance impact of this manoeuvre are shown in the payload-range diagram in Figure 11.4.

11.4. Flight Envelope

The flight envelope defines the operational limits of an aircraft in terms of airspeed and altitude. This diagram also confirms that requirements REQ-CRU.6, REQ-CRU.7, REQ-CRU.7.1 and REQ-CRU.7.2 are met. To be conservative, this diagram has been constructed using MTOW as the weight of the aircraft. As Anderson [69] suggests, it has been assumed that the power of a turboprop engine is proportional to the air density raised to the power of 0.7 and constant with airspeed.

Figure 11.9 illustrates the altitude-velocity flight envelope for the aircraft. The envelope is bounded by the thrust limit in black and the stall limit in red. Additionally, two dashed lines are shown: The blue line V_x shows the location of the maximum climb angle speed for each altitude, and the green line V_y shows the speed for the maximum rate of climb. The resultant maximum climb angle is 7.0% at sea-level and the maximum rate of climb is 1090 $[ft/min]$, also at sea level. Analysis of the OEI case results in a maximum climb angle 4.2%. These values ensure REQ-CRU.7, REQ-CRU.7.1 and REQ-CRU.7.2 are met. At the top of the

figure, where these two lines meet marks the maximum altitude at which the aircraft can fly. It is over 16,000 [ft] meeting the 10,000 [ft] requirement set by REQ-CRU.6. A compliance matrix of the performance requirements is shown in Table 13.2.

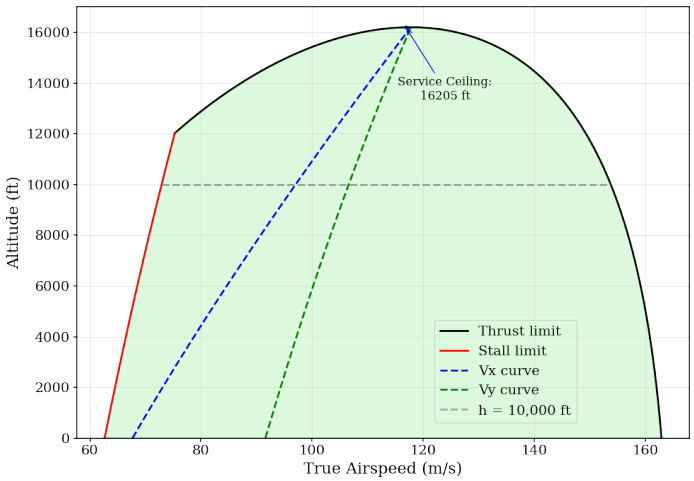

Figure 11.9: *Altitude-Velocity Flight Envelope*

11.5. Take-Off Performance

To estimate the take-off performance a model from Chinvorarat et al. has been implemented [70]. This model works by modelling all forces at each time step and numerically integrating to get the velocities and position of the aircraft at each time step. The modelled forces on this aircraft are: weight, lift, aerodynamic drag, buoyancy, thrust, friction drag by William Froude and water resistance. The forces working in the longitudinal direction are plotted against time in Figure 11.10, while the forces working in the vertical direction are plotted in Figure 11.11. The drop in aerodynamic drag and lift at 71 seconds is due to the retraction of the HLDs, causing a decrease in lift and induced drag. Numerically integrating this, results in the altitude over time plot shown in Figure 11.12 and the x position v.s. y position of the take-off phase shown in Figure 11.13. It can be seen the aircraft get out of the water after about 68 seconds. At this point the aircraft has travelled 1924 [m]. Which complies with REQ-TNL.1.1

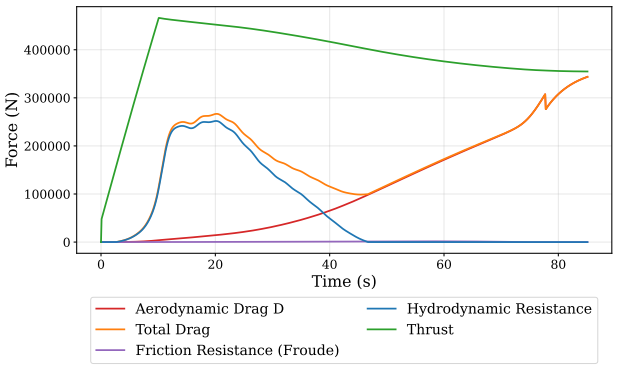

Figure 11.10: *Take-Off Performance (Y Position v.s. Time)*

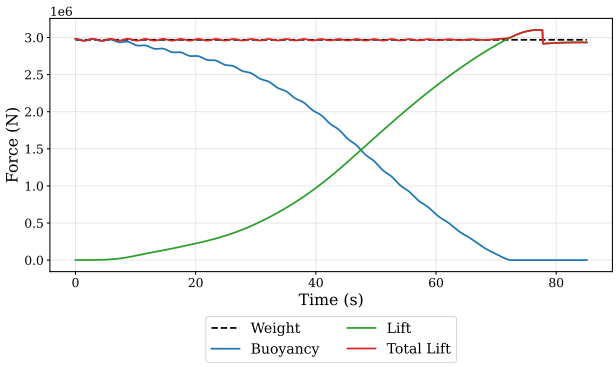

Figure 11.11: *Take-Off Performance (Y Position v.s. X Position)*

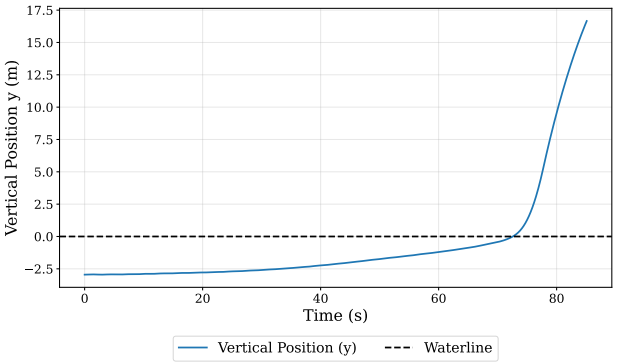

Figure 11.12: *Take-Off Performance (Y Position v.s. Time)*

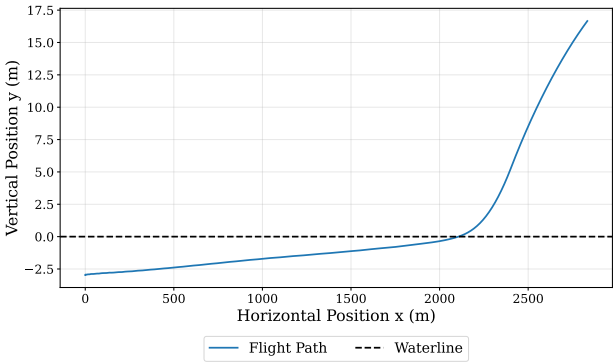

Figure 11.13: *Take-Off Performance (Y Position v.s. X Position)*

Sea State 4 Performance

In order to model the take-off performance in sea state 4, the same model is used with a factor of 1.75 on all hydrodynamic drag forces. This results in the following figures: Figure 11.14 shows the longitudinal forces, Figure 11.15 shows the vertical forces, Figure 11.16 shows the altitude over time and finally, Figure 11.17 shows the horizontal position against the vertical position. Note that the drop in lift and drag at 141 seconds is due to the retraction of the HLDs again.

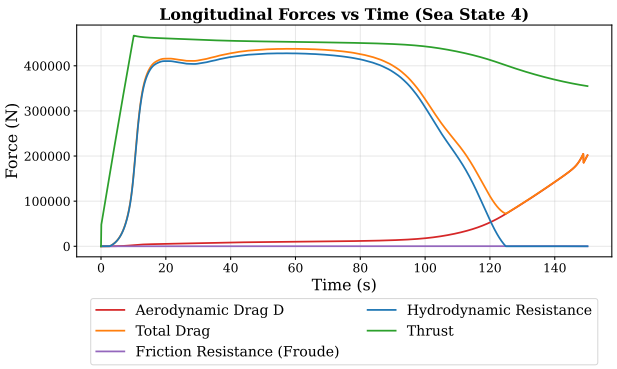

Figure 11.14: *Take-Off Performance Sea State 4 (Longitudinal Forces v.s. Time)*

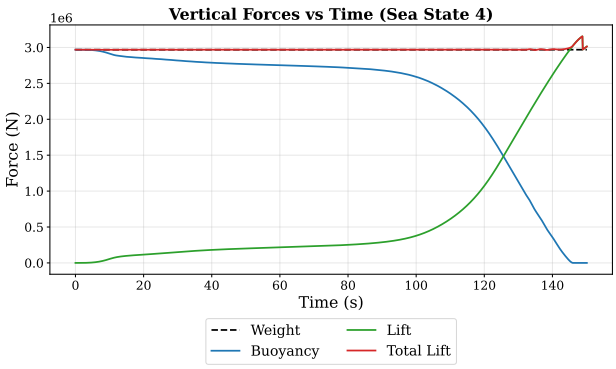

Figure 11.15: *Take-Off Performance Sea State (Vertical Forces v.s. Time)*

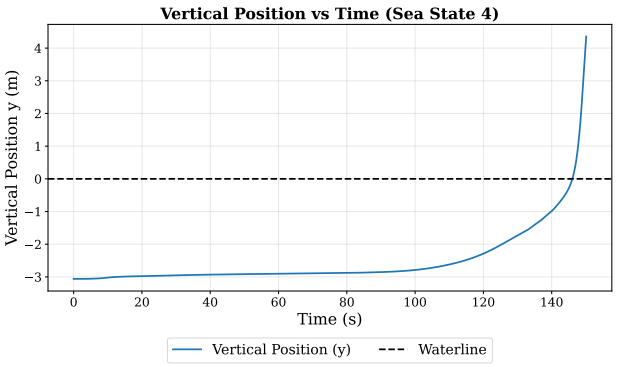

Figure 11.16: *Take-Off Performance Sea State (Y Position v.s. Time)*

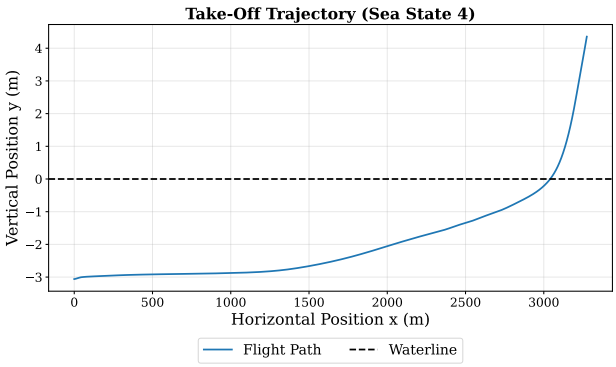

Figure 11.17: *Take-Off Performance Sea State (Y Position v.s. X Position)*

In Figure 11.17, it can be observed that the aircraft exits the water after 166 seconds. At this moment, the distance travelled is 3521 $[m]$, which demonstrates compliance with REQ-TNL.1.1. The required power for take-off, derived from the product of thrust and velocity, is calculated to be 20.9 $[MW]$.

11.6. Climb and Descent Strategy

Although the aircraft is intended to operate in ground effect during most of its cruise, it will have the capability to climb to 10,000 [ft] to avoid large obstacles. The climb and descent strategy is key to ensure the optimum range when performing the obstacle avoidance mission. These strategies will be analysed in this section.

Climb Strategy

Two main climb strategies are considered for this aircraft and mission. The choice depends on the type of obstacle being avoided. If the obstacle is detected with sufficient lead time, pilots follow the V_y line in Figure 11.9, which corresponds to the maximum rate of climb at each speed and altitude. Following this path ensures the aircraft reaches the desired altitude quickly and with high fuel efficiency.

The alternative strategy is the maximum angle of climb, or V_x, also shown in Figure 11.9. This strategy is used when an obstacle cannot be cleared using the maximum rate of climb. It maximizes altitude gain per unit of horizontal distance travelled.

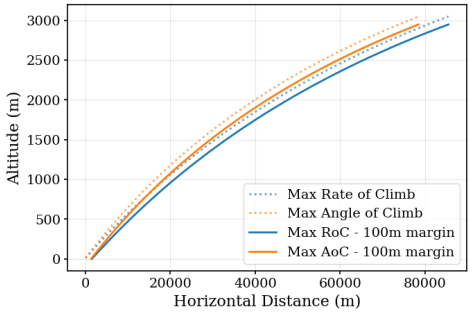

Figure 11.18: *Comparison Between Climb Strategies*

The decision on which strategy suits the best depends on whether the obstacle can be avoided using the more fuel-efficient V_y path. From Figure 11.18, it can be seen that the difference between the two is relatively small. Only if an obstacle lies in the region between both lines including a 100 [m] margin must the max angle of climb strategy be used. If the obstacle lies above both lines the aircraft must turn away from it. The margin is added to leave a safety distance between the obstacle and the aircraft.

Descent Strategy

The descent strategy that will be employed is this mission is straightforward. As the range is the parameter that is being maximised, the descent strategy will maximize horizontal distance gained per unit of altitude lost with the engines only on idle for safety reasons. It has been conservatively assumed that the engines do not produce any thrust during descent and the aircraft is gliding at it minimum glide angle. This descent strategy allows the aircraft to travel over 45 [km] while descending from 10,000 [ft] to about 30 [ft]. The average flight-path angle achieved is -3.64 [deg].

11.7. Obstacle Avoidance

Obstacle avoidance is a key design consideration for wing-in-ground-effect (WIG) aircraft, due to their low altitude and high speed over water. The small clearance from the surface to the bottom of the hull makes collisions with floating or semi-submerged objects potentially catastrophic. Reliable detection and avoidance strategies through onboard sensors are essential to ensure safe operation in maritime environments.

To avoid large obstacles, such as islands, the climb strategy described in Section 11.6 above will be employed. To avoid small obstacles there is two options. The first one is a 2.5g pull up over the obstacle. The second is a turn to avoid it laterally. Due to the low cruise altitude, which limits the maximum turn bank angle to 7.4 [deg], the strategy to turn sharply is climbing a few meters before turning. This, then makes this manoeuvre less effective but still usable in some specific situations.

Below in Figure 11.19 and Figure 11.20, the pull up and turn trajectories are plotted respectively up to a distance of 1000 [m] with some example obstacles that are possible to avoid. Additionally, the reaction time of the pilots and the detection instruments combined has been assumed as a conservative 5 seconds. It is worth noting that the plot starts at a distance to obstacle of 500 [m] for ease of visibility.

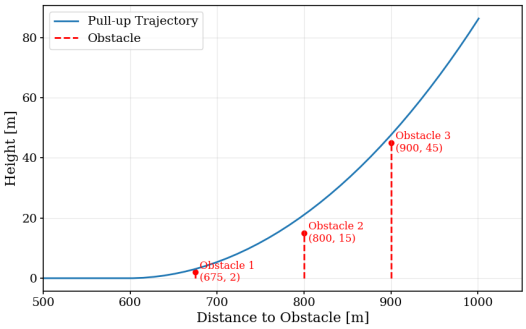

Figure 11.19: *Side View of Pull-Up Obstacle Avoidance Manoeuvre Trajectory*

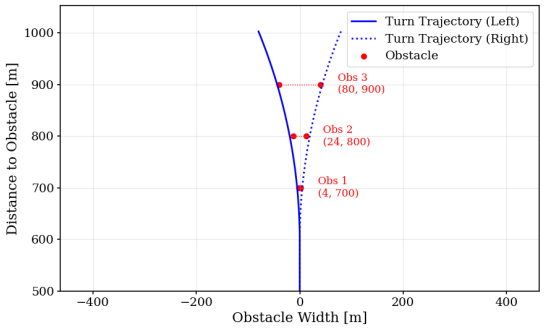

Figure 11.20: *Top View of Turn Obstacle Avoidance Manoeuvre Trajectory*

From Figure 11.19 and Figure 11.20 it is evident the aircraft must be able to detect reasonably small obstacles at a large distance. Obstacles as small as 2 [m] should be able to be detected at a distance of at least 675 [m]. Obstacles which are smaller than 2 [m] can be flown over at cruise altitude as the margin between the sea and the bottom of the aircraft is 2.5 [m].

The radar the equipped on the aircraft can easily detect objects of 0.5 [m^2] at distances of several nautical miles with a fast detection time of 1 second. These characteristics satisfy the required size above and thus allows the aircraft to avoid any obstacle of any size. If for any unlikely reason, such as extreme weather, the radar was unable to detect such small obstacles, the cruise height could be increased by any distance reducing performance but increasing safety.

11.8. High Sea State Performance

All missions shown above are shown in sea state 0 but it is essential to analyse the performance of the aircraft at different sea states. The effect the sea state has on the performance has been simplified using a number of assumptions. First, the cruise altitude is assumed to increase with the wave height to keep the same margin from the highest wave to the bottom of the hull. This height will be kept constant with high precision by using a number of ultrasound altimeters placed in different parts of the aircraft as stated in Figure 10.3. Moreover, the effect of the sea state in take-off has been approximated by increasing the amount of fuel this manoeuvre takes. Values for both the cruise altitude and the increase in fuel burn during take-off are shown in Figure 11.6.

Table 11.6: *Cruise Altitude and Relative Fuel Burn During Take-off for Different Sea States*

Sea State	h_w [m]	h [m]	Δ TO Fuel Burn [%]
0	0.00	10.00	+0.0
1	0.10	10.10	+3.3
2	0.50	10.50	+17
3	1.25	11.25	+42
4	2.50	12.50	+83

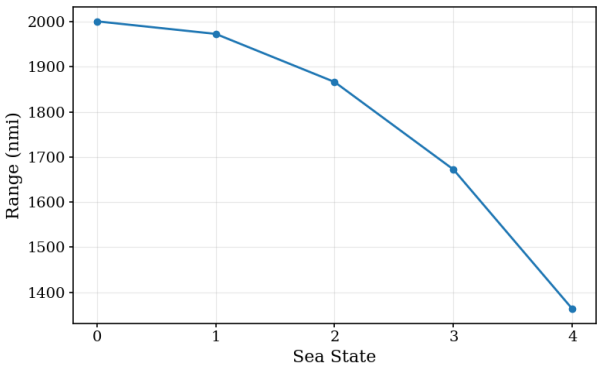

Figure 11.21: *Range of One Leg of Two Way with Varying Sea State*

Using the values from Figure 11.6, the maximum range for each sea state can be determined. The increase in cruise altitude significantly reduces the ground effect, leading to a lower lift-to-drag ratio. Additionally, the higher fuel consumption during take-off leaves less fuel available for the cruise phase, further reducing the overall range. It is worth noting that all missions use the same fuel as the design mission at sea state 0. The result of this calculations can be seen in Figure 11.21. As expected the design mission results in 2000

[nmi] of range in sea state zero and it decreases quadratically until sea state 4 in which the aircraft achieves a range of 1360 [nmi].

11.9. Compliance Matrix

The compliance matrix for the performance section can be found in Table 13.2 below:

Table 11.7: *Compliance Matrix - Performance*

Requirement ID	Requirement Description	Compliance Justification	
REQ-SUS.1	The fuel economy of the design aircraft over the course of the design mission shall be less than 0.14 [$L/tonnes/km$].	Achieved value of 0.125 [$L/tonnes/km$].	
REQ-CRU.2	The design range shall be at least 2000 [nmi].	Achieved value of 2000 [nmi].	
REQ-CRU.3	The ferry range shall be at least 6500 [nmi].	Achieved value of 7360 [nmi].	
REQ-CRU.4	The design cruise speed shall be at least 180 [kts].	Achieved range of 218–228 [kts] (outbound).	
REQ-CRU.5	The aircraft shall be able to cruise in all sea states up to and including sea state 3.	Confirmed capability in sea state 4.	
REQ-CRU.6	The aircraft shall cruise up to 10,000 [ft].	Confirmed capability to 16,200 [ft].	
REQ-CRU.7	Minimum climb rate of 1,000 [ft/min] with 90 [$tonnes$] payload.	Achieved 1,090 [ft/min].	
REQ-CRU.7.1	Climb gradient of at least 3.2% with 90 [$tonnes$].	Achieved 7.0%.	
REQ-CRU.7.2	OEI climb gradient of at least 3.6% during second segment climb.	Achieved 4.2%.	
REQ-CRU.8	Stall speed in ground effect at most 150 [kts].	Achieved 122 [kts].	
REQ-CRU.9	Stall speed at 10,000 [ft] at most 160 [kts].	Achieved 142 [kts].	
REQ-CRU.10	Range of 800 [nmi] with 250 [nmi] obstacle avoidance at 10,000 [ft].	Achieved 1560 [nmi].	
REQ-TNL.1	Take-off in sea states up to and including sea state 4.	According to the model developed by Chinvoratat et al., take-off can be achieved [70].	
REQ-TNL.1.1	Take-off distance on water shall be no larger than 4 [km].	Take-Off distance is 3521 [m].	

12

Budgets

With the complete design performance assessed in the preceding chapters, this chapter focuses on evaluating the key budgets of the aircraft. These include the mass budget, presented in Section 12.1, the power budget, discussed in Section 12.2, and the cost analysis, detailed in Section 12.3. The relevant requirements for budgets are displayed in Table 12.1.

Table 12.1: *Relevant Requirements - Operational Cost [11]*

Requirement ID	Requirement Description	Category	Source
REQ-SHC.7	The operational cost of the aircraft over the course of the design mission shall be less than 0.23 [$/$tonne/km$].	Constraint	

12.1. Mass Budget

This section presents the mass budget. This mass budget includes the masses of all components of the aircraft. In Figure 12.1, the mass budget is illustrated in a pie chart. The miscellaneous part of the pie chart includes electrical systems, furnishings, instrumentation and control systems.

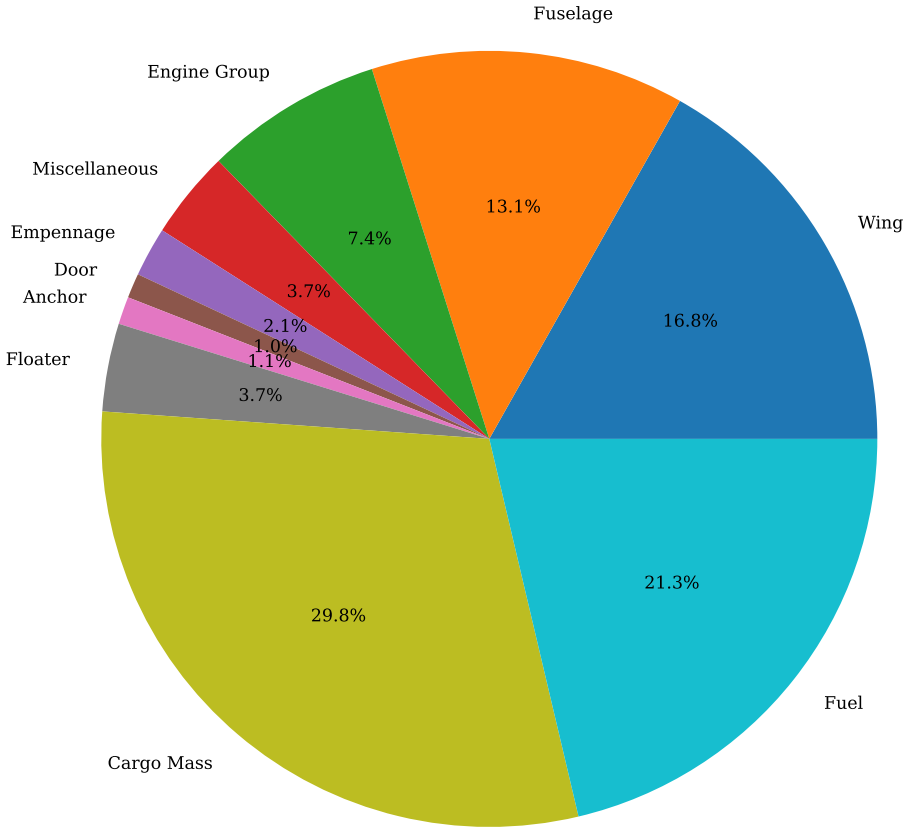

Figure 12.1: *Mass Budget*

In Figure 12.1 the mass budget is presented as percentages of the MTOM, which is 302,700 [kg]. From Figure 12.1 it can be seen that the cargo mass is the biggest contributor to the mass. This is followed by the fuel,

wing, fuselage and engine group, which are all above 5% of the MTOM. From REQ-SHC. it is stated that the MTOM needs to be lower than 500 [$tonnes$]. This means that the design has a margin of 39.6%.

It is well established in aircraft design literature that the weight of an aircraft tends to increase throughout the design process [71]. Scholz proposes a growth factor of 5% for wide-body, long-range aircraft with respect to the Operating Empty Weight (OEW)[71]. Similarly, Raymer[16] recommends applying an additional 5% margin to OEW to account for weight increases observed during the early years of production. When combined, these yield a total anticipated OEW increase of approximately 10%.
At the current stage of the design process, the estimated OEW is 1,448,239 [N]. Applying the combined growth factor results in an adjusted OEW of 1,593,063 [N]. Including the fuel and payload contributions, the resulting MTOW is calculated to be 3,104,538 [N], equivalent to approximately 316.5 [$tonnes$]. This value remains well below the specified MTOW constraint of 500 [$tonnes$], indicating acceptable margin for further development refinements.

12.2. Power Budget

In this section the power budget of the aircraft will be discussed. This power budget was made using estimations for power used in different aircraft [72]. From these different aircraft the A330-200 was chosen, since this aircraft is similar in mass. To tailor the power usages of the A330-200 to the power usage of WAVE some subsystems are changed. Namely the hydraulic components are discussed in Section 10.4 and will take up 80 [kW]. Next up the environmental control system does not need to take up as much power as the A330-200, since this flies at a significantly higher altitude. But WAVE still needs some power for environmental control. For this it was decided to take the power of the first climb phase. Taking all of this into account, the overall power estimate remains conservative. The Environmental Control System (ECS) power for the A330-200 includes systems such as galleys and in-flight entertainment, which are not present on WAVE, a military cargo aircraft. Additionally, the wing anti-icing system has not yet been finalized in this stage of the design. To maintain a conservative estimate, the de-icing power requirement has not been reduced, even though the A330-200 operates at higher altitudes than WAVE and thus requires more extensive de-icing.

The resulting power budget is presented in Figure 12.2 as a bar chart, covering both cruise and high-altitude phases. A detailed overview of the power consumption per subsystem is provided in Table 12.2.

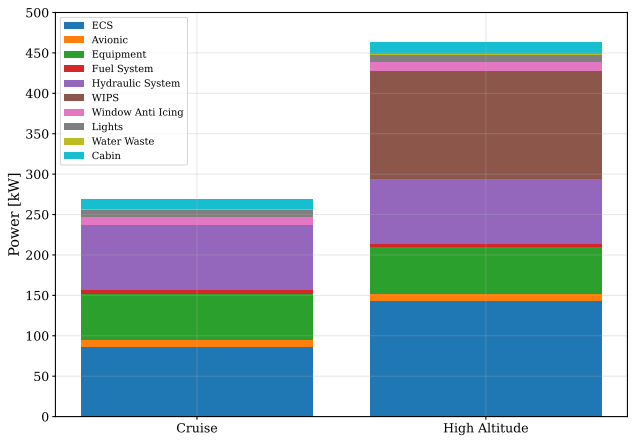

Figure 12.2: *Subsystem Power Budget*

Table 12.2: *Power Budget*

	Cruise	High Altitude
ECS	86	143
Avionic	10	10
Equipment	57	57
Fuel System	5	5
Hydraulic System	80	80
WIPS	0	133
Window Anti Icing	10	11
Lights	10	10
Water Waste	1	0
Cabin	11	14
Total	269	463

Note that Figure 12.2 presents the subsystem power budget layout during cruise phases, thus excluding engine startup power. In Figure 12.2 it can be observed that the Wing Ice Protection System (WIPS), Environmental control system (ECS) and equipment take up the most power. The total power of the cruise phase and high altitude phase are 269 [kW] and 463 [kW] respectively, as illustrated in Table 12.2. The increase in power of the high altitude operation is mostly attributed to the increase in power for ECS and WIPS. In Figure 12.3 it can be seen how the subsystem power adds up to the required power. Comparing the available power and required power it can be shown that the subsystem power has a slight effect.

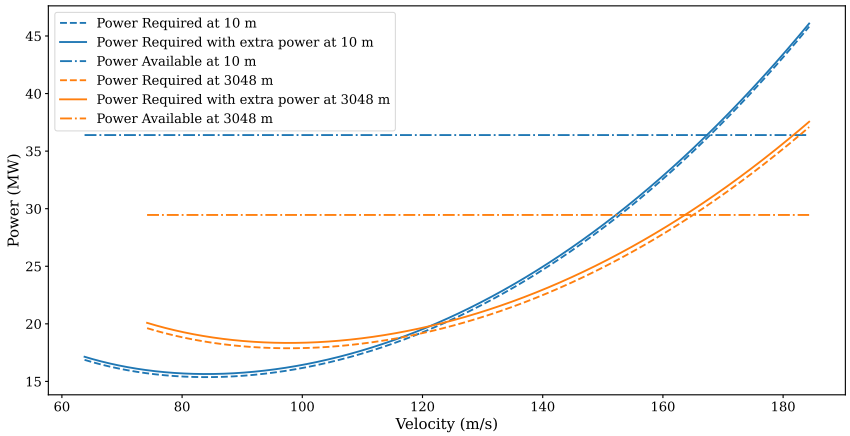

Figure 12.3: *Total Power Required*

12.3. Cost Analysis

This section contains an analysis on the cost of the aircraft. Not only on the unit cost, but also on the operating cost of the aircraft. In addition, the section also contains a Return on Investment (RoI) analysis about the aircraft. The requirement regarding the cost of the aircraft has been identified in Section 2.6.

12.3.1. Unit and Operational Cost Estimation

In order to estimate the unit costs of the aircraft, the DAPCA IV cost estimation method from Raymer's aircraft design book was used [16]. Due to the fact that the DAPCA IV method was created in 1986, all the costs were multiplied with a factor of 2.92 to account for inflation. The factor is based on the worth of 1$ in 2025 compared with 1986[1]. Table 12.3 contains the in- and outputs of the unit cost estimation. As can be seen in the table, the initial estimate of the unit cost of the ground-effect aircraft is about 278 million U.S. Dollars. The unit cost of the C-5 Galaxy in 2025 would be 475[M\$][2] and the C-17 Globemaster would cost 399[M\$][3]. Meaning that the unit cost of the design is very competitive within the market, with the initial estimations outputting that the design will be almost 200[M\$] cheaper than the C-5 and over 100[M\$] cheaper than the C-17.

Table 12.3: *Inputs and Outputs of the Unit Cost Estimation*

	Parameter	Value	Unit		Parameter	Value	Unit
Inputs	Empty Weight	$3.20 \cdot 10^5$	[lbs]	**Outputs**	Development Cost	239	[M\$]
	Maximum Speed	317	[kts]		Flight Test Cost	47.0	[M\$]
	Number of Engines	6.0	[−]		Material Cost	$1.10 \cdot 10^3$	[M\$]
	Engine Max Thrust	80	[kN]		Engine Cost	16.7	[M\$]
	Turbine Inlet Temperature	1450	[K]		Avionics Cost	10.0	[M\$]
	Engine Maximum Mach Number	0.84	[−]		Engineering Cost	$1.78 \cdot 10^3$	[M\$]
	Quantity	50	[−]		Tooling Cost	$1.06 \cdot 10^3$	[M\$]
	Flight Test Aircraft	4	[−]		Quality Control Cost	202	[M\$]
					Manufacturing Cost	$2.41 \cdot 10^3$	[M\$]
					Total Cost (all aircraft)	$1.50 \cdot 10^4$	[M\$]
					Unit Cost	278	[M\$]

Note that the these costs do not include pilot training cost or simulator costs. Then, the operational costs estimations of the aircraft. In Table 12.4, the inputs and outputs of the operational cost estimations are presented.

[1] https://www.in2013dollars.com/us/inflation/1986?amount=1 [Cited 13 June 2025]
[2] https://simple.wikipedia.org/wiki/Lockheed_C-5_Galaxy [Cited 13 June 2025]
[3] https://www.445aw.afrc.af.mil/About-Us/Fact-Sheets/Display/Article/679342/c-17-globemaster-iii/ [Cited 13 June 2025]

Table 12.4: *Inputs and Outputs of the Operational Cost Estimation*

	Parameter	Value	Unit
Inputs	Maximum Take Off Mass	$303 \cdot 10^3$	$[kg]$
	Design Fuel Volume	$8.5 \cdot 10^4$	$[L]$
	Density Sustainable Aviation Fuel(SAF)	0.76	$[kg/L]$
	Density Kerosine	0.82	$[kg/L]$
	Price SAF	1.18[4]	$[\$/L]$
	Kerosene Price	1.11[5]	$[\$/L]$
	Cruise Speed	120	$[m/s]$
	Number of Crew Members	4	$[-]$
	Yearly Flight Hours	600	$[h]$
	Design Payload	90.0	$[tonnes]$
	Design Range	$3.70 \cdot 10^3$	$[km]$
	Maintenance Man Hours per Flight Hour	40.0 [6]	$[h]$
	Labour Wrap Rate	140	$[\$/h]$
Outputs	Fuel Cost Design Mission	$1 \cdot 10^5$	[$]
	Crew Cost Design Mission	$1.71 \cdot 10^4$	[$]
	Maintenance Costs per Mission	$6.9 \cdot 10^4$	[$]
	Total Operational Cost per Mission	$1.17 \cdot 10^5$	[$]
	Operational Cost per Tonne Kilometre (without maintenance)	0.35	$[\$/tonnes/km]$
	Operational Cost per Tonne Kilometre (with maintenance)	0.53	$[\$/tonnes/km]$

From Table 12.4, it can be seen that the operational cost of the design is about 0.35 $[\$/tonnes/km]$ for the design mission. After providing the design mission characteristics of the C-5, C-17, and C-130 as inputs to the model, the resulting operational costs were calculated as 0.50 $[\$/tonnes/km]$, 0.46 $[\$/tonnes/km]$ and 0.40 $[\$/tonnes/km]$ respectively, taken from the market analysis in Section 2.6.

From these results, it can be concluded that the normal operating costs of the design are significantly lower than those of comparable cargo aircraft. Maintenance costs have been excluded from this comparison, as the design is intended to operate in a considerably harsher marine environment. Including these costs would unfairly bias the comparison, since maintenance demands are expected to be higher than for conventional military cargo aircraft. Furthermore, insurance costs have also been omitted due to the limited availability of data on government-owned assets. However, this exclusion does not compromise the comparison, as the aircraft is primarily intended for governmental use. Similar to the C-5, C-17, and C-130, which are also operated by governments, insurance costs are assumed to follow the same pattern and have likewise been excluded in their respective cost estimations. According to REQ-SHC.7, the operational cost of the design must be lower than that of comparable cargo aircraft operating in non-marine conditions, as discussed with the client. As shown in Table 12.4, the operational cost of the design, including maintenance, amounts to 0.53 $[\$/tonne/km]$. This is lower than the costs of the reference aircraft, though the margin is reduced when maintenance is included, as shown in Table 2.7. Nevertheless, the requirement stated in REQ-SHC.7 is satisfied, as summarised in Table 12.5.

[4] https://www.easa.europa.eu/en/domains/environment/eaer/sustainable-aviation-fuels/saf-market#first-trans-atlantic-flight-on-100-drop-in-sustainable-aviation-fuel [Cited 13 June 2025]

[5] https://www.globalpetrolprices.com/kerosene_prices/ [Cited 13 June 2025]

[6] https://www.aoe.vt.edu/content/dam/aoe_vt_edu/people/faculty/praj/avd-fundamentals/A6%20-%20Cost%20Considerations.pdf [Cited 13 June 2025]

Table 12.5: *Compliance Matrix - Operational Cost*

Requirement ID	Requirement Description	Compliance Justification	
REQ-SHC.7	The operational cost of the design aircraft over the course of the design mission shall be less than that of the C5, C17 and C130 in non-marine operating conditions[7].	The requirement is met, as the operating costs are estimated to be lower than the similar military cargo aircraft.	

Although the operating costs have been estimated to be lower than the competition, this aircraft is not designed to make an operational profit. As the aircraft will mostly be used by the military or Non-Governmental Organisations (NGO's) to provide disaster response. Due to the lack of paying customers during the aircraft's operation, making an operational profit is difficult. So, at this stage in the design process it is assumed that there will be no operational profit, only operational costs.

12.3.2. Return on Investment

To estimate the Return on Investment (RoI) of the design, one must determine an approximate price at which the aircraft can be sold and install a target on the number of units to be sold. In addition to the cost values in Table 12.3. This initial estimate can be made by looking at other military cargo aircraft. In Subsection 12.3.1, it was mentioned that the C-5 Galaxy would have a current unit cost of 475 [M\$] and the C-17 Globemaster would sit at about 399 [M\$]. In order to stay competitive with the unit cost of these aircraft, the ground-effect vehicle can be sold for a unit cost in the range of 350-400 [M\$], resulting in a profit of 70-120[M\$] per unit. A conservative quantity of 50 to be produced aircraft has been assumed (54 including test units). This number is conservative, because there were 131[8] units of the C-5 produced and 279[9] of the C-17.

After taking the total cost from Table 12.3(including the production of test aircraft), the total turn over (excluding the sale of test units) was calculated by multiplying the the assumed number of expected sold units with the lowest value in the range of estimated unit price. Resulting in a total turn over of $1.75 \cdot 10^4$ [M\$]. Inputting a total cost of $1.50 \cdot 10^4$ [M\$] and a total turn over of $1.75 \cdot 10^4$ [M\$] in Equation 12.1. A Return on Investment of 16.7% is found. Taking a unit price of 400 [M\$], a RoI of 33.3% is found.

$$\text{RoI} = \frac{\text{Sales Turnover} - \text{Total Cost}}{\text{Total Cost}} \cdot 100\% \tag{12.1}$$

Typical values for the RoI for mid-market businesses lie between 12-33% as stated by Jacob Orosz[10] (president of Morgan & Westfield). Meaning that the RoI values outputted by the estimations are realistic. For the cost break down structure of future events in the design process, refer to Chapter 15.

[7] After conferring with the client on 13-06-2025, it was agreed to change the formulation of this requirement w.r.t. the baseline report[11] to the presented requirement in Table 12.5

[8] https://en.wikipedia.org/wiki/Lockheed_C-5_Galaxy [Cited 15 June 2025]

[9] https://en.wikipedia.org/wiki/Boeing_C-17_Globemaster_III [Cited 15 June 2025]

[10] https://morganandwestfield.com/knowledge/business-valuation-return-on-investment-roi/#:~:text=Common%20multiples%20for%20mid-sized,the%20value%20of%20the%20business. [Cited 15 June 2025]

13

Sustainability Development Strategy

The majority of operations of WAVE are performed in ground effect. This enables significant increase in aerodynamic efficiency, therefore offering much better fuel efficiency and less emission than its competitors such as the C-5. Aside from this, the use of sustainable aviation fuel will also be included. Beyond simply the direct carbon emission from operation, the indirect carbon emission and environmental impact is also been investigated and discussed, which is elaborated in details within this chapter. The relevant requirements for sustainability are displayed in Table 13.1.

Table 13.1: *Relevant Requirements Flight Performance [11]*

Requirement ID	Requirement Description	Category	Source
REQ-SUS.3	Metallic parts of the aircraft that are uncoated against corrosion shall be recycled.	Functional	REQ-CUST-SUST.2

13.1. Environmental Impacts and Mitigation

Microplastic particles could enter the ocean via the nano epoxy coating used on this vehicle, similar to paint from ships and boats [73]. Effort must be made to minimize the amount of microplastics entering the ocean, as the vehicle skin ages and erodes. Detection and characterisation methods, such as those in the study by Gondikas[74] can be used to monitor microplastic leakage into the marine environment, and relevant steps could be taken for mitigation. New research together with marine scientists could be conducted in forming a new model for skin erosion, since a WIG vehicle's operational envelope possesses many differences with that of boats.

The coastal ocean floor could be affected by the wake of the vehicle. This leads to wash-away effect of sedimentation and degradation of habitat of coastal ocean floor. During taxi, a degradation to the ocean floor due to wake would be similar to that of the damage done by ships[75]. On the other hand, during high-energy events, such as take-off and landing, an even stronger wake would be generated, leading to potentially much greater damage to the ocean floor than those of slow moving ships. It is recommended to implement a minimum depth of water, below which high-energy events are not allowed. Research should be conducted on the effect of wake during take-off and landing across different seabed substrate types and compositions. Hence, offering a flexible minimum take-off/landing depth when operating in different geographic regions on earth. Such method will better protect local seabed integrity with respect to take-off and landing. For taxing in regions, such as coral reefs, the buoys could be deployed to reduce the submerged depth of hull, increasing distance between the wake origin and the seabed, further reducing the impact on seabed life forms through wakes.

13.2. Detailed End of Life Procedures and Recycling Plan

At the end of life, the aircraft will not be simply discarded. Rather, its leftover values will be extracted as much as possible. Mostly through engine recycling of structural components and material recycling.

13.2.1. Engine Recycling

Though not stated explicitly through available public information, the engines would likely be largely recycled up to a significant level. This is based on the different programs from its manufacturer and contribu-

tors. Programs such as Revert [1] from Rolls Royce, one of the manufacturers within Europrop International, offered a rate of up to 95% of a used aero engine to be reused and recycled. This is an inherent advantage on sustainability performance offered by the engine selection.

13.2.2. Airframe and Fuselage Recycling

For the end-of-life solution of fuselage, re-purposing is advised instead of recycling for raw material. This is because removing the corrosion resistant paint will emit toxic gas into the atmosphere, while requiring significant amount of energy.

Re-purposing actions could include turning the fuselage into emergency shelters, temporary buildings, as well as sea-side hotels, restaurants and storage containers. The large hull volume of the vehicle provides such opportunities. Ultimately, the exact purpose is up to the costumers. It should be noted that since fuselage has a hull shape, the bottom of the hull forms a line contact with the ground, it could not be placed stable on its own without additional structural modifications. One method is to use additional support beams on the side of the fuselage. Aluminium alloys possesses good machinability and can be easily drilled through for fastener holes for installation of such beam structures. On the other hand, the bottom of the hull could simply be cut off to provide stability. However, this is not recommended as it is a more energy intensive process, requiring either laser cutting or water-jet.

13.2.3. Uncoated Structural Components Recycling

The uncoated structures will be re-cycled as raw materials. Since, these uncoated components are made out of materials, such as titanium and stainless steel, they could withstand the corrosion due to chloride and does not need coating. Within the stainless steel family, austenitic stainless steels, such as 316L are the recommended material due to their high chloride and nickel content. They, however, still present a certain level of risk to stress corrosion cracking and pitting. These types of corrosion introduce metallic elements within ocean minerals into small portions of the alloy, and affect material impurities during re-melting process. Techniques, such as chlorination and sulfurisation could be used to eliminate unwanted metallic elements[76]. The same technique could also be used to remove original alloying elements that are unwanted. Therefore, the recycled alloy could be used to form different alloys. For titanium alloys, producing new materials is an extremely energy intensive process. Recycling will massively reduce this energy expenditure. Titanium is particularly contaminated with oxygen content, due to the high affinity between the two elements. Titanium oxide is what gives the material its corrosion resistance, however, when re-melted into raw material, this brittle ceramic will easily degrade material toughness. Methods introduced in [77], such as hydrogen plasma arc melting can be used for deoxygenation of recycled titanium.

13.2.4. Compliance Matrix Sustainability

Table 13.2: *Compliance Matrix Sustainability*

Requirement ID	Requirement Description	Compliance Justification	
REQ-SUS.3	Metallic parts of the aircraft that are uncoated against corrosion shall be recycled.	The requirement is met, as recycling the materials selected for uncoated components is common industrial practice and is very realistic.	

[1] https://www.rolls-royce.com/media/our-stories/discover/2017/revert.aspx [Cited 18 June 2025]

14

Verification & Validation

In this chapter, the plan for verification and validation is outlined and partly executed, as some steps are not possible within the time constraints and available resources. The V&V consists of model verification & validation (in Section 14.1) as well as the product verification which can be seen in Section 14.5. The final aircraft requires a far more detailed V&V plan and execution, but this is beyond the scope of this report.

14.1. Model Verification

The verification of the design calculation framework model is outlined in this section. It comprises of three primary components. The first component involves unit testing of the underlying code to ensure that individual functions and modules are operating correctly and that expected outputs are produced under a range of input conditions. This step is considered critical for the identification and resolution of implementation errors.

The second component consists of a sensitivity analysis, through which the impact of variations in key assumptions and design parameters on the model's outputs is assessed. This analysis is deemed essential for the evaluation of the robustness of the model and for the identification of parameters that significantly influence model behaviour. Lastly, system-level tests are conducted on the analytical models developed by the team. For example, the structural analysis model is applied to a simpler structure for which hand calculations are available. When close agreement between the model results and hand calculations is observed, the model is considered to be verified.

The unit testing strategy is designed to systematically verify the correctness of all code components by categorizing them based on their function. Functions are classified into two types: those implementing model logic (e.g., data handling) and those defining physical relationships. For model logic functions, tests are focused on the verification of correct handling of input/output formats, boundary conditions, and error cases. These tests ensure that the logical flow and data manipulation comply with the model specifications. For physical relation functions, tests are carried out to validate the mathematical correctness of implemented formulas by comparison of computed outputs against known analytical solutions or values from literature. Where applicable, edge cases (e.g., zero values, discontinuities, or asymptotic behaviour) are also tested. Each code file is accompanied by a dedicated test script to ensure full coverage of every function, enabling the detection of bugs or implementation errors.

During unit testing, for example, incorrect unit conversions in determining the control derivatives were found, leading to issues in evaluating the eigenmotions. Due to the testing, the team was able to promptly identify and correct these errors, preventing the propagation of inaccuracies throughout the analysis. Similarly, boundary condition handling in the aerodynamic force computation was thoroughly tested, revealing scenarios where input parameters at their physical limits caused unexpected model behaviour. These cases were addressed by refining the input validation routines and improving error messaging. Collectively, these testing activities have enhanced the robustness and reliability of the model, reducing the risk of hidden bugs and increasing confidence in the subsequent system-level analyses.

14.1.1. Model System Tests

In this section, system tests are performed on the structural analysis code to verify correct implementation. This is done by hand calculating the corresponding implementation, if necessary on a simpler problem. To verify the structural analysis code, a system test is performed on the fuselage structural analysis class and

the wing analysis class.

For the fuselage, the structure presented in Figure 14.1 is evaluated by hand and implemented in the code used to perform the structural analysis outlined in Subsection 8.4.2.

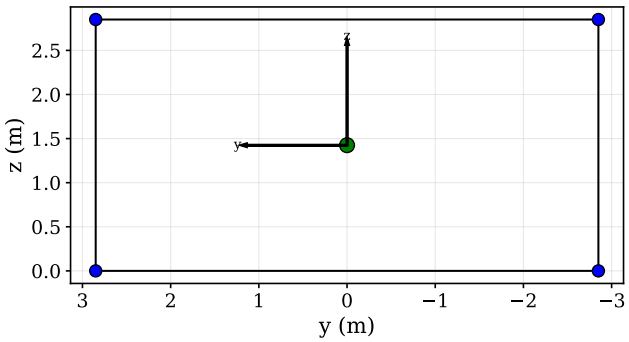

Figure 14.1: *Simple Idealised Beam Section to Verify Fuselage Analysis*

As shown in Figure 14.1, the centroid is located precisely at the midpoint, as expected for a fully symmetric structure. This confirms the correct implementation of the defined geometry. Table 14.1 presents the input parameters used in the hand calculation, following the methodology described in Subsection 8.4.2, alongside a comparison of the resulting shear flow distribution and skin thicknesses from both the hand calculation and the computational model.

Table 14.1: *Input and Output Parameters for Fuselage Structural Analysis Verification*

Inputs			**Outputs**			
Parameter	**Value**	**Unit**	**Parameter**	**Hand-Calc**	**Model Output**	**Unit**
B	6000	[mm^2]	q_{12}	0	0	$[N/m]$
y_{B1}	2.85	[m]	q_{13}	-1754386	-1754386	$[N/m]$
z_{B1}	2.85	[m]	q_{34}	1754386	1754386	$[N/m]$
y_{B2}	-2.85	[m]	q_{42}	0	0	$[N/m]$
z_{B2}	2.85	[m]	t_{12}	3.61	3.59	[mm]
y_{B3}	2.85	[m]	t_{13}	3.68	3.68	[mm]
z_{B3}	0	[m]	t_{34}	3.61	3.59	[mm]
y_{B4}	-2.85	[m]	t_{42}	3.68	3.68	[mm]
z_{B4}	0	[m]				
V_z	10	[MN]				
M_y	5	[MNm]				

As evident from Table 14.1, the results from the computational model closely match those obtained from the hand calculations. The minor differences observed in the skin thickness values are negligible and fall within acceptable numerical tolerance. Consequently, the fuselage structural analysis model is considered verified. While more extensive testing could include validation of stress calculations, this is deemed outside the scope of the current report. Given that the stress evaluation involves straightforward geometric formulae, of which the implementations have already been verified, further testing is not pursued.

Similarly to the verification of the fuselage model, the wing box analysis model is also verified based on a simpler structure. This simplified wingbox structure is shown in Figure 14.2, where the airfoil is modelled as a square, with a rectangular wing box.

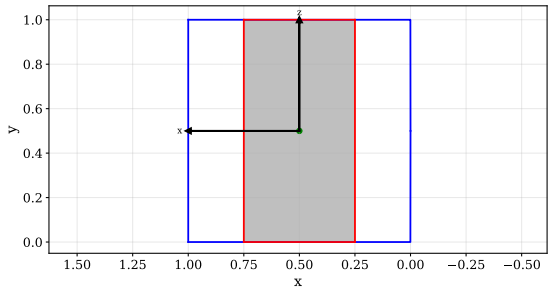

Figure 14.2: *Simplified Wing Section Structure for Verification.*

It can be seen in Figure 14.2 that the centroid is the midpoint of the structure, again as expected since the structure is fully symmetric. Thus, the geometry is implemented correctly. The geometry parameters for this structure are given in Table 14.2, where they are used to calculate the moments of inertia of the section.

Table 14.2: *Input and Output Parameters for Wing Box Structural Analysis Verification*

Inputs			**Outputs**			
Parameter	**Value**	**Unit**	**Parameter**	**Hand-Calc**	**Model Output**	**Unit**
$\frac{x_{\text{front spar}}}{c}$	0.25	[−]	I_{xx}	1.1×10^{-3}	1.1×10^{-3}	$[m^4]$
$\frac{x_{\text{rear spar}}}{c}$	0.75	[−]	I_{yy}	8.1×10^{-4}	8.1×10^{-4}	$[m^4]$
t_{skin}	1	[mm]	I_{xy}	0	0	$[m^4]$
t_{spar}	1	[mm]				
t_{wing}	1	[mm]				
n_{cells}	1	[−]				
Side Length	1	[m]				
	5					

It can be seen in Table 14.2 that the outputs of the hand calculation match those of the model. Following the same logic as for the verification of the fuselage code, the correct implementation of the geometry is key, as the equations to evaluate the stresses based on this geometry have been verified along the way. Therefore, the wing structural analysis model is deemed verified. Similar verification methodologies were applied to the empennage, control surfaces, and wing sizing code. To maintain conciseness and focus, the detailed results of these procedures are omitted from this report. However, these models can be considered verified as well.

14.2. Model Validation

In this section, the validation of the design calculation framework model is outlined. To ensure the model's validity, it is applied to a set of existing, comparable aircraft, such as the C-130 and C-5. The relevant input parameters are derived from the design missions of these aircraft, and the model is used to predict outputs such as MTOM, wing area, and empennage sizing. These results are then compared against actual aircraft data. Model accuracy is evaluated using the average relative error across the outputs; if this error remains below 10%, the model is considered sufficiently accurate for that parameter. Due to the lack of detailed input data for the aerodynamic, structural, and systems-level characteristics of these reference aircraft, validation is limited to the initial weight estimation. Specifically, the model's MTOM predictions for the C-130 and C-5 are compared with known values, providing a simplified yet meaningful assessment of its predictive performance. For this validation, consider Table 14.3 for the results.

Table 14.3: *Inputs and Output for Class I MTOM Validation. Inputs are obtained from the Baseline Report [11, p.11]*

	Parameter	C-130	C-5	Unit
Inputs	Range	5,245	3,981	$[km]$
	SFC	$9.22 \cdot 10^{-8}$	$8.9 \cdot 10^{-6}$	$[kg/J]$ or $[kg/Ns]$
	Cruise Speed	150	221.2	$[m/s]$
	Propulsive Efficiency	0.82	–	$[-]$
	Lift-to-Drag Ratio	14.13	11.28	$[-]$
	Payload	15,876	122,500	$[kg]$
Output	Predicted MTOM	82,322	289,641	$[kg]$
	Actual MTOM	70,305	381,018	$[kg]$
	Relative Error	17%	24%	

As shown in Table 14.3, the relative errors in MTOM prediction for both the C-130 and C-5 exceed the initially targeted margin of 10%. However, for the purpose of validating the initial weight estimation model, this margin is reconsidered. For instance, the initial MTOM estimate for the design aircraft was 258.9 $[tonnes]$ [25, p.35], whereas the final value reached 302.7 $[tonnes]$, a deviation of approximately 15%. This illustrates a fundamental aspect of the design process: various subsystems (e.g., structural and fuselage design) influence the aircraft's weight in ways not fully captured by empirical models such as those used in Chapter 5.

With this context, the observed deviations of 17% and 24% in the C-130 and C-5 MTOM predictions, respectively, are not considered unreasonable. On the contrary, they demonstrate a reasonable degree of accuracy given the high-level nature of the model. Therefore, the weight estimation model is deemed sufficiently accurate and valid for conceptual design purposes. While similar validation procedures were intended for other parameters such as wing area and system-level models, insufficient reference data for comparable aircraft precludes meaningful evaluation in those cases.

14.3. Verification & Validation of Eigenmotion Simulation Model

In addition to the design calculation model, a simulation model is developed to evaluate the eigenmotions of the design and assess its static and dynamic stability. This model is also subject to verification. As the aim is to present a conceptual design, full validation is not feasible, as it would require a physical prototype of the concept. Verification is carried out through unit and module testing of the code, followed by a system-level test. For the system test, a simplified dynamic system is analysed analytically. The same inputs are provided to the simulation model to determine whether identical outputs, such as matching eigenvalues, are produced. Agreement between the hand-calculated and model-derived results is taken as evidence of successful verification.

14.4. Verification & Validation of External Models

In the design process external computational models have been used. Naturally, these models have to be verified and validated as well.

To **verify** an external model, it is first integrated into the design framework. Verification involves running the model with the same input conditions as those provided by the original developers and comparing the outputs. If the reproduced results align closely with those published by the developers, the model can be considered verified, demonstrating that it has been implemented correctly and is functioning as intended.

For **validation**, the focus is on assessing whether the model accurately represents real-world physical behaviour. This typically involves investigating whether the model has been validated by its developers using experimental data. If no validation has been performed by the developer, it may be necessary to perform an independent validation. This is done by performing a real-world test, model the same test with the same inputs and comparing the results of both.

14.4.1. V&V of Used External Models

Although XFLR5, JavaFoil, and XROTOR have not undergone formal certification in the same sense as certified engineering software, such as Ansys Fluent and STAR-CCM+. The use of these tools in this project is justified based on their widespread adoption in academia and conceptual aircraft design contexts. These tools have been extensively validated against experimental data, as was done by Bergmann, and benchmarked with more established software [78]. Demonstrating reliable performance for conceptual and early-stage design purposes.

In addition, the open-source nature of the software tools allow for transparency in methods, and they offer a practical balance between accuracy and computational efficiency. For the scope of this DSE, focused on conceptual analysis rather than final certification, these tools provide sufficiently accurate insights to support informed design decisions. Therefore, due to the time restrictions of this project, these tools will not be further verified.

DATCOM was used to find the stability derivatives in Chapter 6 [33]. After the explanation of the method in the book, example inputs and the corresponding outputs were given to use for verification of the reader's code. Using this example data for every stability derivative, the code (`Derivatives_datcom_asym.py` and `Derivatives_datcom_sym.py`)[1] that calculates the stability derivatives using the DATCOM method is verified.

14.4.2. V&V of Take-off Performance Model

Verification

To verify the take-off performance model developed by Chinvorarat et al., each parameter presented in the original paper is compared with the corresponding output from the implemented model [70]. The first parameter assessed is the coefficient C_R as a function of C_v. Figure 14.3 and Figure 14.4 show the results from the original paper and the implemented model, respectively. As can be seen, the curves are identical, confirming the accuracy of the implementation.

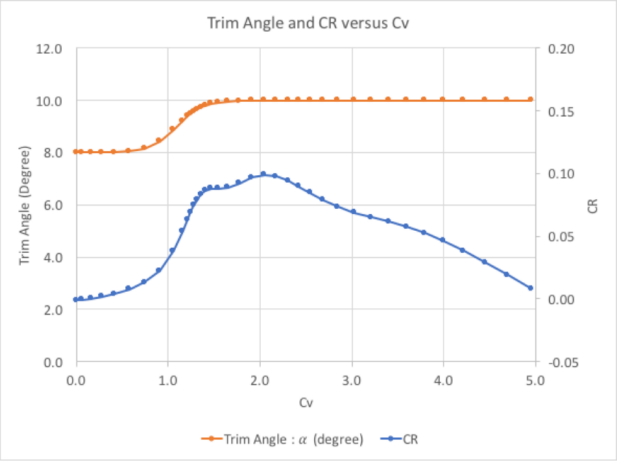

Figure 14.3: *C_R vs C_v from Chinvorarat et al. [70]*

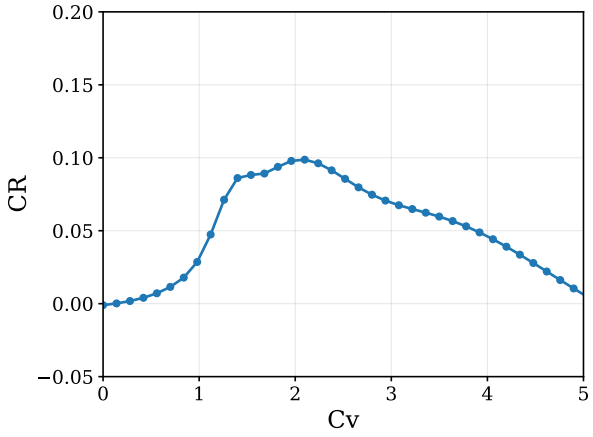

Figure 14.4: *C_R vs C_v from Implemented Model*

Next, the longitudinal forces are compared. Figure 14.5 and Figure 14.6 present the force profiles from the original paper and the implemented model, respectively. Discrepancies are observed in the Froude drag component and in the point at which the water resistance drops to zero. These differences are likely due to variations in hull geometry, as the implemented model is based on the hull design developed in this report, rather than the specific configuration used in the original study. Despite these deviations, the overall trends align closely, suggesting that the model has been correctly implemented.

[1] https://github.com/PaSieg0/Ekranoplan-DSE [Cited 17 June 2025]

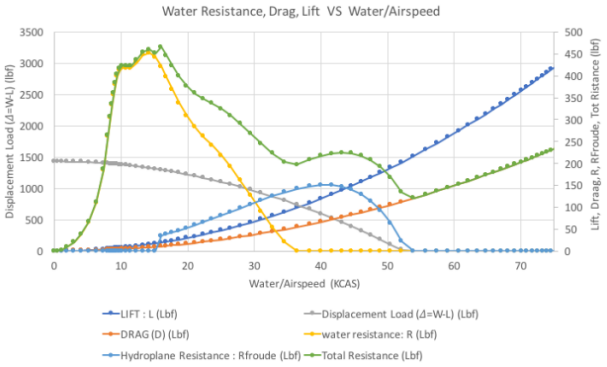

Figure 14.5: *Forces vs Airspeed from Chinvorarat et al. [70]*

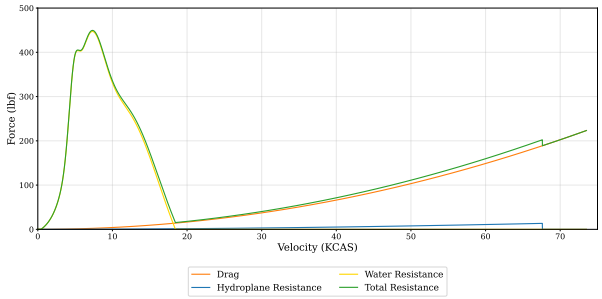

Figure 14.6: *Longitudinal Forces vs Airspeed from Implemented Model*

Finally, the vertical forces are examined. Figure 14.7 shows the vertical force components generated by the implemented model. Once again, the results are consistent with those reported by Chinvorarat et al., confirming the correctness of the model implementation. Based on these comparisons, the model is considered verified.

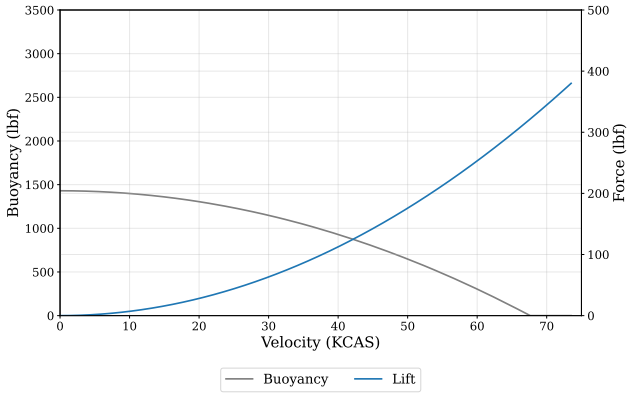

Figure 14.7: *Vertical Forces vs Airspeed from Implemented Model*

Validation

The model has been validated by Chinvorarat et al. through comparison with experimental take-off performance data. Specifically, the take-off distance predicted by the model is 893 $[ft]$, closely matching the measured value of 890 $[ft]$. This corresponds to a relative error of only 0.33%. However, it could still be insightful to validate the model with an outside aircraft with the implemented model. For now, the model is considered to be valid.

14.5. Product Verification

In this section, the product verification procedure is outlined. The main purpose of this verification is to ensure that the final design complies with the requirements. Table 14.4 presents the verification procedure to check the compliance of the design with the requirements. Next to requirement compliance, a sensitivity analysis is performed to verify the product. This analysis is performed on the different mission profiles of the design.

Verification on Requirements

Table 14.5 presents all requirement IDs along with the corresponding verification procedures, as established in the Midterm Report [25]. The rightmost column indicates whether each requirement is compliant. The meaning of the colour codes used is explained in Table 14.4. The table also references the chapter in which the evidence for compliance or non-compliance is provided. For requirements where compliance is still undetermined, the corresponding verification procedures will be carried out in a later stage of the design process.

Table 14.4: *Product Verification Legend*

Requirement is compliant
Requirement is not compliant
Compliance to be evaluated in future

Table 14.5: *Compliance Matrix*

Requirement	Verification procedure	Compliance
REQ-SUS.1	Use Breguet range equation to determine fuel consumption on design mission.	Chapter 11
REQ-SUS.2	Demonstrate zero emissions during on-water operations with batteries.	Chapter 9
REQ-SUS.3	Provide a way the uncoated parts could be reused.	Chapter 13
REQ-STB.1	Perform stability calculations and check if the aircraft is statically stable in stages of flight.	Chapter 6
REQ-STB.1.1	Check if C_{m_α} is negative in all stages of flight.	Chapter 6
REQ-STB.1.3	Check if C_{n_β} is positive in all stages of flight.	Chapter 6
REQ-STB.2	Perform dynamic stability calculations and check all stages of flight.	Chapter 7
REQ-STB.3	Show all control derivatives are the correct sign and magnitude.	Chapter 7
REQ-STB.3.1	Show control derivatives for pitch are the correct sign and magnitude.	Chapter 7
REQ-STB.3.2	Show control derivatives for roll are the correct sign and magnitude.	Chapter 7
REQ-STB.3.3	Show control derivatives for yaw are the correct sign and magnitude.	Chapter 7
REQ-TNL.1	Implement take-off model developed by Chinvorarat [70].	Chapter 11
REQ-TNL.1.1	Implement take-off model by Chinvorarat et al. [70].	Chapter 11
REQ-TNL.2	Perform stress analysis with landing loads.	Chapter 8
REQ-TNL.2.1	Demonstrate standstill within 2 $[km]$ after touchdown in sea state four.	
REQ-TNL.3	Perform stress analysis and power requirement calculations for beaching.	Chapter 8
REQ-TNL.3.1	Show enough power is generated to get on the beach.	Chapter 8
REQ-TNL.3.2	Show enough power is generated to get off the beach.	Chapter 8
REQ-TNL.3.3	Calculate taxi energy and compare with fuel onboard.	
REQ-TNL.3.4	Calculate taxi energy and compare with fuel onboard.	
REQ-TNL.4	Check if anchor is onboard.	Chapter 8
REQ-TNL.5	Determine landing loads with $1.3V_{stall}$ to analyse if the approach speed is correct.	
REQ-CAR.1	Stress analysis with 100 tonnes cargo at higher density.	Chapter 8
REQ-CAR.2	Check cargo volume and confirm by stress analysis.	Chapter 8
REQ-CAR.2.1	Confirm volume is sufficiently big.	Chapter 8
REQ-CAR.2.2	Confirm rectangle can fit along entire length.	Chapter 8
REQ-CAR2.3	Confirm cuboid can fit along entire length.	Chapter 8
REQ-CAR.3	Load/unload aircraft within time limit.	
REQ-CRU.1	Analyse if sufficient lift is created to fly below 100 $[ft]$	Chapter 6
REQ-CRU.2	Use Breguet equation to reach design range. $R = \frac{\eta_p}{g c_p} \frac{L}{D} \ln \frac{W_i}{W_f}$	Chapter 11
REQ-CRU.2.1	Show return mission is possible with remaining fuel.	Chapter 11
REQ-CRU.3	Use Breguet range equation for ferry range.	Chapter 11
REQ-CRU.4	Show aircraft can cruise at at least 180 $[kts]$.	Chapter 11
REQ-CRU.5	Cruise over sea state 3 without violating requirements.	Chapter 11
REQ-CRU.5.1	Wing must clear 1.5 m above wave peaks.	Chapter 8
REQ-CRU.6	Use Breguet equation and verify range is met at altitude. $RoC = \frac{P_a - P_r}{W}$	Chapter 11
REQ-CRU.7	Determine if climb rate is at least 1000 ft/min with 90 tonnes payload.	Chapter 11
REQ-CRU.7.1	Determine if climb gradient is at least 3.2%.	Chapter 11

Requirement	Verification procedure	Compliance
REQ-CRU.7.2	Determine if the climb gradient with OEI is at least 2.4% + n×0.3%.	Chapter 11
REQ-CRU.8	Determine stall speed with WIG and check if it is greater than 150 $[kts]$	Chapter 11
REQ-CRU.9	Determine stall speed at 10000 $[ft]$ and check if it is greater than 160 $[kts]$	Chapter 11
REQ-CRU.10	Use Breguet equation to reach obstacle avoidance mission range. $R = \frac{\eta_p}{g c_p} \frac{L}{D} \ln \frac{W_i}{W_f}$	Chapter 11
REQ-STR.1	Determine wing tip deflection.	Chapter 8
REQ-STR.2	Check stresses vs. yield stress.	Chapter 8
REQ-STR.3	Confirm fuel tank size using Breguet equation.	Chapter 8
REQ-STR.4	Perform vibrational analysis to check for flutter.	Chapter 8
REQ-STR.5	Show cargo hold is able to beach on the mean beach profile	Chapter 8
REQ-STR.6	Show the used coating is hydrophobic	Chapter 11
REQ-STR.6.1	Show the used coating is hydrophobic	Chapter 11
REQ-STR.6.2	Show the used coating is hydrophobic	Chapter 11
REQ-STR.7	Perform towing test in water.	Chapter 8
REQ-STR.8	Perfrom stress analysis with load factors from flight envelope.	Chapter 8
REQ-STR.8.1	Stress analysis with ultimate load factor.	Chapter 8
REQ-STR.8.2	Repeat stress analysis with ultimate factor.	Chapter 8
REQ-PWR.1	Power loading calculation including take-off performance.	Chapter 9
REQ-PWR.2	Determine engine clearance above water in test.	Chapter 9
REQ-PWR.3	Count engines in design.	Chapter 9
REQ-LIF.1	Perform flight cycle analysis.	
REQ-SHC.2	Verify 2035 EIS technology.	
REQ-SHC.3	Calculate MTOM and verify it is lower than 500 $[tonnes]$.	Chapter 5
REQ-SHC.4	Check all regulations.	
REQ-SHC.4.1	Check IMO regulations.	
REQ-SHC.4.2	Check CS-25 regulations.	
REQ-SHC.5	Attend June 27 symposium.	
REQ-SHC.7	Verify total operational cost is within bounds.	Chapter 12

15

Next Steps

In this chapter the post DSE phase of this project is discussed and recommendations given. In Section 15.1 a production plan is laid out giving some preliminary insight of the production of key systems/components. Section 15.2 presents the Design and development logic in the form of a flowchart alongside the cost breakdown of the general phases post DSE. The design and development logic gives a general overview of all steps to be taken to create a final operational design. Finally in Section 15.4 a timeline is layed out for a post DSE phase.

15.1. Manufacturing, Production and Integration Plan

In this section, the manufacturing, production and integration plan of the design is discussed. This consists of the wing, empennage and fuselage manufacturing and integration.

15.1.1. Wing & Empennage Structure Manufacturing

The wing of the aircraft is subject to immense loading and harsh marine conditions. Structural components must therefore be both mechanically robust and corrosion resistant, making manufacturing especially challenging. Aluminium 7075-T651 is selected for the highest-stressed wing components, including the wingbox structure, spars, and ribs. This alloy provides excellent strength, while the T651 condition offers improved resistance to stress corrosion cracking over the T6 condition, which is critical in marine environments. Wing ribs are roughly machined from solid 7075 blocks, heat treated to T651, then precision machined to their final geometry for structural integration.

The wing skin is produced from Aluminium 5052 sheet metal and does not feature varying thickness. The wingbox skin and spars, however, do have varying thicknesses, both on the main wing and empennage. To achieve this, sheets are initially rolled to the maximum required thickness, followed by post-rolling machining to locally reduce thickness where needed. Final contour machining is done on a gantry mill. Spars are made from 7075-T651 sheets, trimmed and joined using rivets into an I-beam configuration. Ribs and spars are coated in zinc chromate, while the outer wingbox skin receives an epoxy coating optimized for chloride resistance. A consistent coating thickness is applied across all components to reduce tooling and production cost.

Stringers are made from off-the-shelf Aluminium 7075-T651 extrusions, selected for manufacturability and reduced cost. While 7000-series alloys have higher strength, their poor ductility prevents use in complex extrusions, and machining or forging alternatives are impractical or costly. Due to the high engine placement, the wing upper surface is exposed to jet exhaust. A thermal analysis is needed to identify high-temperature zones. Aluminium 7075 loses mechanical strength above 180 [$°C$] [79], and its epoxy coating degrades at even lower temperatures. Therefore, Titanium Ti-6Al-4V is used near the engines. In regions exceeding 350 [$°C$], Inconel 718 or Rene 41 panels are required. Expansion joints must be included to manage thermal expansion mismatch. These titanium and nickel alloys are inherently corrosion-resistant and need no additional coatings.

Engine pylons are manufactured using titanium 3D printing. This approach minimizes material waste and enables topology optimization, reducing weight and improving sustainability. Empennage structures follow similar manufacturing methods as the wing and wing box.

15.1.2. Fuselage Manufacturing and Assembly

Fuselage construction includes skin, frames, and stringers. Frames of conventional large aircraft are milled from thick plates with lightning cutouts, requiring large gantry mills and leading to high material waste. In this design, the upper fuselage shares a nearly constant cross-section, allowing modular frame construction as sub-assemblies. Each fuselage frame is divided into three parts: upper, middle, and hull sections. Upper sections are stamped using a single mould for cost efficiency. Middle sections are constant-profile I-beams cut to length from 6061-T651 extrusions. Hull sections vary along the fuselage and are machined individually from 7075-T651 due to geometric differences. These three parts are joined with fasteners, sized for structural integrity. Stringers use off-the-shelf 7075 extrusions. Fuselage skin is made from rolled 7075-T651 sheet. The two hull steps, which contact sand during beaching, require high hardness and strength. To prevent wear or puncture, a sacrificial layer of high-hardness steel is riveted to these contact regions, absorbing impact and distributing compressive loads to the underlying aluminium.

15.1.3. Floaters Manufacturing

Inflatable buoys must be highly puncture- and abrasion-resistant. Though normally not in contact with the ground, they must withstand accidental terrain impact. Kevlar-reinforced polyurethane (PU) is chosen for its strength and durability. RF welding is used to join sections, with additional PU layers applied at seams and valves for robustness.

15.1.4. Integration Plan

The wing, fuselage, and empennage are built as sub-assemblies. Special care is required where dissimilar metals meet. Damaged coatings during assembly can expose aluminium to galvanic corrosion when in contact with higher-ranked metals such as titanium, especially in humid conditions. Final assembly occurs at a facility near water. Power systems (batteries, engines, APU, starter motors) are installed last due to their cost and risk. Once integrated, power systems are tested and debugged prior to certification trials. Water-tightness testing and taxi trials follow, with the aircraft entering the water via a ramp-mounted cart. The ramp slope prevents waves from reaching engine height during entry. Once certified for airworthiness, the aircraft can enter service.

15.2. Project Design and Development Logic and Cost Estimation

This section outlines the activities following the DSE. It begins by presenting the Project Design and Development logic in Subsection 15.2.1, detailing the structured approach taken to further develop the selected concept. Subsequently, a post-DSE cost breakdown is provided in Subsection 15.2.2, which estimates the expenses associated with completing the design and transitioning toward prototyping or production phases.

15.2.1. Design and development Logic

The Project Design & Development (PDD) logic, shown in Figure 15.1, illustrates the ordered activities for the project's post-DSE phases.

Since this project delivers only a preliminary design, additional work is necessary to achieve a finalised version. This predicted work is divided into three distinct phases: Design, Manufacturing, and Testing. A key focus has been placed on addressing the unique aspects of this aircraft compared to conventional designs, as exemplified by tasks such as D11, D32, and D56. The manufacturing phase is presented generally here, with more detailed information available in Section 15.1. Similarly, the testing phase remains general due to the project's evolving nature. Following these stages, standard aviation procedures, including certification, will be undertaken.

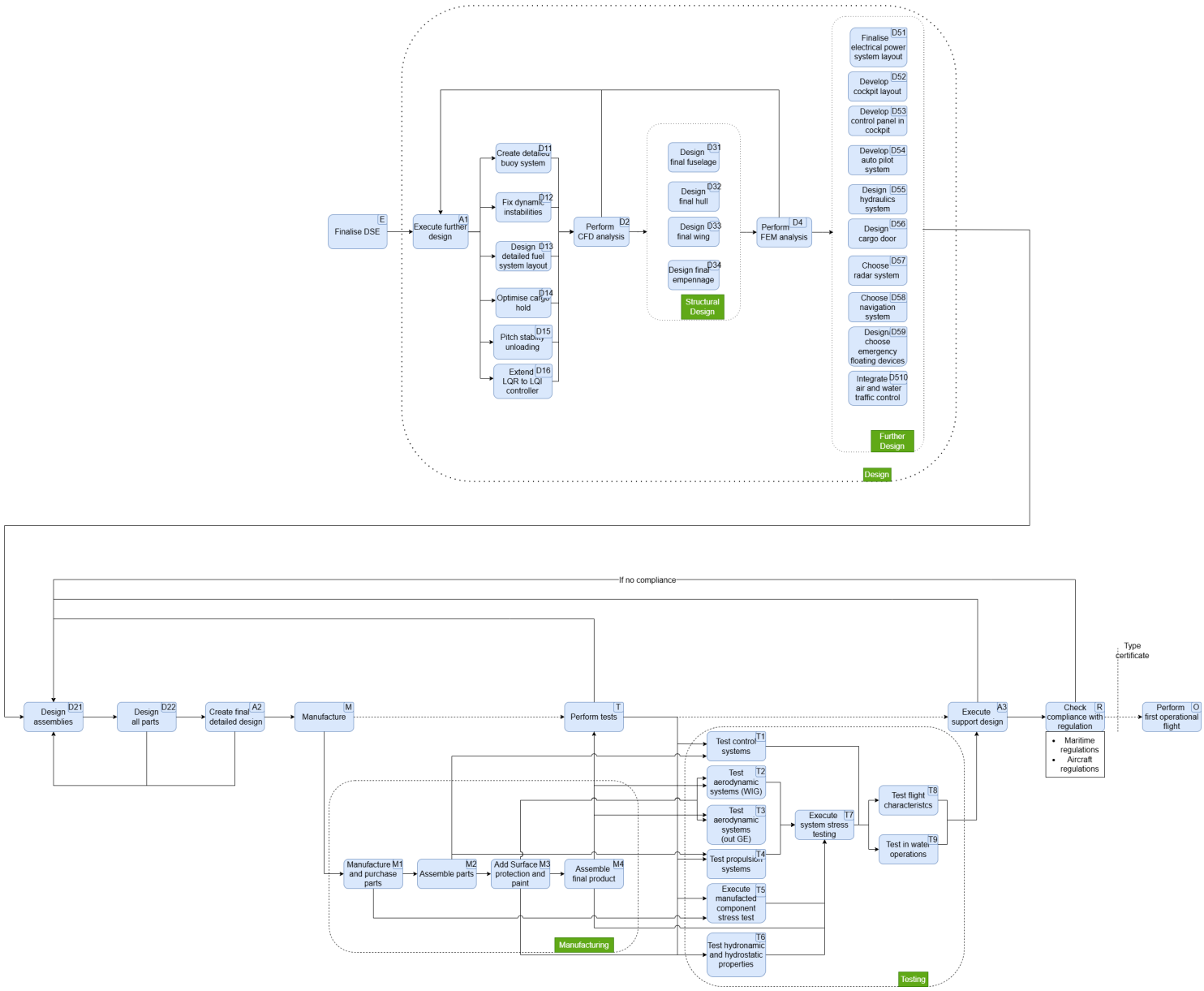

Figure 15.1: *Project Design and Development Logic Diagram*

15.2.2. Cost Breakdown structure

The cost breakdown structure in Figure 15.2 below, gives an overview of the different categories costs that are involved in the development and production of the aircraft. It is mostly concerned with the processes that take place after the DSE.

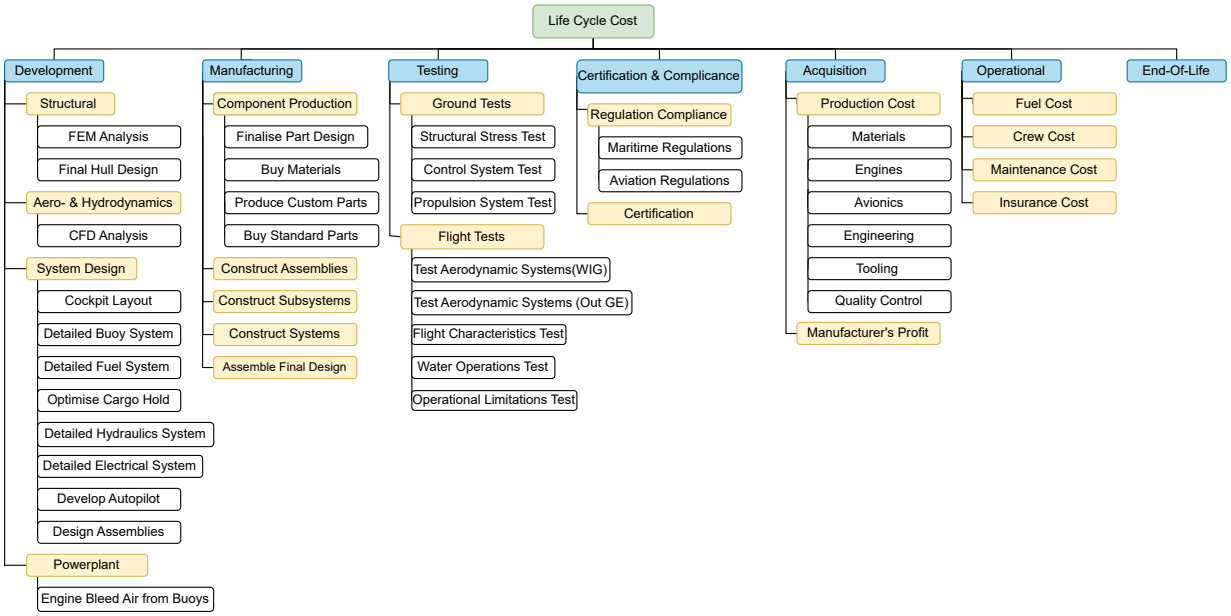

Figure 15.2: *Cost Breakdown Structure*

15.3. Recommended Research Areas

This section highlights key areas for further research following the DSE process. These topics were identified as having high potential to improve reliability or sustainability but could not be fully explored within the project time frame. Subsection 15.3.1 discusses the use of corrosion-resistant materials in critical areas exposed to the sea environment. In Subsection 15.3.2, the possibility of omitting the APU is explored, with alternatives for engine start and backup power proposed.

15.3.1. Detailed Material Selection

A recommended step in the post-DSE design process is to evaluate the use of advanced materials in critical structural and maintenance-sensitive areas. One of the major risks for this aircraft is corrosion resulting from continuous exposure to the marine environment. While several mitigation strategies have been proposed, such as protective coatingsSubsection 8.2.1, historical evidence suggests that corrosion remains a persistent issue for seaplanes and other maritime aircraft[80][81] . Even with careful design, the aggressive nature of the sea environment has often been a leading cause of premature degradation and failure.

To address this long-term reliability concern, future work should include dedicated research into material selection tailored for high-corrosion-risk zones. The sea environment poses a unique challenge, as saltwater exposure can reach areas of the aircraft that are not easily accessible for routine inspection or maintenance. This increases the likelihood of undetected corrosion-related damage over time. In particular, replacing aluminium with corrosion-resistant alternatives such as titanium or advanced composite materials in hard-to-reach or maintenance-intensive sections could significantly reduce the risk of failure and extend the aircraft's operational lifespan. An interesting solution to corrosion could be the novel technique of self healing polymers[82][83]. Additionally, integrating smart corrosion monitoring systems could help detect early signs of material degradation, enabling predictive maintenance and further enhancing safety.

15.3.2. Omitting APU

One of the recommended next steps in the post-DSE design process is to explore the possibility of omitting the Auxiliary Power Unit (APU). Eliminating the APU would improve the aircraft's sustainability by reducing emissions associated with its operation. Currently, the APU supplies bleed air to start one of the engines. Once that engine is running, the remaining engines are started using cross-bleed air. As described in Section 8.3, the aircraft is equipped with floaters to enable beaching. Due to time constraints, it was not feasible to estimate the amount of bleed air required to start the engines. With this data, a system could be developed to repurpose the compressed air stored in the floaters to start the first engine, potentially eliminating

the need for the APU. Provided the floaters can supply the required pressure without compression, this solution would not place additional demands on the battery system. Otherwise, the compressors used to inflate the floaters can compress the air. Doing this will require some additional battery power, which must be taken into account in the battery sizing.

Alternatively, an electrically powered compressor could be used to generate the necessary bleed air for engine start, replacing the APU in this function. While this would increase battery mass due to higher power demands, it remains a viable option. The additional battery weight must be weighed against the mass reduction from removing the APU and assessed alongside sustainability benefits.

Beyond engine start, the APU also serves as a backup power source for flight control systems in the event of engine failure. This role could similarly be fulfilled by the battery system, which would need to be resized accordingly. This again results in an increase in battery mass, which must be carefully evaluated in comparison to the removed APU weight. Ultimately, the three alternatives—using air from the floaters, employing an electric compressor, or retaining the APU—should be compared in a comprehensive trade-off analysis using appropriate criteria.

So, the aircraft's sustainability could be enhanced by replacing the APU with alternative systems. The suggested options should be analysed in detail in future design phases and compared to the current configuration to assess their respective advantages and disadvantages, potentially leading to a more environmentally friendly design.

15.3.3. Floor Loads

Another step in the development process would be to perform a complete analysis of the floor loading capacity of the aircraft. This would entail testing whether the floor may be loaded with concentrated point loads without any chance of failure, especially in loading and moving heavy machinery. Also considering the higher load cases (e.g. 2.5 g pull-up and 4.0 g landing load). Luckily, the current design of the fuselage is broad enough to offer sufficient interior space to include extra structural reinforcements in the fuselage hull if needed. Furthermore, the material to be used for floors must be carefully evaluated. It could be towards developing modular, replaceable floor tiles tailored to mission requirements, which would provide greater flexibility and convenience of maintenance for the cargo compartment. For instance, having the option to switch between a roller and a smooth floor.

15.4. Project Gantt Chart

The timeline for after this phase of the project is important, as this will give an estimation for when the aircraft will enter into service. These steps consist of four general phases: the detailed design phase, prototyping, testing and certification, and manufacturing. Their timeline is indicated in the Gantt chart at the end of the chapter. The duration is indicated by purple, possible delays with the dashed line, and a review in yellow. During a review, a decision is made whether the project can progress to the next phase, requires additional attention or redesign, or is discontinued entirely. The required amount of people (engineers or technicians) is displayed in the right most column.

The detailed design phase consists mainly of the Class III design of the aircraft. It also includes the production of a small scale model. Then, there is the prototype. The most important part of this phase, is the manufacturing of the prototype and testing if it is flight ready. After this, the aircraft can be tested in flight and get certified by sea and airworthiness authorities. Lastly, the ordered aircraft are manufactured. When delivered, the design team will provide assistance and support over a prolonged period of time. Using this timeline, it is estimated that the first flight will take place in September 2030. With the aircraft being expected to enter service in December 2035, which is highlighted by a yellow vertical bar in the Gantt chart.

Project Gantt Chart

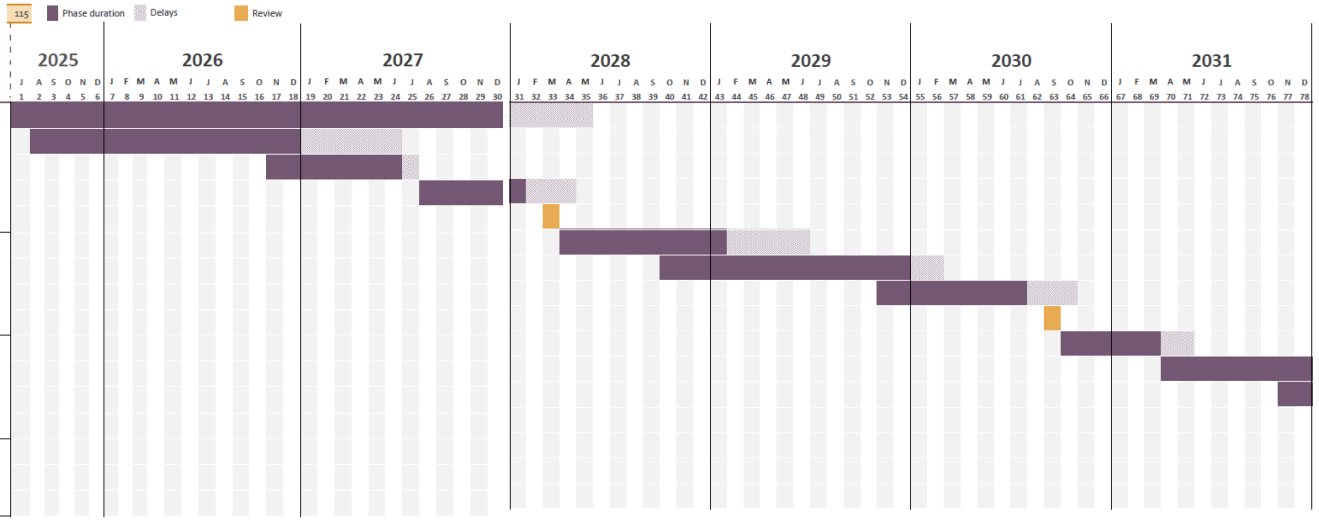

ACTIVITY	PLAN START	PLAN DURATION	ACTUAL START	ACTUAL DURATION	REQUIRED PEOPLE
Class III Detail Design	1	35	1	30	70
Supplier Engagement	2	23	2	17	15
Sub-Scale Model Design/Build	17	9	17	8	15
Sub-Scale Testing	26	9	26	6	20
Preliminary Design Review	150	1	33	1	25
Manufacturing preparation	34	15	34	10	25
Prototype Manufacturing	40	17	40	15	150
Ground/Water Static & Systems Testing	53	12	53	9	30
Flight Readiness Review	150	1	63	1	50
Flight Testing - Early Envelope	64	8	64	6	20
Flight Testing - Full Performance	70	12	70	10	40
Certification Flight Testing	77	25	77	22	60
Type Certification Review	150	1	100	1	25
Manufacturing preparation	101	12	101	9	150
First Customer Deliveries	107	13	107	11	400
Entry Into Service (EIS)	115	40	115	40	50

Project Gantt Chart

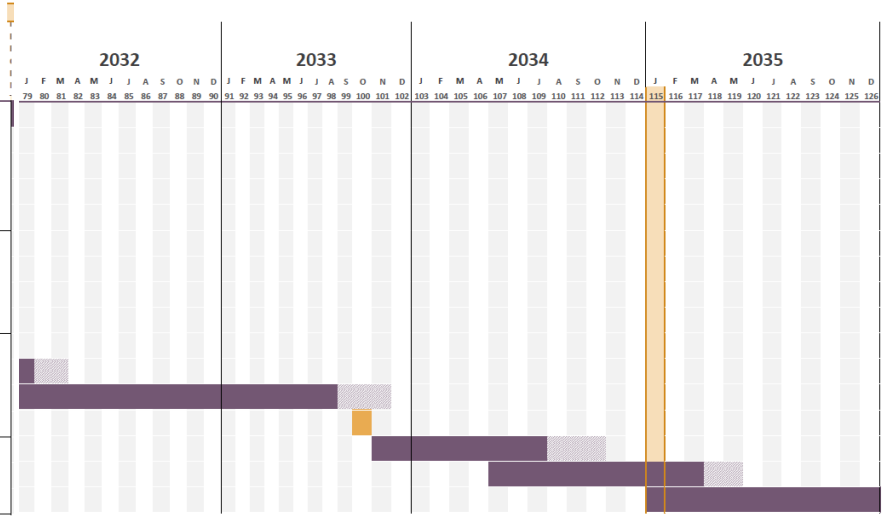

ACTIVITY	PLAN START	PLAN DURATION	ACTUAL START	ACTUAL DURATION	REQUIRED PEOPLE
Class III Detail Design	1	35	1	30	70
Supplier Engagement	2	23	2	17	15
Sub-Scale Model Design/Build	17	9	17	8	15
Sub-Scale Testing	26	9	26	6	20
Preliminary Design Review	150	1	33	1	25
Manufacturing preparation	34	15	34	10	25
Prototype Manufacturing	40	17	40	15	150
Ground/Water Static & Systems Testing	53	12	53	9	30
Flight Readiness Review	150	1	63	1	50
Flight Testing - Early Envelope	64	8	64	6	20
Flight Testing - Full Performance	70	12	70	10	40
Certification Flight Testing	77	25	77	22	60
Type Certification Review	150	1	100	1	25
Manufacturing preparation	101	12	101	9	150
First Customer Deliveries	107	13	107	11	400
Entry Into Service (EIS)	115	40	115	40	50

16

Technical Risk Assessment

In this chapter the technical risk assessment of the final phase in the DSE will be performed. First off the risks will be identified and it will be analysed what risks came up during the final phase. This together with the initial risk map will be presented in Section 16.1. Next up a mitigation and contingency plan will be set up for the critical risks in Section 16.2.

16.1. Risk Identification

In this section the risk identification will be performed. First off the risks that changed compared to the midterm phase will be identified. The main risk that changed is FPTR-6. This risk is changed from 'APU produces emissions' to 'Emission free APU is not compliant with current technological advancements'. Updating this risk was necessary, since the technological advancement of emission free APU's turns out to be a limiting factor in the design as mentioned in Section 9.3. Furthermore risk GTR-9 is changed from 'Final cost exceeds $98.5 million (FY2025 adjusted)' to 'Final cost is not competitive with the comparable aircraft'. This was due to the initial cost estimate being off. Also CRTR-17 has been added to accompany REQ-STB.3 and is 'The aircraft is not controllable'.
The risks have been adjusted in location in the risk map in accordance with the progress made in the final phase. The risk map has been displayed below in Figure 16.1.

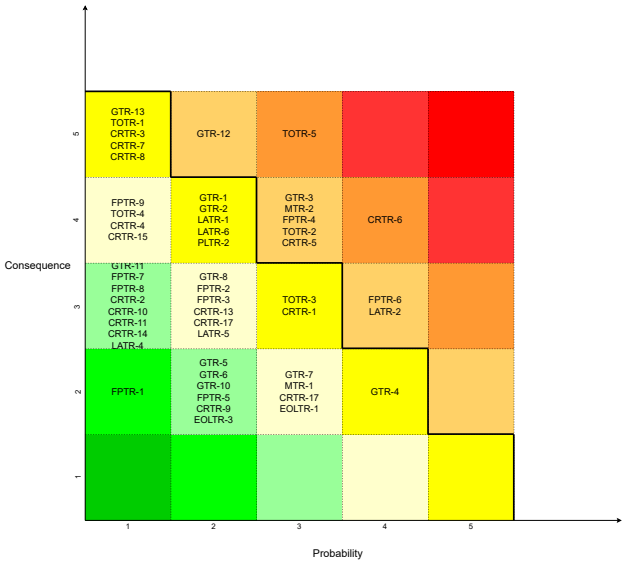

Figure 16.1: *Risk Map*

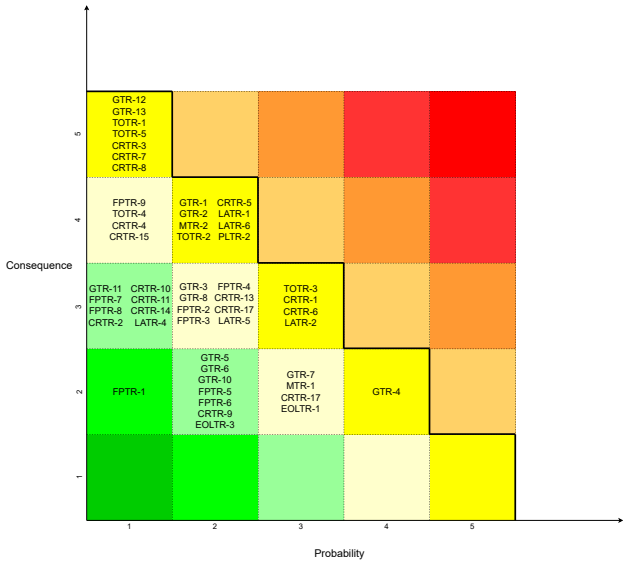

Figure 16.2: *Mitigated Risk Map*

For a detailed description of the risks one is referred to the midterm report[25]. Furthermore the acronyms for the risks are displayed in the nomenclature. Each of the risks in Figure 16.1 is assigned a probability of occurring and a level of consequence. The consequence scale from 1-5 with the description of a level below:

- 1: Negligible: The consequence would have a very minor impact on the project and would not affect the schedule, cost, or performance in a meaningful way.
- 2: Marginal: Although, the consequence could result in some cost increases or delays, it is unlikely to significantly influence the projects development.

- 3: Medium: The project's major deliverables may be impacted by the consequence, needing rework, budget modifications, or team effort to stay on track.
- 4: Critical: The project would be severely disrupted by the consequence, perhaps leading to significant delays or the need for extensive redesigns.
- 5: Catastrophic: The entire project might be in danger, which could result in mission failure, cancellation, or serious safety or legal consequences.

The probabilities scale linearly, meaning a level 1 probability has an approximate chance of occurrence between 0-20% and the level 5 probability has an 80-100% chance of occurring.
In Figure 16.1 one can also notice a black diagonal line going through the matrix. What the line represents, is the separation between non-acceptable (above) and acceptable (below) risks.

The changes in risk assessment, which lead to a crossing of a risk from the critical to a non-critical region are presented in Table 16.1.

Table 16.1: *Overview of Risks that Crossed Critical Line*

Code	Description	Comments
GTR-1	Statistical data is not accurate enough	Moved out of critical region due to validation being performed , yielding approximately expected results.
GTR-4	No public simulation tools are available	Moved out of critical region. In the scope of this project, simulation tools were found that yielded acceptable results
GTR-7	Not all design options are considered	Moved out of critical region. This risk concerned the baseline/midterm phase of this project, and is not as applicable to this phase of the report.
FPTR-6	APU produces emissions	Moved into critical region. Risk has been altered in order to better represent reality.
TOTR-1	WIG aircraft are more prone to stalling	Moved out of critical region. Wing analysis has been performed in Chapter 6, which gives more confidence on stalling behaviour.
CRTR-7	Plane is dynamically unstable after design.	Moved out of critical region. Stability analysis has been performed in Section 6.10 and in Subsection 7.2.5

16.2. Risk Mitigation

In this section the risk mitigation of the risks identified in Section 16.1. For the risks that exceed the critical black line a mitigation strategies is applied. These mitigation strategies are displayed in Table 16.2. Table 16.2 also displays an contingency plan and when the mitigation strategy is applied. The moment the mitigation strategy is applied is important in this report, since most mitigation strategies are now being applied.

Table 16.2: *Risk Mitigation Strategies*

#ID	Risk Description	Mitigation Strategy	When	Contingency Plan
GTR-3	Assumptions lead to high discrepancies.	Monitor and document all assumptions.	All design phases	Trace discrepancies back to specific assumptions.
GTR-12	Structure deforms too much due to aerodynamic forces.	Minimize deformation via aerodynamic and structural design.	Final and after DSE phase	Avoid conditions where aerodynamic deformation becomes excessive.
MTR-2	Corrosion from sea environment not considered properly.	Use appropriate corrosion free coating.	Final and after DSE phase	Avoid water contact.
FPTR-4	Outdoor storage accelerates degradation due to weather.	Implement corrosion free coating.	Final and after DSE phase	Use inside storage.
FPTR-6	Emission free APU is not compliant with current technological advancements.	Use APU that is available with current technology.	Final and after DSE phase	Consider APU decision carefully.
TOTR-2	Sea conditions too rough for take-off (oscillations).	Place the propellers and end plate buoys sufficiently high up.	Final and after DSE phase	Taxi to safer take-off location.
TOTR-5	Transition from hydrodynamic to aerodynamic operation is unstable.	Make stability a design priority.	After DSE phase	Establish and adhere to a safe flight envelope.
CRTR-5	Stalling during transition out of ground effect.	Treat the transition as a limiting factor.	After DSE phase	Reduce angle of attack.
CRTR-6	Icing risk at 10,000 ft due to fast climb from humid conditions.	Use active heating or hydrophobic coatings.	After DSE phase	Fly at lower altitudes to avoid icing.
LATR-2	Environmental factors: High sea states (waves), crosswinds, or floating debris can make landing unsafe.	Use appropriate shape for the fuselage and place propellers/buoys sufficiently high up.	Final and after DSE phase	Divert to alternate landing area with safer conditions or hold position until conditions improve.

When the mitigation strategies from Table 16.2 are applied the risk map in Figure 16.2 results.
Looking at the critical region in Figure 16.2 it can be observed that no critical risks are present. This is desired at the end of the project.

17

Conclusion

This report finalises the conceptual design of WAVE, or the Wing-in-Ground-Effect Aerial Vessel for Emergencies, developed to provide rapid, large-scale cargo transport in disaster zones without reliance on existing infrastructure. The aircraft is capable of delivering 90 $[tonnes]$ of payload over 2,000 $[nmi]$ at a cruise speed exceeding 180 $[kts]$, with the ability to climb to 10,000 $[ft]$ for obstacle avoidance.

Building upon the midterm configuration, WAVE has evolved through iterative system-level development into a robust high-wing layout optimised for ground effect operations. Key refinements include a shift from a forward cargo ramp to a rear loading configuration, enabled by the adoption of a twin vertical tail. This change accommodates direct access and improves cargo handling during beaching scenarios without compromising stability. The fuselage cross-section was adapted to support modular cargo configurations and to ensure both hydrodynamic and aerodynamic efficiency, while robust side buoys ensure safe flotation in varied sea conditions. The propulsion system consists of six TP400-D6 turboprop engines powering custom-designed, six-bladed propellers with a diameter of 6.00 $[m]$. The blades are carbon-reinforced with a 48.8 $[deg]$ twist, maximising propeller efficiency to 91.4%. An integrated lithium-ion battery system supports essential functions during water operations, ensuring compliance with the zero-emission requirement for on-water phases. Structurally, the wing box features four spars distributed across three cells to resist the extreme slamming force imposed by the wing tip buoy load case. A summary of the final design parameters is presented in Table 17.1.

Table 17.1: *Final Design Parameters of WAVE*

Parameter	Value	Unit	Parameter	Value	Unit
MTOM	302,700	$[kg]$	OEW	147,600	$[kg]$
Wing Area	706	$[m^2]$	Wing Span	75	$[m]$
Aspect Ratio	8	$[-]$	Fuel Economy	0.125	$[L/tonne/km]$
Fuselage Length	52	$[m]$	Engine	6×TP400-D6	$[-]$
Horizontal Tail Area	135	$[m^2]$	Vertical Tail Area (x2)	91	$[m^2]$
One-way Design Endurance	9	$[h]$	Ground Effect Efficiency	40%	$[-]$
Max Range (Ferry)	7360	$[nmi]$	Max Range (Obstacle Avoidance)	1830	$[nmi]$
Cruise Speed	234	$[kts]$	Service Ceiling	16,205	$[ft]$

Compared to the midterm configuration, the MTOM increased from 254,000 $[kg]$ to 302,700 $[kg]$, while the wing area grew from 508 $[m^2]$ to 706 $[m^2]$, resulting in enhanced lift capability necessary for the larger MTOM. The wing span was extended from 63.7 $[m]$ to 75 $[m]$, and more accurate mass distribution modelling improved the OEW estimate. Although, the final design process led to a worse fuel economy, rising from 0.070 to 0.125 $[L/tonne/km]$, WAVE remains well within sustainability benchmarks and outperforms reference aircraft for the corresponding design missions. These refinements reflect a transition from preliminary assumptions to a more mission-ready and robust configuration, addressing operational needs and system integration with greater fidelity. All primary systems have been verified for accuracy, and the aircraft is fully compliant with all mission and performance requirements. Further design phases will involve CFD validation, more detailed structural analysis, and manufacturing planning.

In conclusion, WAVE is a capable, efficient, and adaptable solution for rapid response in crisis environments, fulfilling the project objective and satisfying the need outlined in the mission need statement.

Bibliography

[1] Phillips, W. F., and Hunsaker, D. F., "Lifting-Line Predictions for Induced Drag and Lift in Ground Effect," , 2013.

[2] Torenbeek, E., *Synthesis of Subsonic Airplane Design*, Delft University Press, Dordrecht, The Netherlands, 1982.

[3] Brakenridge, G. R., "Global Active Archive of Large Flood Events, 1985-Present," https://floodobservatory.colorado.edu/Archives/index.html, apr 2025. Accessed April 2025.

[4] Lowman, P.D., jr, "A global tectonic activity map with orbital photographic supplement," Tech. Rep. 19810011153, NASA, 2013. URL https://ntrs.nasa.gov/citations/19810011153, revision 05.

[5] Luijendijk, A., Hagenaars, G., Ranasinghe, R., Donchyts, G., and Aarninkhof, S., "The State of the World's Beaches," *Scientific Reports*, Vol. 8, 2018. doi:10.1038/s41598-018-24630-6.

[6] Hallin, C., "Long-term beach and dune evolution Development and application of the CS-model," Ph.D. thesis, 05 2019. doi:10.13140/RG.2.2.36390.37447.

[7] Dolan, T. J., and Dean, R. G., "Multiple longshore sand bars in the upper Chesapeake Bay," *Estuarine, Coastal and Shelf Science*, Vol. 21, No. 5, 1985, pp. 727–743. doi:https://doi.org/10.1016/0272-7714(85)90069-1, URL https://www.sciencedirect.com/science/article/pii/0272771485900691.

[8] Bosboom, J., and Stive, M. J., *Coastal Dynamics*, TU Delft, 2021.

[9] Vos, K., Deng, W., Harley, M. D., Turner, I. L., and Splinter, K. D. M., "Beach-face slope dataset for Australia," *Earth System Science Data*, Vol. 14, No. 3, 2022, pp. 1345–1357. doi:10.5194/essd-14-1345-2022.

[10] Okazaki, S.-i., and Sunamura, T., "Quantitative Predictions for the Position and Height of Berms," *2*, 1994.

[11] El Assal, A. M., Stoll, M., de Salas, J., Pjetri, M., Sigolo, L., Moon, O., Guo, Q., Nijdam, S., Antens, T., and Schorren, V., "Baseline Report D.S.E. Group 2: Airborne Emergency Disaster Response Vehicle," Tech. rep., Delft University of Technology, 2025. Design Synthesis Exercise, Group 2.

[12] Roskam, J., *Airplane Design Part III: Layout Design of Cockpit, Fuselage, Wings and Empennage: Cutaways and Inboard Profiles*, DARcorporation, Lawrence, Kansas, 1986.

[13] Dalmora, G. P. V., Borges Filho, E. P., Maraschin Conterato, A. A., Roso, W. S., Pereira, C. E., and Dettmer, A., "Methods of corrosion prevention for steel in marine environments: A review," *Results in Surfaces and Interfaces*, Vol. 18, 2025, p. 100430. doi:https://doi.org/10.1016/j.rsurfi.2025.100430, URL https://www.sciencedirect.com/science/article/pii/S2666845925000170.

[14] Rees, A. B., Gallagher, A., Wright, L. A., Wood, J., Cathery, T., Harrison, B., Down, C., and Comber, S., "Leisure craft sacrificial anodes as a source of zinc and cadmium to saline waters," *Marine Pollution Bulletin*, Vol. 158, 2020, p. 111433. doi:https://doi.org/10.1016/j.marpolbul.2020.111433, URL https://www.sciencedirect.com/science/article/pii/S0025326X20305518.

[15] Vallejo-Olivares, A., Høgåsen, S., Kvitthyl, A., and Kvithyld, A., "Thermal De-coating Pre-treatment for Loose or Compacted Aluminum Scrap and Consequences for Salt–Flux Recycling," *Journal of Sustainable Metallurgy*, Vol. 8, No. 4, 2022, pp. 1485–1497. doi:10.1007/s40831-022-00612-x, URL https://doi.org/10.1007/s40831-022-00612-x.

[16] Raymer, D. P., *Aircraft Design: A Conceptual Approach*, 2nd ed., American Institute of Aeronautics and Astronautics, 1992.

[17] Mooij, E., and Verhagen, W., "DSE-PM-SE Workshop 2 (Q2 2024-2025): Project Management and Systems Engineering in the DSE," Delft Aerospace Engineering Course Material, 2025. Slides adapted from Michel van Tooren and Rob Hamann.

[18] Leonard, A., and Others, "Breakthroughs in satellite remote sensing of floods," *Frontiers in Remote Sensing*, Vol. 1, No. December, 2023, pp. 1–18. URL https://www.frontiersin.org/articles/10.3389/frsen.2023.1280654/full, review highlighting operational readiness of satellite flood mapping since 1970s.

[19] Airbus SAS, "A380-800 Flight Deck and Systems Briefing for Pilots," Tech. rep., Airbus SAS, Customer Services Directorate, Blagnac, France, March 2006. Informational brochure, STL 945.1380/05 Issue 2.

[20] Collins General Aviation Division, *Collins TWR-850 Turbulence Weather Radar System: Pilot's Guide*, Rockwell Collins, Cedar Rapids, IA, 2nd ed., 1992. Includes WXI-711A controls and displays.

[21] Leonardo Electronics, "Osprey Multi-Mode AESA Surveillance Radar," Product datasheet / technical report, Leonardo, 2025. URL https://www.leonardo.us/hubfs/Product%20Brochures/Osprey%20AESA%20-%20Datasheet%20LQ%20%28mm08527%29.pdf, second-generation X-band AESA with STM, SAR, MTI, E-Scan beam steering.

[22] WaveAerospace, Inc., "Falcon II LE Overview Brochure," https://www.waveaerospace.com, September 2024. Version: 9-15-24.

[23] Song, J., Bagoren, O., Andigani, R., Sethuraman, A. V., and Skinner, K. A., "TURTLMap: Real-time Localization and Dense Mapping of Low-texture Underwater Environments with a Low-cost Unmanned Underwater Vehicle," , 2024. URL https://arxiv.org/abs/2408.01569.

[24] Airbus, "The Importance of the Pre-Flight Flight Controls Check," *Safety First – The Airbus Safety Magazine*, , No. 36, 2023, pp. 10–13. URL https://safetyfirst.airbus.com/the-importance-of-the-pre-flight-flight-controls-check/, accessed: 2025-06-17.

[25] El Assal, A. M., Stoll, M., de Salas, J., Pjetri, M., Sigolo, L., Moon, O., Guo, Q., Nijdam, S., Antens, T., and Schorren, V., "Midterm Report D.S.E. Group 2: Airborne Emergency Disaster Response Vehicle," Tech. rep., Delft University of Technology, 2025. Design Synthesis Exercise, Group 2.

[26] Canamar, A., and Smrcek, L., "Advance Seaplane Conceptual Design Adapting Trimaran Boat Hull Concept," *28th International Congress of the Aeronautical Sciences (ICAS)*, ICAS, 2012. URL https://www.icas.org/icas_archive/ICAS2012/PAPERS/198.PDF, university of Glasgow.

[27] Pratt & Whitney, "APS3200 Auxiliary Power Unit," , 2021. https://filecache.mediaroom.com/mr5mr_prattwhitney/183870/download/APS3200.pdf [Accessed 18 June 2025].

[28] Liang, Y., Alan, B., and Johnny, D., "WIG craft and ekranoplan ground effect craft technology," , 2010.

[29] Bergmann, O., Götten, F., Braun, C., and Janser, F., "Comparison and evaluation of blade element methods against RANS simulations and test data," , 2021.

[30] Lange, R., and Moore, J., *Large wing-in-ground effect transport aircraft*, 2012. doi:10.2514/6.1979-845, URL https://arc.aiaa.org/doi/abs/10.2514/6.1979-845.
[31] Yang, W., and Yang, Z., "Aerodynamic investigation on tiltable endplate for WIG craft," *Aircraft Engineering and Aerospace Technology*, Vol. 84, No. 1, 2012, pp. 4–12. doi:10.1108/00022661211194933.
[32] Oliviero, F., "Lift Drag Estimation Methods - Aerospace Design and Systems Engineering Elements II – AE2111-II," , 2023.
[33] Corporation, M. D., "USAF STABILITY AND CONTROL DATCOM," , 1978.
[34] Lee, S. H., and J, L., "Optimization of Three-Dimensional Wings in Ground EffectUsing Multiobjective Genetic Algorithm," , 2011.
[35] Torenbeek, E., "Advanced Aircraft Design," , 2013.
[36] Scholz, D., "11 Empennage sizing," , 2021.
[37] Mulder, J., "AE3202 Flight Dynamics: Lecture notes," , 2013. Delft University of Technology.
[38] Cook, M. V., "Chapter 13 - Aerodynamic Stability and Control Derivatives," *Flight Dynamics Principles (Third Edition)*, edited by M. V. Cook, Butterworth-Heinemann, 2013, third edition ed., pp. 371–439. doi:https://doi.org/10.1016/B978-0-08-098242-7.00013-4, URL https://www.sciencedirect.com/science/article/pii/B9780080982427000134.
[39] Al-Shamma, O., Ali, R., and Hasan, H., "Employing control surface model in preliminary aircraft design software," *International Journal of Engineering and Technology(UAE)*, Vol. 7, 2018, pp. 135–140. doi:10.14419/ijet.v7i2.31.13426.
[40] European Union Aviation Safety Agency (EASA), *Certification Specifications and Acceptable Means of Compliance for Large Aeroplanes (CS-25)*, EASA, Cologne, Germany, 12 2023. URL https://www.easa.europa.eu/en/document-library/certification-specifications/cs-25-amendment-28, amendment 28.
[41] "Chapter 7 - Seakeeping," *The Maritime Engineering Reference Book*, edited by A. F. Molland, Butterworth-Heinemann, Oxford, 2008, pp. 483–577. doi:https://doi.org/10.1016/B978-0-7506-8987-8.00007-X.
[42] Goetzendorf-Grabowski, T., Mieszalski, D., and Marcinkiewicz, E., "Stability analysis using SDSA tool," *Progress in Aerospace Sciences*, Vol. 47, No. 8, 2011, pp. 636–646. doi:https://doi.org/10.1016/j.paerosci.2011.08.007, URL https://www.sciencedirect.com/science/article/pii/S037604211100073X, special Issue - Modeling and Simulating Aircraft Stability and Control.
[43] Lancaster, P., and Rodman, L., *Algebraic riccati equations*, Clarendon press, 1995.
[44] Atmaca, D., Stroosma, O., and Kampen, E.-J. V., *Piloted Evaluation of Flying-V with Incremental Nonlinear Dynamic Inversion and Envelope Protection*, 2025. doi:10.2514/6.2025-0973, URL https://arc.aiaa.org/doi/abs/10.2514/6.2025-0973.
[45] Fujiwara, G., and Nguyen, N., "Adaptive Aeroelastic Wing Shape Optimization for High-Lift Configurations," 2015. doi:10.13140/RG.2.1.2308.8484.
[46] International Martime Organisation (IMO), *Guidelines for Wing-in-Ground Craft*, IMO, London, United Kingdom, 5 2018. URL https://wwwcdn.imo.org/localresources/en/OurWork/Safety/Documents/MSC.1-CIRC.1592.pdf, mSC.1/Circ.1592.
[47] Kutz, M., *Handbook of Environmental Degradation of Materials*, 2nd ed., William Andrew Publishing, Oxford, 2012.
[48] Boyer, R., *Titanium for Engineering Applications*, ASM International, 1996.
[49] Niinomi, M., "Titanium alloys: characteristics and applications," *Materials Science and Engineering: A*, Vol. 243, No. 1–2, 2003, pp. 231–236.
[50] Donachie, M., *Titanium: A Technical Guide*, ASM International, 2000.
[51] Latash, M., *Biomechanics and Motor Control: Defining Central Concepts*, Elsevier, 2016.
[52] Matthews, G., *Welding Titanium*, Woodhead Publishing, 2012.
[53] Reed, R., *The Superalloys: Fundamentals and Applications*, Cambridge University Press, 2008.
[54] Sims, C., Stoloff, N., and Hagel, W., *Superalloys II: High-Temperature Materials for Aerospace and Industrial Power*, John Wiley & Sons, 1987.
[55] Donachie, M., and Donachie, S., *Superalloys: A Technical Guide*, ASM International, 2002.
[56] Taylor, S., *Encyclopedia of Materials: Science and Technology*, Elsevier Science, Oxford, 2001.
[57] Rosseland, B. O., Eldhuset, T. D., and Staurnes, M., "Environmental Effects of Aluminium," *Environmental Geochemistry and Health*, Vol. 12, No. 1–2, 1990, pp. 17–27. doi:10.1007/BF01734045, pMID: 24202562.
[58] Kamal, K., *Handbook of Fly Ash*, 1st ed., Butterworth–Heinemann, Oxford, 2021.
[59] Chopra, I., Ola, S. K., Priyanka, Dhayal, V., and Shekhawat, D., "Recent Advances in Epoxy Coatings for Corrosion Protection of Steel: Experimental and Modelling Approach—A Review," *Materials Today: Proceedings*, Vol. 62, 2022, pp. 1658–1663. doi:10.1016/j.matpr.2022.04.659, URL https://www.sciencedirect.com/science/article/pii/S2214785322028267, international Conference on Recent Advances in Modelling and Simulations Techniques in Engineering and Science.
[60] Thurston, D. B., *Design For Flying*, 2nd ed., McGraw-Hill, South Portland, Maine, 1994.
[61] Roskam, J., *Airplane Design Part VI: Preliminary Calculation of Aerodynamic, Thrust and Power Characteristics*, Roskam's Airplane Design Series, DARcorporation, Lawrence, Kansas, 2007. Section APP-C3, covering hydrodynamic design and considerations for seaplanes.
[62] Smiley, R. F., and Haines, G. A., "Comparison of Water-Load Distributions Obtained During Seaplane Landings with Bureau of Aeronautics Specifications," Tech. Rep. NACA RM SL9G01, National Advisory Committee for Aeronautics (NACA), August 1949. URL https://ntrs.nasa.gov/citations/19930086880, research Memorandum for the Bureau of Aeronautics, Department of the Navy.
[63] Siemes, C., "AE3212-I Flight Dynamics: Frames and Transformations," https://brightspace.tudelft.nl/, 2025. Lecture slides, based on material by Erwin Mooij and Marc Naeije.
[64] Megson, T., *Aircraft Structures for Engineering Students*, 6th ed., Elsevier Aerospace Engineering Series, Butterworth-Heinemann, 2016.

[65] Dimitriadis, G., *Introduction to Nonlinear Aeroelasticity*, Aerospace Series, John Wiley & Sons Ltd, Chichester, West Sussex, UK, 2017. URL https://www.wiley.com/go/Dimitriadis/NonlinearAeroelasticity.

[66] Gur, O., *Propeller Design*, American Institute of Aeronautics and Astronautics, 2024.

[67] European Aviation Safety Agency (EASA), "EASA Type-Certificate Data Sheet No. P.012 – Ratier-Figeac FH385/FH386 Series Propellers," Type-Certificate Data Sheet (TCDS) P.012, Issue 04, EASA, Cologne, Germany, 12 2015. URL https://www.easa.europa.eu/sites/default/files/dfu/TCDS%20P%20012%20-%20FH385-FH386%20Series%20-%20Issue04%20_20151512_1.0.pdf.

[68] Moir, I., and Seabridge, A., *Aircraft Systems: Mechanical, Electrical and Avionics Subsystems Integration*, 3rd ed., Wiley, Chichester, UK, 2008.

[69] Anderson, J. D., *Aircraft Performance and Design*, McGraw-Hill, New York, NY, 1999.

[70] Chinvorarat, S., Watjatrakul, B., Nimdum, P., Sangpet, T., and Vallikul, P., "Takeoff Performance Analysis of a Light Amphibious Airplane," *IOP Conference Series: Materials Science and Engineering*, Vol. 1137, No. 1, 2021, p. 012010. doi:10.1088/1757-899X/1137/1/012010, URL https://dx.doi.org/10.1088/1757-899X/1137/1/012010.

[71] Scholz, D., "Understanding the aircraft mass growth and reduction factor," *Proceedings of the 15th European Workshop on Aircraft Design Education (EWADE 2020) and Research and Education in Aircraft Design (READ 2020), Warsaw, Poland*, 2020, pp. 21–23.

[72] Voth, V., Lübbe, S. M., and Bertram, O., "Estimating Aircraft Power Requirements: A Study of Electrical Power Demand Across Various Aircraft Models and Flight Phases," , 2024.

[73] Tamburri, M. N., Soon, Z. Y., Scianni, C., Øpstad, C. L., Oxtoby, N. S., Doran, S., and Drake, L. A., "Understanding the Potential Release of Microplastics from Coatings Used on Commercial Ships," *Frontiers in Marine Science*, Vol. 9, 2022, p. 1074654. doi:10.3389/fmars.2022.1074654, URL https://www.frontiersin.org/articles/10.3389/fmars.2022.1074654/full.

[74] Gondikas, A., Mattsson, K., Asplund, M., and Sobek, A., "Methods for the detection and characterization of boat paint microplastics in the marine environment," *Frontiers in Environmental Chemistry*, Vol. 4, 2023, p. 1090704. doi:10.3389/fenvc.2023.1090704, URL https://www.frontiersin.org/articles/10.3389/fenvc.2023.1090704/full.

[75] Xue, C., Yang, Y., Zhao, P., Wei, D., Gao, J., Sun, P., Huang, Z., and Jia, J., "Impact of Ship Traffic on the Characteristics of Shelf Sediments: An Anthropocene Prospective," *Frontiers in Marine Science*, Vol. 8, 2021, p. 678845. doi:10.3389/fmars.2021.678845, URL https://www.frontiersin.org/articles/10.3389/fmars.2021.678845/full.

[76] Liu, J., Song, X., and Zeng, X., "An integrated assessment of provincial industrial ecology: A case study of Jiangsu Province," *Journal of Industrial Ecology*, Vol. 28, No. 2, 2024, pp. 535–550. doi:10.1111/jiec.13304, URL https://onlinelibrary.wiley.com/doi/abs/10.1111/jiec.13304.

[77] Jiang, B., Wang, L., Zhou, G., Liu, X., Lu, H., Zhu, G., Du, J., Zhao, C., Su, B., Wang, B., Chen, R., and Su, Y., "Environmentally Friendly and Simple Recycling of Titanium Alloy Scrap via Deoxygenation with Hybrid Hydrogen Plasma Arc," *Advanced Science*, Vol. 12, No. 10, 2025, p. 2414747. doi:https://doi.org/10.1002/advs.202414747, URL https://advanced.onlinelibrary.wiley.com/doi/abs/10.1002/advs.202414747.

[78] Bergmann, O., Götten, F., Braun, C., et al., "Comparison and evaluation of blade element methods against RANS simulations and test data," *CEAS Aeronautical Journal*, Vol. 13, 2022, pp. 535–557. doi:10.1007/s13272-022-00579-1.

[79] Butt, M., Ullah, S., Khan, M. R., Ahmad, S., and Ilyas, S. Z., "Effect of thermal exposure on the strength and stress relaxation response of AA-7075-T6 material," *Materials Chemistry and Physics*, Vol. 270, 2021, p. 124791. doi:https://doi.org/10.1016/j.matchemphys.2021.124791, URL https://www.sciencedirect.com/science/article/pii/S0254058421005745.

[80] Czaban, M., "Aircraft corrosion–review of corrosion processes and its effects in selected cases," *Fatigue of Aircraft Structures*, 2018.

[81] Hoffman, M. E., and Hoffman, P. C., "Corrosion and fatigue research—structural issues and relevance to naval aviation," *International Journal of Fatigue*, Vol. 23, 2001, pp. 1–10.

[82] Yimyai, T., Crespy, D., and Rohwerder, M., "Corrosion-responsive self-healing coatings," *Advanced Materials*, Vol. 35, No. 47, 2023, p. 2300101.

[83] Stankiewicz, A., Szczygieł, I., and Szczygieł, B., "Self-healing coatings in anti-corrosion applications," *Journal of Materials Science*, Vol. 48, 2013, pp. 8041–8051.

A

Inputs Class II Weight Estimation

This appendix contains two tables with all inputs used in the component weight estimation by Raymer [16].

Table A.1: *Inputs for Component Weight Estimation (1/2)*

Parameter	Value	Unit
fudge factor	1.25	[-]
A	8	[-]
A_h	4.5	[-]
A_v	1.5	[-]
B_h	74.11	$[ft]$
B_w	244.43	$[ft]$
D	22.73	$[ft]$
F_w	18.70	$[ft]$
H_t/H_v	1	[-]
I_y	$4.45{\cdot}10^9$	$[lb \cdot ft^2]$
K_{door}	1.12	[-]
K_{Lg}	1	[-]
K_{ng}	1.017	[-]
K_r	1.133	[-]
K_{tp}	0.793	[-]
K_{uht}	1.143	[-]
λ	0.4	[-]
L_f	171.01	$[ft]$
$\Lambda_{c/4}$	0	$[deg]$
$\Lambda_{c/4_{ht}}$	0	$[deg]$
$\Lambda_{c/4_{vt}}$	15	$[deg]$
K_{ws}	0.0	[-]
L	171.01	$[ft]$
L_a	883.33	$[ft]$
L_t	41.01	$[ft]$
K_y	12.30	$[ft]$
K_z	41.01	$[ft]$
N_c	5	[-]
N_{en}	6.0	[-]
L_{ec}	283.13	$[ft]$
N_f	3	[-]
N_{gen}	2	[-]

Table A.3: *Inputs for Component Weight Estimation (2/2)*

Parameter	Value	Unit
N_{Lt}	13.78	$[ft]$
N_m	2	[-]
N_p	5	[-]
N_t	2	[-]
N_w	4.27	$[ft]$
N_z	3.75	[-]
R_{kva}	50	$[kV{\cdot}A]$
S_c	2119.14	$[ft^2]$
S_{cs}	1606.41	$[ft^2]$
S_{csw}	863.20	$[ft^2]$
S_e	863.20	$[ft^2]$
S_f	10113.76	$[ft^2]$
S_{ht}	1220.43	$[ft^2]$
S_n	1653.84	$[ft^2]$
S_{vt}	835.06	$[ft^2]$
S_w	7468.54	$[ft^2]$
$(t/c)_{root}$	0.1426	[-]
V_p	0	$[gal]$
V_{pr}	0	$[ft^3]$
V_t	23892.88	$[gal]$
V_i	23892.88	$[gal]$
W_c	220462.26	$[lb]$
W_{dg}	655823.29	$[lb]$
W_{ec}	4409.25	$[ln]$
W_{en}	4188.78	$[lb]$
W_{uav}	1400	$[lb]$
$W_{APU_{uninstalled}}$	3606.76	$[lb]$